

AD-A053 005

ILLINOIS UNIV AT URBANA-CHAMPAIGN ELECTROMAGNETICS LAB
STUDY OF MICROSTRIP ANTENNAS, MICROSTRIP PHASED ARRAYS, AND MIC--ETC(U)
DEC 77 Y T LO, D SOLOMON, F R ORE
F19628-76-C-0140

F/G 9/5

UNCLASSIFIED

UIEM-77-23

RADC-TR-77-406

NL

1 OF 2
AD
A053005



2
SC

AD A 053005

18
19
RADC TR-77-406

6
STUDY OF MICROSTRIP ANTENNAS, MICROSTRIP PHASED ARRAYS, AND
MICROSTRIP FEED NETWORKS,



Electromagnetics Laboratory
Department of Electrical Engineering
University of Illinois at Urbana-Champaign
Urbana, Illinois 61801

11 Dec 77

13 1717

DECEMBER 1977

10
Y. T. /Lo, D. /Solomon, F. R. /Gre,
D. D. /Harrison G. A. /Deschamps

9
Final Report, 2 Feb 1976 - 9 Sep 1977
Contract No. F19628-76-C-0140

15
16 2305
17 J4

Distribution Unlimited

14 UIEM-77-23, UILU-ENG-77-2265

Prepared for

ADVANCED RESEARCH PROJECTS AGENCY
1400 Wilson Boulevard
Arlington, Va. 22209

ROME AIR DEVELOPMENT CENTER
Deputy for Electronic Technology (RADC/ETER)

DDC
RECEIVED
APR 20 1978
B

DISTRIBUTION STATEMENT A
Approved for public release;
Distribution Unlimited

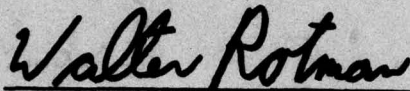
408 102

AD No.
DDC FILE COPY

Title of Report: Study of Microstrip Antennas, Microstrip Phased
Arrays, and Microstrip Feed Networks

This Technical Report has been reviewed and approved for publication.

APPROVED:



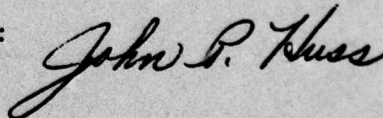
WALTER ROTMAN, Chief
Antennas and RF Components Branch
Electromagnetic Sciences Division

APPROVED:



ALLAN C. SCHELL, Acting Chief
Electromagnetic Sciences Division

FOR THE COMMANDER:



Plans Office

UNCLASSIFIED

SECURITY CLASSIFICATION OF THIS PAGE (When Data Entered)

REPORT DOCUMENTATION PAGE		READ INSTRUCTIONS BEFORE COMPLETING FORM
1. REPORT NUMBER RADC-TR-77-406✓	2. GOVT ACCESSION NO.	3. RECIPIENT'S CATALOG NUMBER
4. TITLE (and Subtitle) STUDY OF MICROSTRIP ANTENNAS, MICROSTRIP PHASED ARRAYS, AND MICROSTRIP FEED NETWORKS		5. TYPE OF REPORT & PERIOD COVERED Final Report 2 February 1976-9 Sept. 1977
		6. PERFORMING ORG. REPORT NUMBER EM 77-23;UILU-ENG-77-2265✓
7. AUTHOR(s) Y. T. Lo D. D. Harrison D. Solomon G. A. Deschamps F. R. Ore		8. CONTRACT OR GRANT NUMBER(s) AF19628-76-C-0140 ^{new}
9. PERFORMING ORGANIZATION NAME AND ADDRESS Electromagnetics Laboratory✓ Department of Electrical Engineering University of Illinois, Urbana, Illinois 61801		10. PROGRAM ELEMENT, PROJECT, TASK AREA & WORK UNIT NUMBERS 61102F 2305J429
11. CONTROLLING OFFICE NAME AND ADDRESS Deputy for Electronic Technology (RADC) Hanscom AFB Massachusetts 01731 Monitor/John A. Strom/ETER		12. REPORT DATE December 1977
		13. NUMBER OF PAGES 170
14. MONITORING AGENCY NAME & ADDRESS (if different from Controlling Office)		15. SECURITY CLASS. (of this report) Unclassified
		15a. DECLASSIFICATION/DOWNGRADING SCHEDULE
16. DISTRIBUTION STATEMENT (of this Report) Approved for public release; distribution unlimited		
17. DISTRIBUTION STATEMENT (of the abstract entered in Block 20, if different from Report)		
18. SUPPLEMENTARY NOTES		
19. KEY WORDS (Continue on reverse side if necessary and identify by block number) microstrip antennas cavities resonators impedance variation		
20. ABSTRACT (Continue on reverse side if necessary and identify by block number) Microstrip antennas are inherently narrow band devices with low efficiency. On the other hand, they have many unique and attractive properties: they are low in profile, light in weight, compact and conformable in structure, and easy to fabricate and to be integrated with solid-state devices. They are superior to the conventional flush-mount antennas since they are truly ^{thin} antennas, requiring no cavity backing. There seems to be little doubt that they will find more and more applications as more compact efficient solid state sources, amplifiers, and self-matching networks are developed to compensate for the (OVER)		

DD FORM 1 JAN 73 1473

EDITION OF 1 NOV 65 IS OBSOLETE

UNCLASSIFIED

SECURITY CLASSIFICATION OF THIS PAGE (When Data Entered)

20.(Cont.) shortcomings.

In this investigation a simple and useful theory, based on the cavity model, has been developed to analyze and predict the fundamental behavior of microstrip antennas of various basic shapes. In general, there is a good agreement between the theory and experiment.

From this theory, the general behavior of the radiation pattern can be predicted by simply noting the relative modal field directions along the edges of the antenna. For numerical results, the computation is simple and straightforward.

A microstrip antenna can be fed in many different ways. The input impedance at the feed can be computed from the modal field expansion. In particular, the real part of the impedance can be computed from the power radiated and lost in the cavity while the reactive part can be obtained from the stored energy associated with the cavity field. The impedance varies rapidly with frequency. As the frequency sweeps through the resonant value for a particular mode, the susceptance changes the sign and the conductance passes through a minimum. Thus the resonant admittance is a stationary point and for frequencies in the neighborhood of resonance the admittance locus follows approximately a constant conductance circle in the Smith chart plot (except for multiple resonances). Since the real power can easily be computed, the admittance locus is determined immediately.

The theory predicts that the input impedance varies with the feed location if the feed is applied along the edge with nonuniform field distribution. This is verified experimentally. Therefore, by simply locating the feed properly, the antenna can be matched to the feeder over a wide impedance range.

Most radiation takes place along the edge with uniform field distribution. Thus the longer the edge is, the higher the efficiency and the wider the bandwidth. Parasitic elements of proper dimensions have the function to broaden the resonant frequency region or to cause multiple resonances near to each other. In some symmetrical geometries, the degenerate resonant frequency can split into two close values if the symmetry is perturbed slightly. This can also cause multiple resonances, resulting in multiple loops in the impedance locus.

The most challenging problem in microstrip antennas is how to broaden the bandwidth and increase the efficiency. It is believed that this investigation has provided some guidance. A demonstration was made to show an improvement in the bandwidth by two or three folds by testing a series of specially constructed microstrip antennas. However, further work is needed.

EVALUATION STATEMENT

Contract F19628-76-C-0140

This report is the Final Report on this contract. It covers research performed on microstrip antennas during the period 2 February 1976 to 9 September 1977. The work deals with the development of analysis and synthesis techniques for the canonical shapes of this radiating element. The microstrip is light in weight, compact and conformal in structure, low in profile and easy to fabricate; however, it is inherently narrow band with low efficiency. This effort has addressed these drawbacks by creating a better understanding of the physical and electrical properties and generating techniques to minimize their effects. Accurate theory has been developed to characterize both the radiation patterns and input impedance. This antenna provides an attractive radiator, individually or in array, for integration in the next generation of Air Force tactical communication and radar systems.

John A. Strom

JOHN A. STROM
Contract Monitor
Antennas & RF Components Branch
Electromagnetic Sciences Division

ACCESSION for		
NTIS	Write Section	<input checked="" type="checkbox"/>
DDC	Buff Section	<input type="checkbox"/>
UNANNOUNCED		<input type="checkbox"/>
JUSTIFICATION		
BY		
DISTRIBUTION/AVAILABILITY CODES		
Dist.	AVAIL. and/or	SPECIAL
A		

TABLE OF CONTENTS

	Page
LIST OF FIGURES	vi
SUMMARY.	xi
PREFACE	xiii
REFERENCES.	xvi
PART A. THEORETICAL AND EXPERIMENTAL INVESTIGATION OF MICROSTRIP ANTENNAS	xviii
PART B. EXPERIMENTAL EVALUATION OF MICROSTRIP ANTENNAS OF VARIOUS CANONICAL SHAPES	67
PART C. IMPEDANCE VARIATION WITH THE FEED LOCATION.	105
PART D. EVALUATION OF COUPLING EFFECTS OF IMPEDANCE.	121
PART E. CONCLUDING REMARKS AND DISCUSSIONS	145

LIST OF FIGURES

Figure	Page
1. Geometry of microstrip antenna.	2
2. Geometry of rectangular microstrip antenna.	5
3. Cavity model of rectangular microstrip antenna.	6
4. Cross-sectional view of waveguide	7
5. \vec{K} -current distribution at edge of rectangular microstrip. . .	10
6. \vec{K} -current distribution for different resonant modes of rectangular cavity.	11
7. Transmission line of impedance Z_0 terminated in a load of admittance Y_0	14
8. Theoretical and experimental impedance characteristics of rectangular microstrip antenna.	17
9. Theoretical and experimental impedance characteristics of rectangular microstrip antenna.	19
10. Theoretical and experimental impedance characteristics of rectangular microstrip antenna.	20
11. Theoretical and experimental impedance characteristics of rectangular microstrip antenna.	22
12. Variation of frequency and Q for a center-fed rectangle . . .	23
13. Experimental frequency vs. corrected theoretical frequency for the rectangle of Figure 12.	28
14. Radiation pattern for a rectangular microstrip antenna. . . .	29
15. Geometry of disk microstrip antenna	30
16. \vec{K} -current distribution for mn-th mode	35
17. Theoretical and experimental impedance characteristics of disk microstrip antenna	36
18. Radiation pattern of disk microstrip antenna.	38
19. Geometry of 1/2 - disk microstrip antenna	42
20. \vec{K} -current distribution for different resonant modes of 1/2 - disk microstrip	44

Figure		Page
21	Theoretical and experimental impedance characteristics of disk microstrip antenna.	46
22	Radiation pattern of disk microstrip antenna.	49
23	Radiation pattern of disk microstrip antenna	50
24	Geometry of equilateral triangular microstrip antenna of side "a"	52
25	Theoretical and experimental impedance characteristics of equilateral triangular microstrip antenna	55
26	Corner-fed rectangle	60
27	Radiation pattern of equilateral triangular microstrip antenna	62
28	Radiation pattern of equilateral triangular microstrip antenna.	63
B-1	The various microstrip antenna shapes and feed locations which have been constructed and measured (impedance and patterns).	69
B-2	Sketch showing the microstrip antenna feed connector and feed transmission line details	71
B-3	Radiation patterns of square microstrip antenna.	73
B-4	Impedance of the center-fed, square microstrip antenna near resonance of the (0,1) mode	74
B-5	Impedance of the off-center fed, square microstrip antenna near resonance of the (0,1) and (1,0) modes. . . .	75
B-6	Radiation patterns of square, corner-fed microstrip antenna and rectangular, wide-side-fed microstrip antenna.	76
B-7	Impedance of square, corner-fed microstrip antenna near resonance of (0,1) and (1,0) modes	77
B-8	Impedance of rectangular, broad-side centered microstrip antenna near resonance of (0,1) mode	78
B-9	Radiation patterns of rectangular, wide-side off-center fed microstrip antenna for (e_1) mode (1,0), (e_2) mode (0,1).	79
B-10	Impedance of rectangular, wide-side off-center fed microstrip antenna near resonance of mode (0,1).	80
B-11	Impedance of rectangular, wide-side off-center fed microstrip antenna near resonance of mode (0,1).	81

Figure		Page
B-12	Radiation patterns of rectangular (f) narrow-side center fed microstrip antenna of mode (0,1), (g_1) corner-fed microstrip antenna of mode (0,1)	82
B-13	Impedance of rectangular, narrow-side center fed microstrip antenna near resonance of mode (0,1)	83
B-14	Impedance of rectangular, corner-fed microstrip antenna near resonance of mode (0,1)	84
B-15	Radiation patterns of (g_2) rectangular, corner-fed microstrip antenna of mode (1,0), (h_1) circular antenna of mode (1,1)	85
B-16	Impedance of rectangular, corner-fed microstrip antenna near resonance of mode (1,0)	86
B-17	Impedance of circular microstrip antenna near resonance of mode (1,1)	87
B-18	Radiation patterns of (h_2) circular microstrip antenna of mode (2,1), (i_1) semicircular, center of half-circle fed microstrip antenna of mode (2,1)	88
B-19	Impedance of circular microstrip antenna near resonance of mode (2,1)	89
B-20	Impedance of semicircular, center of half-circle fed microstrip antenna near resonance of mode (2,1)	90
B-21	Radiation patterns of semicircular (j) center of straight side fed microstrip antenna of mode (0,1), (k_1) off-center of straight side fed microstrip antenna of order mode (1,1)	91
B-22	Impedance of semicircular, off-center of straight side fed microstrip antenna near resonance of mode (1,1)	92
B-23	Impedance of semicircular, off-center of straight side fed microstrip antenna near resonance of mode (1,1)	93
B-24	Radiation patterns of (k_2) semicircular, off-center of straight side fed microstrip antenna of mode (2,1), (1) equiangular triangle, one tip fed microstrip antenna of modes (0,1), (1,0)	94
B-25	Impedance of semicircular, off-center of straight side fed microstrip antenna near resonance of mode (2,1)	95
B-26	Impedance of an equiangular triangle, one tip fed microstrip antenna near resonance of modes (0,1) and (1,0)	96

Figure		Page
B-27	Radiation patterns of equiangular triangle, middle of one side fed microstrip antennas, (m_1) of modes (0,1) and (1,0), (m_2) of mode (1,1)	97
B-28	Impedance of equiangular triangle middle of one side fed microstrip antenna near resonance of modes (0,1) and (1,0)	98
B-29	Impedance of equiangular triangle middle of one side fed microstrip antenna near resonance of mode (1,1) (0,2) and (2,0)	99
B-30	Radiation patterns of equiangular triangles (n_1) off-center of one side fed microstrip antenna of modes (0,1) and (1,0), (n_2) off-center of one side microstrip antenna of mode (1,1)	100
B-31	Impedance of equiangular triangle off-center of one side fed microstrip antenna near resonance of modes (0,1) and (1,0)	101
B-32	Impedance of equiangular triangle off-center of one side fed microstrip antenna near resonance of mode (1,1)	102
C-1a	Input impedance test configuration for the rectangular element, near (1,0) mode resonance	107
C-1b	Table of results for the x-axis fed input impedance	107
C-1c	Variation of resonant impedance against the feed location .	108
C-2	Impedance plot for x-axis feed with $d = 0.71$ cm	109
C-3	Impedance plot for x-axis feed with $d = 1.43$ cm	110
C-4	Impedance plot for x-axis feed with $d = 2.14$ cm	111
C-5	Impedance plot for x-axis feed with $d = 2.86$ cm	112
C-6	Impedance plot for x-axis feed with $d = 3.57$ cm	113
C-7	Impedance plot for x-axis feed with $d = 4.29$ cm	114
C-8	Impedance plot for x-axis feed with $d = 5.0$ cm.	115
C-9	Radiation patterns of the rectangular element at (1,0) mode resonance for different feedpoints	118
C-10	Radiation patterns of the rectangular element near (1,0) mode resonance for different feedpoints	119
D-1	General form of element to stripline coupling, and the configuration of the coaxial feed	123

Figure		Page
D-2	Impedance plot of the rectangular element with strip-line feed	125
D-3a	Impedance plot of the rectangular element with coaxial feed	126
D-3b	Impedance plot of the rectangular element with coaxial feed.	127
D-4	Geometry of two interacting rectangular microstrip antennas excited with (1,0) mode and aligned with the y-axis.	128
D-5	Geometry of two interacting rectangular microstrip antennas excited with (1,0) mode and aligned with the y-axis.	128
D-6	Input admittance locus of a rectangular microstrip antenna in the presence of a parasitic element of the	
D-11	same geometry at various values of separation d along the x-axis as shown in Figure D-4	129-134
D-12	Same as in Figure D-6 to D-11 except for the orientation being shown in Figure D-4 where d is the separation	
D-19	along the y-axis.	136-142
D-20	Input admittance locus of the parasitic element used in Figures D-6 to D-11 in the absence of the parasitic element.	144
D-21	Changes in resonant frequency vs. the separation d for the two orientations	145
E-1	Impedance locus of a rectangular microstrip antenna of 5.5" x 3".	150
E-2	Impedance locus of a rectangular microstrip antenna of 5.5" x 8.05".	151
E-3	Impedance locus of a rectangular microstrip antenna of 5.5" x 10"	152
E-4	Impedance locus of a rectangular microstrip antenna of 5.5" x 0.97".	153

SUMMARY

Microstrip antennas are inherently narrow band devices with low efficiency. On the other hand, they have many unique and attractive properties: they are low in profile, light in weight, compact and conformable in structure, and easy to fabricate and to be integrated with solid-state devices. They are superior to the conventional flush-mount antennas since they are truly "thin" antennas, requiring no cavity backing. There seems to be little doubt that they will find more and more applications as more compact efficient solid state sources, amplifiers, and self-matching networks are developed to compensate for the shortcomings.

In this investigation a simple and useful theory, based on the cavity model, has been developed to analyze and predict the fundamental behavior of microstrip antennas of various basic shapes.

From this theory, the general behavior of the radiation pattern can be predicted by simply noting the relative modal field directions along the edges of the antenna. For numerical results, the computation is simple and straightforward.

A microstrip antenna can be fed in many different ways. The input impedance at the feed can be computed from the modal field expansion. In particular, the real part of the impedance can be computed from the power radiated and lost in the cavity while the reactive part can be obtained from the stored energy associated with the cavity field. The impedance varies rapidly with frequency. As the frequency sweeps through the resonant value for a particular mode, the susceptance changes the

sign and the conductance passes through a minimum. Thus the resonant admittance is a stationary point and for frequencies in the neighborhood of resonance the admittance locus follows approximately a constant conductance circle in the Smith chart plot' (except for multiple resonances). Since the real power can easily be computed, the admittance locus is determined immediately.

The theory predicts that the input impedance varies with the feed location if the feed is applied along the edge with nonuniform field distribution. This is verified experimentally. Therefore, by simply locating the feed properly, the antenna can be matched to the feeder over a wide impedance range.

Most radiation takes place along the edge with uniform field distribution. Thus the longer the edge is, the higher the efficiency and the wider the bandwidth. Parasitic elements of proper dimensions have the function to broaden the resonant frequency region or to cause multiple resonances near to each other. In some symmetrical geometries, the degenerate resonant frequency can split into two close values if the symmetry is perturbed slightly. This can also cause multiple resonances, resulting in multiple loops in the impedance locus.

The most challenging problem in microstrip antennas is how to broaden the bandwidth and increase the efficiency. It is believed that this investigation has provided some guidance. A demonstration was made to show an improvement in the bandwidth by two or three folds by testing a series of specially constructed microstrip antennas. However, further work is needed.

PREFACE

Microstrip devices have widely been used as microwave circuit elements, such as transmission lines, filters, etc. The successful operation of, for example, the microstrip resonators seems to suggest that basically they are poor radiators. Despite this weakness, microstrip antennas have received much attention in recent years because of their many unique and attractive properties — low in profile, light in weight, compact and conformable in structure, and easy to fabricate and to be integrated with solid state devices. They are superior to the conventional flush-mount antennas in that they are truly "thin" antennas, requiring no cavity backing. There seems to be little doubt that they will find many applications in practice in much the same manner as in the modern hi-fi systems where the inefficiency of small speaker systems is traded for their compactness. Likewise, the shortcomings can perhaps be compensated for with more efficient solid-state sources, amplifiers, and adaptive impedance-matching networks.

A few short papers published in recent years [1] - [3] are concerned mainly with the experiments to demonstrate many design possibilities of the microstrip antennas. A general rigorous theory for this new family of antennas appears to be very involved. It is possible to formulate the problem in terms of the spatial spectrum of the current in the microstrip plate and to solve the integral equation by Galerkin's method. This approach has been initiated in the Quarterly Report No. 1 [Feb. - May 1976]. In view of the success of treating this type of structures as cavities in microstrip circuits, the rigorous attack is temporarily suspended in favor of a much simpler approach based on the cavity model theory [Quarterly Report No. 2, May - August 1976].

The modal fields in the cavity of many geometrical shapes can easily be determined. Using the equivalence theorem, the far field can thus be computed approximately. In fact the general behavior of the radiation pattern can readily be predicted by simply observing the nodes and antinodes of the modal field distribution along the edges of the microstrip antenna without computation. Even for quantitative results the computation needed is quite simple. For all the geometries considered, the theoretically predicted patterns agree very closely with the measured patterns.

A microstrip antenna can be excited in many different ways. However, the cavity model theory fails to predict the input impedance at any feed point correctly, in particular at resonance, since the input impedance of a lossless cavity is always reactive and becomes either zero or infinity at resonance. Even if the dissipative losses in the cavity are considered, the cavity theory still does not take the radiated power into account, which, as is obvious, is of primary interest in this study. However, this difficulty can be alleviated by first computing the radiated power from the pattern function and then from this power and losses in the cavity computing the resonant input resistance. In a similar manner, one can compute the input impedance at any frequency off resonance. The input impedance locus so computed is found to be in good agreement with the measurement for many cases.

This report summarizes the major work performed during the contract period in five parts. Some other results which are either of secondary interest, or which are not yet completed (in order to direct the effort to more fruitful investigations), have been reported in the regular Quarterly Reports and will not be repeated here.

Part A deals with the approximate theory based on the cavity model. In particular four geometries (rectangle, circular disk, semi-circular disk, and equilateral triangle) have been analyzed in detail. In each case, a comparison between the theoretical and experimental results for several typical dimensions has been made. The objective of the work in Part B is to document the major properties of many microstrip antennas of canonical shapes in order to gain some insight into the radiation mechanism and impedance variation of these antennas.

In Part C it is shown that a wide range of impedance values is available for matching purposes by choosing the feed location properly. Although this investigation has so far been performed for rectangular microstrip antennas only, without any doubt the same technique can be applied to other geometries as well. Part D considers the question of coupling between a microstrip antenna and its feeder and also between two similar microstrip antennas.

The most objectionable property of microstrip antennas is their inherent narrow bandwidth and low efficiency (high Q) as radiators. The "angels" in the microwave circuit application certainly become the "devils" in the antenna application. To seek improved designs in the latter application, one must explore in a new direction, a direction opposite to the circuit engineers'. It is believed that this research has provided us with some guidance. This is discussed in Part E with some experimental evidence. Without doubt, much effort is urgently needed in this area.

REFERENCES

1. See References 1 - 10 in Part A.
2. J. Q. Howell, "Microstrip antennas," IEEE Trans. Antennas Propagat., vol. AP-23, pp. 90-93, January 1975.
3. L. C. Shen, S. A. Long, M. R. Allerding, and M. D. Walton, "Resonant frequency of a circular disc printed-circuit antenna," IEEE Trans. Antennas Propagat., vol. AP-25, pp. 595-596, July 1977.

PART A.

THEORETICAL AND EXPERIMENTAL INVESTIGATION
OF MICROSTRIP ANTENNAS

CHAPTER 1. INTRODUCTION

The microstrip antenna has the attractive features that it requires little space, is light in weight, easy to fabricate and reproduce, and can be conformal to any surface [1]. It also has the potential to be integrated with active devices.

Early work on the microstrip was done by Deschamps [2] at the Federal Telecommunications Laboratories. More recently, Munson [1] and Derneryd [3] have analyzed the microstrip rectangular antenna as two-slot radiators in parallel. The radiation pattern from a disk microstrip antenna has also been considered [4]. Carver and Coffey [5] solved for the radiation pattern of a microstrip antenna of arbitrary shape by using numerical methods.

Microstrip circuit elements have been analyzed [6]-[8] by enclosing the inner region by a magnetic wall at the edge of the plate. Evaluation of the Q-factor for circles and triangles has been made according to this method [9]. A circular polarized microstrip antenna has also been developed [10].

It is the purpose of this report to further develop methods to analyze the properties of microstrip antennas. We attempt to develop a theory to predict the radiation patterns and impedance of a microstrip antenna excited at an arbitrary frequency.

The geometry of the microstrip antenna is shown in Fig. 1. It consists of a thin conducting plate separated from an infinite conducting ground plane by a thin layer of dielectric where the thickness of the dielectric is much less than one wavelength. On the basis of this geometry the following assumptions may be made about the fields in the dielectric region of the microstrip (the region of the dielectric that is underneath the metal conductor).

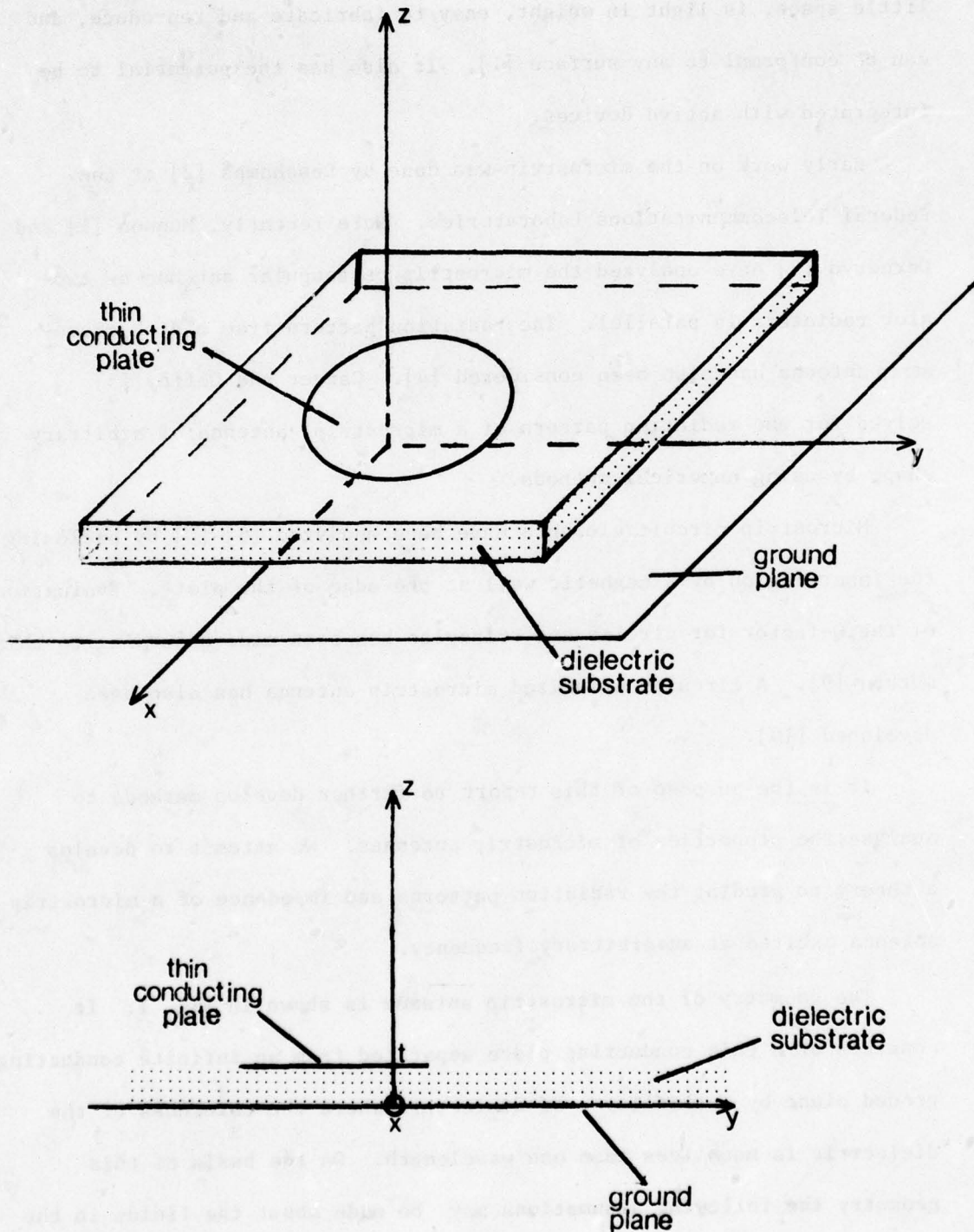


Figure 1. Geometry of microstrip antenna. t is the thickness of the dielectric.

i) The E-field has a z-component only (normal to the microstrip) and the H-field has xy-components only (tangential to the microstrip).

ii) The fields have no z-variation.

iii) The component of the current normal to the edge of the microstrip approaches zero at the edge. This implies that the tangential component of the H-field at the edge is negligibly small.

On the basis of these assumptions the fields in the dielectric region of the microstrip can be determined by modeling the microstrip as a cavity bounded on the top and bottom by an E-wall and on the sides by an H-wall. The latter is based on assumption iii) that the component of the H-field tangent to the edge is small at the edge so that forcing the tangential component of the H-field at the edge to zero does not greatly affect the fields in the rest of the dielectric region of the microstrip. Thus the fields within the dielectric region of the microstrip can be determined by solving a cavity problem instead of an open region problem.

Once the field within the dielectric region of the microstrip is known, the induced currents in the conducting plate can be determined and the radiated fields can be solved for. Alternatively, the induced magnetic current, \vec{K} , in the H-wall can be determined and the radiation field due to the \vec{K} -current calculated. Since it is more efficient to perform a line integral than a surface integral for the electric current, it is this second approach that is used throughout this thesis.

The exact solution to the cavity problem can easily be obtained for certain canonical geometries. In the following chapters the electrical behavior of several different microstrip antennas is determined on the basis of the above model and the results are compared with experimental results.

CHAPTER 2. THE RECTANGULAR MICROSTRIP ANTENNA

2.1 General Field Analysis

For the rectangular microstrip antenna the conducting plate in Fig. 1 takes the form of a rectangle with dimensions shown in Fig. 2. The antenna is fed with a microstrip line. The field that exists underneath the microstrip line is assumed to consist of the incident and reflected TEM waves where the E-field has only a z-component and the H-field an x-component. On the basis of our model the edge of the rectangle is surrounded by a magnetic wall. By using the equivalence principle, the microstrip feed line can be replaced by an electric current source \vec{J} parallel to the z-axis and backed by a magnetic wall. Thus the cavity problem in Fig. 3 must be considered.

This problem may be attacked by treating the cavity as a waveguide with a boundary at $y = 0$ and $y = b$. A cross-sectional view of the waveguide is shown in Fig. 4. It is bounded at $z = 0$ and $z = t$ by an E-wall (t is the thickness of the dielectric) and at $x = 0$ and $x = a$ by an H-wall.

A solution for this waveguide with an E-field with a z-component only is

$$E_z = \sum_{n=0}^{\infty} \left[A_n^+ \cos \left(\frac{n\pi}{a} x \right) e^{-j\beta_n y} + A_n^- \cos \left(\frac{n\pi}{a} x \right) e^{+j\beta_n y} \right] \quad (1a)$$

$$H_x = \sum_{n=0}^{\infty} \left[A_n^+ \frac{\beta_n}{\omega\mu} \cos \left(\frac{n\pi}{a} x \right) e^{-j\beta_n y} - A_n^- \frac{\beta_n}{\omega\mu} \cos \left(\frac{n\pi}{a} x \right) e^{+j\beta_n y} \right] \quad (1b)$$

$$H_y = \sum_{n=0}^{\infty} \left[A_n^+ \frac{j}{\omega\mu} \left(\frac{n\pi}{a} \right) \sin \left(\frac{n\pi}{a} x \right) e^{-j\beta_n y} + A_n^- \frac{j}{\omega\mu} \sin \left(\frac{n\pi}{a} x \right) e^{+j\beta_n y} \right] \quad (1c)$$

where

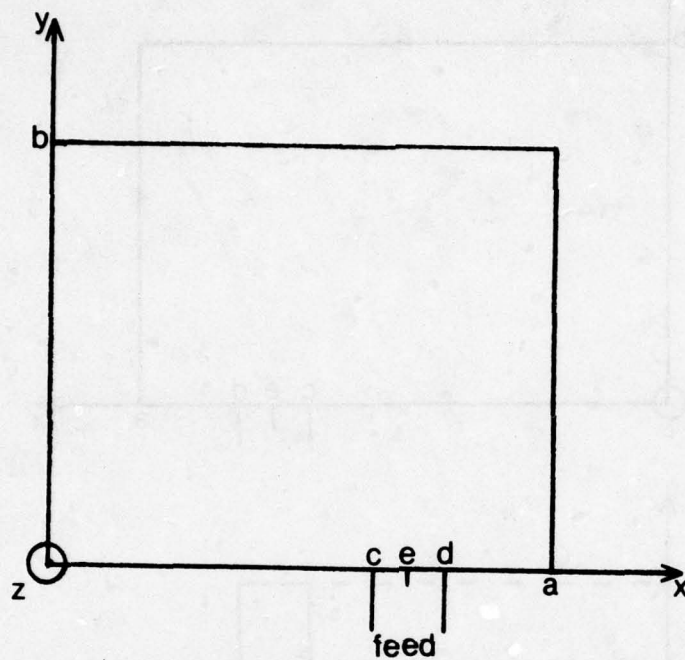


Figure 2. Geometry of rectangular microstrip antenna.

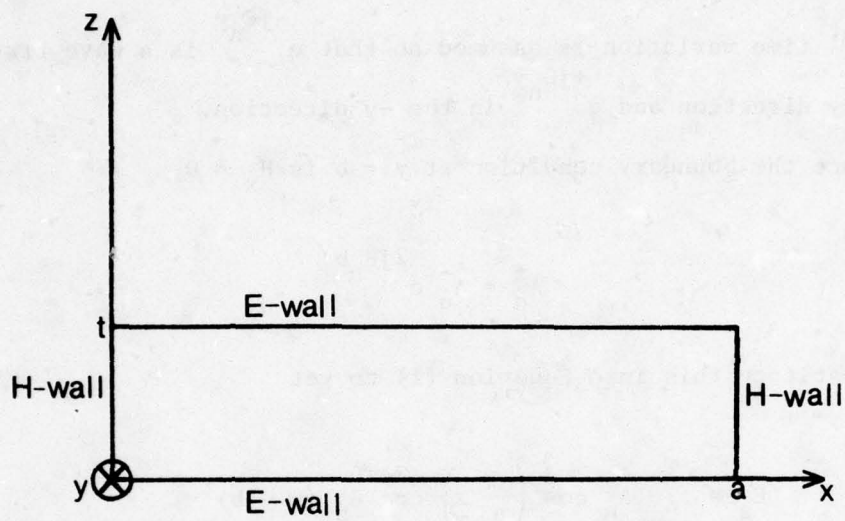


Figure 4. Cross-sectional view of waveguide.

$$\beta_n = \begin{cases} +\sqrt{k^2 - \left(\frac{n\pi}{a}\right)^2} , & k > \frac{n\pi}{a} \\ -j\sqrt{\left(\frac{n\pi}{a}\right)^2 - k^2} , & \frac{n\pi}{a} > k \end{cases} , \quad k = \omega\sqrt{\mu\epsilon} \quad (1d)$$

and $e^{+j\omega t}$ time variation is assumed so that $e^{-j\beta_n y}$ is a wave traveling in the $+y$ direction and $e^{+j\beta_n y}$ in the $-y$ direction.

Since the boundary condition at $y = b$ is $H_x = 0$,

$$A_n^+ = A_n^- e^{2j\beta_n b} .$$

Substitute this into Equation (1) to get

$$E_z = \sum_{n=0}^{\infty} A_n \cos\left(\frac{n\pi}{a} x\right) \cos \beta_n (y - b) \quad (2a)$$

$$H_x = \frac{-j}{\omega\mu} \sum_{n=0}^{\infty} A_n \beta_n \cos\left(\frac{n\pi}{a} x\right) \sin \beta_n (y - b) \quad (2b)$$

$$H_y = \frac{j}{\omega\mu} \sum_{n=0}^{\infty} A_n \left(\frac{n\pi}{a}\right) \sin\left(\frac{n\pi}{a} x\right) \cos \beta_n (y - b) . \quad (2c)$$

Now the boundary condition at $y = 0$ is assumed to be

$$H_x(x, y = 0) = \begin{cases} J , & c < x < d \\ 0 , & \text{elsewhere} \end{cases} . \quad (3)$$

Expand H_x at $y = 0$ in terms of $\cos \frac{n\pi}{a} x$ to get

$$H_x(x, y = 0) = \frac{J(d - c)}{a} + \sum_{n=1}^{\infty} \frac{4J}{n\pi} \left[\sin \frac{n\pi}{2a} (d - c) \cos \frac{n\pi}{2a} (d + c) \right] \cos\left(\frac{n\pi}{a} x\right) . \quad (4)$$

Equating (2b) at $y = 0$ to (4) yields

$$A_0 = -j\omega\mu J \frac{d - c}{ak \sin kb} \quad (5a)$$

$$A_n = -j\omega\mu J \frac{4}{n\pi} \frac{\left[\sin \frac{n\pi}{2a} (d - c) \right] \left[\cos \frac{n\pi}{2a} (d + c) \right]}{\beta_n \sin \beta_n b} ; n = 1, 2, \dots \quad (5b)$$

Using Equation (5) in Equation (2a) gives the electric field in the dielectric region of the microstrip, which in turn gives the induced \vec{K} -currents. The \vec{K} -current distribution at the four edges $[(x, y) = (0, y), (a, y), (x, 0) \text{ and } (x, a)]$ is given by

$$\vec{K} = \hat{n} \times \hat{z} E \quad (7)$$

where \hat{n} is normal to the edge and \vec{K} is shown in Fig. 5.

At certain frequencies one of the terms in the expressions for E_z and \vec{K} blows up. This occurs when

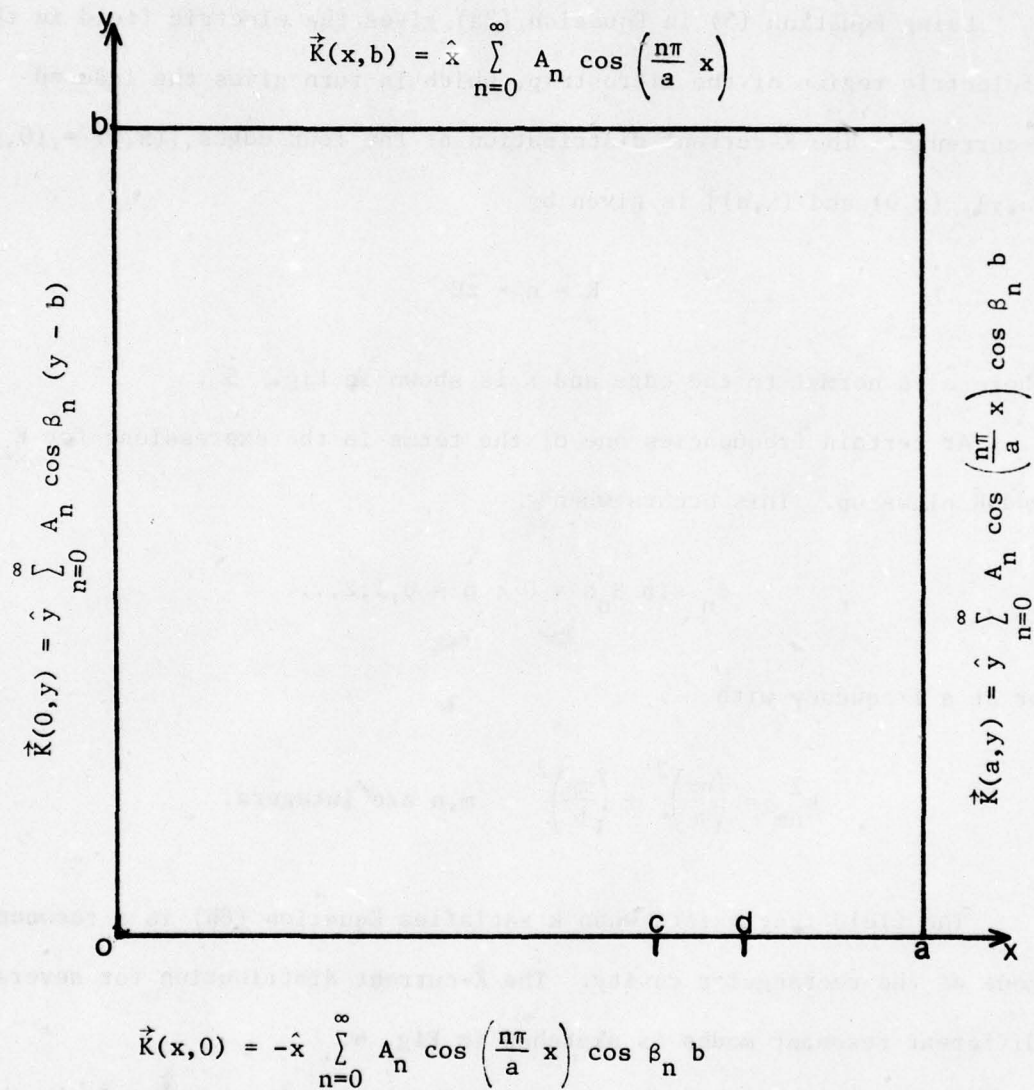
$$\beta_n \sin \beta_n b = 0 ; n = 0, 1, 2, \dots \quad (8a)$$

or at a frequency with

$$k_{nm}^2 = \left(\frac{n\pi}{a} \right)^2 + \left(\frac{m\pi}{b} \right)^2 \quad m, n \text{ are integers.} \quad (8b)$$

The field that exists when k satisfies Equation (8b) is a resonant mode of the rectangular cavity. The \vec{K} -current distribution for several different resonant modes is sketched in Fig. 6.

The field structure for the $n, m = (0, 1)$ mode is the sum of the two TEM waves — one traveling in the $+y$ direction and one in the $-y$ direction. A similar interpretation exists for the $n, m = (1, 0)$ mode except that the two TEM waves travel in the $+x$ and $-x$ directions. For modes with $m \neq 0$ and $n \neq 0$, similar interpretations may be given, except that the waves



A_n is defined in Equation (5)

β_n is defined in Equation (1d)

Figure 5. \vec{K} -current distribution at edge of rectangular microstrip.

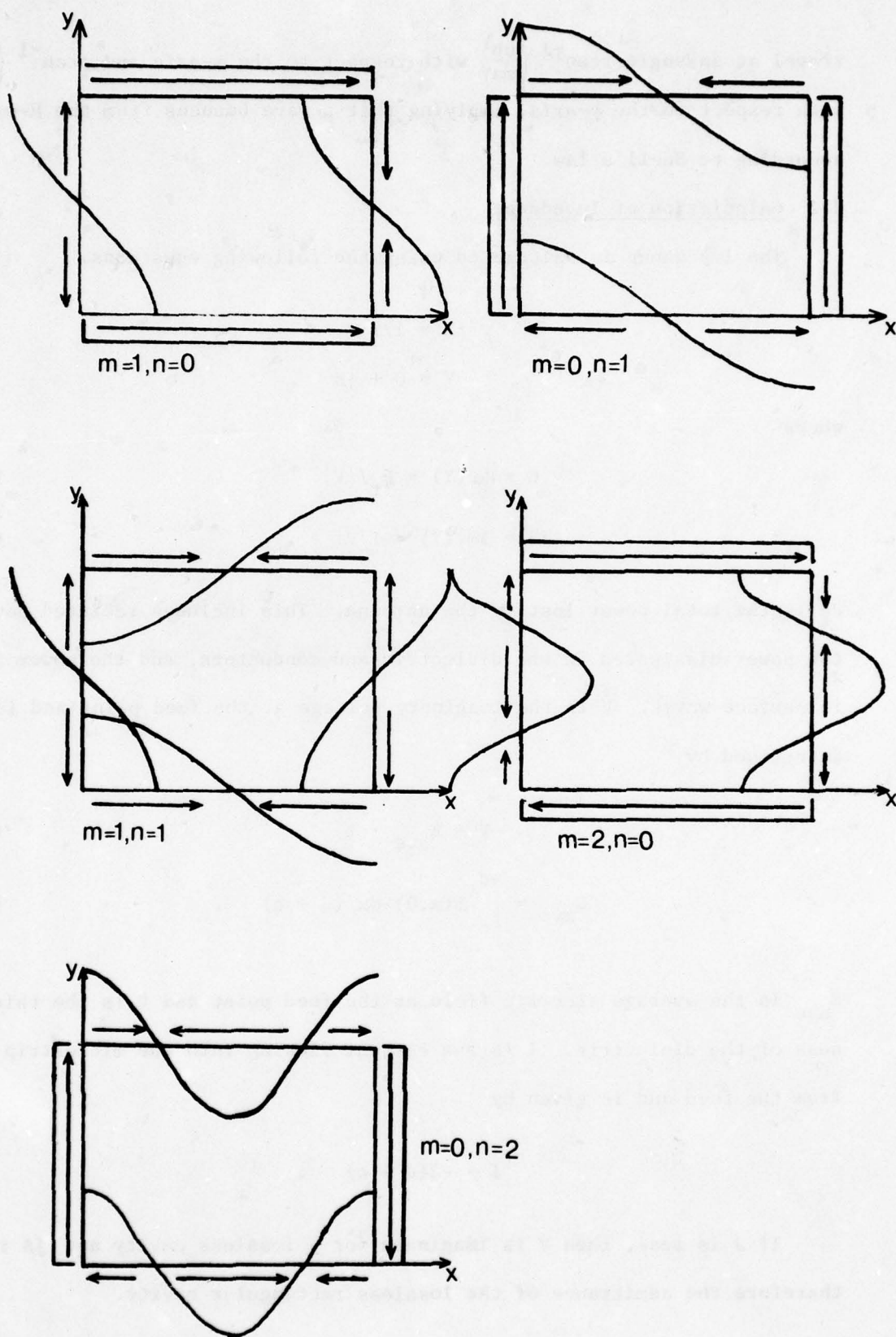


Figure 6. \vec{K} -current distribution for different resonant modes of rectangular cavity.

travel at an angle $\pm \tan^{-1} \left(\frac{nb}{ma} \right)$ with respect to the x-axis and $\pm \tan^{-1} \left(\frac{ma}{nb} \right)$ with respect to the y-axis, implying that a wave bounces from the H-walls according to Snell's law.

2.2 Calculation of Impedance

The impedance is calculated using the following equations.

$$Z = 1/Y \quad (9a)$$

$$Y = G + jB \quad (9b)$$

where

$$G = \text{Re}(Y) = P_t / |V|^2 \quad (10a)$$

$$jB = \text{Im}(Y) = I/V \quad (10b)$$

P_t is the total power lost in the antenna. This includes radiated power, the power dissipated in the dielectric and conductors, and the power lost in surface waves. V is the imaginary voltage at the feed point and is determined by

$$V = E_{\text{ave}} \cdot t \quad (12a)$$

$$E_{\text{ave}} = \int_c^d E(x,0) dx / (d - c) \quad (12b)$$

E_{ave} is the average electric field at the feed point and t is the thickness of the dielectric. I is the current flowing into the microstrip from the feed and is given by

$$I = -J(d - c) \quad (13)$$

If J is real, then V is imaginary for a lossless cavity and jB is therefore the admittance of the lossless rectangular cavity.

That G is the real part of the admittance [Equation (10a)] can be shown as follows. Refer to Fig. 7, a transmission line of impedance Z_0 , terminated in a load of admittance Y_L . The condition at the load is

$$Y_L = \frac{I_L}{V_L} = \frac{I_i + I_r}{V_i + V_r} = \frac{1}{Z_0} \frac{V_i - V_r}{V_i + V_r} = \frac{1}{Z_0} \frac{1 - \Gamma}{1 + \Gamma} \quad (14)$$

$$G = \text{Re}(Y_L) = \frac{1}{Z_0} \text{Re} \frac{1 - |\Gamma|^2 + (\Gamma^* - \Gamma)}{|1 + \Gamma|^2} = \frac{1}{Z_0} \frac{1 - |\Gamma|^2}{|1 + \Gamma|^2} \quad (15)$$

The total power into the load is

$$P_t = \frac{|V_i|^2}{Z_0} (1 - |\Gamma|^2) \quad (16)$$

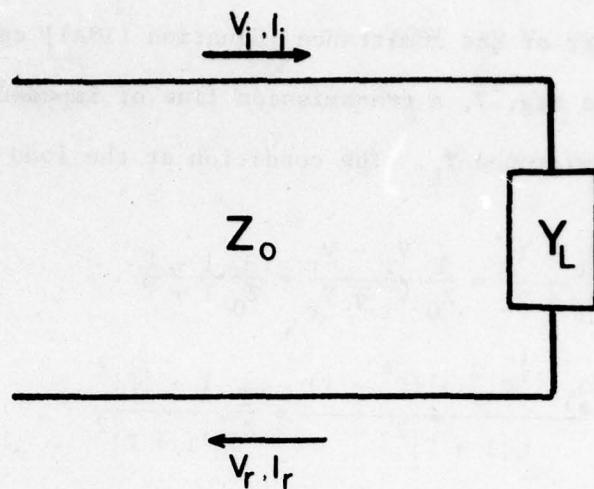
The result of substituting Equation (16) into (15) is Equation (10a). Now we consider the total power lost, P_t .

$$P_t = P_r + P_d + P_c + P_s \quad (17)$$

P_r is the power radiated by the antenna. Because the dielectric is very thin for the first approximation, the presence of the dielectric is neglected in calculating P_r from the \vec{K} -current distribution. Also, using the fact that \vec{K} -current is only a very small distance above an infinite conducting plane, the electric vector potential at (r, θ, ϕ) due to a $\vec{K}(x', y')$ is

$$\vec{F}(\vec{r}) \approx - \frac{e^{-jkr}}{4\pi r} \int_L 2\vec{K}(x', y') e^{jk(x' \sin\theta \cos\phi + y' \sin\theta \sin\phi)} d\ell' \quad (18)$$

where $d\ell' = \sqrt{dx'^2 + dy'^2}$, L = magnetic wall boundary of the cavity.



V_i, I_i is incident wave
 V_r, I_r is reflected wave
 $V_L = V_i + V_r$
 $I_L = I_i - I_r$
 $\Gamma = V_r / V_i$

Figure 7. Transmission line of impedance Z_0 terminated in a load of admittance Y_0 .

The far field at (r, θ, ϕ) is then

$$E_{\theta} = jkF_{\phi} = \eta H_{\phi} \quad (19a)$$

$$E_{\phi} = -jkF_{\theta} = -\eta H_{\theta} \quad (19b)$$

where $\eta = 377 \Omega$ is the impedance of free space.

The total radiated power is then

$$P_r = \text{Re} \int_0^{\pi/2} d\theta \int_0^{2\pi} d\phi (E_{\theta} H_{\phi}^* - E_{\phi} H_{\theta}^*) r^2 \sin \theta \quad (20)$$

The power dissipated in the dielectric, P_d , is given by the equation

$$P_d = \iiint_V \sigma |E|^2 dv \quad (21)$$

where the integration is performed over the volume of the cavity and σ is the conductivity of the dielectric.

The loss in the conductors is given by

$$P_c = \frac{1}{2\sigma_c \delta} \iint_A |H|^2 da \quad (22)$$

where the integration performed over the conductor surfaces at $z = 0$ and $z = t$, σ_c is the conductivity of the conductor, and δ is the skin depth.

P_s is the power lost in surface waves. Our estimate for several cases shows that it is negligible compared to P_r and P_d .

2.3 Comparison of Experiment and Theory

Measurements were made using copper clad 1/16" thick Rexolite 2200. The relative permittivity is 2.62 and the loss tangent is approximately .0009.

The measured and theoretical values of the impedance of a microstrip of dimensions $7.60 \text{ cm} \times 11.40 \text{ cm}$ is shown in Figs. 8 - 11. The antenna is fed by a 50Ω microstrip line centered at point "e" on one side of the antenna. Measurements are made for four different feed points over a frequency range of about 750 MHz to 1650 MHz. Within this range several different resonant modes are excited.

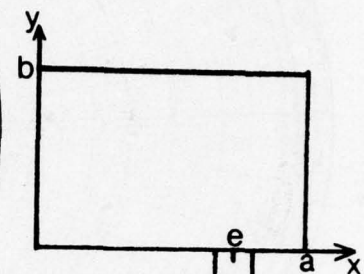
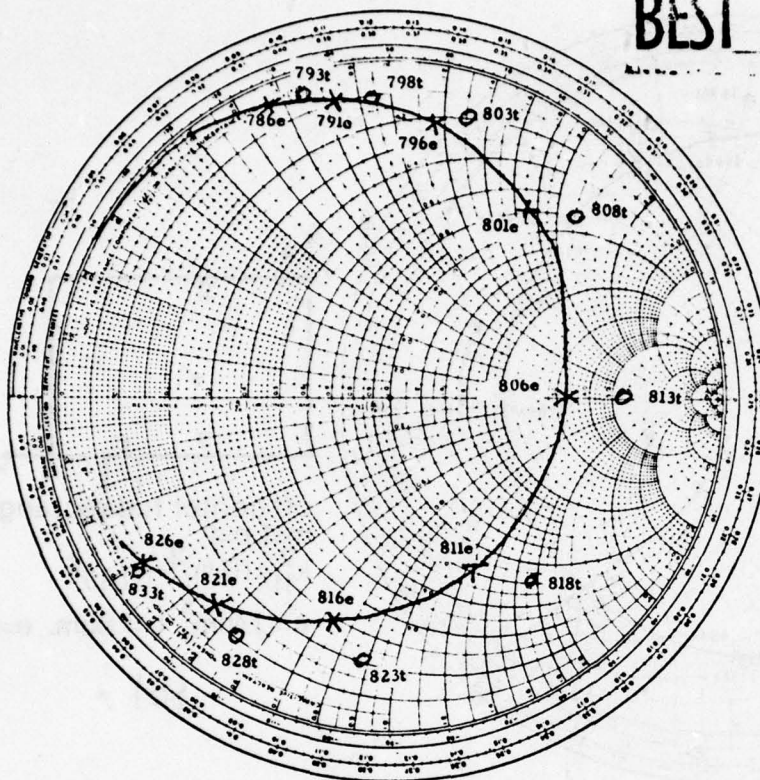
The resonant frequency is the frequency at which the reactance or the susceptance vanishes (the impedance crosses the real axis of the Smith chart). As can be seen from Figs. 8 - 11, the theoretical value of the resonant frequency is greater than the measured value. In these figures the points labeled with "o" and the numbers with "t" are theoretical points, the "x's" and numbers with "e" are measured points. Frequency is in MHz.

Much can be learned about the impedance by studying the \vec{K} -distribution along the edge because it is proportional to the \vec{E} -field. For the $(n,m) = (0,1)$ mode the impedance is independent of the feed point for a rectangle fed from the $y = 0$ edge. This is true because the electric field is constant along the $y = 0$ edge for this mode so that the coupling between the feed and the antenna is the same at any feed point along the $y = 0$ edge. This is illustrated by comparing Figs. 8b and 9a. The impedance at resonance is the same, although the feed points are different. The same argument applies to the $m = 2, n = 0$ mode (see Figs. 10d, 11b).

However, for the $(n,m) = (1,0)$ mode where there is a sinusoidal variation in the \vec{E} -field along the $y = 0$ edge, changing the position of the feed point changes the input impedance. If the rectangle is fed exactly at the center along the $y = 0$ edge, then this mode is not excited.

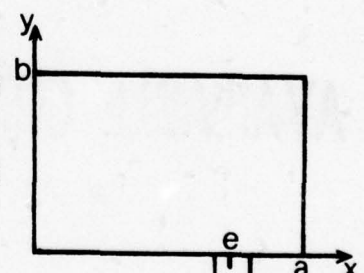
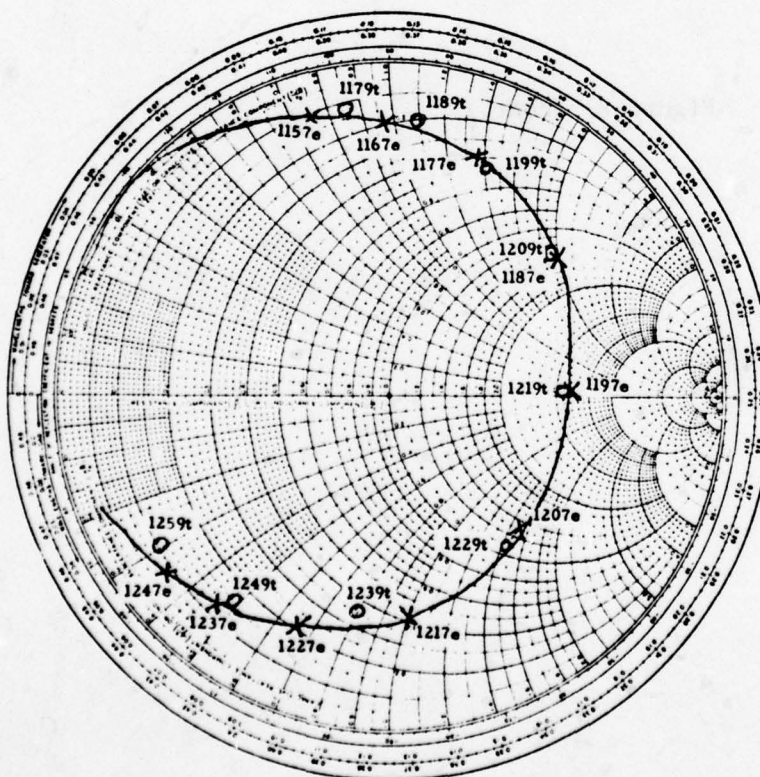
Investigation has also been made on the effect of the dimensions of the rectangle on the impedance and the resonant frequency. In Fig. 12

BEST AVAILABLE COPY



off center fed rectangle
 $m=0, n=1$ $k_{10}=\pi/a$
 $a=11.4\text{cm. } b=7.6\text{cm. } e=8.38\text{cm.}$

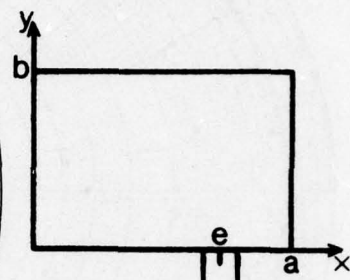
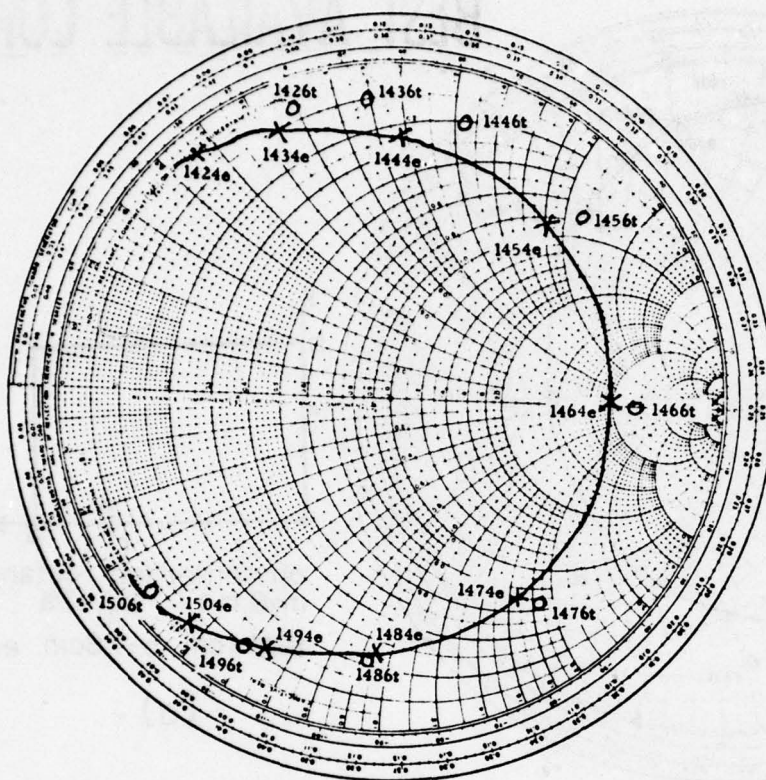
(a)



off center fed rectangle
 $m=1, n=0$ $k_{01}=\pi/b$
 $a=11.4\text{cm. } b=7.6\text{cm. } e=8.38\text{cm.}$

(b)

Figure 8. Theoretical and experimental impedance characteristics of rectangular microstrip antenna.
 X-X-X-X experimental points o-theoretical points,
 e-experimental frequency (MHz), t-theoretical frequency (MHz),
 (n,m)-dominate mode at resonance.



off center fed rectangle

$m=1, n=1$

$$k_{11}^2 = (\pi/a)^2 + (\pi/b)^2$$

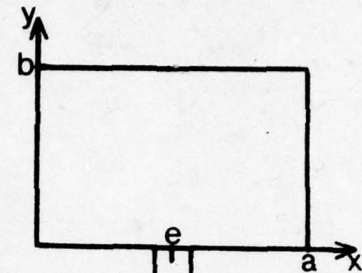
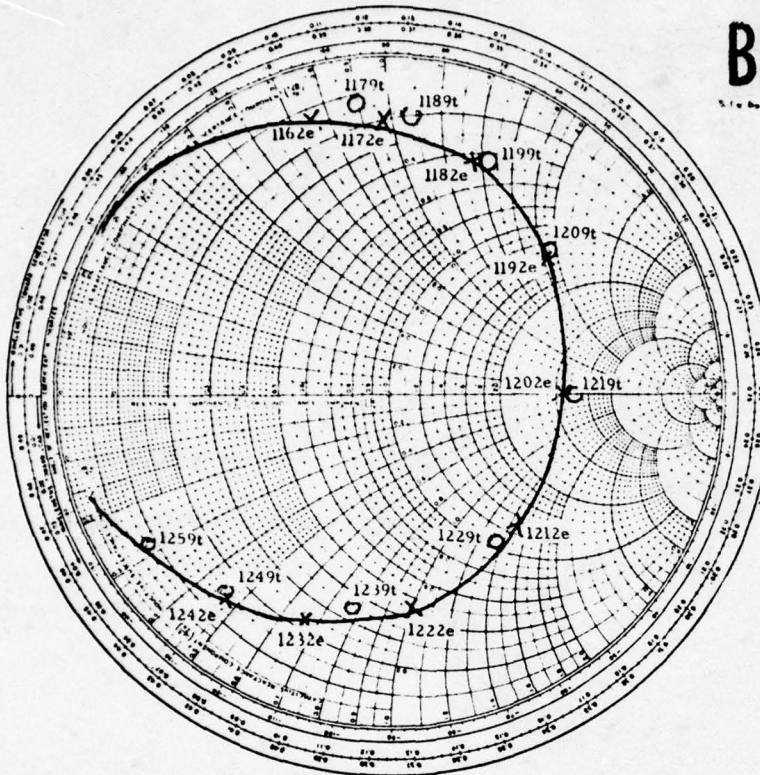
$a=11.4\text{cm. } b=7.6\text{cm. } e=8.38\text{cm.}$

(c)

Figure 8. (cont.)

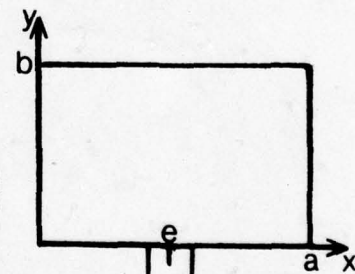
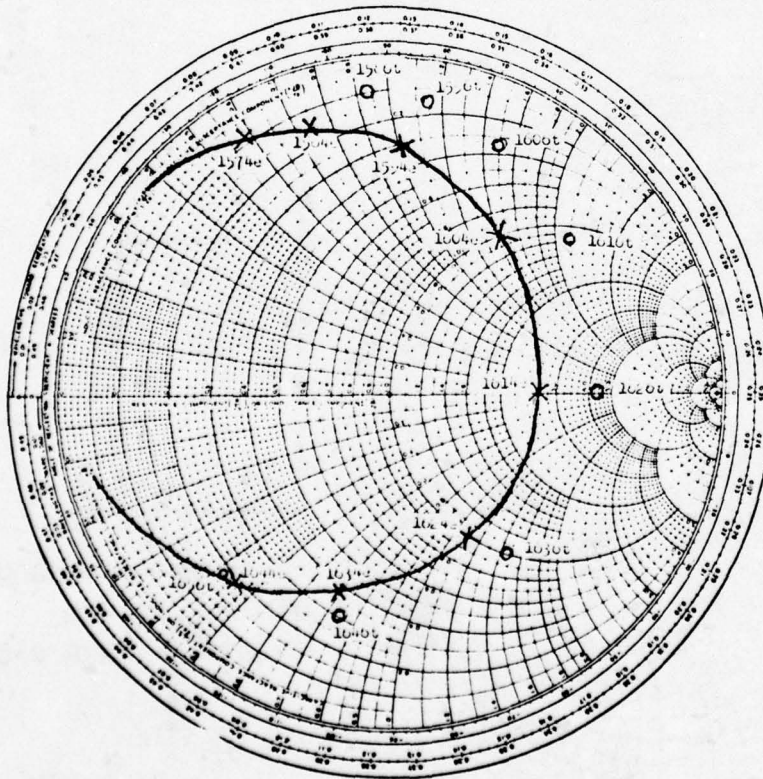
BEST AVAILABLE COPY

5. The Board of Directors of the Corporation shall have the right to purchase the shares of the Corporation owned by any person who is not a resident of the State of New York, at the same price as the shares are then being sold to the public, if the Board of Directors shall so determine.



center fed rectangle
 $m=1, n=0$ $k_{01} = \pi/b$
 $a=11.4\text{cm.}$ $b=7.6\text{cm.}$ $e=5.7\text{cm.}$

(a)

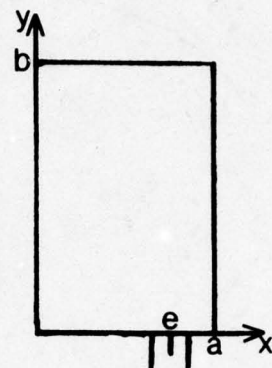
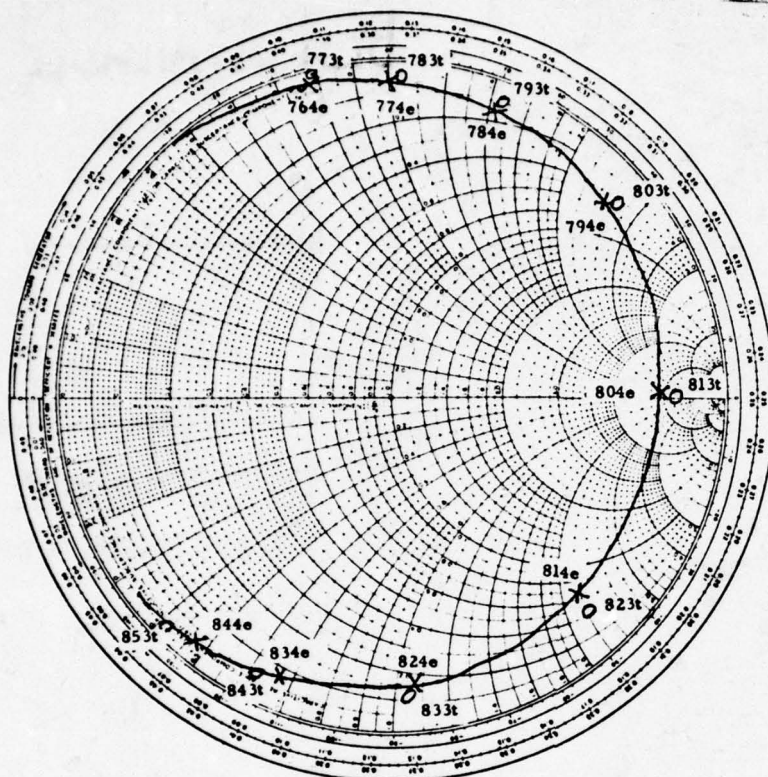


center fed rectangle
 $m=0, n=2 \quad k_{20} = 2\pi/a$
 $a=11.4\text{cm.} \quad b=7.6\text{cm.} \quad e=5.7\text{cm.}$

(b)

Figure 9. Theoretical and experimental impedance characteristics of rectangular microstrip antenna. x-x-x-x experimental points o-theoretical points, e-experimental frequency (MHz), t-theoretical frequency (MHz), (n,m)-dominate mode at resonance.

BEST AVAILABLE COPY

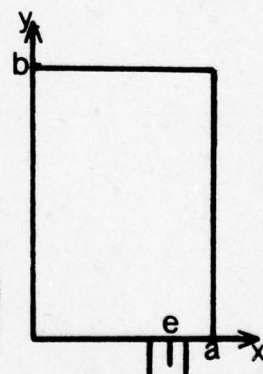
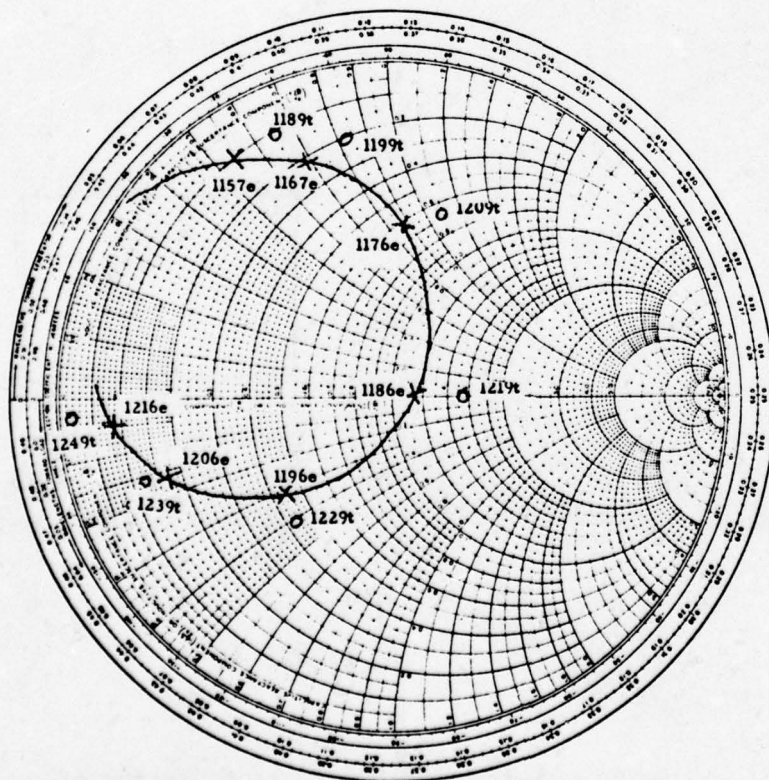


off center fed rectangle

$$m=1, n=0 \quad k_{01} = \pi/b$$

$a=7.6\text{cm}$. $b=11.4\text{cm}$. $e=5.63\text{cm}$.

(a)



off center fed rectangle

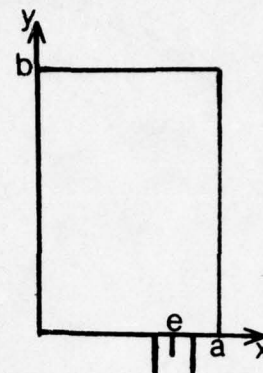
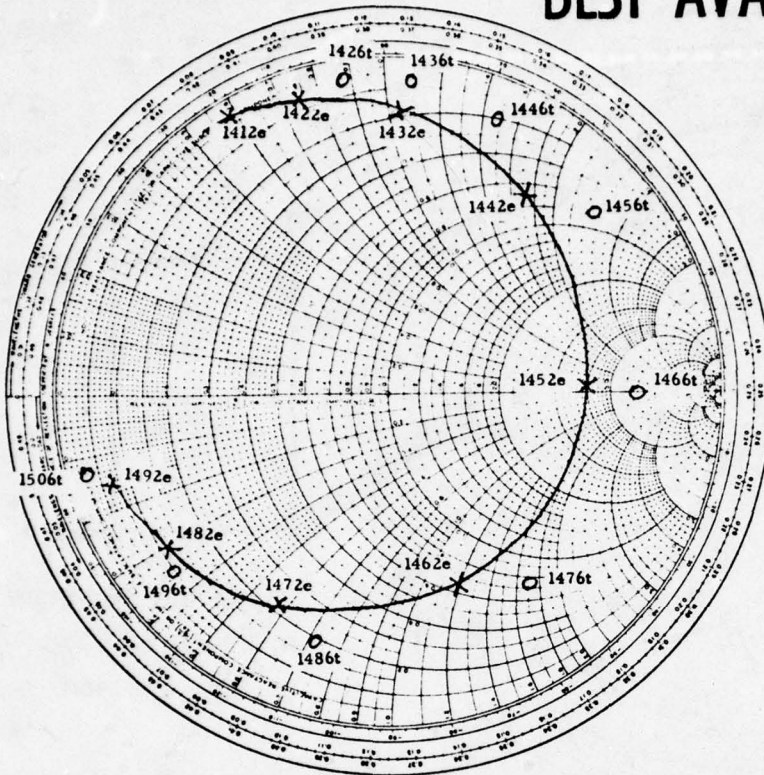
$$m=0, n=1 \quad k_{10} = \pi/a$$

$a=7.6\text{cm}$. $b=11.4\text{cm}$. $e=5.63\text{cm}$.

(b)

Figure 10. Theoretical and experimental impedance characteristics of rectangular microstrip antenna. X-X-X-X experimental points o-theoretical points, e-experimental frequency (MHz), t-theoretical frequency (MHz), (n,m)-dominate mode at resonance.

BEST AVAILABLE COPY



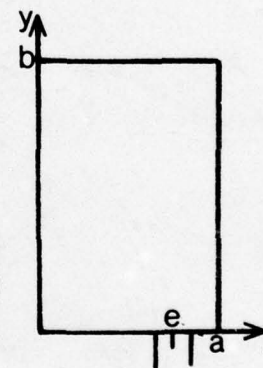
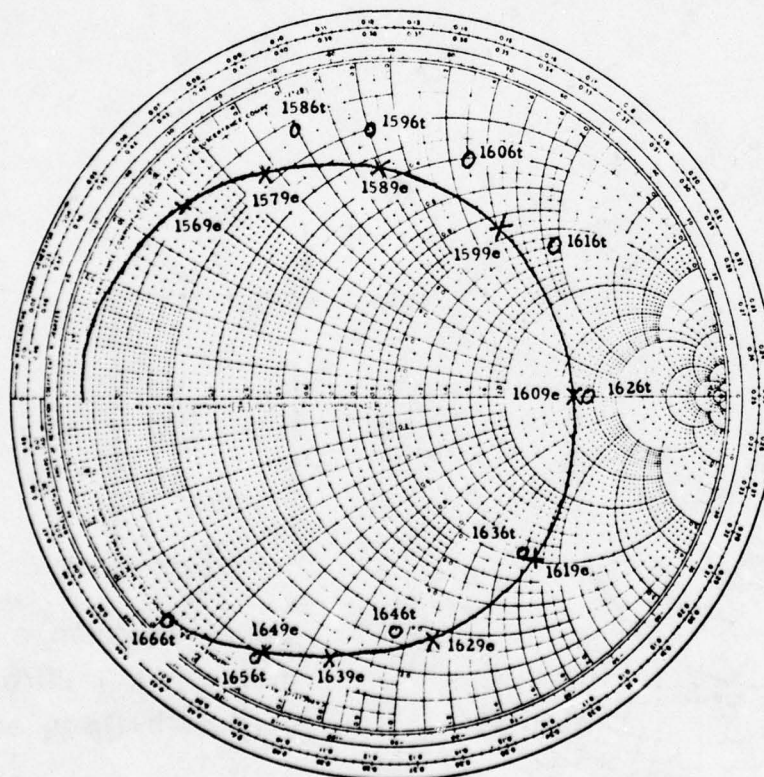
off center fed rectangle

$$m=1, n=1$$

$$k_{11}^2 = (\pi/a)^2 + (\pi/b)^2$$

$$a=7.6\text{cm. } b=11.4\text{cm. } e=5.63\text{cm.}$$

(c)



off center fed rectangle

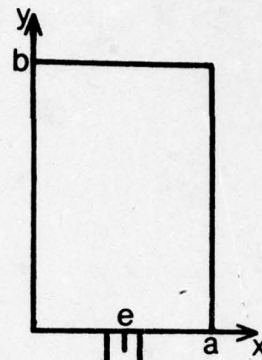
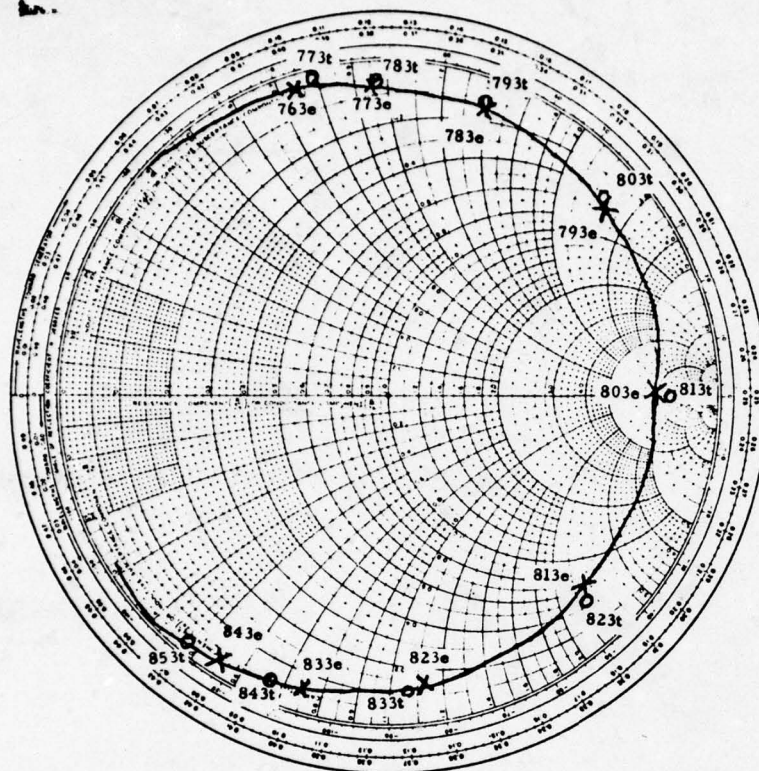
$$m=2, n=0 \quad k_{02} = 2\pi/b$$

$$a=7.6\text{cm. } b=11.4\text{cm. } e=5.63\text{cm.}$$

(d)

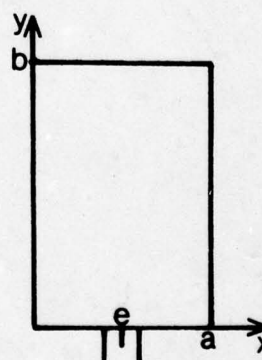
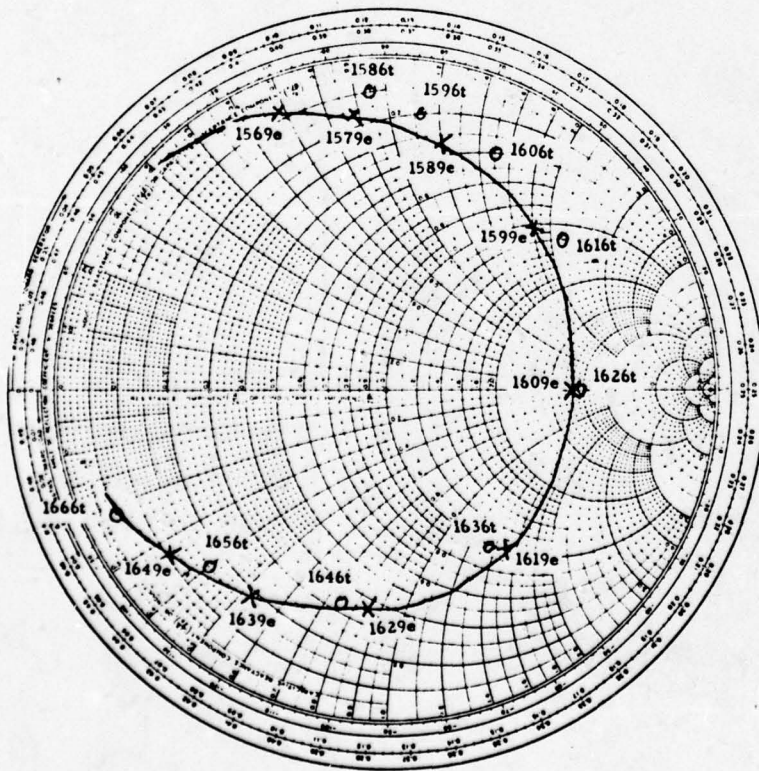
Figure 10. (cont.)

BEST AVAILABLE COPY



center fed rectangle
 $m=1, n=0 \quad k_{01} = \pi/b$
 $a=7.6\text{cm. } b=11.4\text{cm. } e=3.8\text{cm.}$

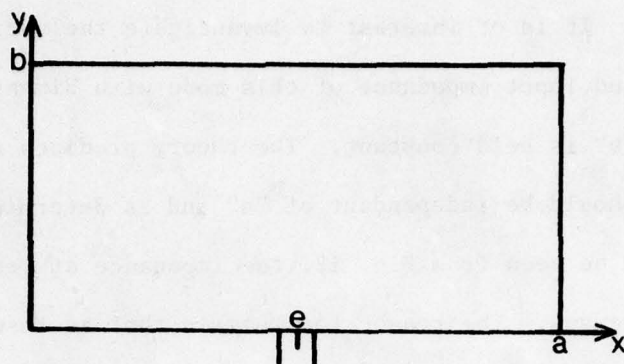
(a)



center fed rectangle
 $m=2, n=0 \quad k_{02} = 2\pi/b$
 $a=7.6\text{cm. } b=11.4\text{cm. } e=3.8\text{cm.}$

(b)

Figure 11. Theoretical and experimental impedance characteristics of rectangular microstrip antenna. X-X-X-X experimental points o-theoretical points, e-experimental frequency (MHz), t-theoretical frequency (MHz), (n,m)-dominate mode at resonance.



$$b=5.95\text{cm. } e=a/2$$

a(cm.)	$Z(\Omega)$ -exp.	$Z(\Omega)$ -theory	experimental		ϵ_{eff}	$f_r(a_2)(\text{Mhz})$
			resonant freq(Mhz)	Q		
20.00	50	50	1507	43.4	2.5896	1507
16.05	70	68	1509	49.0	2.5827	1511
10.10	140	136	1518	62.6	2.5630	1520
8.10	205	196	1524	73.2	2.5507	1526
6.05	320	329	1535	93.0	2.5309	1534
4.05	675	681	1552	133.2	2.4965	1547

Figure 12. Variation of frequency and Q for a center-fed rectangle.

is shown a rectangle fed in the center so that only the $n,m = (1,0)$ mode is excited. It is of interest to investigate the variation of resonant frequency and input impedance of this mode with dimension "a" while dimension "b" is held constant. The theory predicts that the resonant frequency should be independent of "a" and is determined from $k = \pi/b$.

As can be seen from Fig. 12, the impedance at resonance increases as "a" decreases. The reason for this is that at resonance $B = 0$, and therefore by Equation (9) and (10a),

$$Z = 1/G = |V|^2/P_t \quad . \quad (23)$$

As "a" is varied $|V|$, the voltage at the feed, is unchanged for the $n,m = (0,1)$ mode, but the power radiated decreases as "a" decreases because the radiating aperture decreases in length.

The measured resonant frequency changes by 3 percent as "a" is varied from 4.05 cm to 20.00 cm as shown in Fig. 12. There may be three possible factors that affect the resonant frequency.

i) The $n,m = (0,1)$ mode consists of waves traveling along the $\pm y$ -axis between $y = 0$ and $y = 5.95$. The reflection coefficient at these edges may not be purely real so that the reflected wave has a phase shift which will affect the resonant frequency. This may be modeled by extending the H-wall from the actual edge an amount Δ such that the phase delay in the wave traveling the distance 2Δ is equal to the phase shift of the reflection coefficient at the edge.

ii) The propagation constant of a wave traveling in a microstrip line cannot be determined by the dielectric constant of the substrate alone, since the wave includes fringing fields that extend into free space along the edges $x = 0$ and a . A formula derived by Schneider [11] for the

wavelength of a wave in a microstrip line is

$$\frac{\lambda_g}{\lambda_0} = \frac{1}{(\epsilon_r \epsilon_{\text{eff}})^{1/2}} \frac{(\epsilon_{\text{eff}})^{1/2} f_n^2 + (\epsilon_r)^{1/2}}{(f_n^2 + 1)} \quad (24)$$

where

λ_g = the wavelength in the microstrip line

λ_0 = free space wavelength

ϵ_r = relative permittivity

$$\epsilon_{\text{eff}} = \frac{\epsilon_r + 1}{2} + \frac{\epsilon_r - 1}{2} \frac{1}{\left(1 + \frac{10t}{a}\right)^{1/2}}, \quad f_n = \frac{4t(\epsilon_r - 1)}{\lambda_0}$$

t = thickness of the substrate.

For our case Equation (24) can be approximated by

$$\frac{\lambda_g}{\lambda_0} = \frac{1}{\sqrt{\epsilon_{\text{eff}}}} \quad (25)$$

Since ϵ_{eff} is a function of "a," λ_g and the resonant frequency must be also.

iii) The resonant frequency of a cavity varies with the Q of the cavity. Slater [12] shows that the resonant frequency of a cavity varies with Q_w to the first order and with Q_d to the second order where

$$Q_d = \frac{\omega \mathcal{E}}{P_d} = Q \text{ due to dielectric loss}$$

$$Q_w = \frac{\omega \mathcal{E}}{P_w} = Q \text{ due to loss in the walls}$$

P_d is power lost in the dielectric, P_w is the power lost in the walls of the cavity, and \mathcal{E} is the energy stored in the cavity. In our problem the loss

in the wall consists of that in the electric conducting plates at $z = 0$ and $z = t$ and that due to radiation through the H-walls. The former is found to be negligible, whereas the latter is equal to P_r given earlier. Then the resonant frequency is given by

$$f_r = f_{r0} \left(1 - \frac{1}{2Q_r} \right) \quad (27)$$

where

$$Q_r = \frac{\omega \xi}{P_r} \quad (28)$$

and f_{r0} is the resonant frequency of the lossless cavity.

The resonant wavelength for the $n,m = (0,1)$ mode is then, using (i) and Equation (27),

$$\lambda_r = 2(b + 2\Delta) / \left(1 - \frac{1}{2Q_r} \right) \quad (29)$$

From Equation (25) this yields

$$f_r = \frac{C_0}{\lambda_0} = \frac{C_0}{\lambda_r \sqrt{\epsilon_{\text{eff}}}} = \frac{C_0}{2\sqrt{\epsilon_{\text{eff}}}} \frac{\left(1 - \frac{1}{2Q_r} \right)}{(b + 2\Delta)} \quad (30)$$

where C_0 is the speed of light in free space.

ϵ_{eff} and Q_r are functions of "a" (see Fig. 12). If it is assumed that Δ is not dependent on "a," then if the resonant frequency for some value of $a = a_1$ is known, the resonant frequency for $a = a_2$ can be determined from

$$f_r(a_2) = \frac{\left[1 - \frac{1}{2Q_r(a_1)} \right]}{\left[1 - \frac{1}{2Q_r(a_2)} \right]} \sqrt{\frac{\epsilon_{\text{eff}}(a_2)}{\epsilon_{\text{eff}}(a_1)}} f_r(a_1) \quad (31)$$

In Fig. 12 $f_r(a_2)$ is calculated from $f_r(a_1)$ where $a_1 = 20.00$ cm and $f_r(a_1) = 1507$ MHz. From this $\Delta = .082$ cm, which is 51 percent of the substrate thickness. Figure 13 compares a plot of $f_r(a_2)$ with experimental values of resonant frequency and also shows the uncorrected theoretical value of resonant frequency.

In Fig. 14 some typical measured and computed radiation patterns for an antenna of dimensions $a = 11.43$ cm, $b = 7.62$ cm and fed at $e = 8.57$ cm are shown. The x's are the theoretical points and the continuous solid or dashed curves are the measured patterns. Both E_θ and E_ϕ were measured in each of the two cuts, $\phi = 0$ and $\phi = 90^\circ$. In Fig. 14 one component of polarization was negligible when compared to the other in each case and is not shown. This applies to patterns referred to later in the report. In Figs. 14a and 14b the $n,m = (1,0)$ mode is excited and in 14c and 14d the $n,m = (0,1)$ mode is excited.

As is seen, there is very good agreement between theoretical and experimental radiation patterns for the two modes shown in Fig. 14. It may also be noted that there is good agreement for the impedance for the $(n,m) = (0,1)$ mode (Figs. 8b, 9a, 10a, 11a) and the $(n,m) = (0,2)$ mode (Figs. 10d, 11b) but that agreement is not as favorable for the other modes shown.

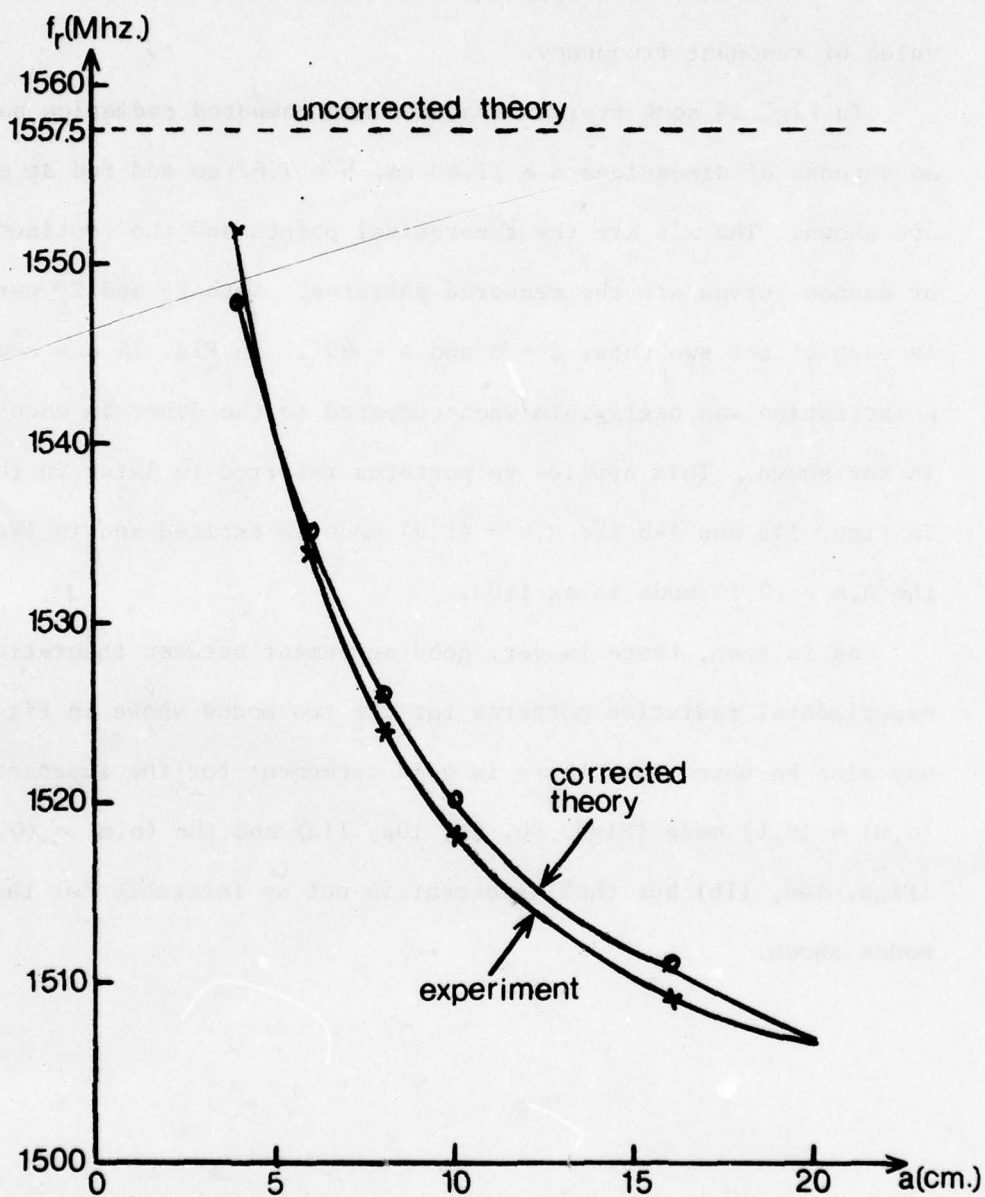


Figure 13. Experimental frequency vs. corrected theoretical frequency for the rectangle of Figure 12.

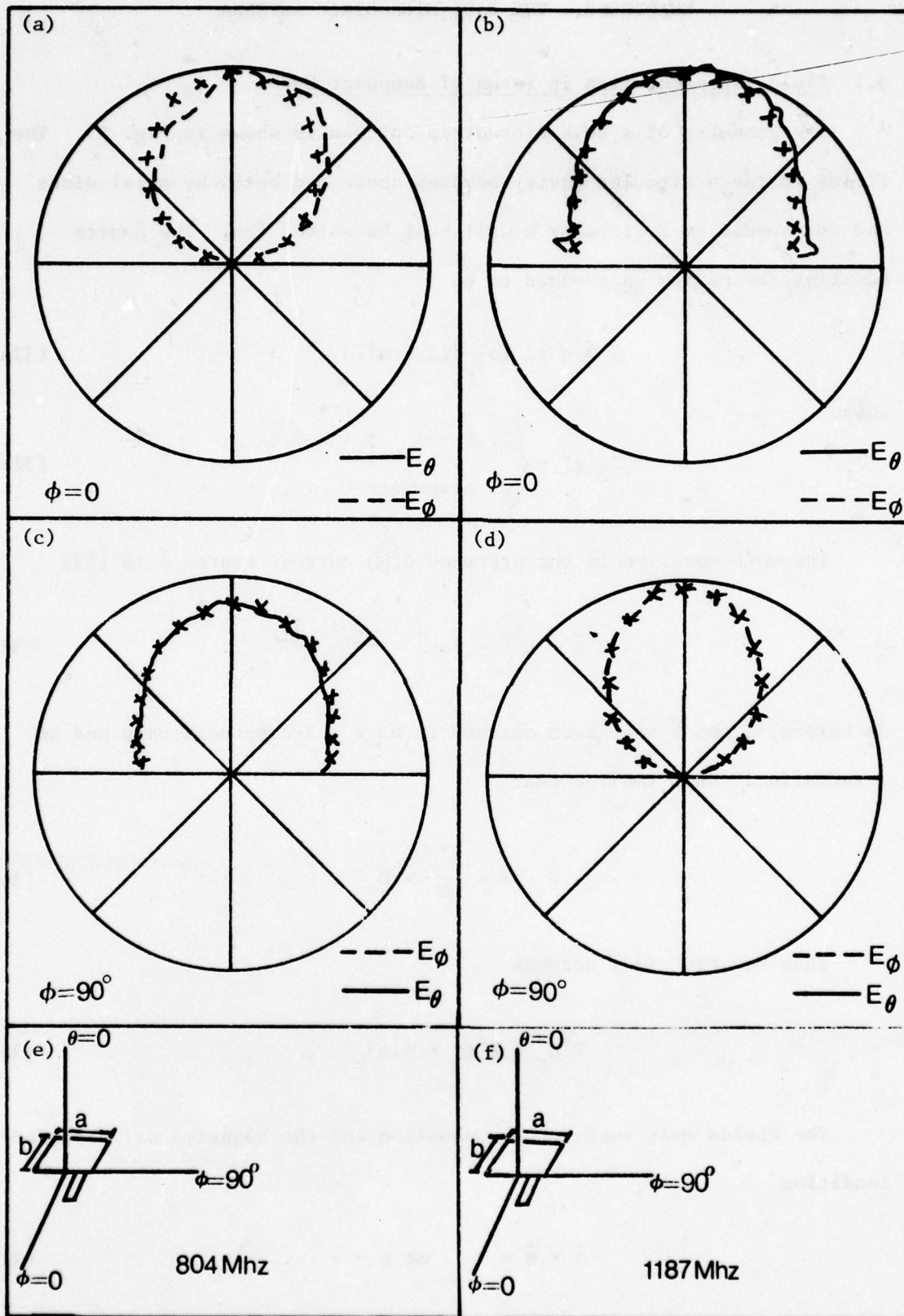


Figure 14. Radiation pattern for a rectangular microstrip antenna. Solid or dashed line-measured pattern, x-theoretical pattern.

CHAPTER 3. THE DISK MICROSTRIP ANTENNA

3.1 Field Representation in Terms of Resonant Modes

The geometry of a disk microstrip antenna is shown in Fig. 15. The fields inside a circular cavity bounded above and below by metal disks and surrounded by a circular H-wall must be solved for. The source exciting the cavity is assumed to be

$$\vec{J} = \hat{z} J_z(\phi) \delta(\rho - a)/a \quad (32a)$$

where

$$J_z(\phi) = \begin{cases} J, & \pi - \delta < \phi < \pi + \delta \\ 0, & \text{elsewhere} \end{cases} \quad (32b)$$

The wave equation in the presence of a current source \vec{J} is [13]

$$\nabla^2 \vec{E} + k^2 \vec{E} = j\omega\mu \vec{J} - \frac{\nabla(\nabla \cdot \vec{J})}{j\omega\epsilon} \quad (33)$$

As before, \vec{J} and \vec{E} have been assumed to have a z-component only and no z-variation. This implies that

$$\vec{\nabla} \cdot \vec{J} = \frac{\partial J_z}{\partial z} = 0 \quad (34)$$

Thus Equation (33) becomes

$$\nabla^2 E_z + k^2 E_z = j\omega\mu J_z \quad (35)$$

The fields must satisfy this equation and the magnetic wall boundary condition

$$\hat{\rho} \times \vec{H} = 0 \quad \text{at } \rho = a \quad (36)$$

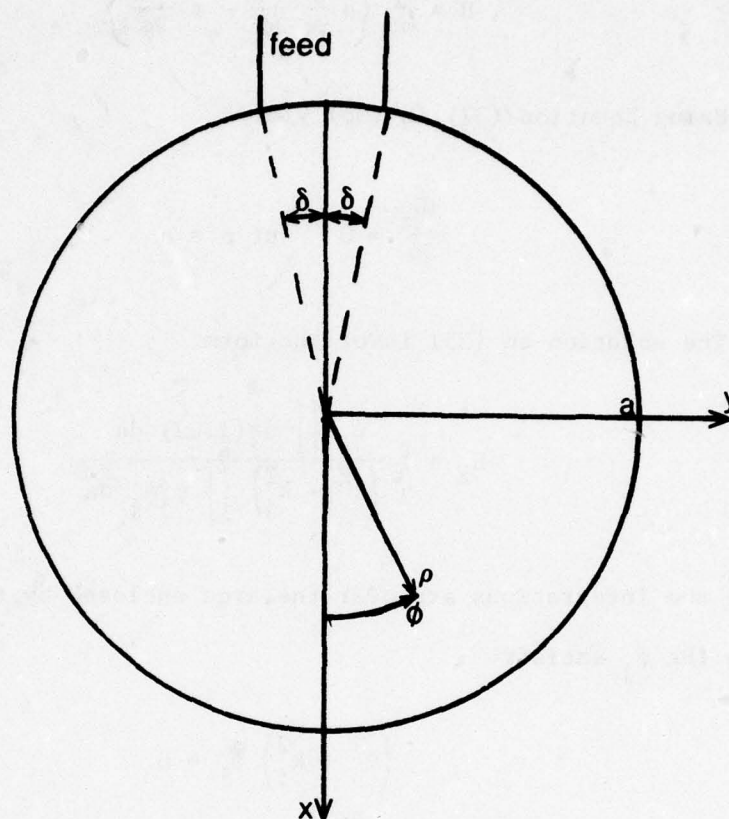


Figure 15. Geometry of disk microstrip antenna.

Since \vec{E} has a z-component only

$$\vec{H} = \frac{j}{\omega\mu} \left\{ \hat{\rho} \frac{1}{\rho} \frac{\partial E_z}{\partial \phi} - \hat{\phi} \frac{\partial E_z}{\partial \rho} \right\} . \quad (37)$$

Using Equation (37) in (36) yields

$$\frac{\partial E_z}{\partial \rho} = 0 \quad \text{at } \rho = a . \quad (38)$$

The solution to (35) is of the form

$$E_z = \sum_j \frac{\psi_j \iint \psi_j^* (j\omega\mu J) da}{(k^2 - k_j^2) \iint \psi_j^* \psi_j da} \quad (39)$$

where the integrations are over the area enclosed by the magnetic walls

where the ψ_j satisfy

$$(\nabla^2 + k_j^2) \psi_j = 0 \quad (40a)$$

$$\left. \frac{\partial \psi_j}{\partial \rho} \right|_{\rho=a} = 0 . \quad (40b)$$

In general the solutions to Equation (40) consist of an infinite set of eigenfunctions $\{\psi_j\}$ with corresponding eigenvalues $\{k_j\}$ where eigenfunctions corresponding to distinct eigenvalues are orthogonal.

For the disk the solutions to Equation (40) are of the form

$$\psi_{mn} = J_n(k_{mn}\rho) e^{jn\phi}, \quad \begin{array}{l} n = 0, 1, 2, \dots \\ m = 1, 2, \dots \end{array} \quad (41a)$$

where J_n are Bessel functions of order n and k_{mn} are solutions to

$$\left. \frac{\partial J_n(k_{mn}\rho)}{\partial \rho} \right|_{\rho=a} = 0 \quad (41b)$$

Using the expressions for \vec{J} given by Equation (32) and Equation (41) in (39) one obtains

$$E_z = j\omega\mu J \left\{ \begin{aligned} & \frac{2\delta}{k^2 \pi a} + \sum_{m=2}^{\infty} \frac{2\delta}{(k^2 - k_{m0}^2)} \frac{J_0(k_{m0}\rho)}{\pi a J_0(k_{m0}a)} \\ & + \sum_{m=1}^{\infty} \sum_{n=1}^{\infty} \frac{4a(\sin n\delta) \cos n(\phi - \pi) J_n(k_{mn}\rho)}{n(k^2 - k_{mn}^2) \pi \left(a^2 - \frac{n^2}{k_{mn}^2} \right) J_n(k_{mn}a)} \end{aligned} \right\} \quad (42)$$

Resonance occurs when

$$k = k_{mn} = \chi_{mn}/a \quad (43)$$

where χ_{mn} is the m^{th} zero of the derivative of $J_n(x)$. The first few χ_{mn} 's are

$$\begin{aligned} \chi_{10} &= 0 \\ \chi_{11} &= 1.84118 \\ \chi_{12} &= 3.05424 \\ \chi_{20} &= 3.83171 \\ \chi_{13} &= 4.20119 \end{aligned} \quad (44)$$

The \vec{K} -current in the magnetic wall at $\rho = a$ is derived by using Equation (42) in

$$\vec{K}(a, \phi) = -\hat{\rho} \times \hat{z} E_z(a, \phi) = -\hat{\phi} E_z(a, \phi) \quad (45)$$

to get

$$\vec{K}(a, \phi) = -\hat{\phi} j \omega \mu J \left\{ \frac{2\delta}{k^2 \pi a} + \sum_{m=2}^{\infty} \frac{2\delta}{(k^2 - k_{m0}^2) \pi a} + \sum_{m=1}^{\infty} \sum_{n=1}^{\infty} \frac{4a(\sin n\delta) [\cos n(\phi - \pi)]}{n(k^2 - k_{mn}^2) \pi \left(a^2 - \frac{n^2}{k_{mn}^2} \right)} \right\} \quad (46)$$

The \vec{K} -current distribution around the edge for the mn^{th} term is proportional to $\cos n(\phi - \pi)$. This is illustrated in Fig. 16.

3.2 Comparison of Theoretical and Experimental Impedances and Radiation Patterns

From the \vec{K} -current distribution the radiated power, P_r , can be determined by using Equation (46) in Equations (18) - (20). Power loss in the dielectric is found by using Equation (42) in (21). P_c (loss in conductors) and P_s (loss due to surface waves) which were found to be negligible for the rectangular microstrip are neglected so that total power lost is

$$P_t \approx P_r + P_d \quad (47)$$

Impedance is then computed by applying Equations (9) - (10).

The accuracy of the theory is checked against experiment on a disk of radius $a = 6.75$ cm. As in the case of the rectangular microstrip, the uncorrected theoretical values of the resonant frequency are greater than the measured ones, as shown in Fig. 17. In general the agreements in the impedance characteristics between the theory and experiments are reasonably close.

Radiation patterns for the disk antenna are shown in Figs. 18a and 18b. Again both E_θ and E_ϕ components were measured and computed in each

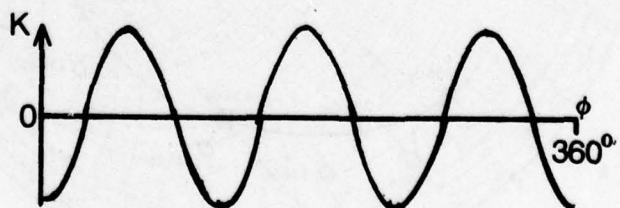
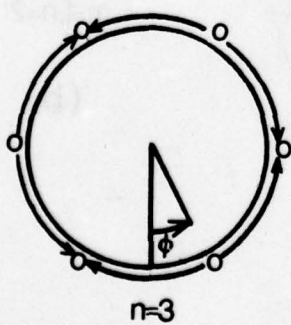
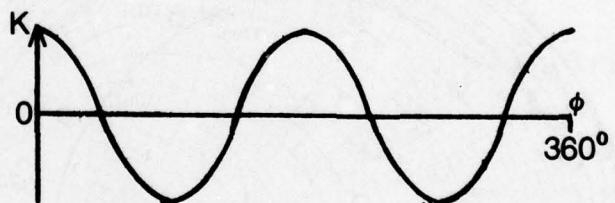
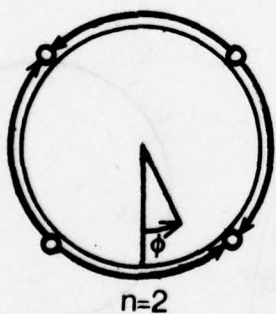
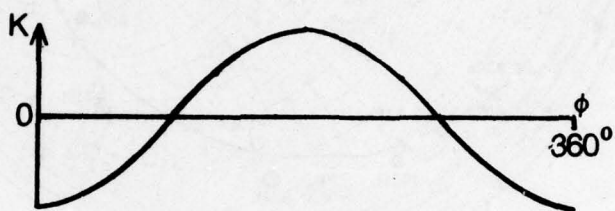
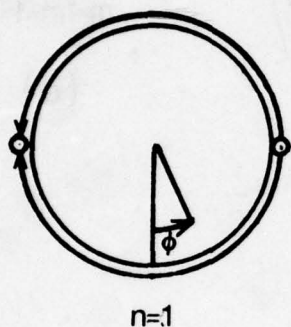
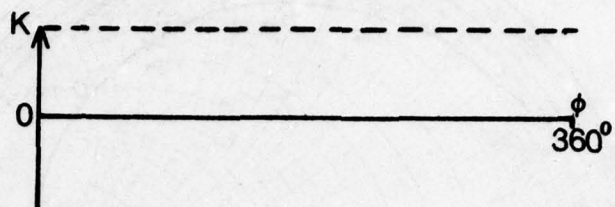
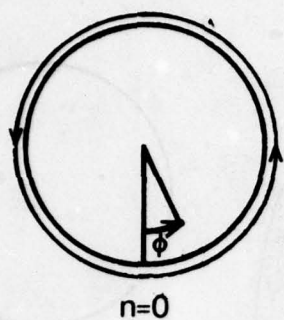
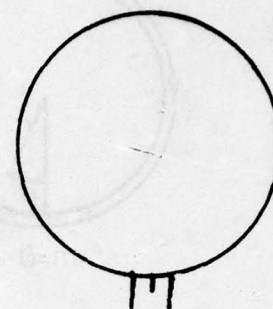
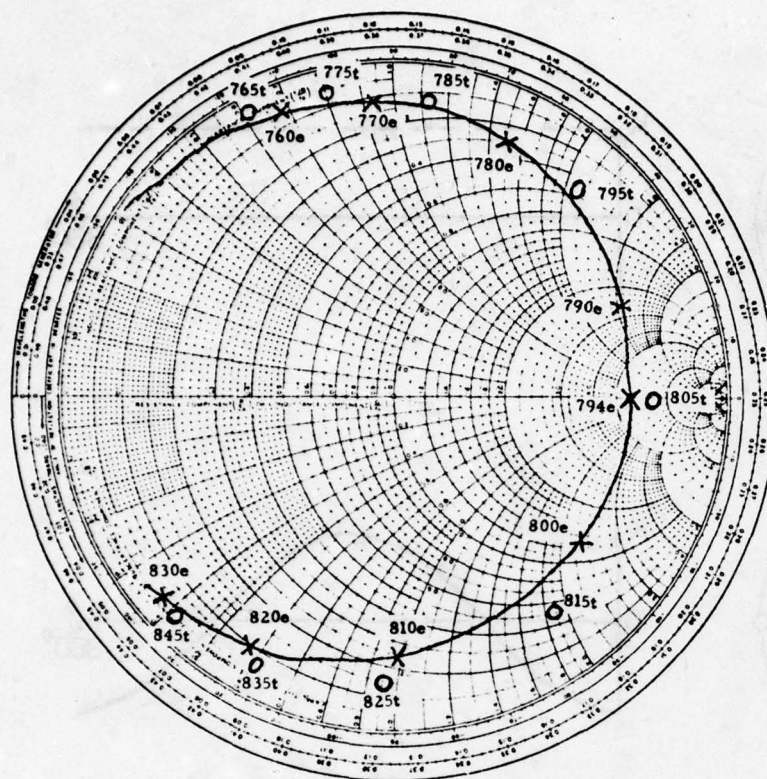
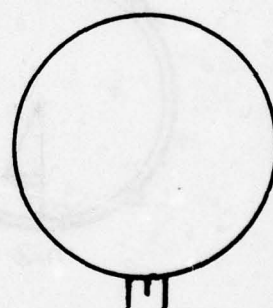
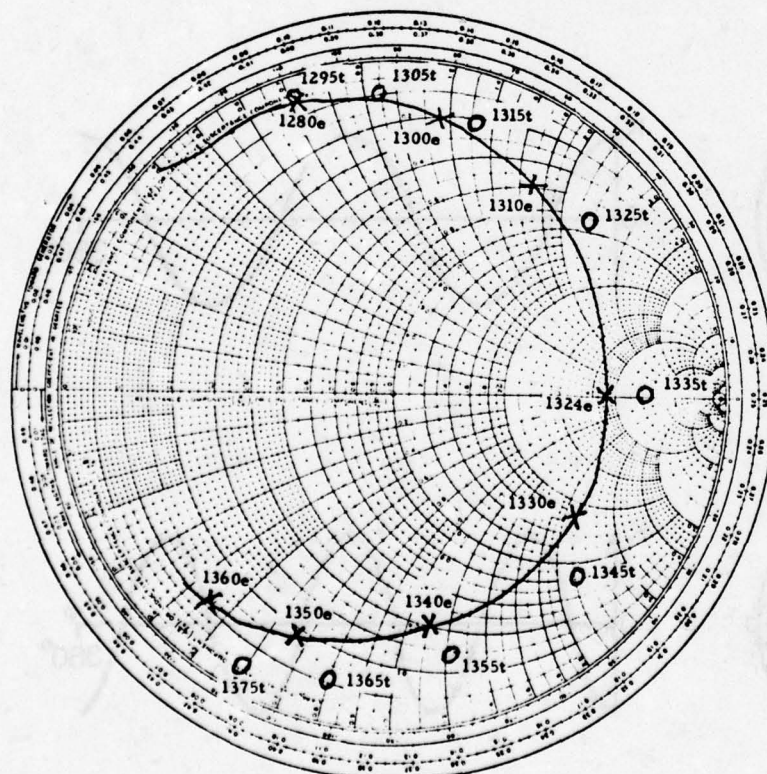


Figure 16. \vec{K} -current distribution for mn -th mode.



$a=6.75\text{cm.}$
 $m=1, n=1$

(a)

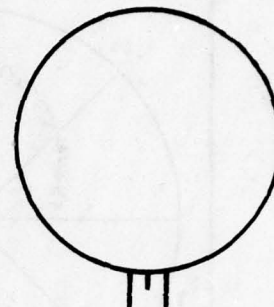
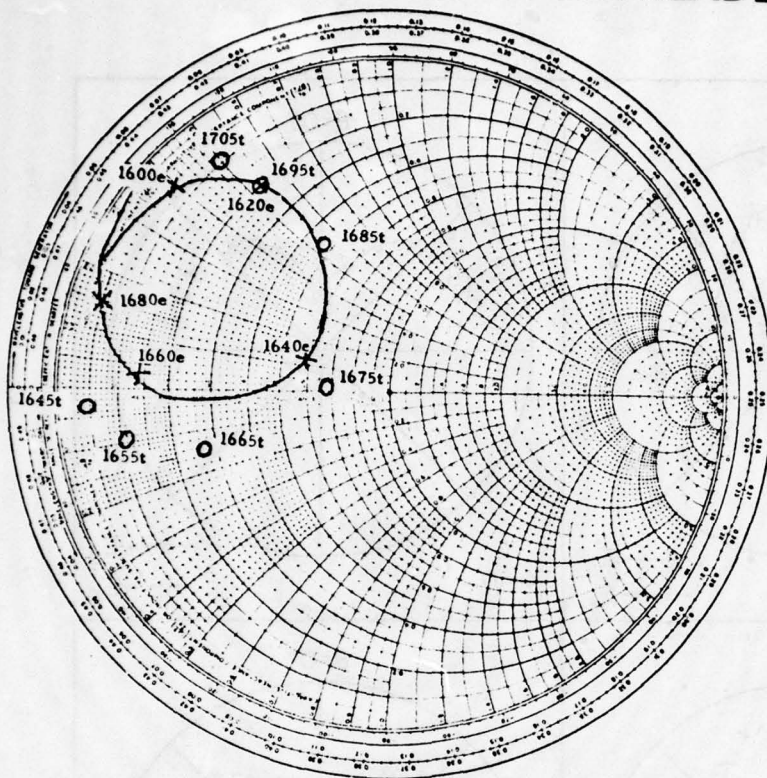


$a=6.75\text{cm.}$
 $m=1, n=2$

(b)

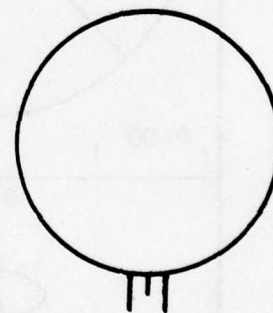
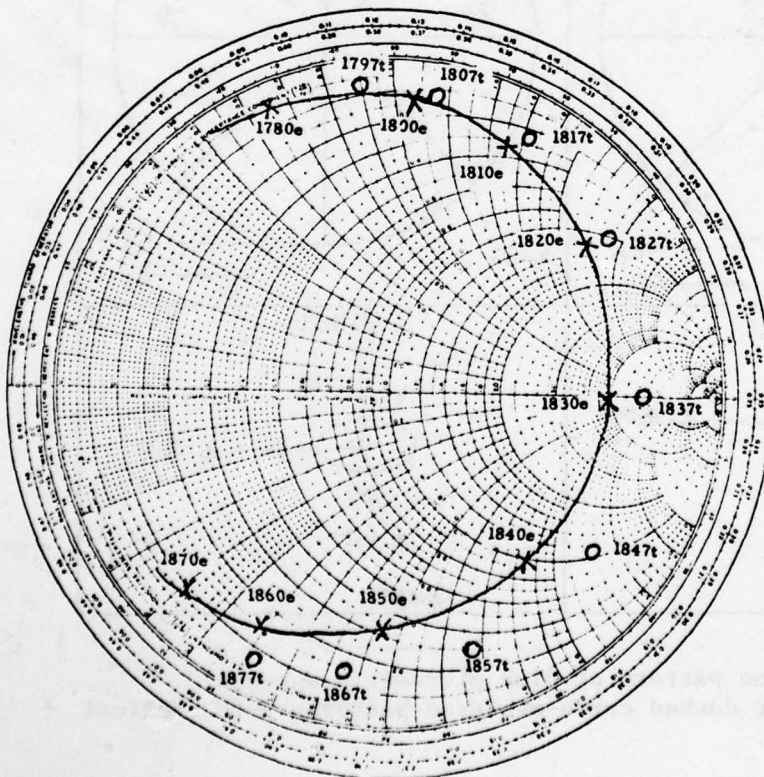
Figure 17. Theoretical and experimental impedance characteristics of disk microstrip antenna. X-X-X-X experimental points o-theoretical points, e-experimental frequency (MHz), t-theoretical frequency (MHz), (m,n)-dominate mode of resonance.

BEST AVAILABLE COPY



$a=6.75\text{cm.}$
 $m=2, n=0$

(c)



$a=6.75\text{cm.}$
 $m=1, n=3$

(d)

Figure 17. (cont.)

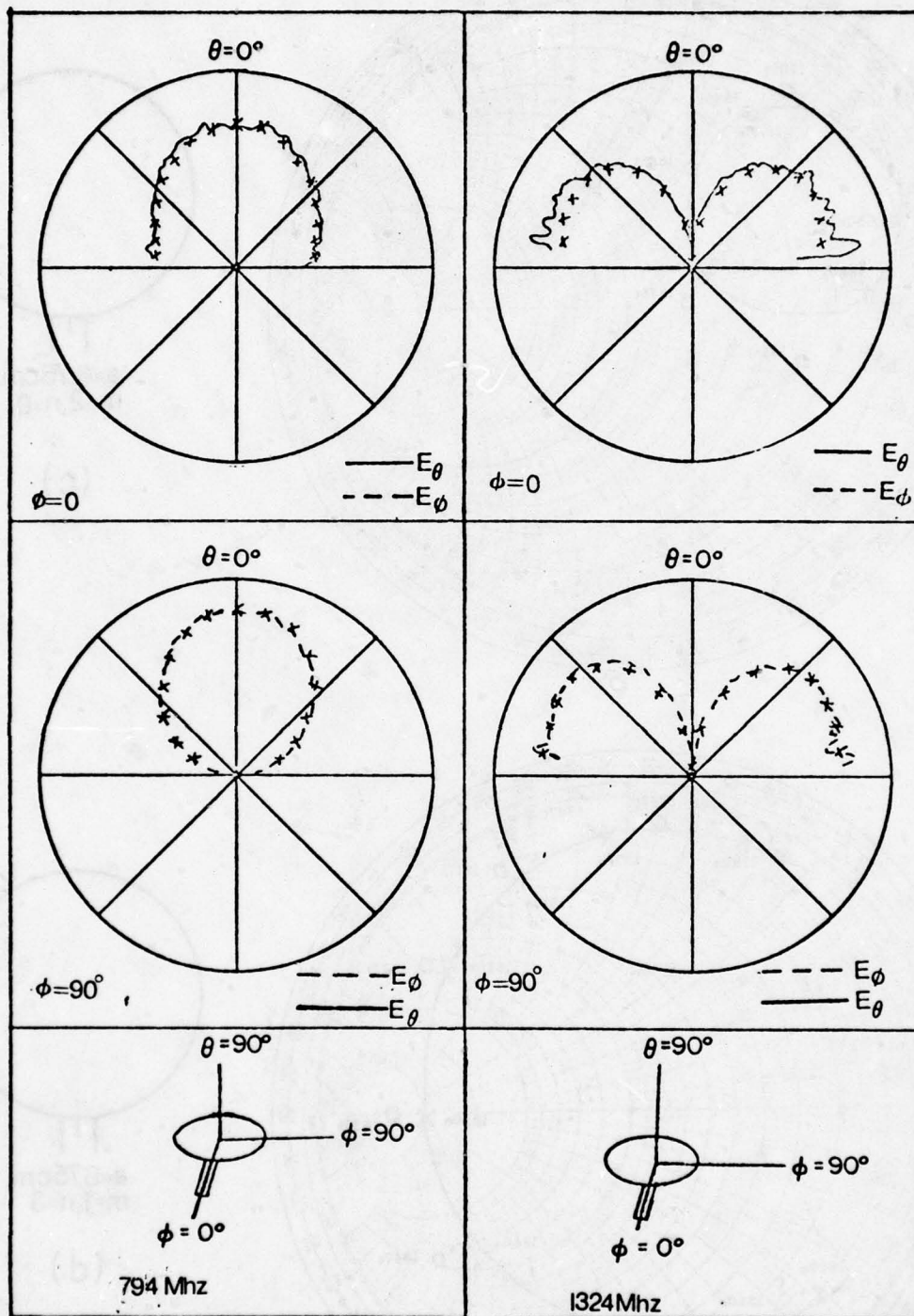


Figure 18a. Radiation pattern of disk microstrip antenna. Solid or dashed curve-measured pattern, x-theoretical pattern.

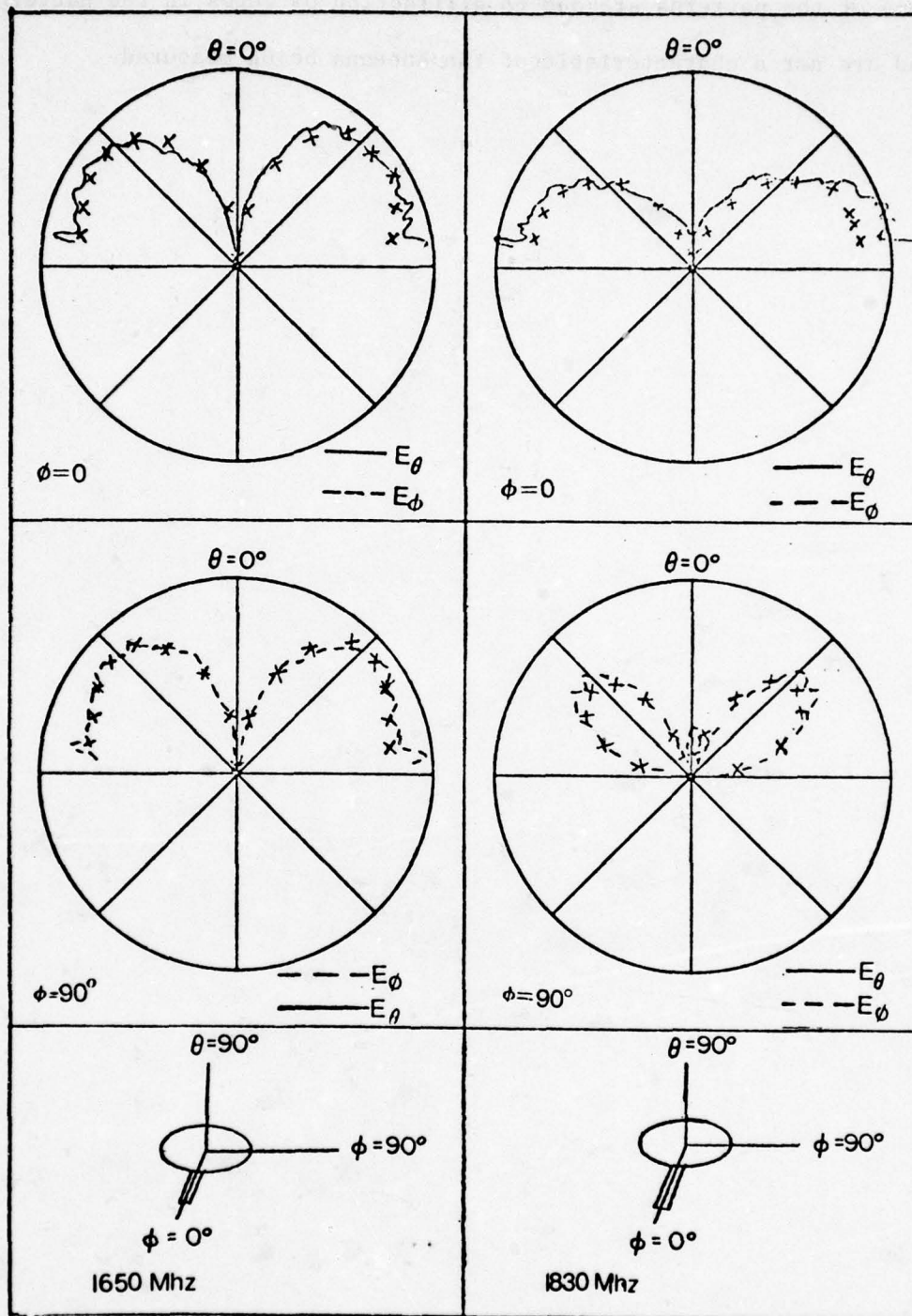
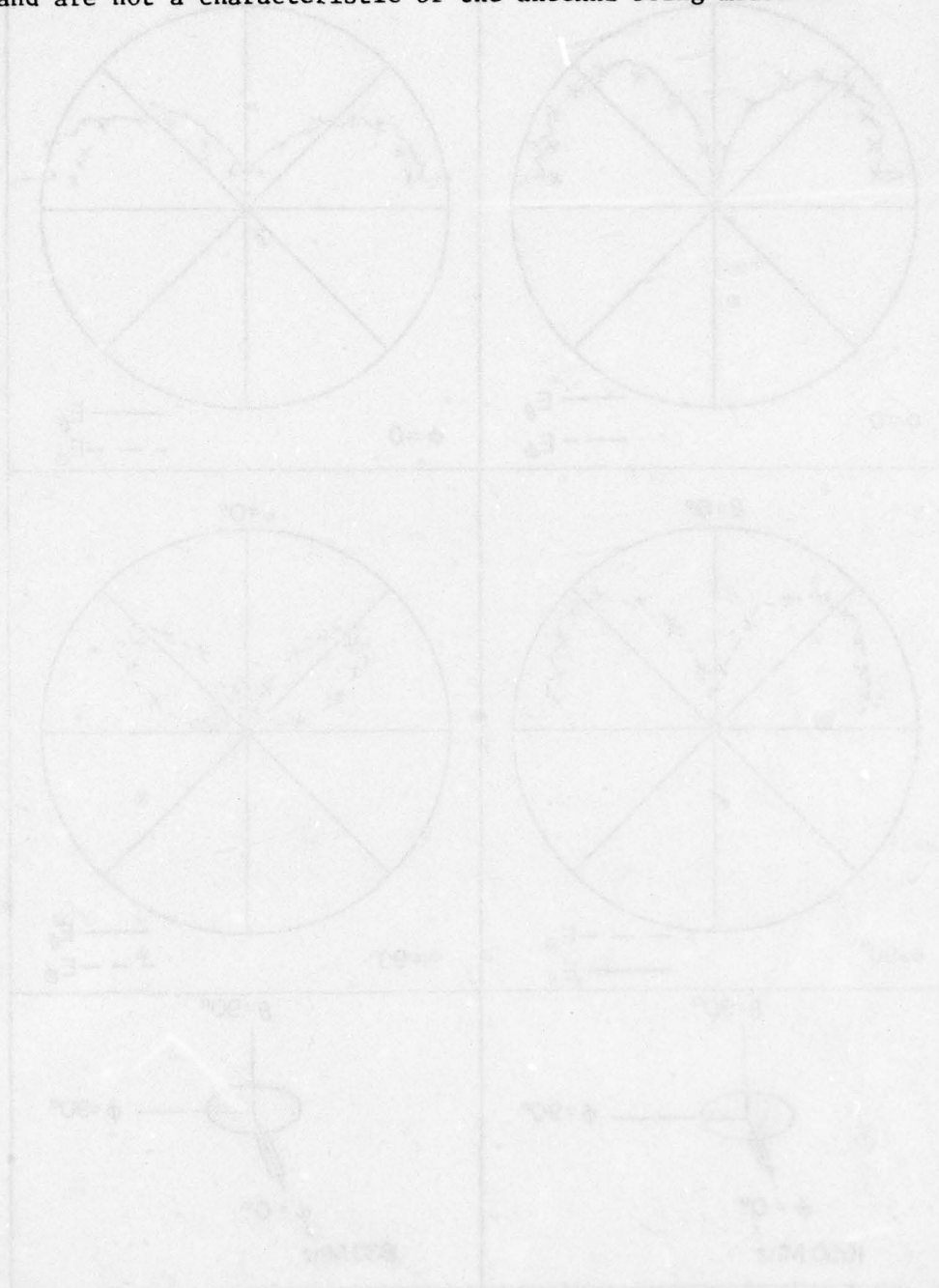


Figure 18b. Radiation pattern of disk microstrip antenna. Solid or dashed curve-measured pattern, x-theoretical pattern.

of the $\phi = 0$ and 90° cuts. The narrow lobes exhibited near $\theta = 90^\circ$ in some of the patterns are due to diffraction of edges in the pattern range and are not a characteristic of the antenna being measured.



CHAPTER 4. THE HALF-DISK MICROSTRIP ANTENNA

4.1 Field Representation in Terms of Resonant Modes

The geometry of the half-disk microstrip antenna is shown in Fig. 19. The cavity is bounded above and below by metal half disks, surrounded by a magnetic wall and excited by a source along $y = 0$

$$\vec{J} = \hat{z} J_z(\rho) \delta(\phi) / \rho \quad (48a)$$

where

$$J_z(\rho) = \begin{cases} J & \text{if } c < \rho < d \\ 0 & \text{elsewhere} \end{cases} \quad (48b)$$

The electric field must satisfy Equation (35), i.e.,

$$\nabla^2 E_z + k^2 E_z = j\omega\mu J_z$$

and the magnetic wall boundary conditions.

As was done for the case of the full disk, E_z may be expanded in terms of eigenfunctions [Equation (39)] which satisfy (40a) and the magnetic wall boundary conditions at $\rho = a$ and $\phi = 0, \pi$.

These eigenfunctions are

$$\psi_{mn} = J_n(k_{mn}\rho) \cos n\phi, \quad \begin{matrix} n = 0, 1, 2, \dots \\ m = 1, 2, \dots \end{matrix} \quad (49a)$$

where J_n are Bessel functions of order n and the k_{mn} are determined from

$$\left. \frac{dJ(k_{mn}\rho)}{d\rho} \right|_{\rho=a} = 0 \quad (49b)$$

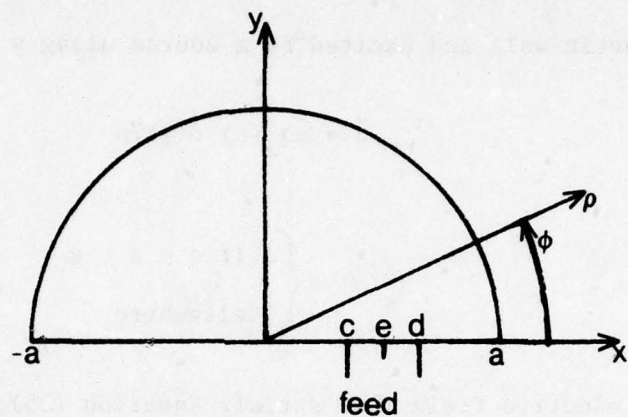


Figure 19. Geometry of 1/2 - disk microstrip antenna.

Substitute Equation (49) into (39) to obtain

$$E_z = j\omega\mu J \left\{ \frac{d-c}{2\pi a^2 k^2} + \sum_{m=1}^{\infty} \sum_{n=0}^{\infty} \frac{(d-c) J_n \left(k_{mn} \frac{d+c}{2} \right) J_n(k_{mn} \rho) \cos n\phi}{\left(k^2 - k_{mn}^2 \right) \frac{1}{2} \pi \left(a^2 - \frac{n^2}{k_{mn}^2} \right) J_n^2(k_{mn} a)} \right\} \quad (50)$$

where \sum' implies that the term $m = 1, n = 0$ is omitted in the summation.

The \vec{K} -current distribution around the edge of the half disk is given below.

$$(a) \text{ for } \phi = \begin{pmatrix} \pi \\ 0 \end{pmatrix} \text{ and } 0 \leq \rho \leq a$$

$$\vec{K} \begin{pmatrix} \pi \\ \rho, \\ 0 \end{pmatrix} = \hat{x} j\omega\mu J \left\{ \frac{F_{10}}{N_{10} k^2} + \sum_{m=1}^{\infty} \sum_{n=0}^{\infty} \frac{\begin{pmatrix} (-1)^n \\ 1 \end{pmatrix} F_{mn} J_n(k_{mn} \rho)}{\left(k^2 - k_{mn}^2 \right) N_{mn}} \right\} \quad (51a)$$

where

$$\begin{cases} (-1)^n \text{ is taken if } \phi = \pi \\ 1 \text{ is taken if } \phi = 0 \end{cases}$$

$$(b) \text{ for } \rho = a \text{ and } 0 < \phi < \pi$$

$$\vec{K}(a, \phi) = \hat{\phi} j\omega\mu J \left\{ \frac{F_{10}}{N_{10} k^2} + \sum_{m=1}^{\infty} \sum_{n=0}^{\infty} \frac{J_n(k_{mn} a) F_{mn} \cos n\phi}{\left(k^2 - k_{mn}^2 \right) N_{mn}} \right\} \quad (51b)$$

where

$$F_{mn} \equiv (d-c) J_n \left[k_{mn} \left(\frac{d+c}{2} \right) \right], \quad F_{10} = (d-c) \quad (52a)$$

$$N_{mn} \equiv \frac{1}{2} \pi \left(a^2 - \frac{n^2}{k_{mn}^2} \right) J_n^2(k_{mn} a), \quad N_{10} = \frac{1}{2} \pi a^2 \quad (52b)$$

and

$$k_{mn} = \chi_{mn}/a \quad (53)$$

where the χ_{mn} have been defined in Equation (44).

The \vec{K} -current distribution for several resonant frequencies is sketched in Fig. 20.

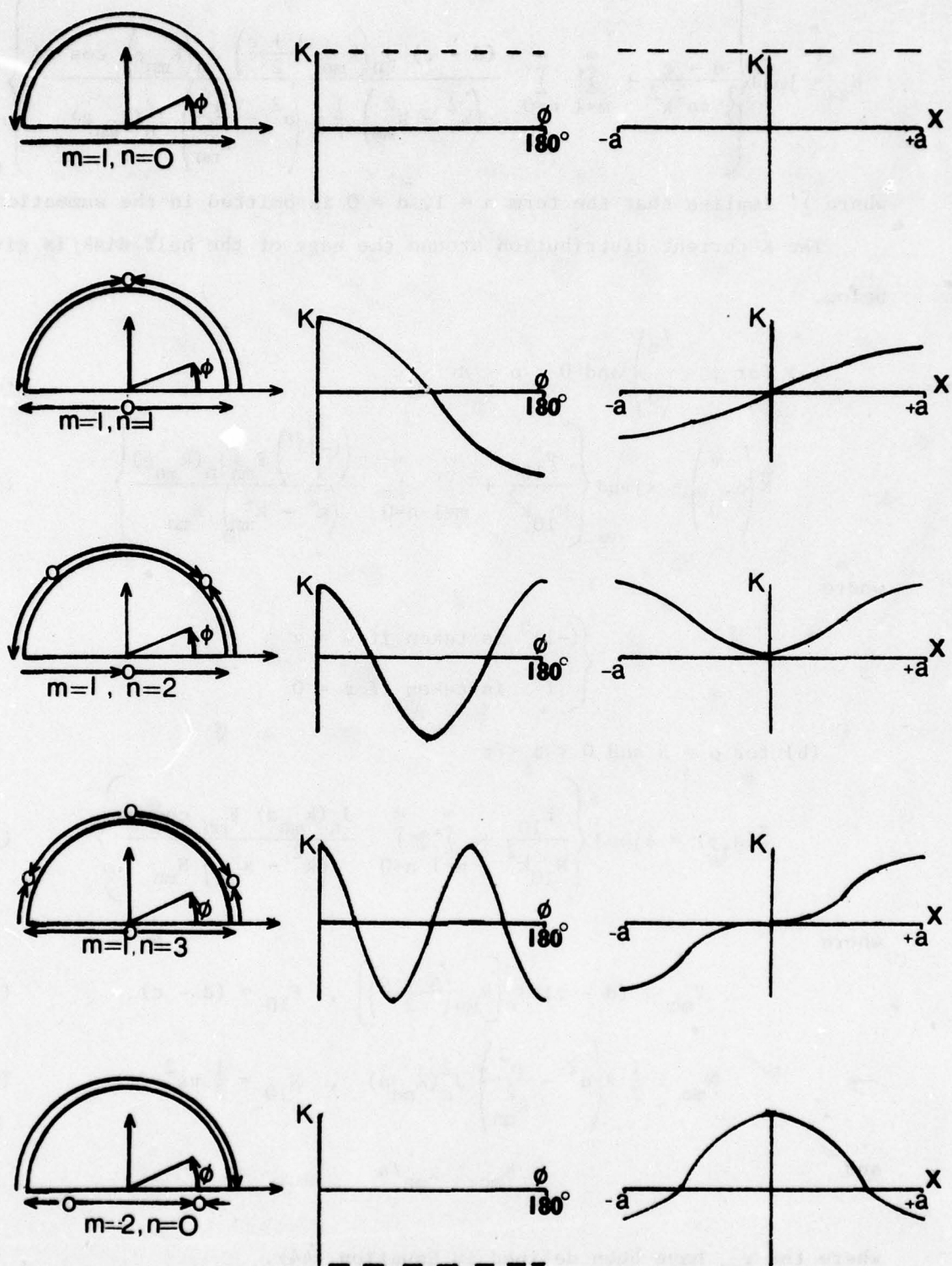
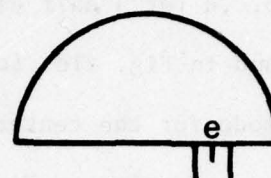
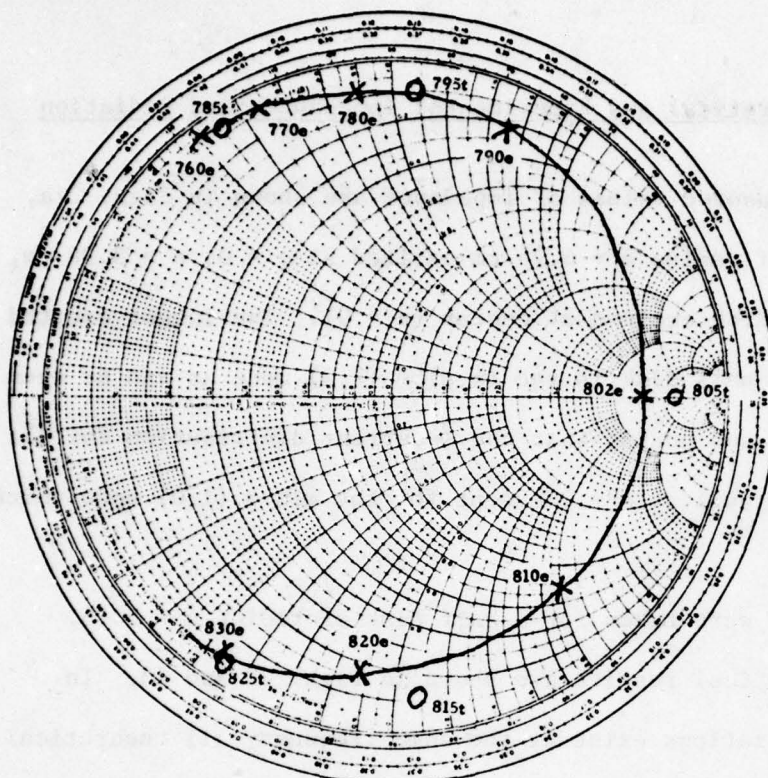


Figure 20. \vec{K} -current distribution for different resonant modes of $1/2$ -disk microstrip.

4.2 Comparison of Theoretical and Experimental Impedances and Radiation Patterns

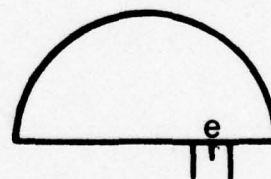
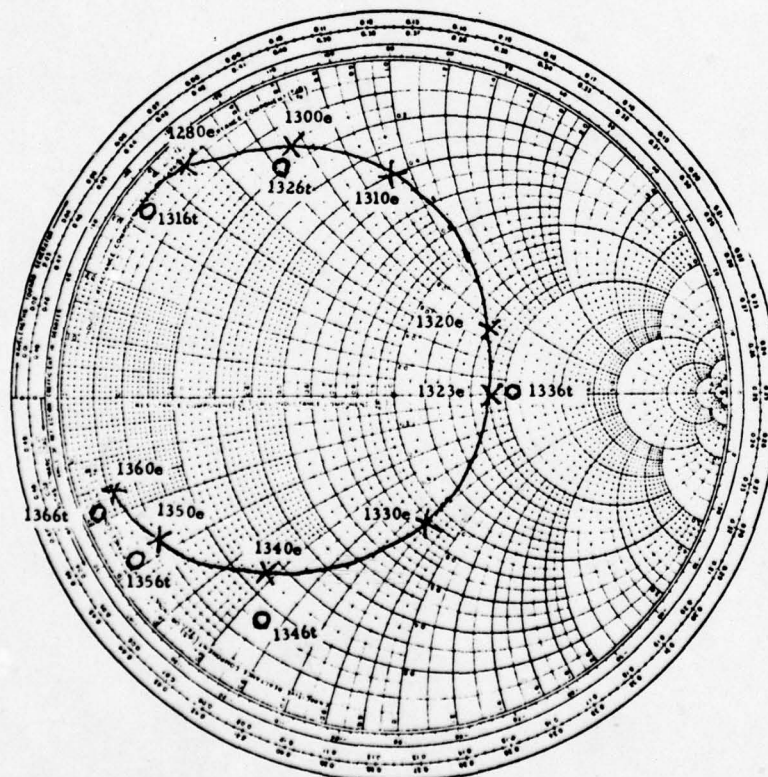
Theoretical and measured values of impedance are shown in Figs. 21a, b, c, d for a half disk of radius $a = 6.75$ cm excited at $\phi = 0$, $e = 3.38$ cm, and in Fig. 21e for a disk excited at center ($e = 0$). The lowest excited mode for the center-fed half disk is the $(m,n) = (2,0)$ mode as can be seen by referring to Fig. 20 and noting that the \vec{K} -current distribution for all lower-order modes has a null at $\rho = 0$ except for the $m,n = (1,0)$ mode which is resonant at dc.

Radiation patterns were taken for a half disk of radius $a = 6.75$. The measured and theoretical results are shown in Figs. 22 and 23. In cases where both polarizations exist at the same frequency all theoretical points are normalized with respect to the $\theta = 90^\circ$ point of the dominant polarization.



off center fed 1/2-disk
 $a=6.75\text{cm}$. $e=3.38\text{cm}$.
 $m=1, n=1$

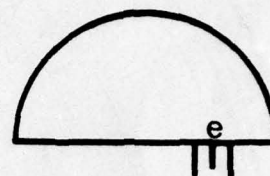
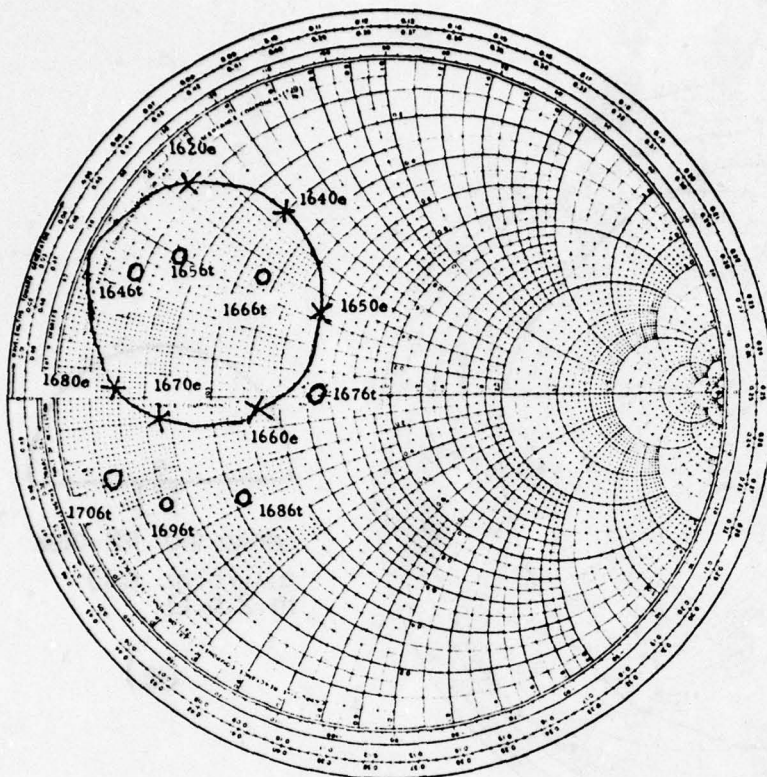
(a)



off center fed 1/2-disk
 $a=6.75\text{cm}$. $e=3.38\text{cm}$.
 $m=1, n=2$

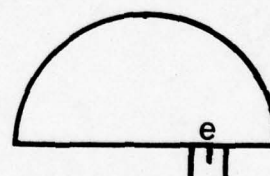
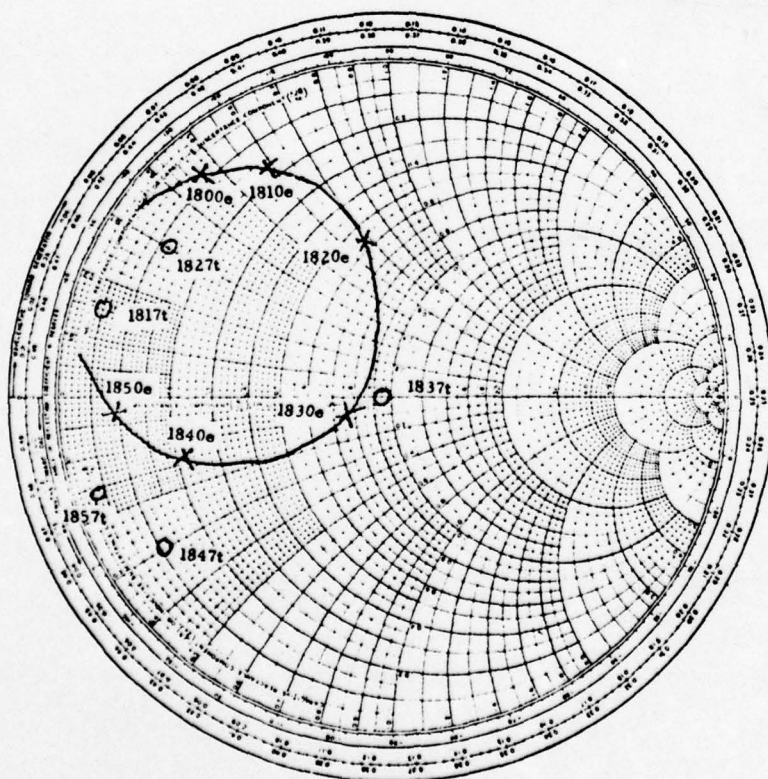
(b)

Figure 21. Theoretical and experimental impedance characteristics of disk microstrip antenna. X-X-X-X experimental points o-theoretical points, e-experimental frequency (MHz), t-theoretical frequency (MHz), (m,n)-dominate mode at resonance.



off center fed 1/2-disk
 $a=6.75\text{cm}$. $e=3.38\text{cm}$.
 $m=2, n=0$

(c)

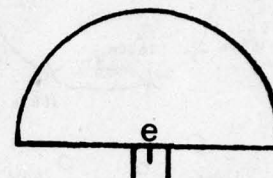
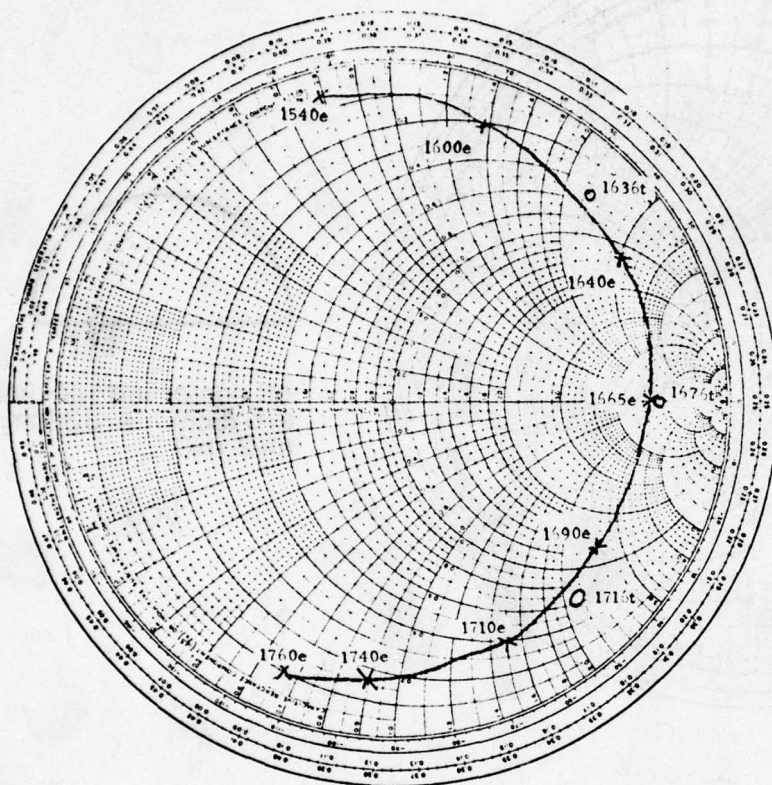


off center fed 1/2-disk
 $a=6.75\text{cm}$. $e=3.38\text{cm}$.
 $m=1, n=3$

(d)

Figure 21. (cont.)

BEST AVAILABLE COPY



center fed 1/2-disk
 $a=6.75\text{cm}$. $e=0$
 $m=2, n=0$

(e)

Figure 21. (cont.)

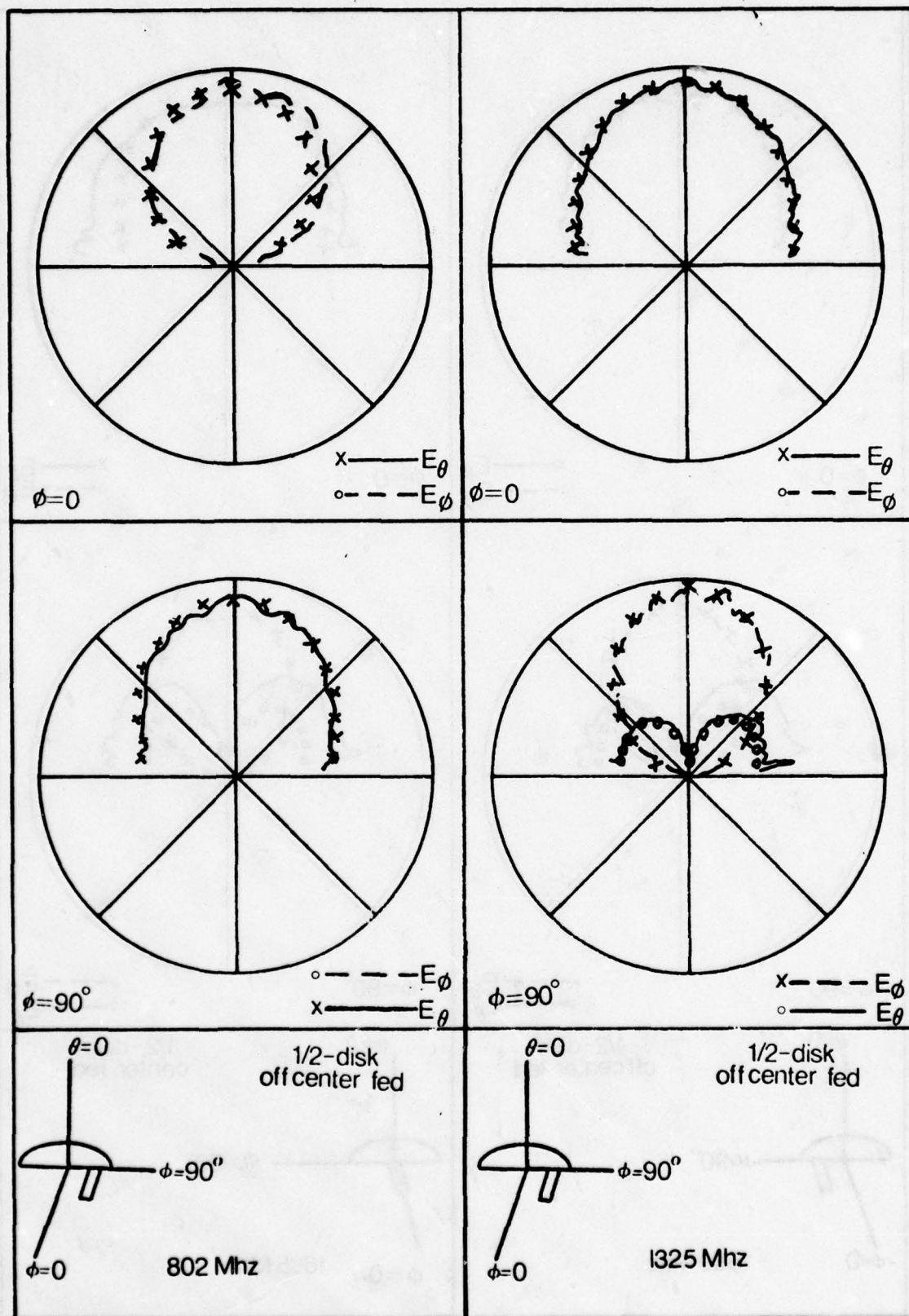


Figure 22. Radiation pattern of disk microstrip antenna. Solid or dashed curve-measured pattern, o, x-theoretical pattern.

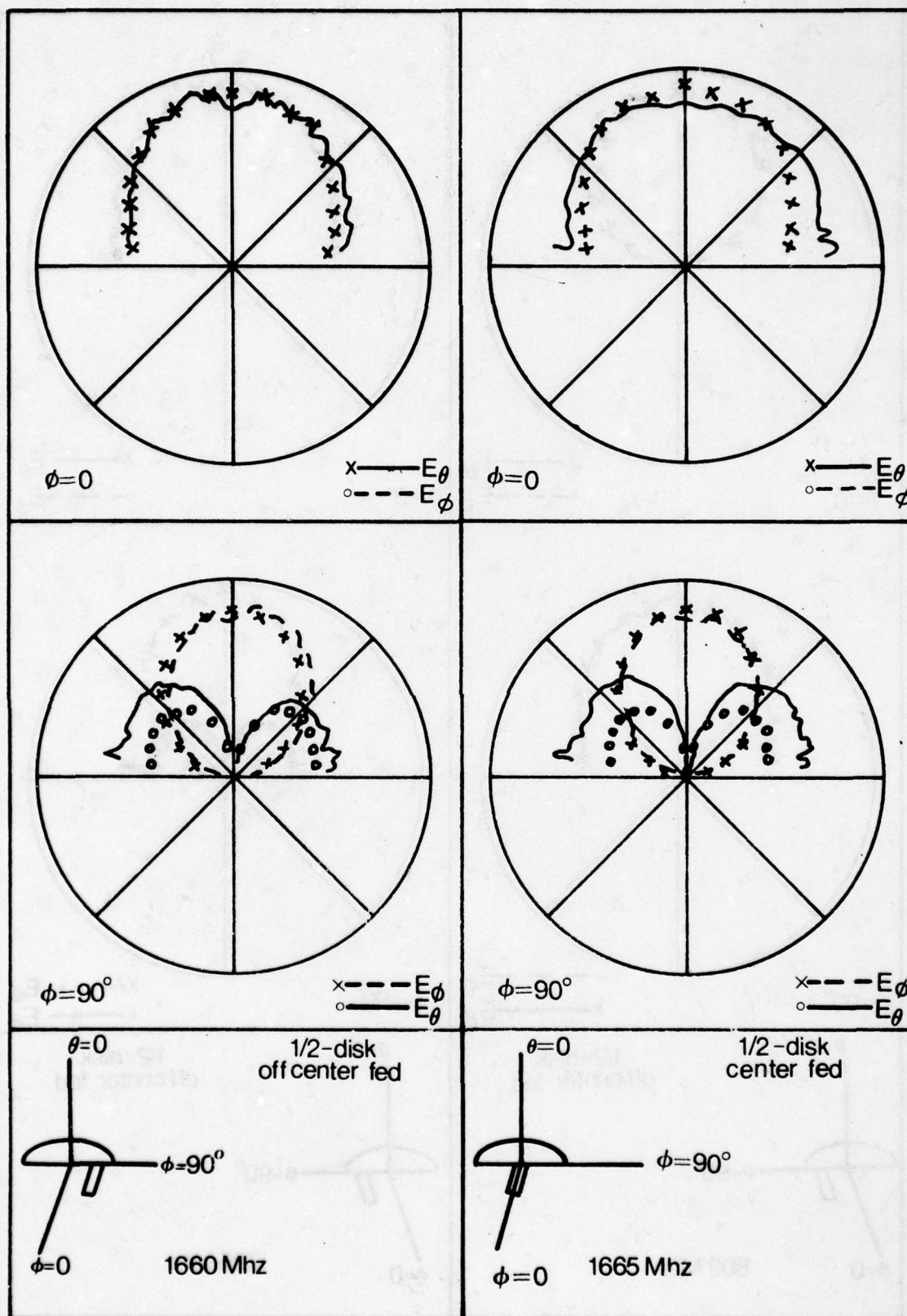


Figure 23. Radiation pattern of disk microstrip antenna. Solid or dashed curve-measured pattern, o, x-theoretical pattern.

CHAPTER 5. EQUILATERAL TRIANGULAR MICROSTRIP ANTENNA

5.1 Resonant Modes and Field Representation

The geometry of the equilateral triangular microstrip antenna is shown in Fig. 24. Applying the cavity model by surrounding the triangle with a magnetic wall, we may solve for the electric field in Equation (39) where the eigenfunctions and eigenvalues are found from Equation (40a) with the appropriate boundary conditions.

The eigenfunctions consist of functions of the form [14]

$$\begin{aligned} \psi_{mn}^{(1)}(x,y) = & \cos \frac{2\pi\ell}{3b} \left(\frac{u}{2} + b \right) \cos \frac{\pi(m-n)(v-w)}{9b} \\ & + \cos \frac{2\pi m}{3b} \left(\frac{u}{2} + b \right) \cos \frac{\pi(n-\ell)(v-w)}{9b} \\ & + \cos \frac{2\pi n}{3b} \left(\frac{u}{2} + b \right) \cos \frac{\pi(\ell-m)(v-w)}{9b} \end{aligned} \quad (54a)$$

where

$$\ell = -(m+n) \quad (54b)$$

$$u = \frac{\sqrt{3}}{2} x + \frac{y}{2} \quad (54c)$$

$$v-w = -\frac{\sqrt{3}}{2} x + \frac{3}{2} y \quad (54d)$$

$$b = \frac{a}{2\sqrt{3}} \quad (54e)$$

The eigenvalue k_{mn}^2 associated with $\psi_{mn}^{(1)}(xy)$ is

$$k_{mn}^2 = \left(\frac{4\pi}{3a} \right)^2 (m^2 + n^2 + mn) \quad (55)$$

It can be shown that solutions with m and/or n less than zero can be reduced to solutions with $m, n \geq 0$. Also $\psi_{mn}^{(j)} = \psi_{nm}^{(j)}$ so only solutions with $m \geq n$ need be used. The conditions on the indices m, n are then

$$m \geq n \geq 0 \quad (56)$$

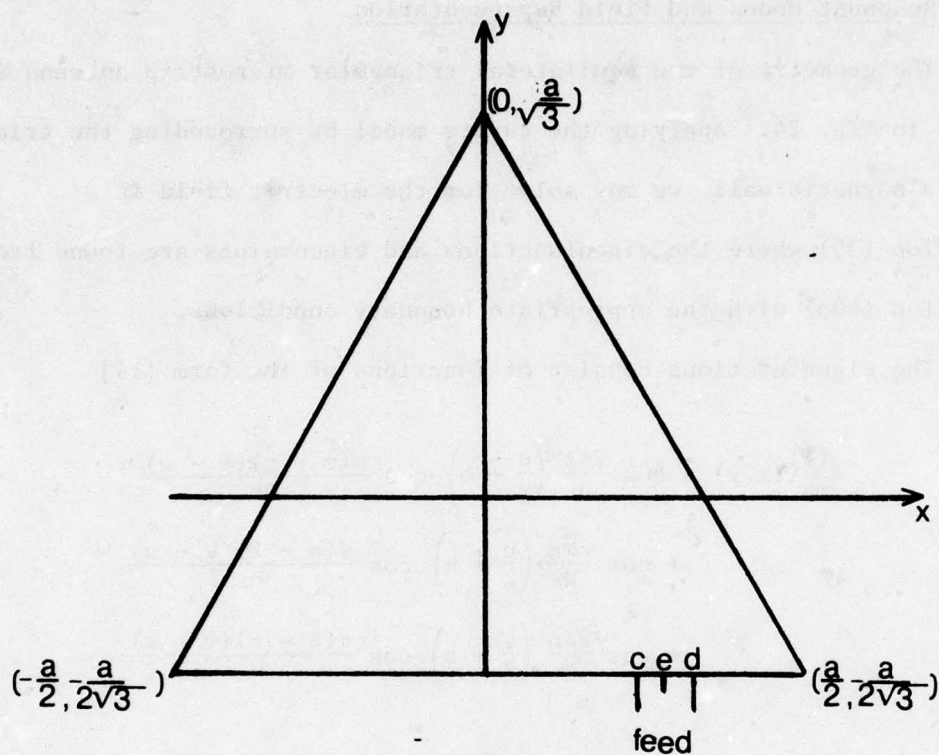


Figure 24. Geometry of equilateral triangular microstrip antenna of side "a".

The set of solutions given by Equation (54a) is not complete. To see why this is so, let the coordinate system be rotated 120° and let these new coordinates be designated $x'y'$.

The solution to the equilateral triangle problem in the $x'y'$ coordinate system is the same as Equation (54) where x,y has been replaced by x',y' . To transform the solution back to the xy coordinate system apply

$$x' = x \cos 120^\circ + y \sin 120^\circ \quad (57a)$$

$$y' = -x \sin 120^\circ + y \cos 120^\circ. \quad (57b)$$

Substituting Equations (57a) and (57b) into (54), we get a solution $\psi_{mn}^{(2)}(x,y)$, which, in general, is linearly independent of $\psi_{mn}^{(1)}(x,y)$ but has the same eigenvalue.

A third function, $\psi_{mn}^{(3)}$, which is linearly independent of $\psi_{mn}^{(1)}$ but has the same eigenvalue, can be found by rotating the xy -coordinates 240° . However, of these three functions, $\psi_{mn}^{(1)}$, $\psi_{mn}^{(2)}$, $\psi_{mn}^{(3)}$, it can be shown that no more than two are linearly independent.

Thus any two of this set of three functions may be taken and orthogonalized by the Schmidt orthogonalization procedure. The orthogonalization of $\psi_{mn}^{(1)}$ and $\psi_{mn}^{(2)}$ yields

$$\psi_{mn}^{(1)'} = \psi_{mn}^{(1)} \quad (58a)$$

$$\psi_{mn}^{(2)'} = \psi_{mn}^{(2)} - \psi_{mn}^{(1)} \iint_{\Delta} \psi_{mn}^{(2)} \psi_{mn}^{(1)'} da \quad (58b)$$

where the integration is over the area of the triangle.

The field E_z can be determined by using the eigenfunctions of Equations (58a) and (58b) with eigenvalues given by Equation (55) in Equation (39) where the current source \vec{J} is

$$\vec{J} = \hat{z} J_z(x) \delta\left(y + \frac{a}{2\sqrt{3}}\right) \quad (59a)$$

$$J_z(x) = \begin{cases} J, & c < x < d \\ 0, & \text{elsewhere} \end{cases} \quad (59b)$$

5.2 Comparison of Theoretical and Experimental Impedances

The \vec{K} -current in the magnetic wall is obtained from the electric field in the cavity. The radiated power is calculated using Equations (18) - (20) and the power lost in the dielectric is calculated using Equation (21). The impedance is calculated by applying Equations (9) and (10). Comparison of theoretical and experimental results for an equilateral triangle of side $a = 15.36$ cm is shown in Fig. 25. Figures 25 a, b, c are for a center-fed triangle ($e = 0$) and 20 d, e, f are for an off-center feed with $e = 3.84$. In general the agreement between theory and experiment is not as close as in previous examples.

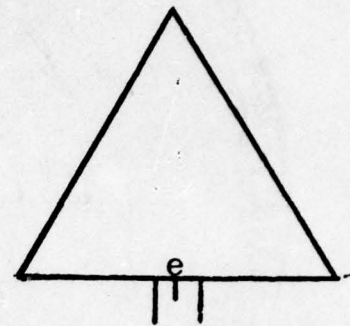
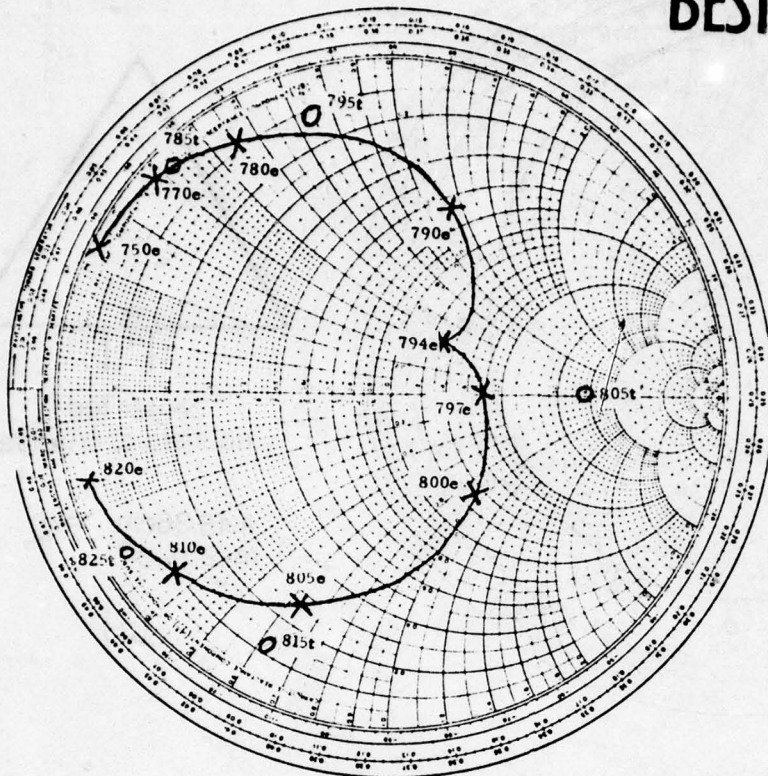
5.3 Degenerate Modes

The unusual behavior of the measured impedance in Fig. 25a, namely a cusp at 797 MHz, is believed to be caused by the imperfect construction of the triangle so that a degenerate resonant frequency splits into two close ones. To verify this conjecture a square and a slightly perturbed square are examined, with the results shown in Fig. 26. When both sides are exactly equal (to four digits), $a = b = 11.30$ cm, no cusp is observed, but when $a = 11.30$ cm and $b = 11.20$ cm a cusp is developed at 815 MHz.

Suppose in the solution to the cavity there exist two eigenfunctions $\psi_j, \psi_{j'}$, with corresponding eigenvalues $k_j, k_{j'}$, such that $k_j \approx k_{j'}$. If the antenna is excited at a frequency such that

$$k \approx k_j, k_{j'}, \quad (60)$$

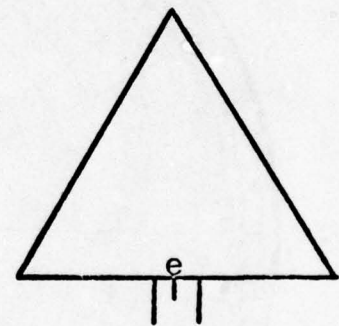
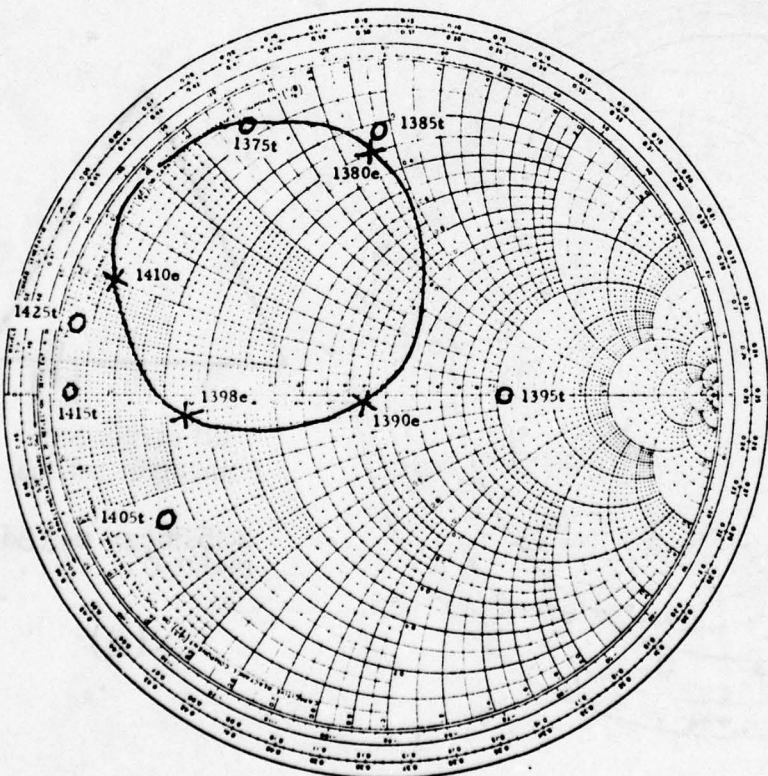
BEST AVAILABLE COPY



center fed
equilateral triangle

$a=15.36\text{cm. } e=0$
 $m=1, n=0$

(a)

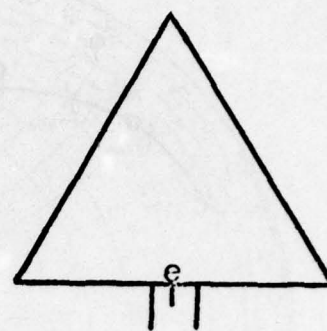
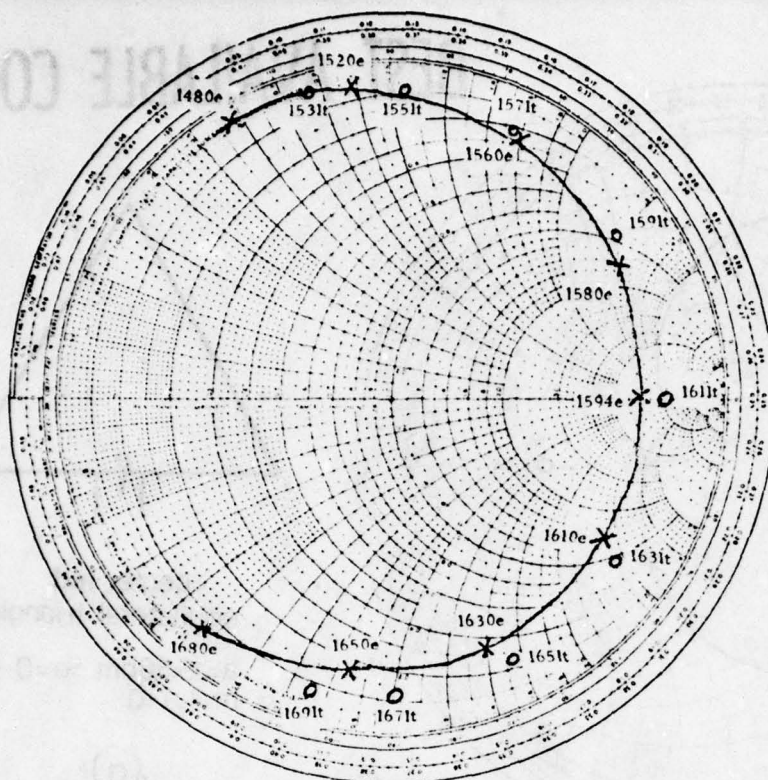


center fed
equilateral triangle

$a=15.36\text{cm. } e=0$
 $m=1, n=1$

(b)

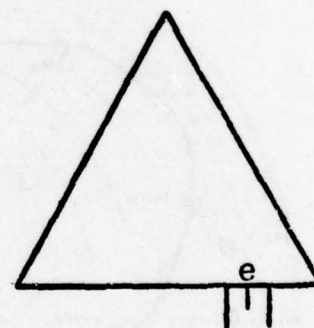
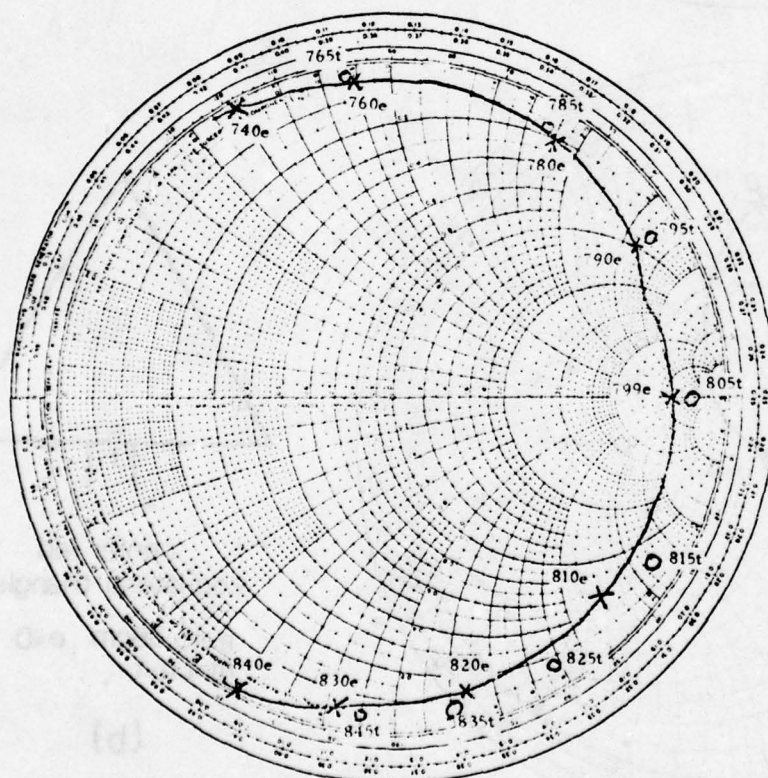
Figure 25. Theoretical and experimental impedance characteristics of equilateral triangular microstrip antenna. X-X-X-X experimental points o-theoretical points, e-experimental frequency (MHz), (m,n)-dominate mode at resonance.



center fed
equilateral triangle

$a=15.36\text{cm}$ $e=0$
 $m=2, n=0$

(c)

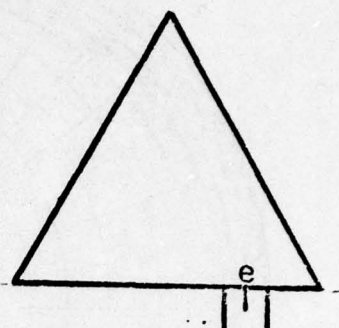
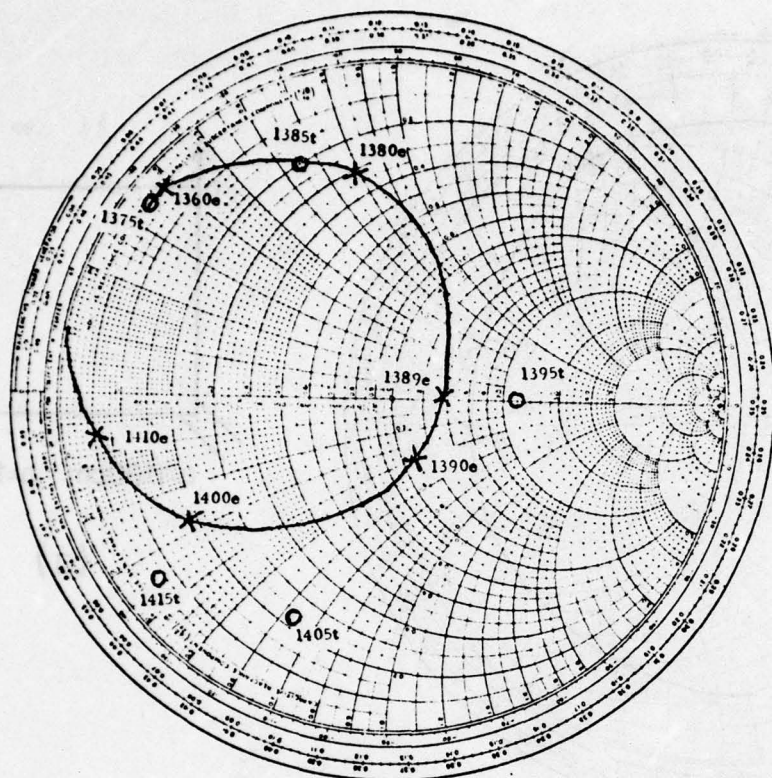


off center fed
equilateral triangle

$a=15.36\text{cm}$ $e=3.84\text{cm}$
 $m=1, n=0$

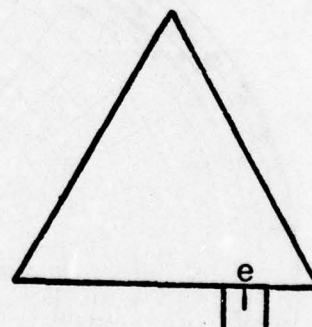
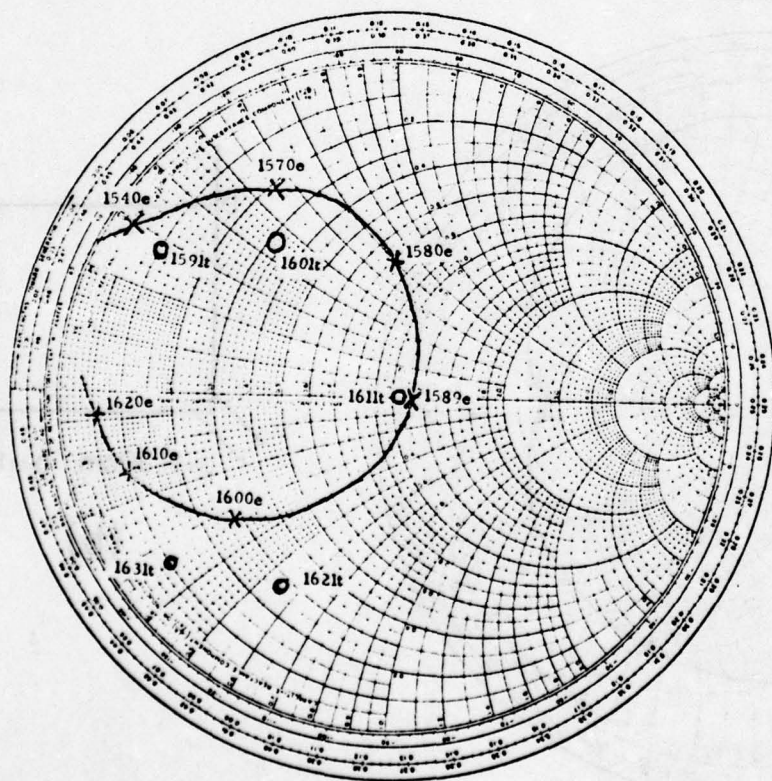
(d)

Figure 25. (cont.)



off center fed
equilateral triangle
 $a=15.36\text{cm.}$ $e=3.84\text{cm.}$
 $m=1, n=1$

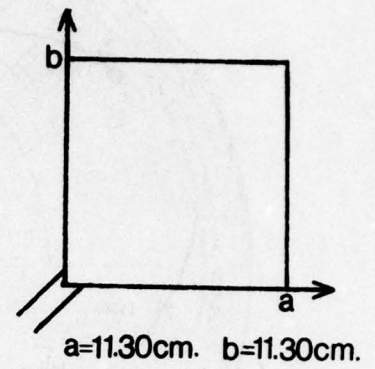
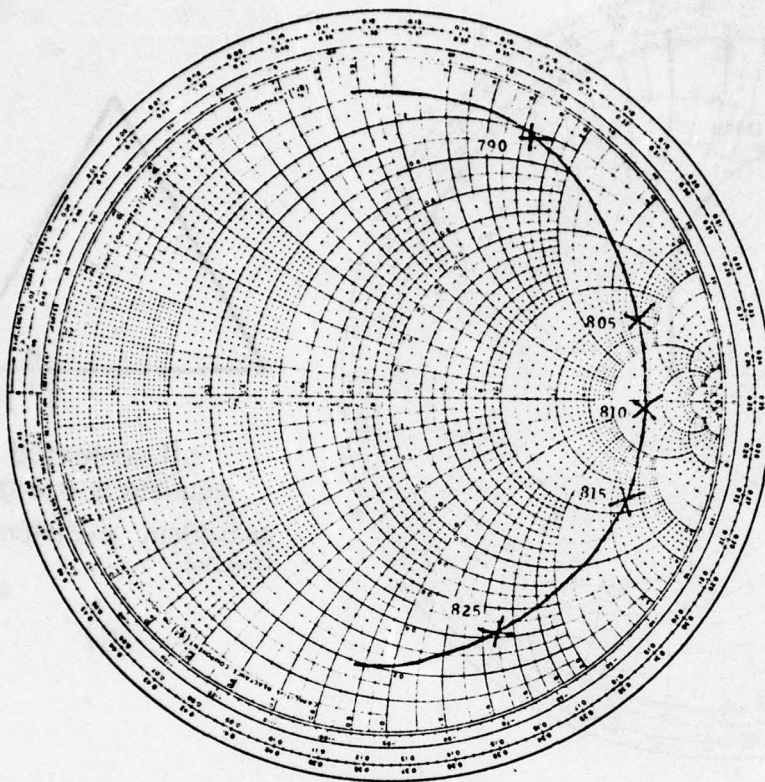
(e)



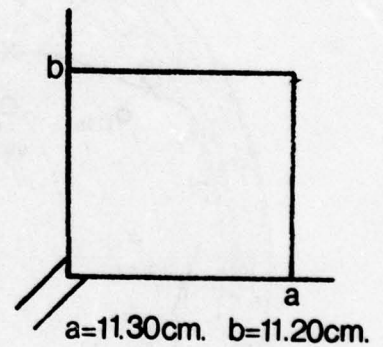
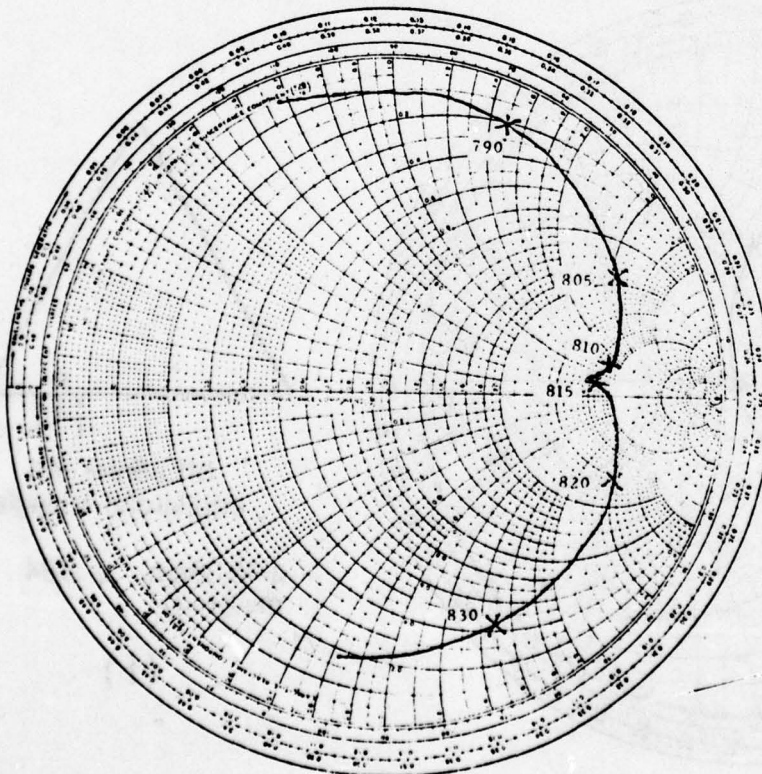
off center fed
equilateral triangle
 $a=15.36\text{cm.}$ $e=3.84$
 $m=2, n=0$

(f)

Figure 25. (cont.)



(a)



(b)

Figure 26. Corner-fed rectangle.

then the expansion, Equation (39), becomes

$$E_z \approx \frac{\psi_j \iint \psi_j^*(j\omega\mu J) da}{(k^2 - k_j^2) \iint \psi_j^* \psi_j da} + \frac{\psi_{j'} \iint \psi_{j'}^*(j\omega\mu J) da}{(k^2 - k_{j'}^2) \iint \psi_{j'}^* \psi_{j'} da} \quad (61)$$

Define

$$A_n = \frac{\psi_n \iint \psi_n^*(j\omega\mu J) da}{\iint \psi_n^* \psi_n da} \quad (62)$$

then Equation (61) becomes

$$E_z \approx \frac{A_j}{k^2 - k_j^2} + \frac{A_{j'}}{k^2 - k_{j'}^2} \quad (63)$$

for k near k_j and $k_{j'}$.

For a given feed point the resonant admittance G is dependent on the field structure but not on the magnitude of the field. If k_j and $k_{j'}$ are widely separated in value, then as k is varied around k_j the first term of Equation (63) is dominant and we have

$$E_z \approx \frac{-A_j}{|k^2 - k_j^2|}, \quad k < k_j \quad (64a)$$

$$E_z \approx \frac{A_j}{|k^2 - k_j^2|}, \quad k > k_j \quad (64b)$$

Thus as k varied around k_j the magnitude of E_z changes as $\frac{1}{k^2 - k_j^2}$ but not the field structure which is proportional to A_j . The same reasoning applies if $k_j = k_{j'}$, i.e., if ψ_j and $\psi_{j'}$ are degenerate.

Now if $k_j \approx k_{j'}$ and $k_j < k_{j'}$, then as k is varied around $k_j, k_{j'}$, we have, from Equation (63),

$$E_z \approx - \left(\frac{A_j}{|k^2 - k_j^2|} + \frac{A_{j'}}{|k^2 - k_{j'}^2|} \right), \quad k < k_j \quad (65a)$$

$$E_z \approx \frac{A_j}{|k^2 - k_j^2|} - \frac{A_{j'}}{|k^2 - k_{j'}^2|}, \quad k_j < k < k_{j'} \quad (65b)$$

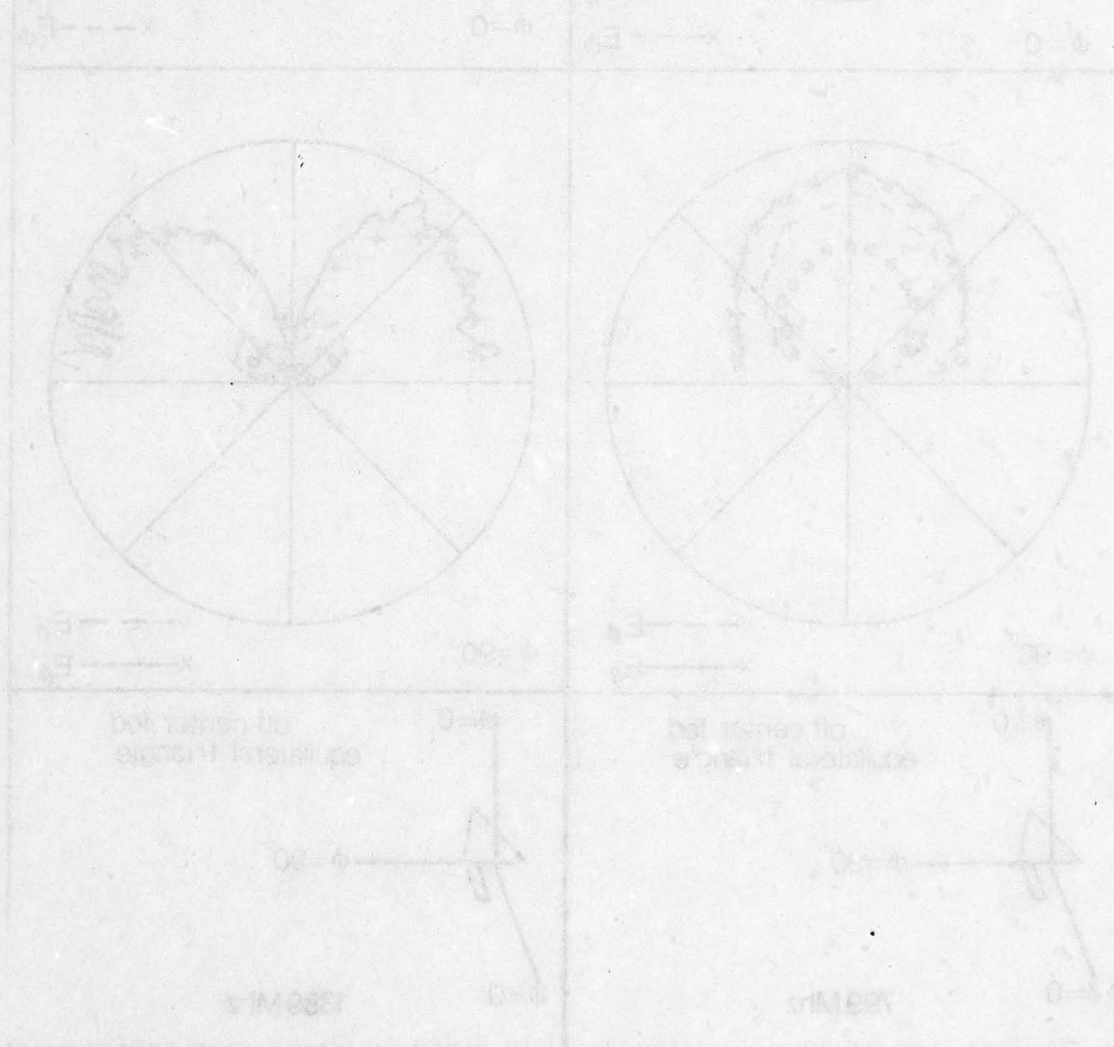
$$E_z \approx \frac{A_j}{|k^2 - k_j^2|} + \frac{A_{j'}}{|k^2 - k_{j'}^2|}, \quad k > k_{j'} \quad (65c)$$

The field structure changes radically as k is varied, as can be seen by comparing Equation (65a or c) with (65b); therefore G changes radically. For the square of Fig. 26a the $(m,n) = (1,0)$ and $(0,1)$ are excited and are degenerate; therefore the field structure is essentially unchanged as k is varied around $k_{10} = k_{01}$ and G is essentially constant. For the rectangle of Fig. 26b the $m,n = (1,0)$ mode is excited when $k = \pi/b$ and the $(0,1)$ mode is excited when $k = \pi/a$. Since $a \approx b$, $k_{10} \approx k_{01}$. Therefore the situation as depicted by Equations (65a,b,c) holds for $k \approx k_{10}, k_{01}$ and the field structure changes rapidly as k is varied with a corresponding rapid change in G . This results in a cusp on the Smith chart.

For the case of the equilateral triangle the two modes associated with $m,n = (1,0)$ should have degenerate eigenvalues. However, in the actual model under test there may exist small asymmetries that cause the degenerate eigenfunction to split into two having slightly different eigenvalues or resonant frequencies. These asymmetries may result from imprecise construction of the triangle or from the presence of the feed line. By previous argument this may account for the cusp in Fig. 25a.

5.4 Comparison of Theoretical and Experimental Radiation Patterns

Radiation patterns were also measured for the equilateral triangle of side $a = 15.36$ cm and they are shown in Figs. 27 and 28. The dashed or solid curves are the measured patterns for the indicated polarization and the small circles and x's are the corresponding theoretical patterns. The theoretical data are normalized with respect to one measured data point. It may be noted that while theory gives the correct shape of the radiation pattern, the relative magnitude between E_θ and E_ϕ polarizations is not in complete agreement with all those measured.



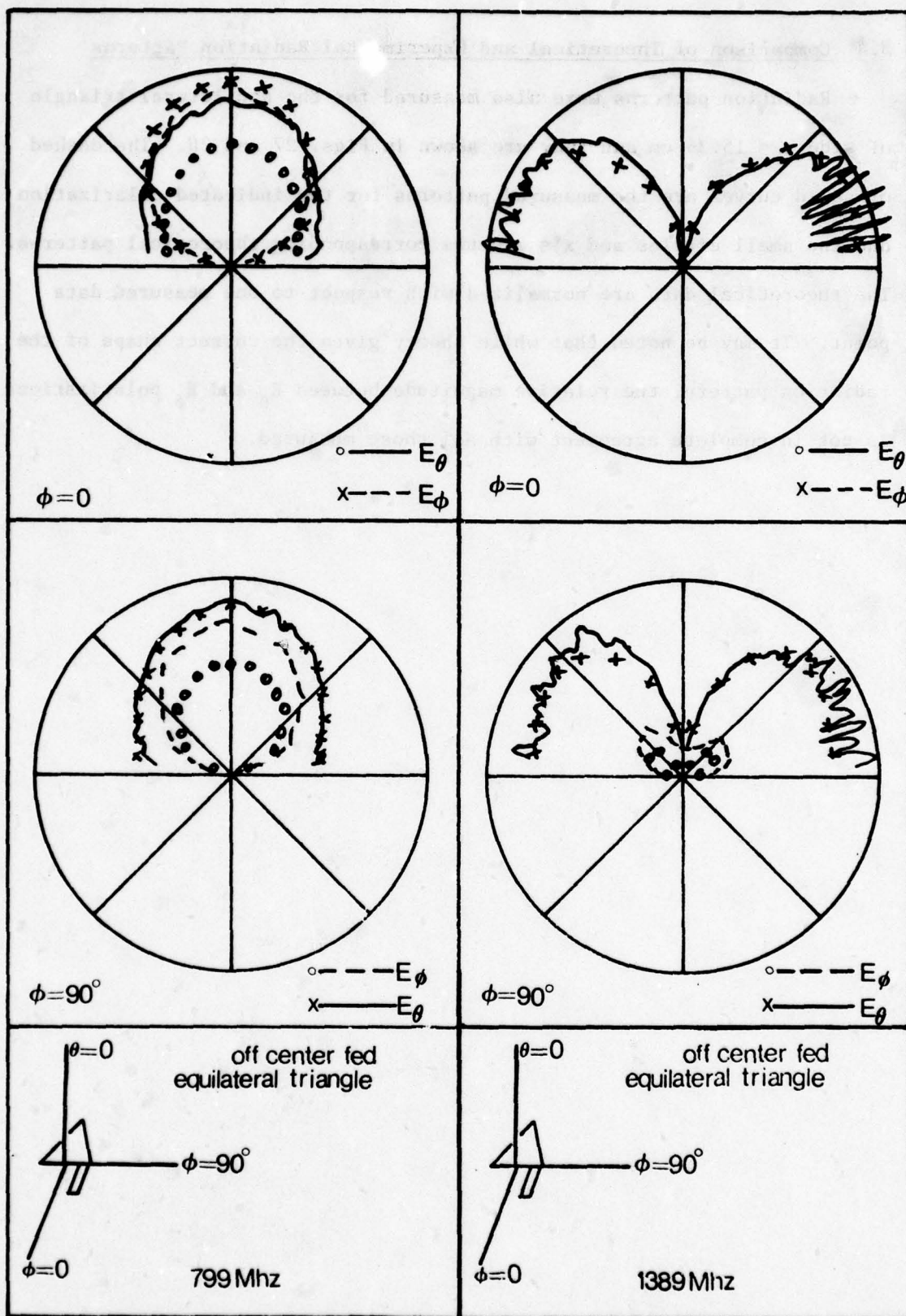


Figure 27. Radiation pattern of equilateral triangular microstrip antenna.
Solid or dashed curve-measured pattern.
o, x-theoretical pattern.

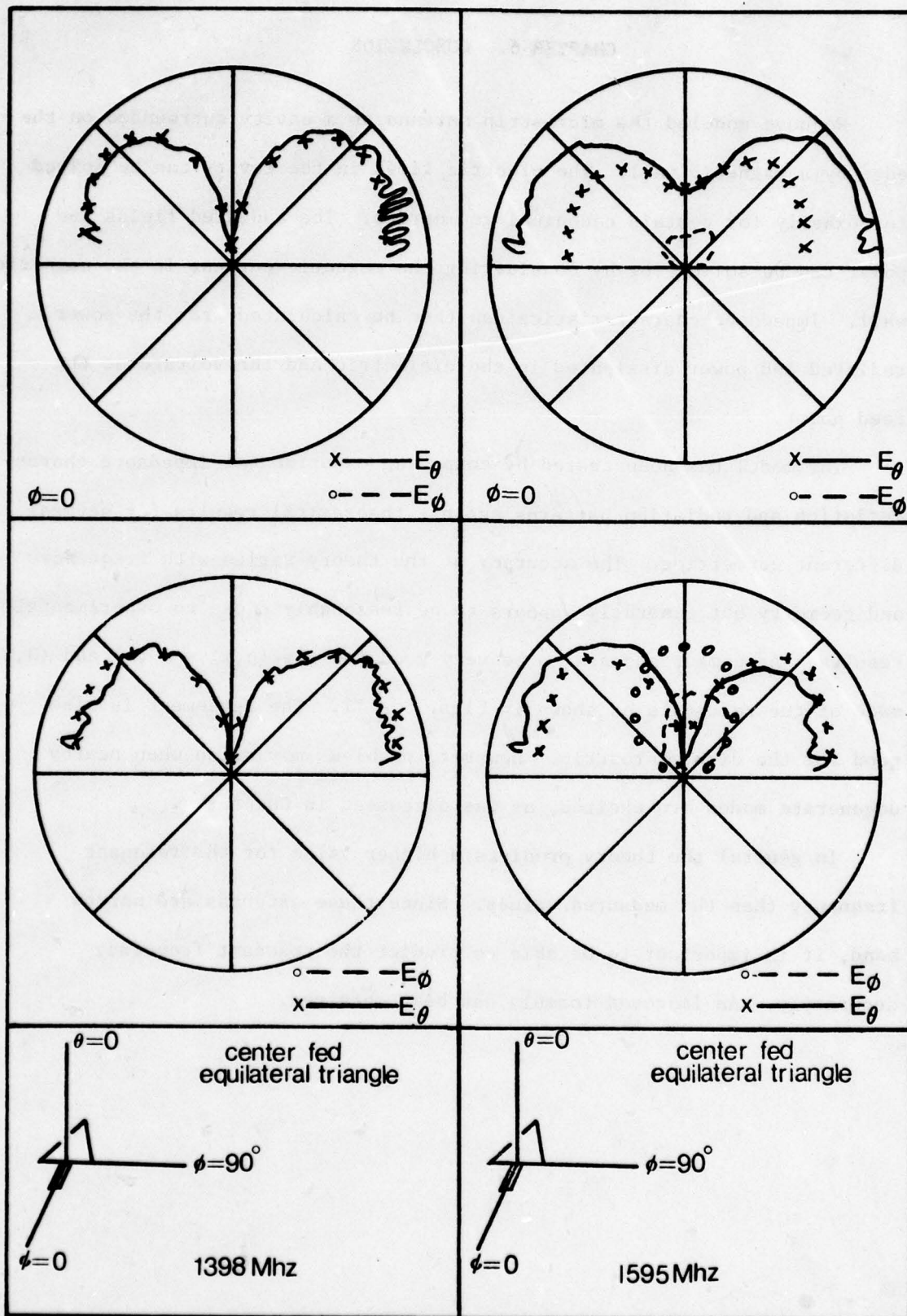


Figure 28. Radiation pattern of equilateral triangular microstrip antenna. Solid or dashed curve-measured pattern. o, x-theoretical pattern.

CHAPTER 6. CONCLUSION

We have modeled the microstrip antenna as a cavity surrounded on the edge by a magnetic wall. The electric field in the cavity can be solved for exactly for certain canonical geometries. The radiated fields and power can be solved for by considering the magnetic current in the magnetic wall. Impedance characteristics can then be calculated from the power radiated and power dissipated in the dielectric and the voltage at the feed point.

The model has been tested by comparing experimental impedance characteristics and radiation patterns against theoretical results for several different geometries. The accuracy of the theory varies with frequency and geometry but generally appears to be reasonably close to experimental results. Agreement appears to be very good for the $(n,m) = (0,1)$ and $(0,2)$ modes of the rectangle as shown in Figs. 8 - 11. The agreement is also good for the disk microstrip. However, problems may arise when nearby degenerate modes are excited, as was discussed in Chapter 4.

In general the theory predicts a higher value for the resonant frequency than the measured values. Since these antennas are narrow band, it is important to be able to predict the resonant frequency accurately. An improved formula has been obtained.

REFERENCES

1. R. E. Munson, "Conformal microstrip antennas and microstrip phased arrays," IEEE Trans. Antennas Propagat., vol. AP-22, no. 1, pp. 74-78, January 1974.
2. Georges A. Deschamps, "Microstrip microwave antennas," presented at the 3rd USAF Symposium, 1953.
3. Anders G. Derneryd, "Mutual coupling in array antennas," School of Elect. Eng., Chalmers University of Technology, Goteborg, Sweden, Tech. Report No. 60, February 1976.
4. K. R. Carver, "The radiation pattern of a microstrip disc antenna," Physical Science Laboratory, New Mexico State University, Las Cruces, New Mexico, PSL Tech. Memorandum, November 29, 1976.
5. E. L. Coffey, III, and K. R. Carver, "Towards the theory of microstrip antenna patterns," in Proceedings of the 1977 Antenna Applications Symposium, Electromagnetics Laboratory, University of Illinois, Urbana, Illinois, April 27 - 29, 1977.
6. T. Okoshi and T. Miyoshi, "The planar circuit - an approach to microwave integrated circuitry," IEEE Trans. Microwave Theory Tech., vol. MTT-20, no. 4, pp. 245-253, April 1972.
7. T. Itoh and R. Mittra, "Analysis of microstrip disk resonator," Arch. Elek. Übertagung, vol. 27, pp. 456-458, November 1973.
8. T. Itoh, "Analysis of microstrip resonators," IEEE Trans. Microwave Theory Tech., vol. MTT-22, no. 11, pp. 946-952, November 1974.
9. M. Cu, "Radiation from triangular and circular resonators in microstrip," Electrical Engineering Department, University of Ottawa, January 11, 1977.
10. D. Weinschel, "A cylindrical array of circularly polarized microstrip antennas," 1975 AP-S International Symposium (p. 177 of Digest).
11. Martin V. Schneider, "Microstrip dispersion," Proc. IEEE, vol. 60, no. 1, pp. 144-146, January 1972.
12. John C. Slater, Microwave Electronics. New York: D. Van Nostrand Company, Inc., 1950, pp. 67-70.
13. Robert E. Collin, Field Theory of Guided Waves. New York: McGraw-Hill Book Company, 1960, p. 21.
14. S. A. Schelkunoff, Electromagnetic Waves. New York: D. Van Nostrand Company, Inc., 1943, pp. 393-394.

PART B.

EXPERIMENTAL EVALUATION OF MICROSTRIP ANTENNAS OF VARIOUS CANONICAL SHAPES

Microstrip antennas have many more physical parameters than do other conventional antennas. They can assume any geometrical shape with any set of dimensions. It is therefore impossible to make an exhaustive investigation of their properties. The objective of this part of the study is to document the radiation patterns and input impedances of many typical microstrip antennas of canonical shapes for which the rigorous solutions of their corresponding cavity models can be found. Those included in this report are shown in Fig. B-1, whereas a few others, such as circular rings, elliptical disks and rings, and circular and elliptical sectors will be investigated in the next contract period. Since the accuracy of the theory for all these geometries has been tested separately with several experiments in Part A of this report, no further theoretical computation will be made in this part. In general, the qualitative behavior of the pattern can readily be predicted from the magnetic current distributions along the edges without computation.

The geometries of microstrip antennas under this investigation are summarized in Fig. B-1. The measured data for these antennas can be located by referring to Table I.

Each of these microstrip antennas was etched on one side of a 1/16-inch, double-clad, one-ounce foil, Rexolite 2200 printed circuit board. The relative dielectric constant of the Rexolite in the frequency range considered was approximately 2.65, which results in an approximate 61.4 percent reduction in velocity of propagation from that in free space. In each case, the 50 ohm microstrip feed line was physically two inches long and 0.175 inches wide (the width was determined experimentally). The feed connector was a slightly modified feed-through General RF, type N printed circuit board connector (see Fig. B-2 for details).

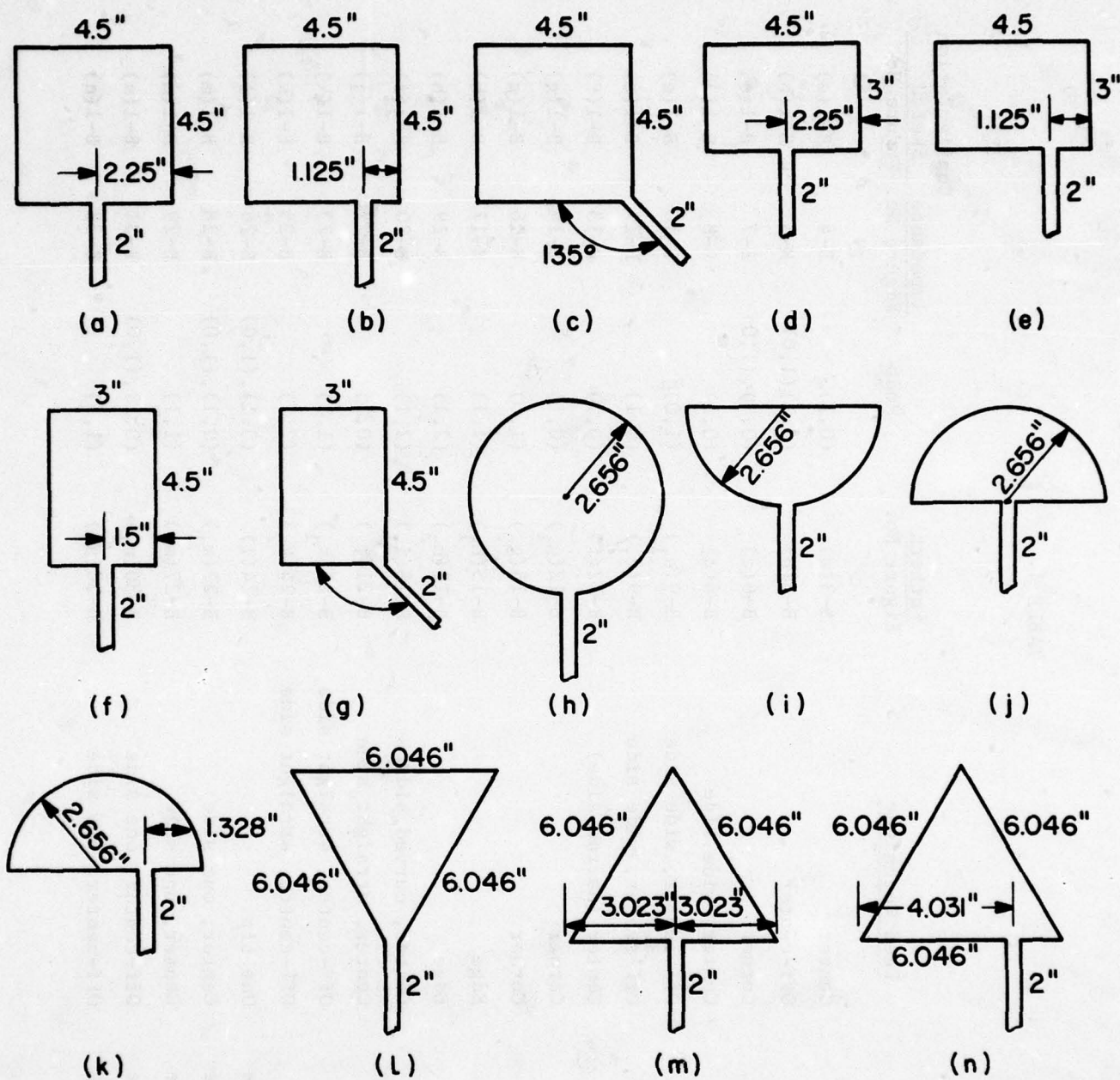


Figure B-1. The various microstrip antenna shapes and feed locations which have been constructed and measured (impedance and patterns).

TABLE I.

Antenna Shape	Feed Technique	Pattern Figure No.	Mode	Configuration	
				Impedance Figure No.	Sketch Figure No.
Square	Center	B-3(a)	(0,1)	B-4	B-1(a)
Square	Off-center	B-3(b)	(0,1),(1,0)	B-5	B-1(b)
Square	Corner	B-6(c)	(0,1),(1,0)	B-7	B-1(c)
Rectangle	Center, wide side	B-6(d)	(0,1)	B-8	B-1(d)
Rectangle	Off-center, wide side	B-9(e ₁)	(1,0)	B-10	B-1(e)
Rectangle	Off-center, wide side	B-9(e ₁)	(0,1)	B-11	B-1(e)
Rectangle	Center (narrow side)	B-12(f)	(0,1)	B-13	B-1(f)
Rectangle	Corner	B-12(g ₁)	(0,1)	B-14	B-1(g)
Rectangle	Corner	B-15(g ₂)	(1,0)	B-16	B-1(g)
Circle	Edge	B-15(h ₁)	(1,1)	B-17	B-1(h)
Circle	Edge	B-18(h ₂)	(2,1)	B-19	B-1(h)
Semicircle	Center, curved side	B-18(i ₁)	(2,1)	B-20	B-1(i)
Semicircle	Center, straight side	B-21(j)	(0,1)	B-22	B-1(j)
Semicircle	Off-center, straight side	B-21(k ₁)	(1,1)	B-23	B-1(k)
Semicircle	Off-center, straight side	B-24(k ₂)	(2,1)	B-25	B-1(k)
Equiangular Triangle	One tip	B-24(l)	(0,1),(1,0)	B-26	B-1(l)
Equiangular Triangle	Center, one side	B-27(m ₁)	(0,1),(1,0)	B-28	B-1(m)
Equiangular Triangle	Center, one side	B-27(m ₂)	(1,1)	B-29	B-1(m)
Equiangular Triangle	Off-center, one side	B-30(n ₁)	(0,1),(1,0)	B-31	B-1(n)
Equiangular Triangle	Off-center, one side	B-30(n ₂)	(1,1)	B-32	B-1(n)

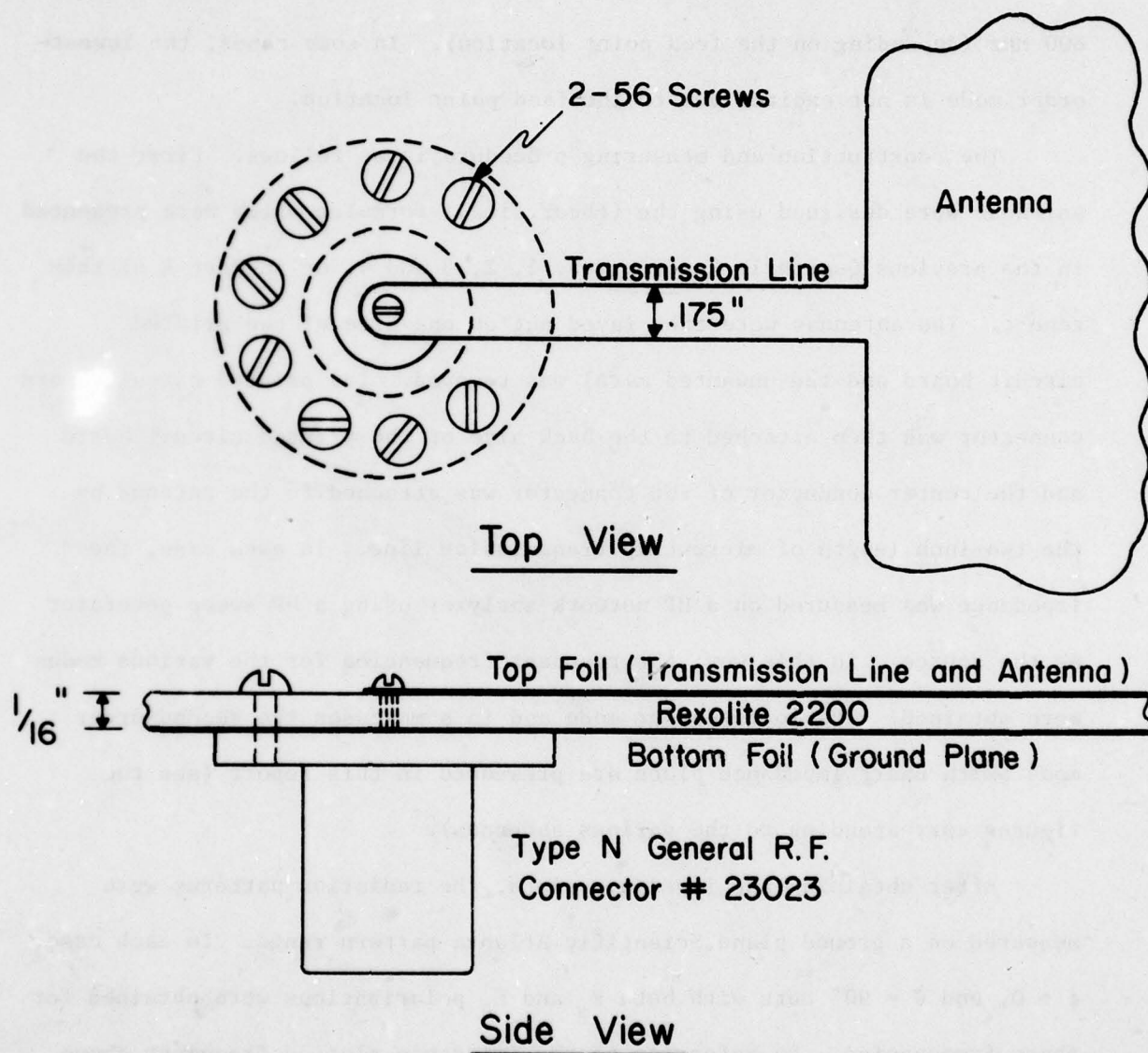


Figure B-2. Sketch showing the microstrip antenna feed connector and feed transmission line details.

The printed circuit board with microstrip antenna, feed line and connector was attached, by screws along the edge of the printed circuit board, to an adapter plate which allowed positioning the microstrip antenna at the center of a 13 by 13 foot Scientific Atlanta ground screen pattern range.

The antennas were all designed to have at least one resonance at about 800 MHz (depending on the feed point location). In some cases, the lowest-order mode is not excited due to the feed point location.

The construction and measuring procedure is as follows. First the antennas were designed using the (theoretical) formulas which were presented in the previous Quarterly Reports Nos. 1, 2, 3 and 4, or in Part A of this report. The antennas were then layed out on one side of the printed circuit board and the unwanted metal was removed. The printed circuit board connector was then attached to the back side of the printed circuit board and the center conductor of the connector was attached to the antenna by the two-inch length of microstrip transmission line. In each case, the impedance was measured on a HP network analyzer using a HP sweep generator as the source. In this way, the resonant frequencies for the various modes were obtained. The lowest-order mode and in some cases the second-order mode Smith chart impedance plots are presented in this report (see the figures corresponding to the various antennas).

After obtaining the impedance plots, the radiation patterns were measured on a ground plane Scientific Atlanta pattern range. In each case, $\phi = 0$, and $\theta = 90^\circ$ cuts with both E_ϕ and E_θ polarizations were obtained for three frequencies. By referring to the impedance plot, a frequency above and a frequency below the resonant frequency were selected where the VSWR was approximately 20 to 1. In general, it was found that the radiation patterns for the three frequencies remained very nearly the same, indicating

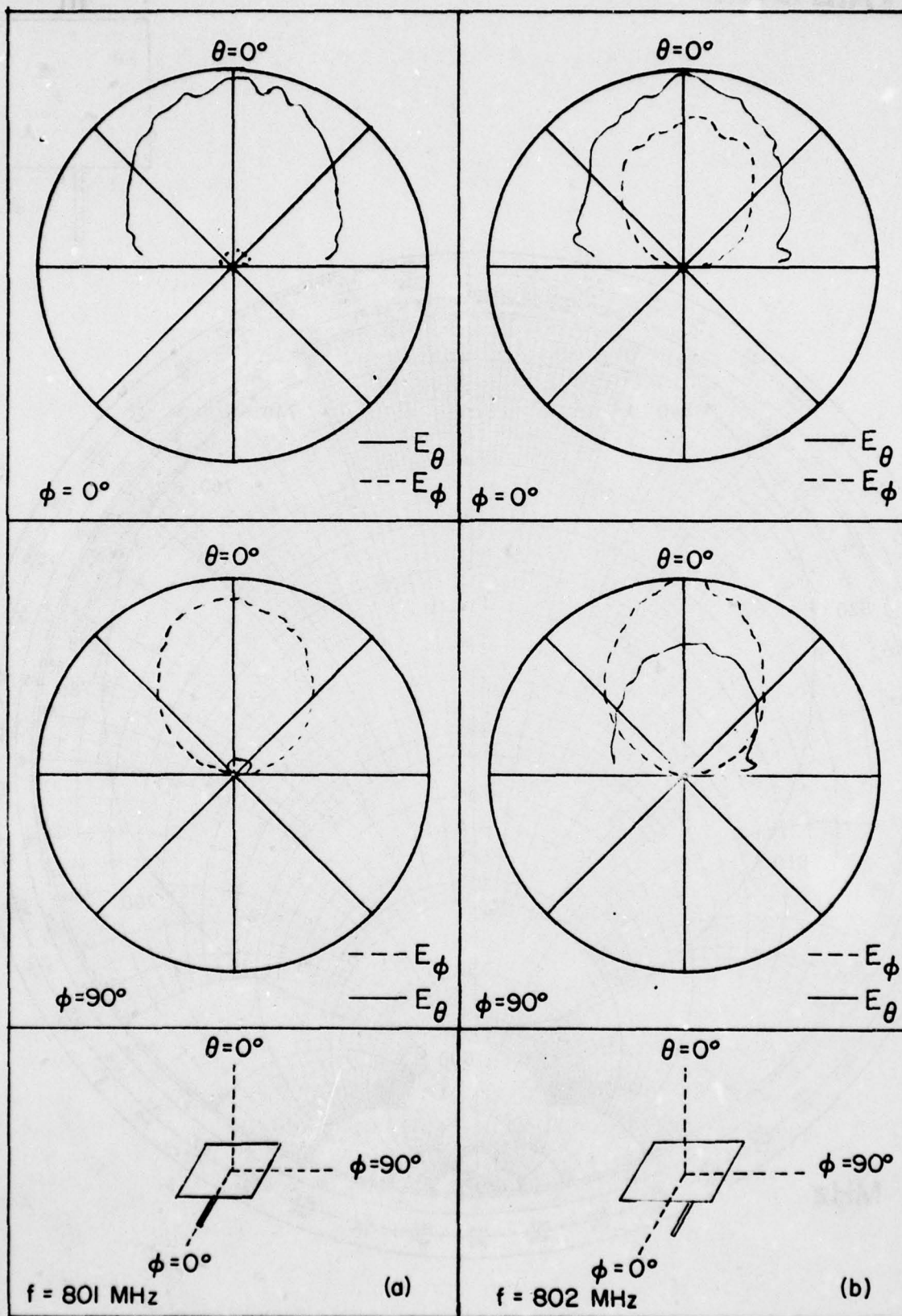


Figure B-3. Radiation patterns of square microstrip antenna .
 (a) center-fed and (b) off-center fed.

BEST AVAILABLE COPY

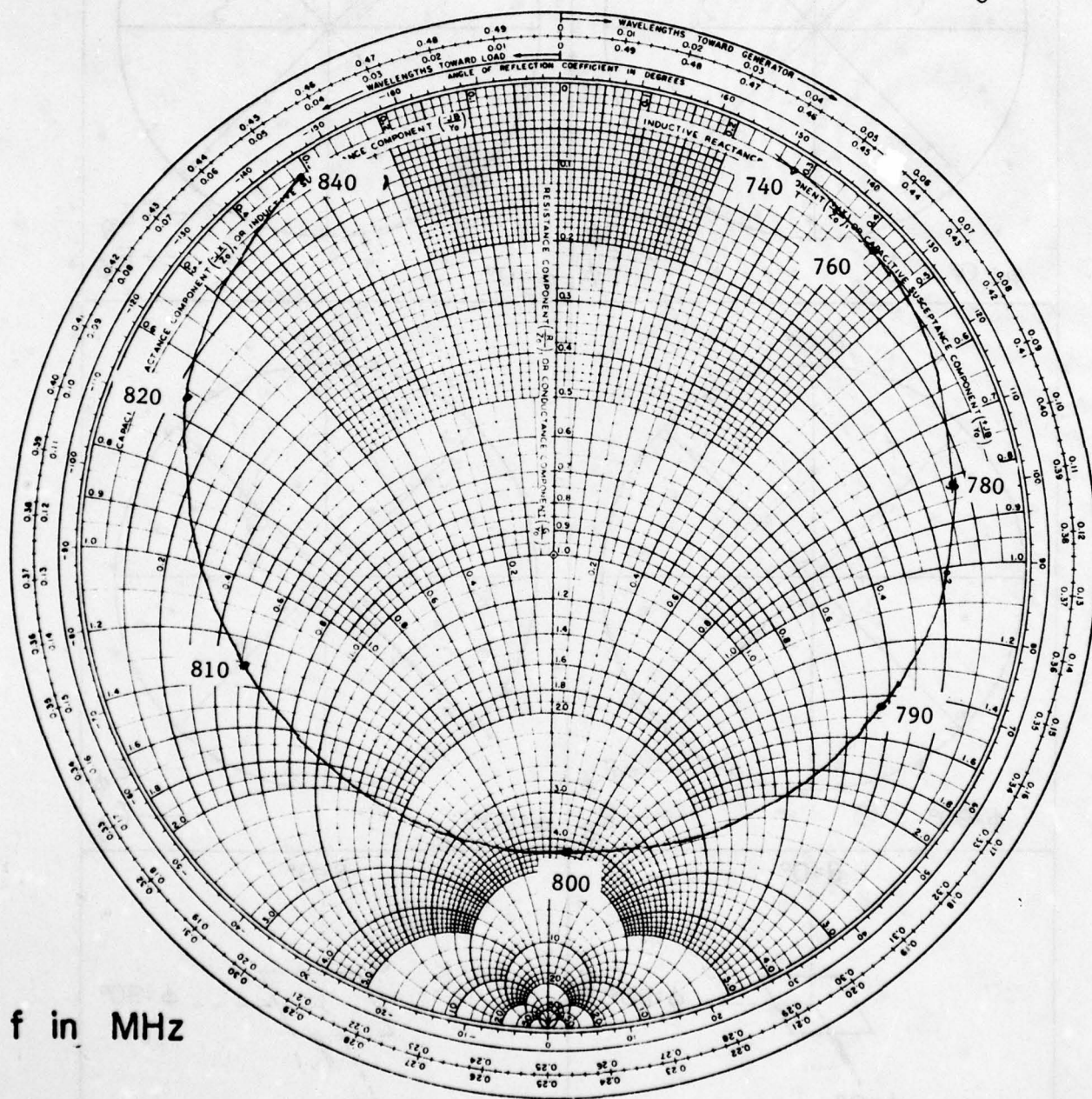
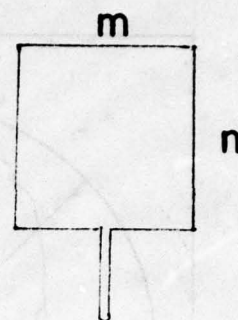


Figure B-4. Impedance of the center-fed, square microstrip antenna near resonance of the (0,1) mode.

BEST AVAILABLE COPY

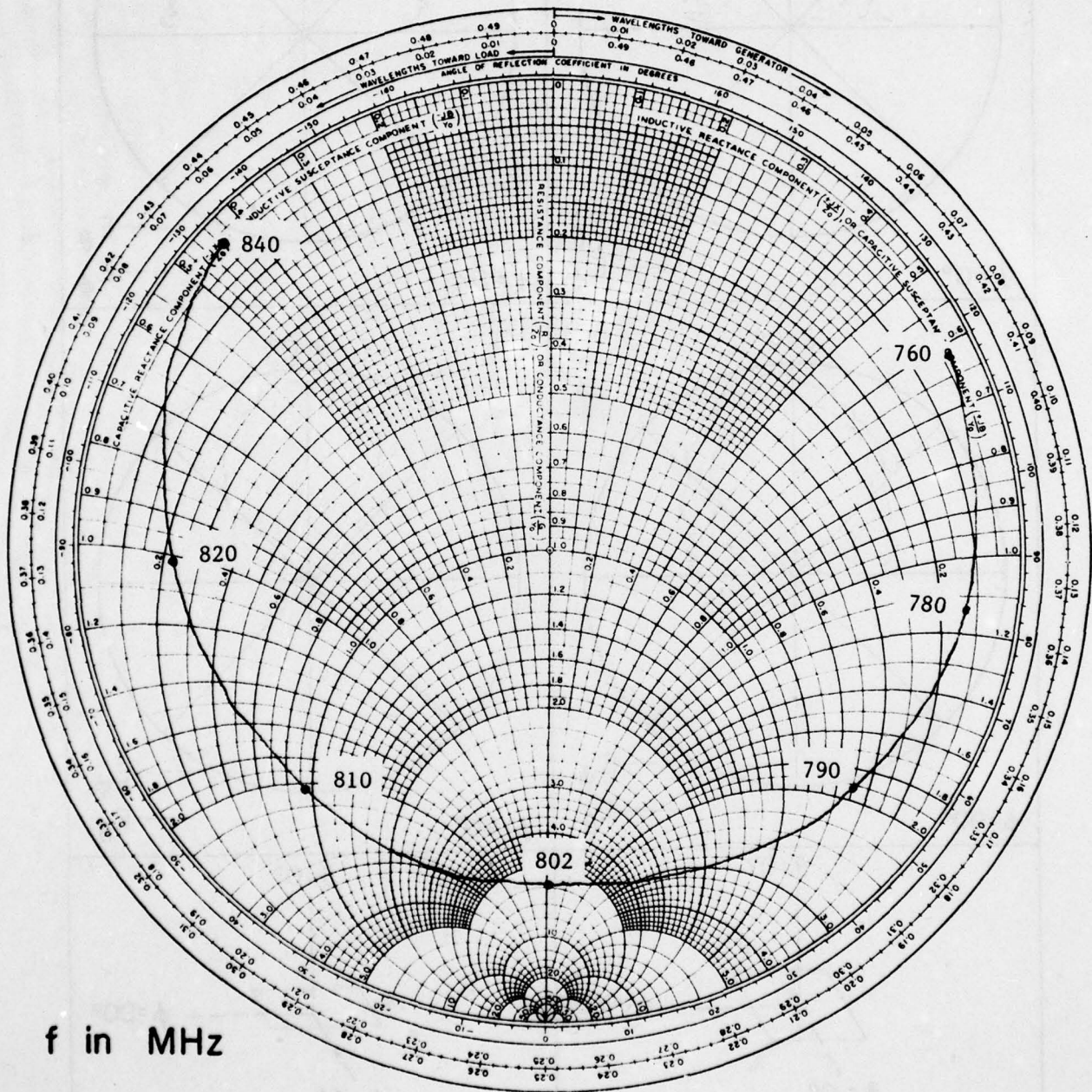
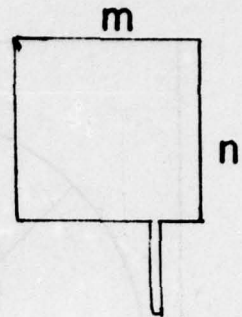


Figure B-5. Impedance of the off-center fed, square microstrip antenna near resonance of the (0,1) and (1,0) modes.

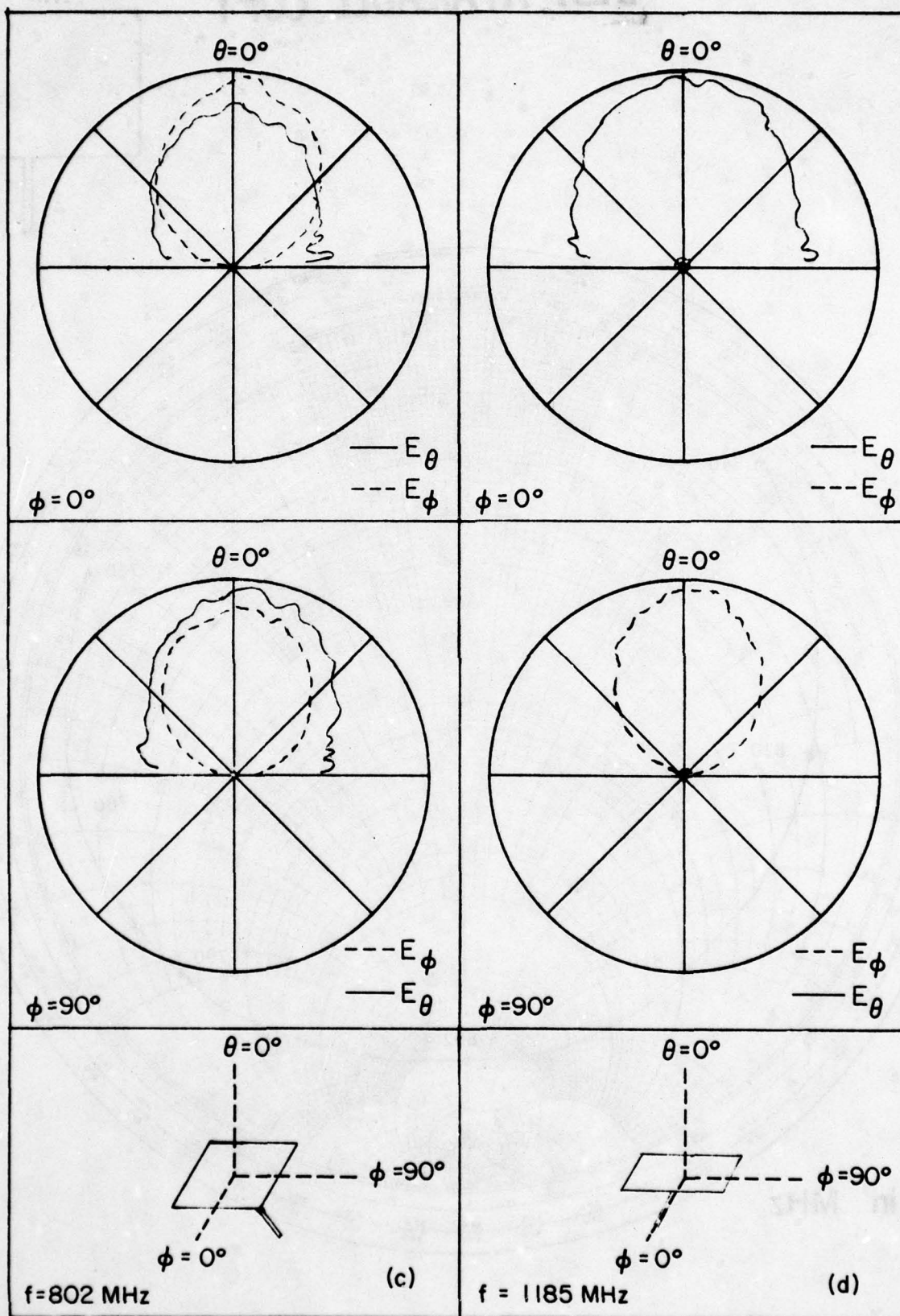


Figure B-6. Radiation patterns of square, corner-fed microstrip antenna and rectangular, wide-side-fed microstrip antenna.

BEST AVAILABLE COPY

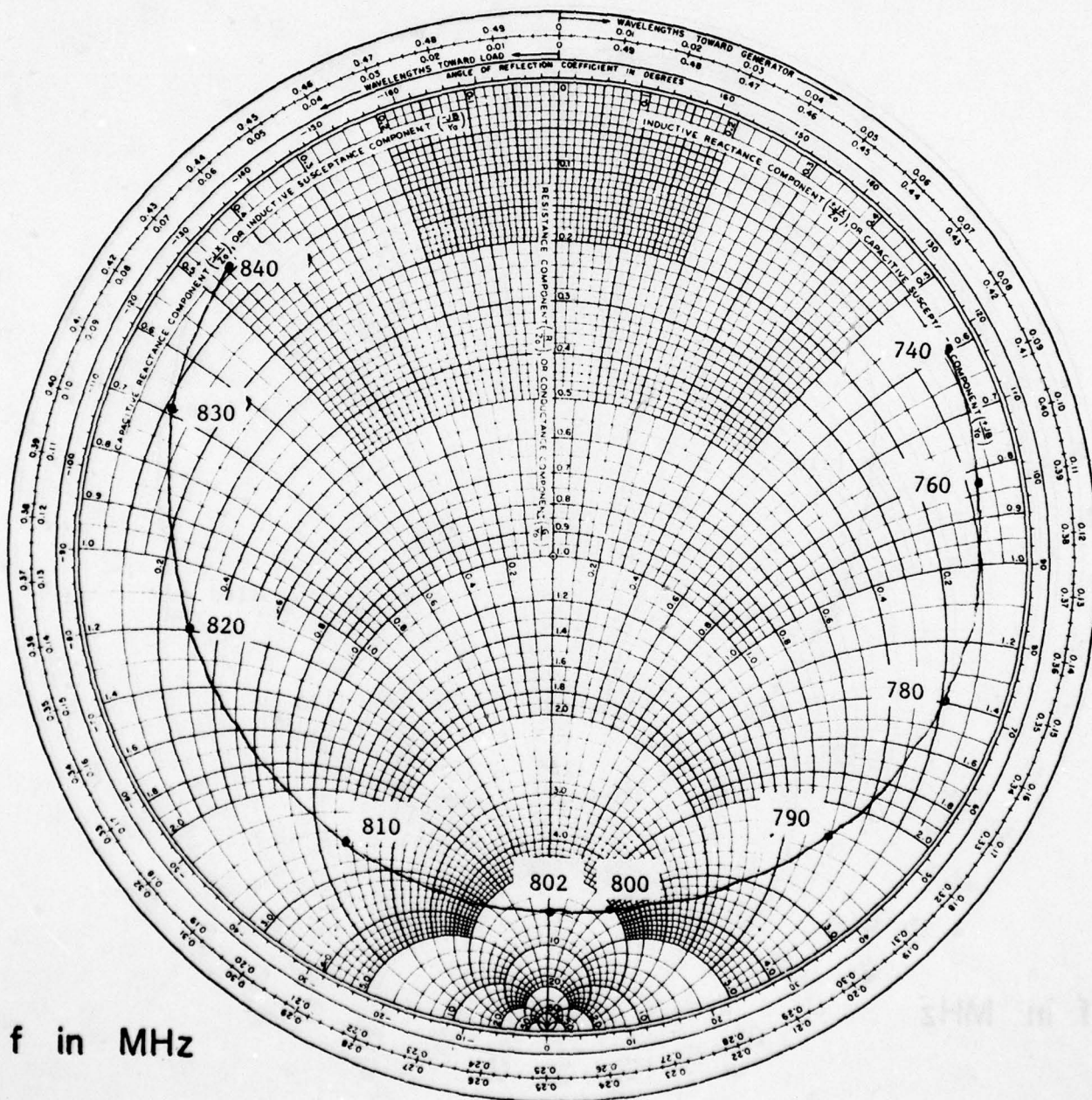
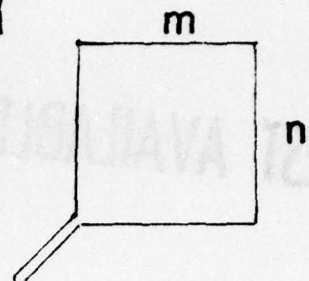
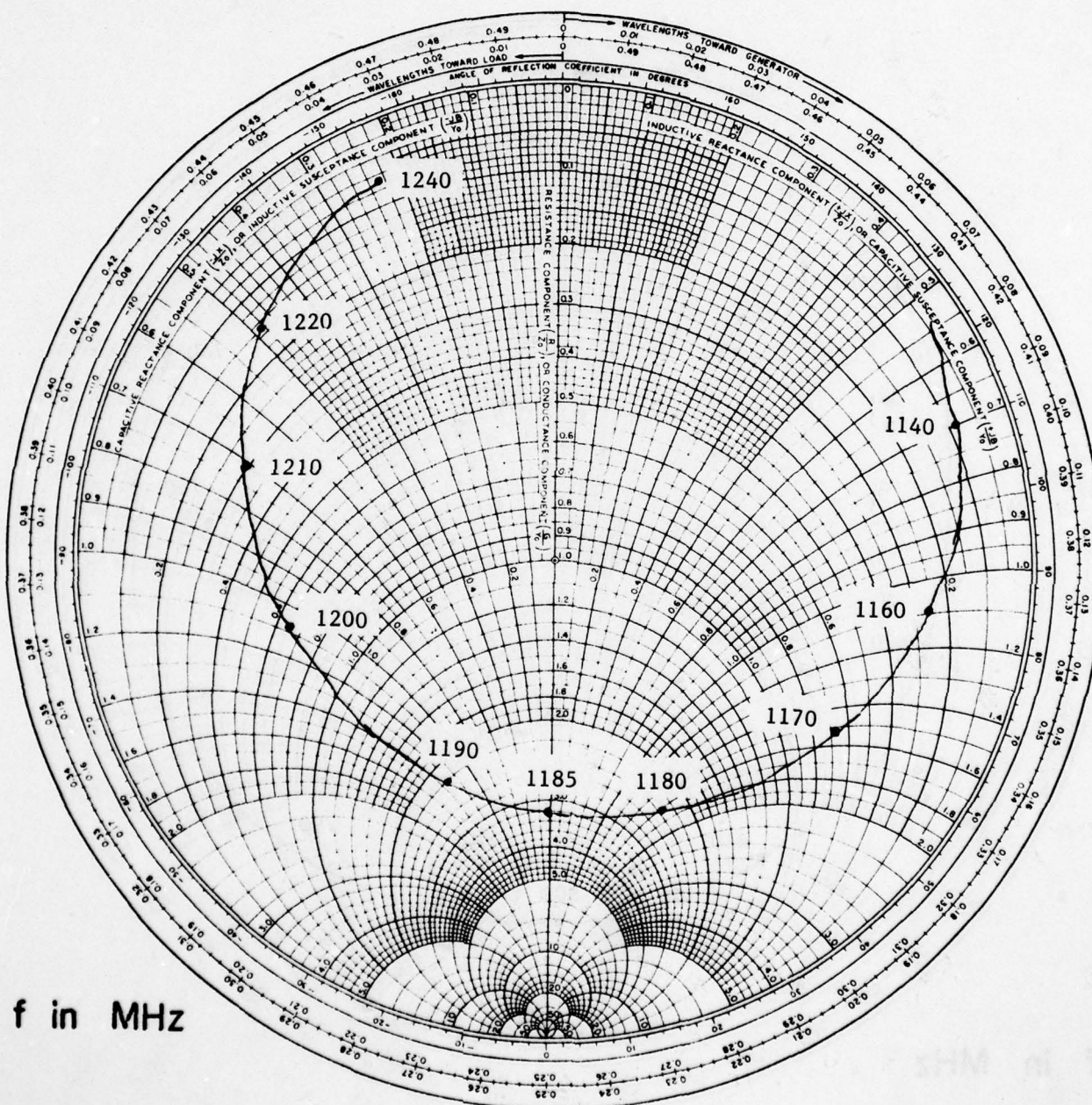
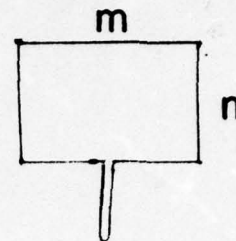


Figure B-7. Impedance of square, corner-fed microstrip antenna near resonance of (0,1) and (1,0) modes.

BEST AVAILABLE COPY



f in MHz

Figure B-8. Impedance of rectangular, broad-side centered microstrip antenna near resonance of (0,1) mode.

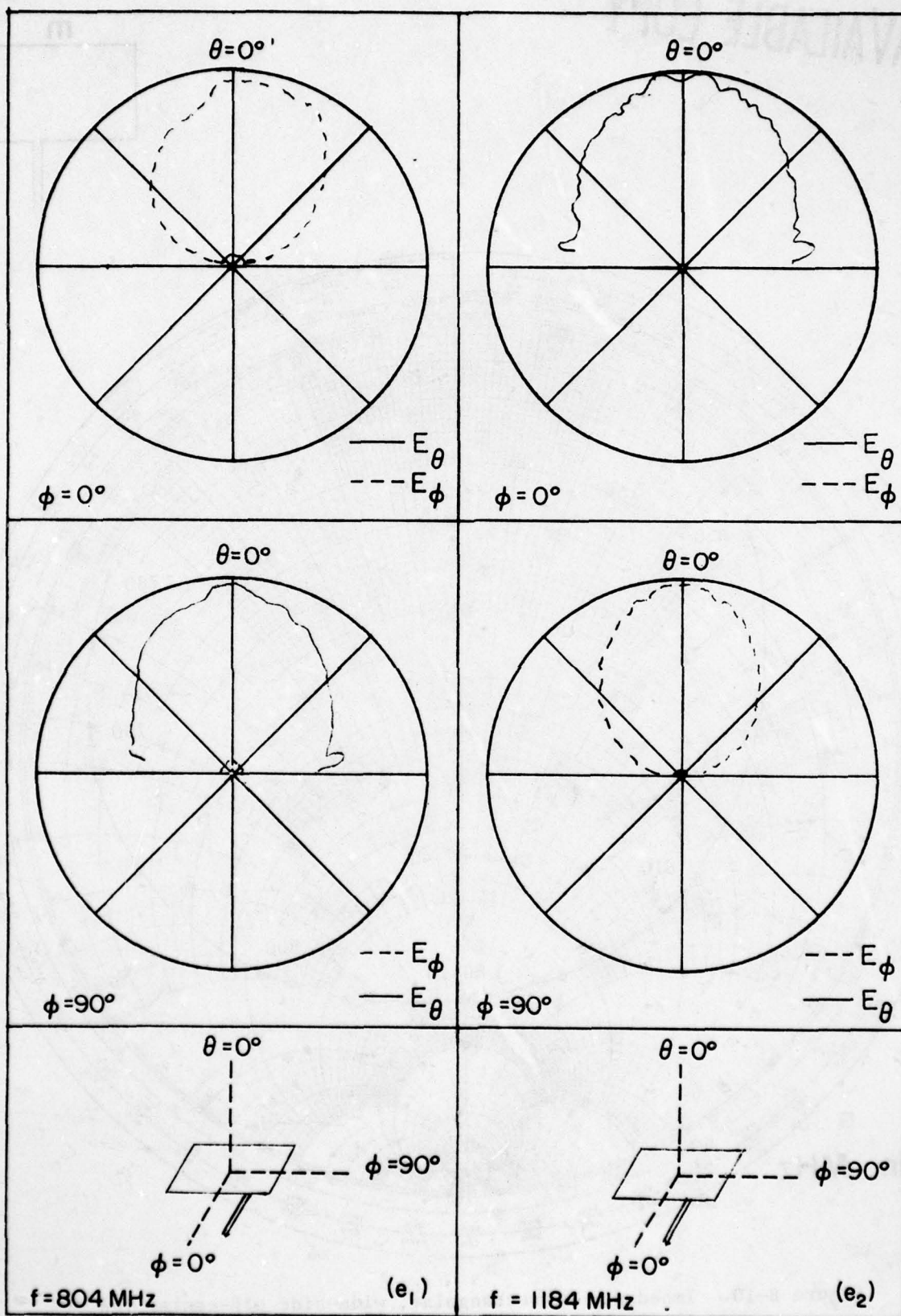


Figure B-9. Radiation patterns of rectangular, wide-side off-center fed microstrip antenna for (e_1) mode (1,0), (e_2) mode (0,1).

AD-A053 005

ILLINOIS UNIV AT URBANA-CHAMPAIGN ELECTROMAGNETICS LAB
STUDY OF MICROSTRIP ANTENNAS, MICROSTRIP PHASED ARRAYS, AND MIC--ETC(U)

F/G 9/5

DEC 77 Y T LO, D SOLOMON, F R ORE

F19628-76-C-0140

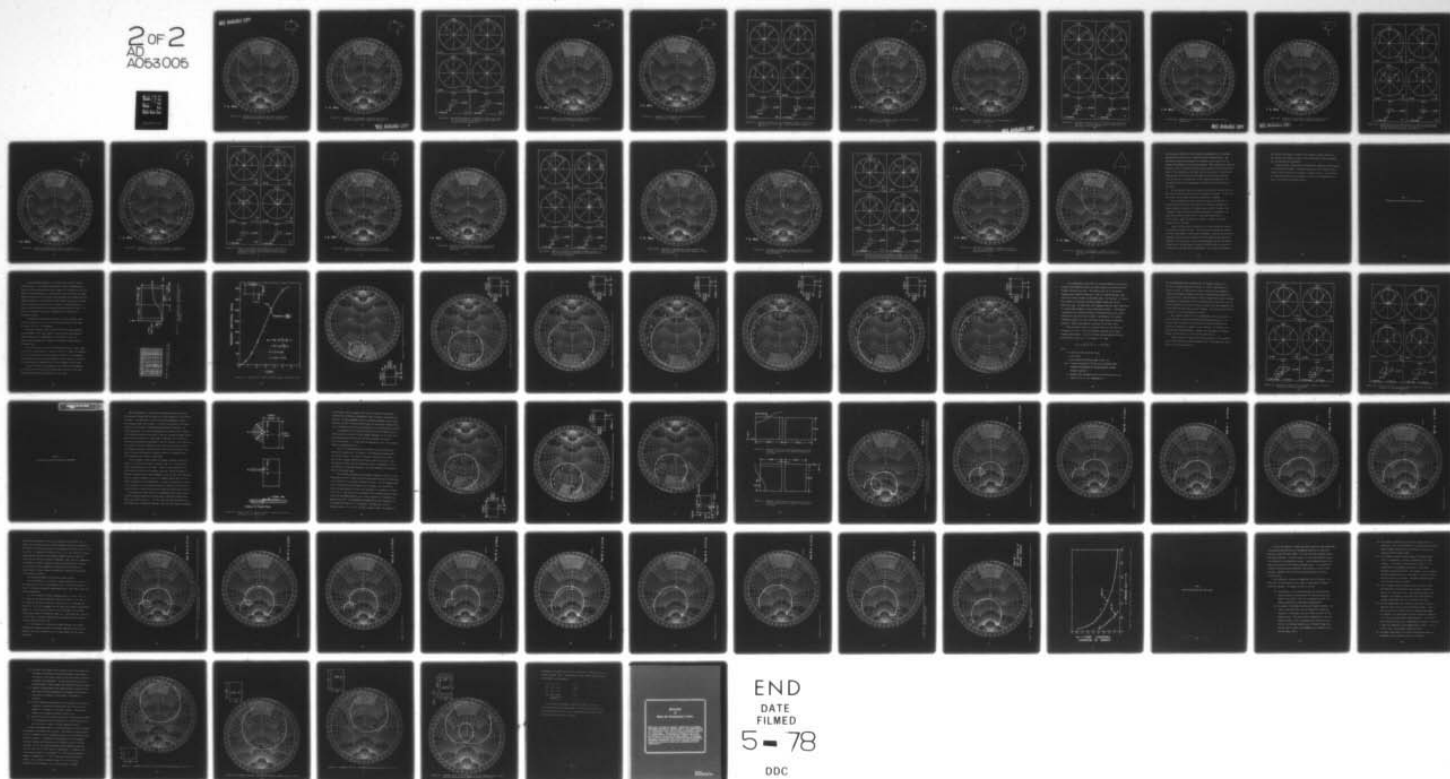
UNCLASSIFIED

UIEM-77-23

RADC-TR-77-406

NL

2 OF 2
AD
A053005



END
DATE
FILMED

5 - 78

DDC

BEST AVAILABLE COPY

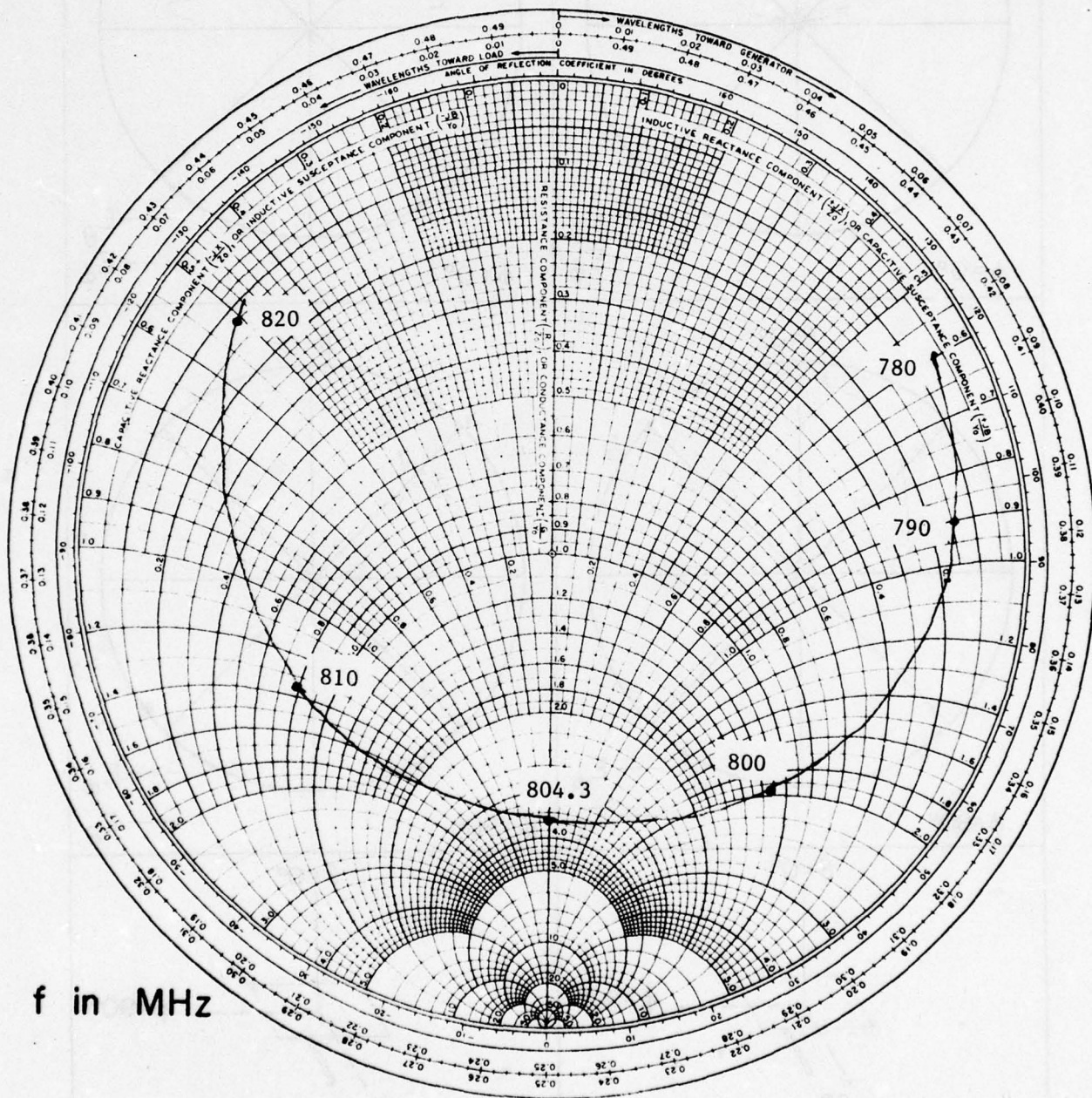
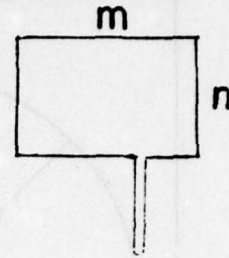


Figure B-10. Impedance of rectangular, wide-side off-center fed microstrip antenna near resonance of mode (0,1).

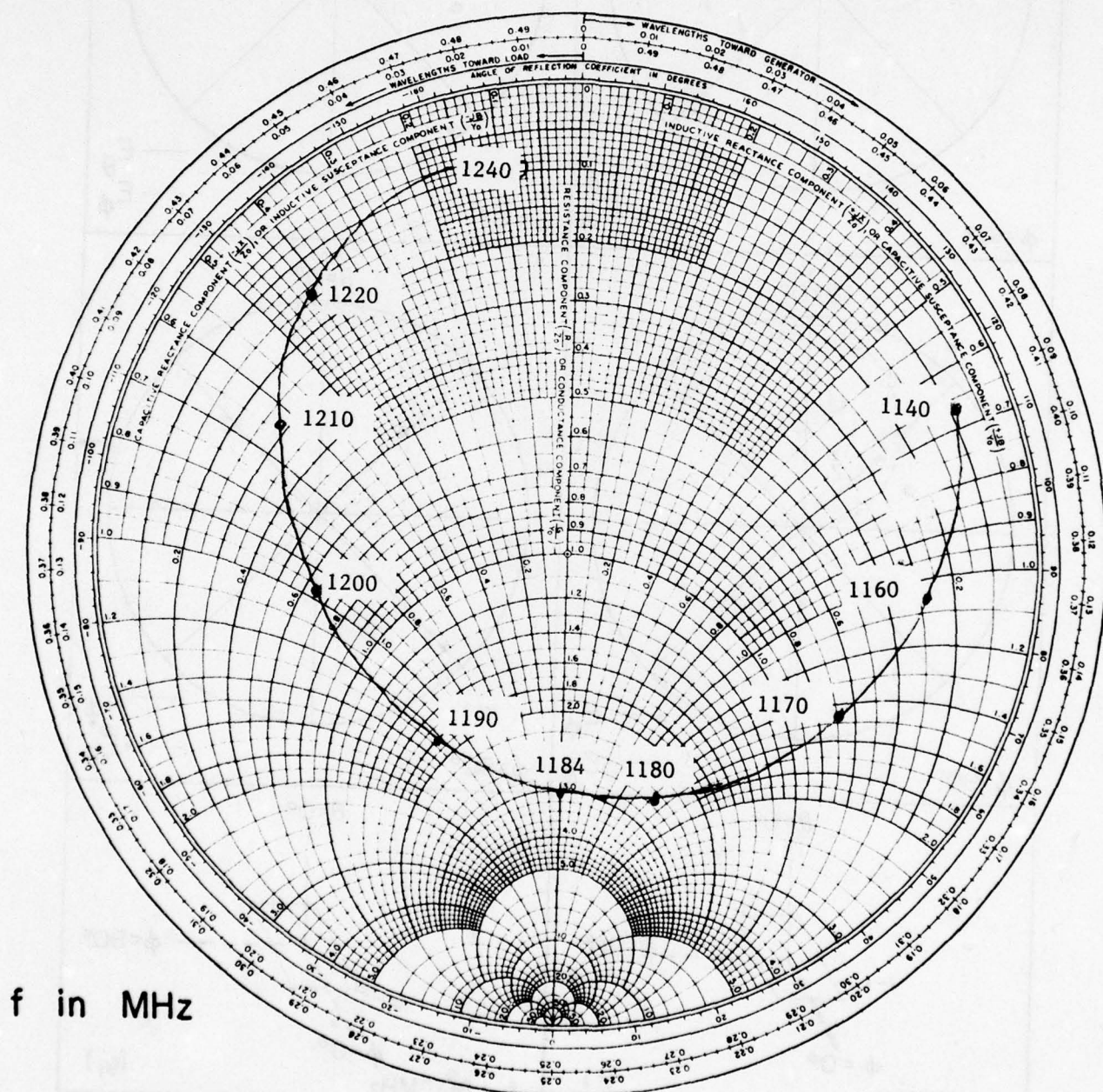
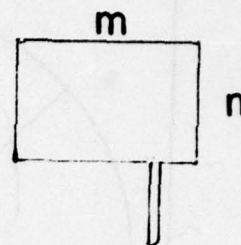


Figure B-11. Impedance of rectangular, wide-side off-center fed microstrip antenna near resonance of mode (0,1).

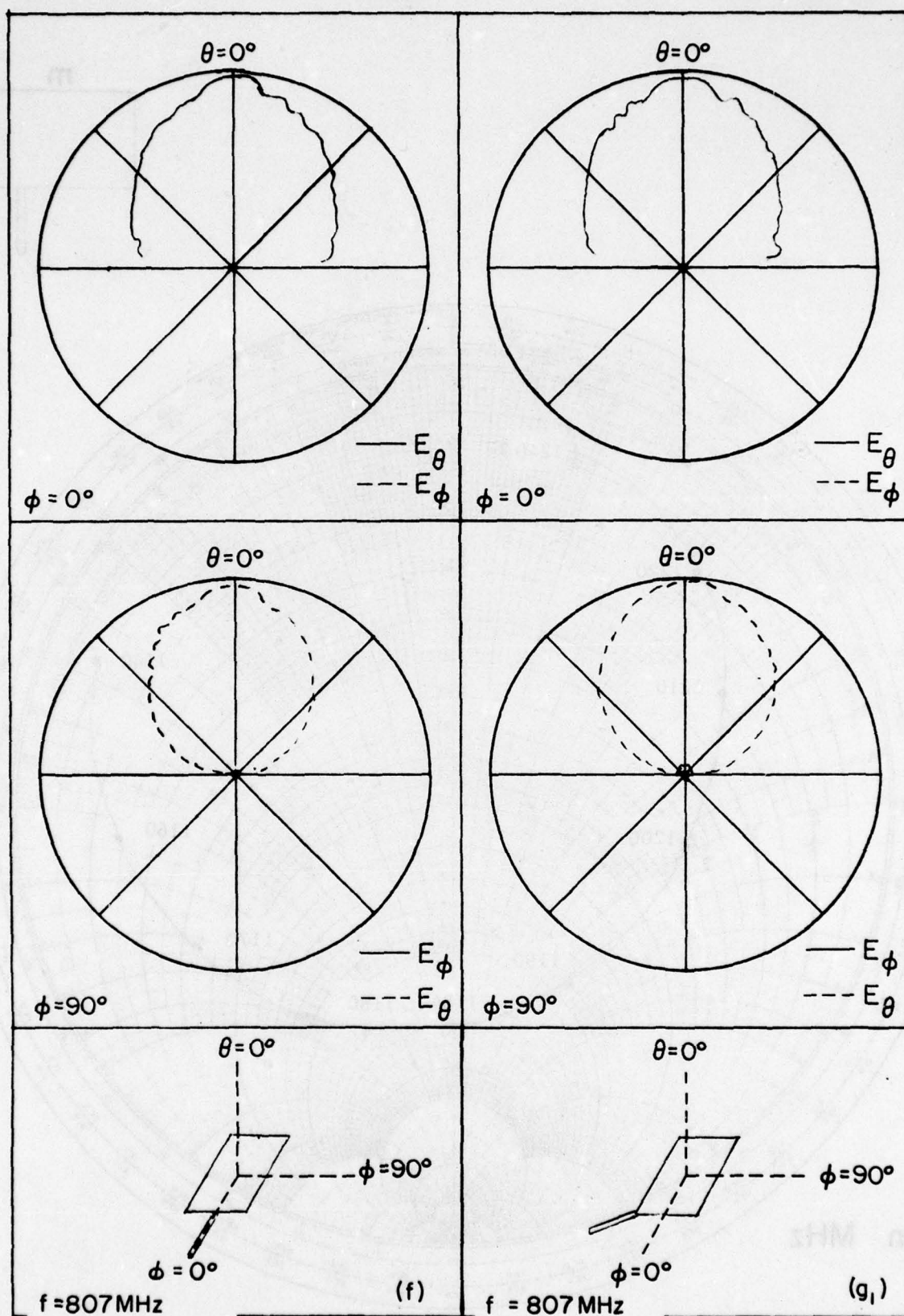


Figure B-12. Radiation patterns of rectangular (f) narrow-side center fed microstrip antenna of mode (0,1), (g₁) corner fed microstrip antenna of mode (0,1).

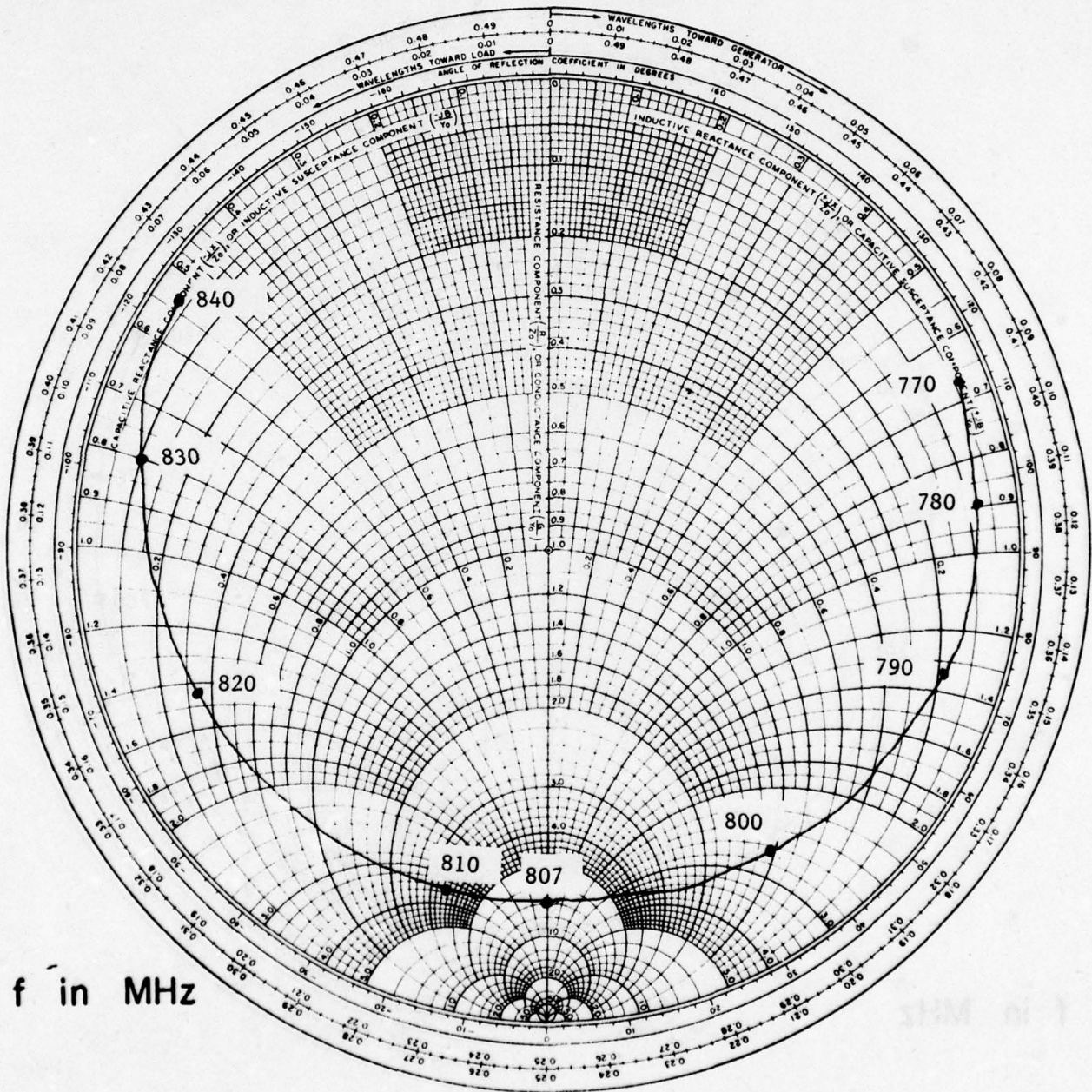
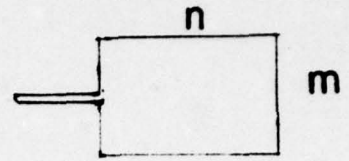


Figure B-13. Impedance of rectangular, narrow-side center fed microstrip antenna near resonance of mode (0,1).

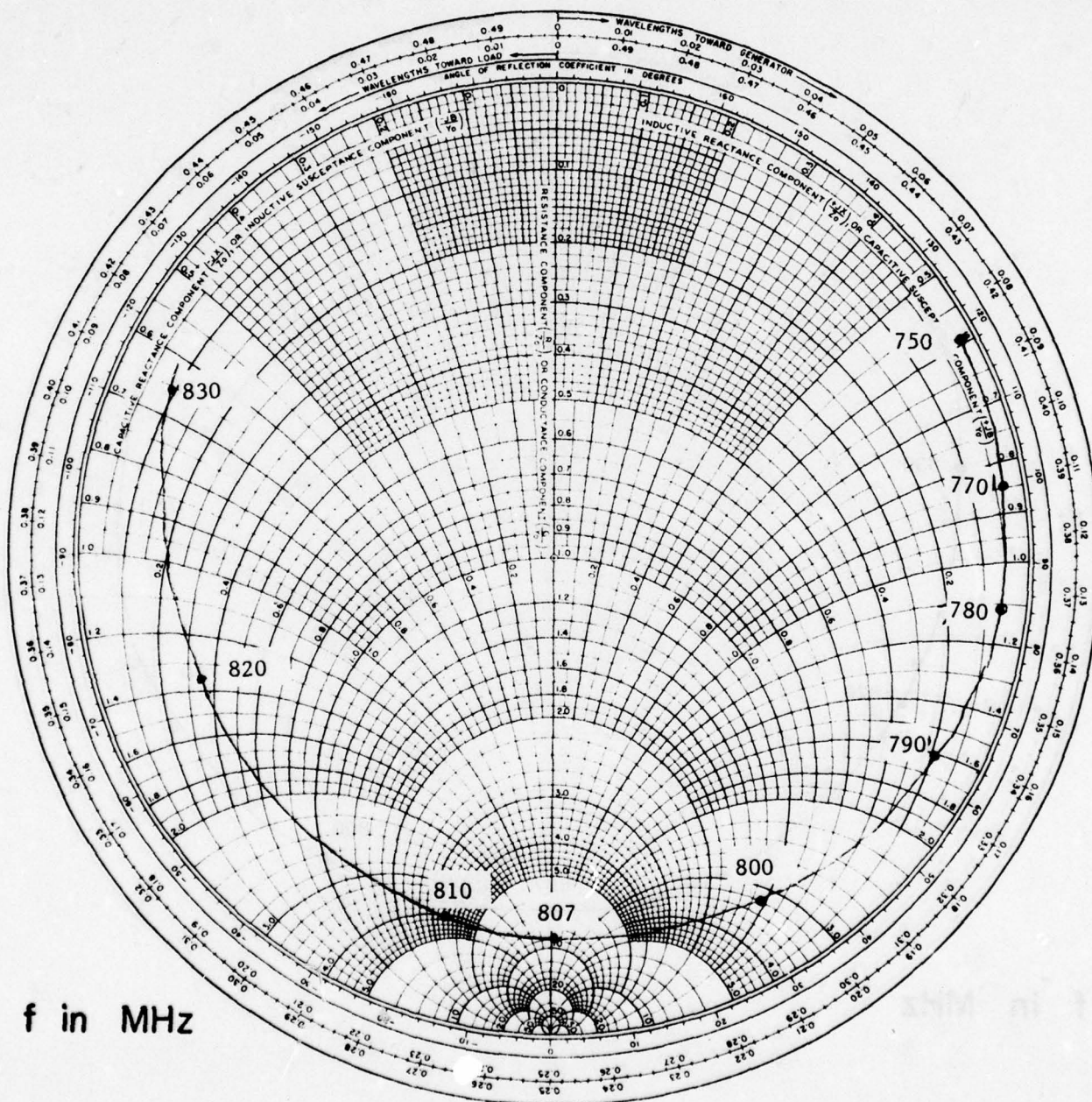
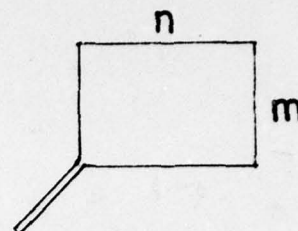


Figure B-14. Impedance of rectangular, corner fed microstrip antenna near resonance of mode (0,1).

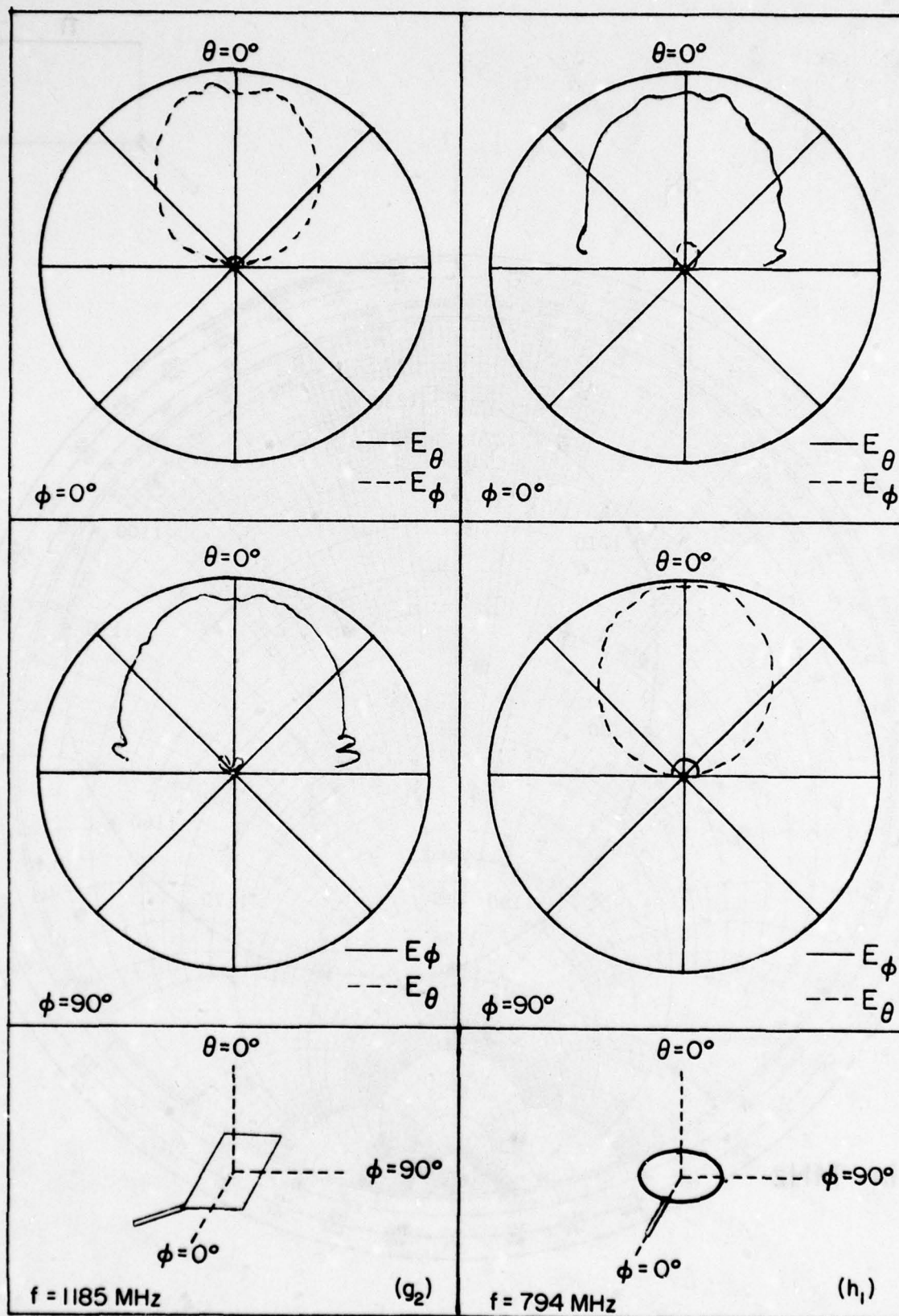
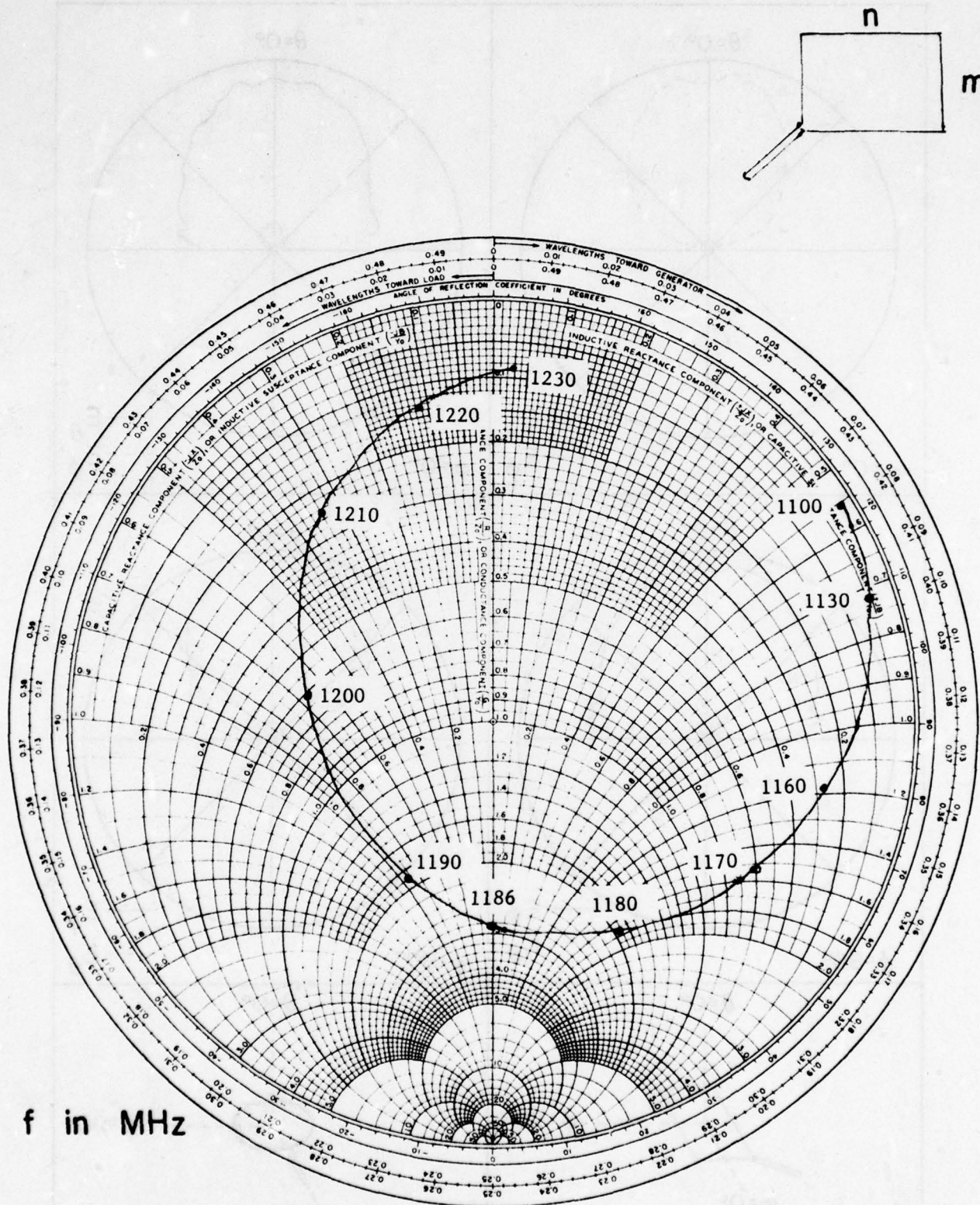
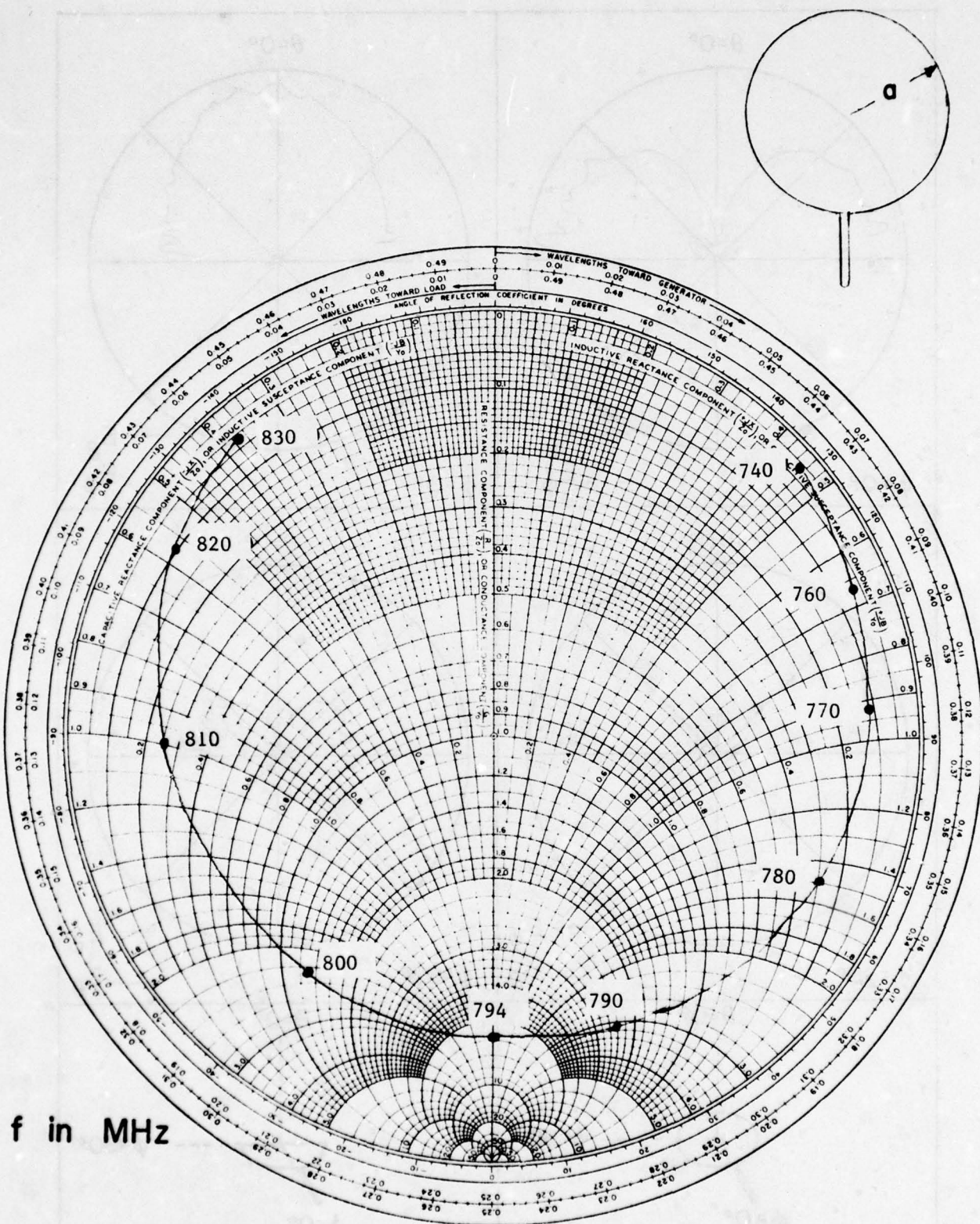


Figure B-15. Radiation patterns of (g_2) rectangular, corner fed microstrip antenna of mode (1,0), (h_1) circular microstrip antenna of mode (1,1).



f in MHz

Figure B-16. Impedance of rectangular, corner fed microstrip antenna near resonance of mode (1,0).



f in MHz

Figure B-17. Impedance of circular microstrip antenna near resonance of mode (1,1).

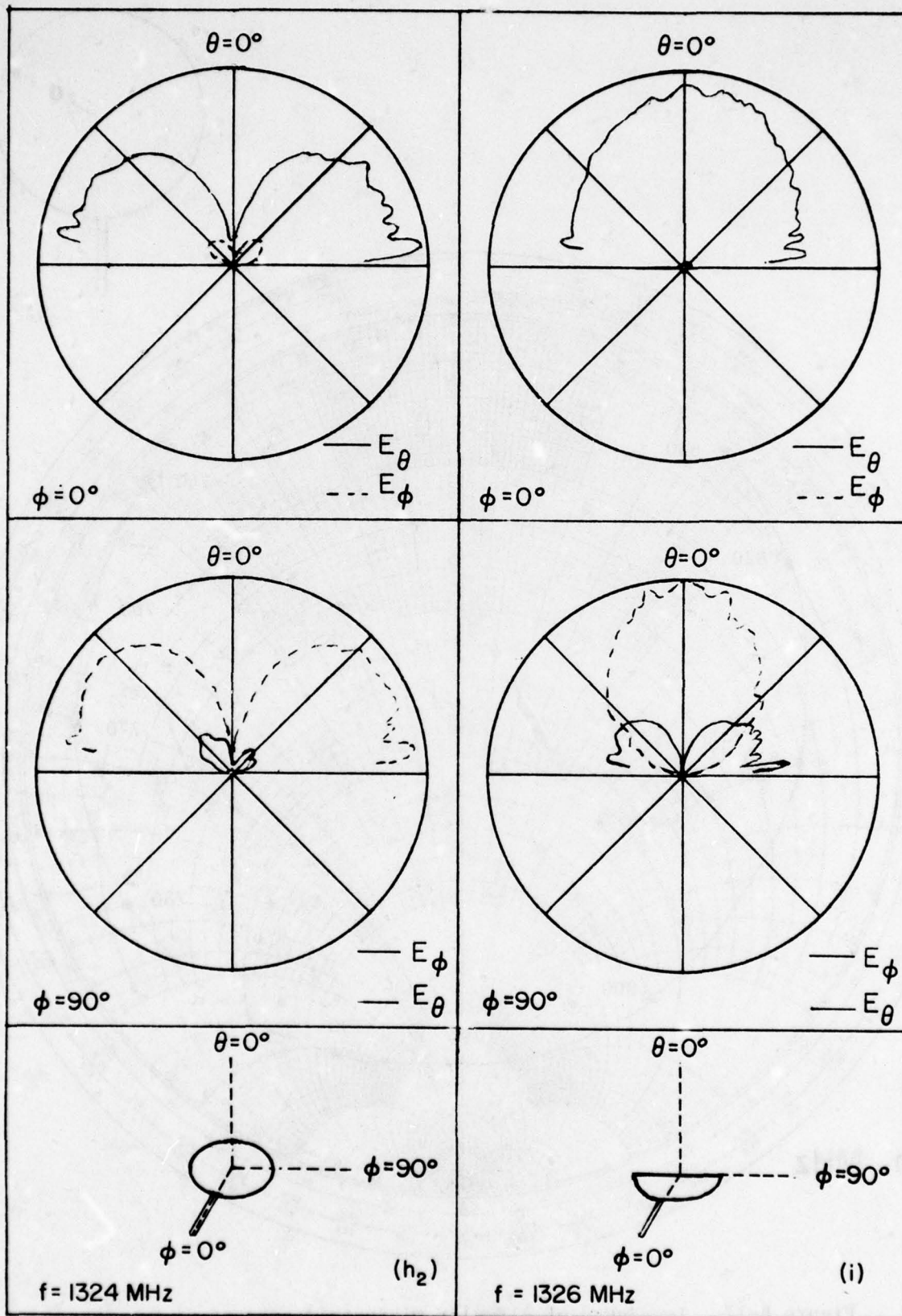
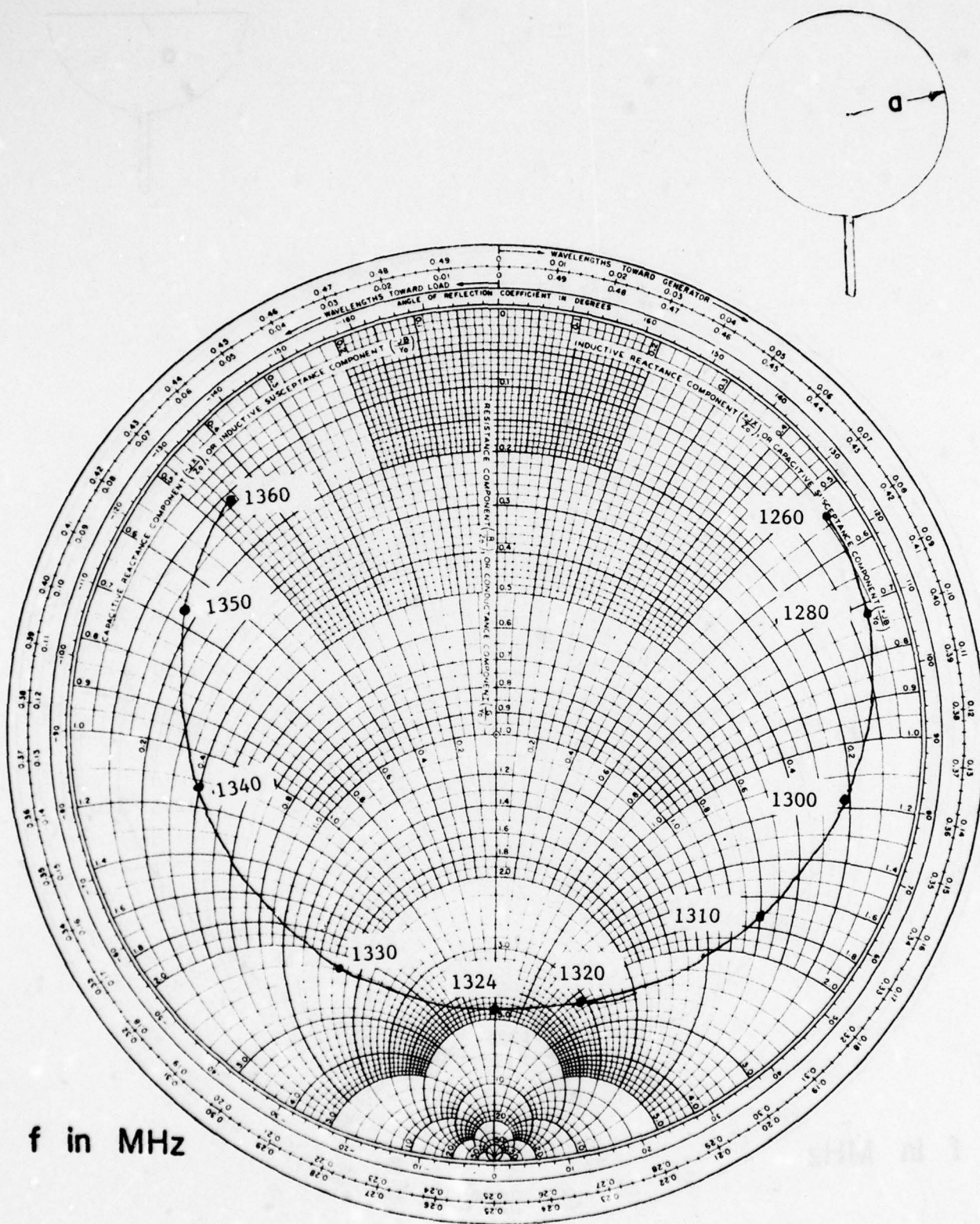
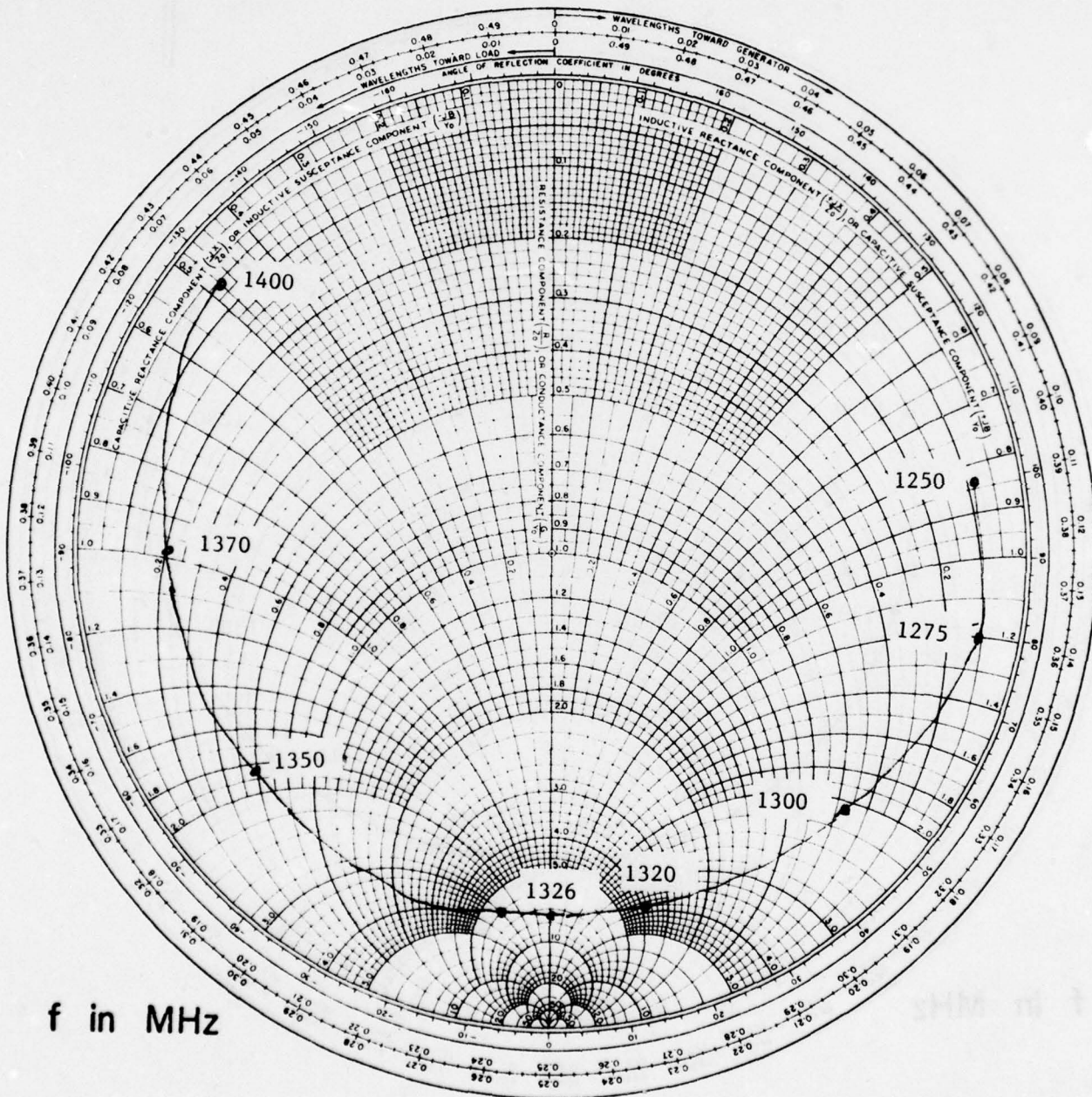
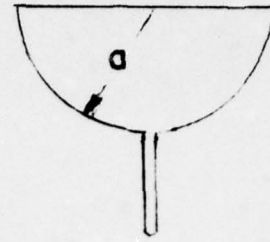


Figure B-18. Radiation patterns of (h_2) circular microstrip antenna of mode $(2,1)$, (i_1) semicircular, center of half-circle fed microstrip antenna of mode $(2,1)$.



f in MHz

Figure B-19. Impedance of circular microstrip antenna near resonance of mode (2,1).



f in MHz

Figure B-20. Impedance of semicircular, center of half-circle fed microstrip antenna near resonance of mode (2,1).

BEST AVAILABLE COPY

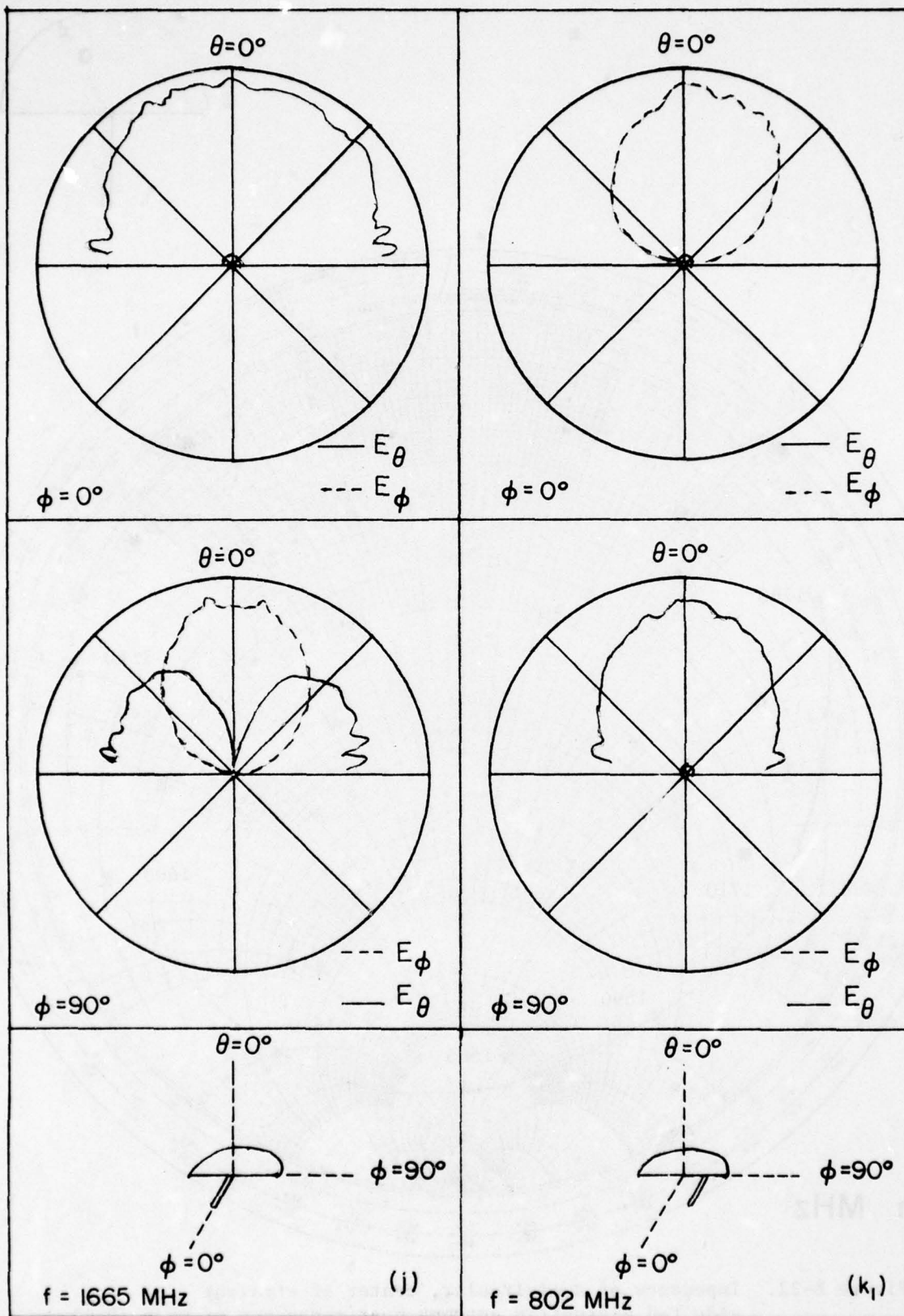


Figure B-21. Radiation patterns of semicircular (j) center of straight side fed microstrip antenna of mode (0,1), (k_1) off-center of straight side fed microstrip antenna of order mode (1,1).

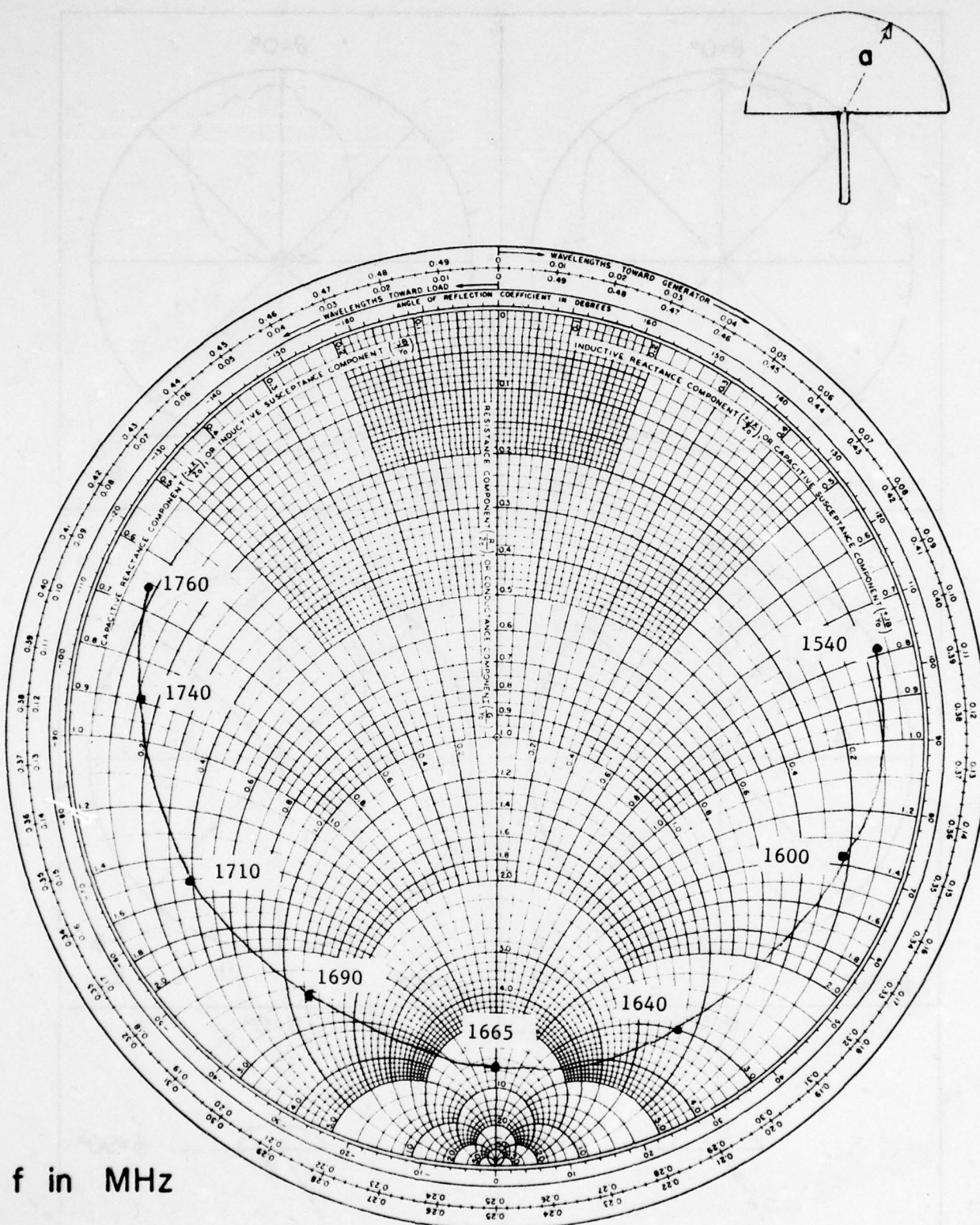
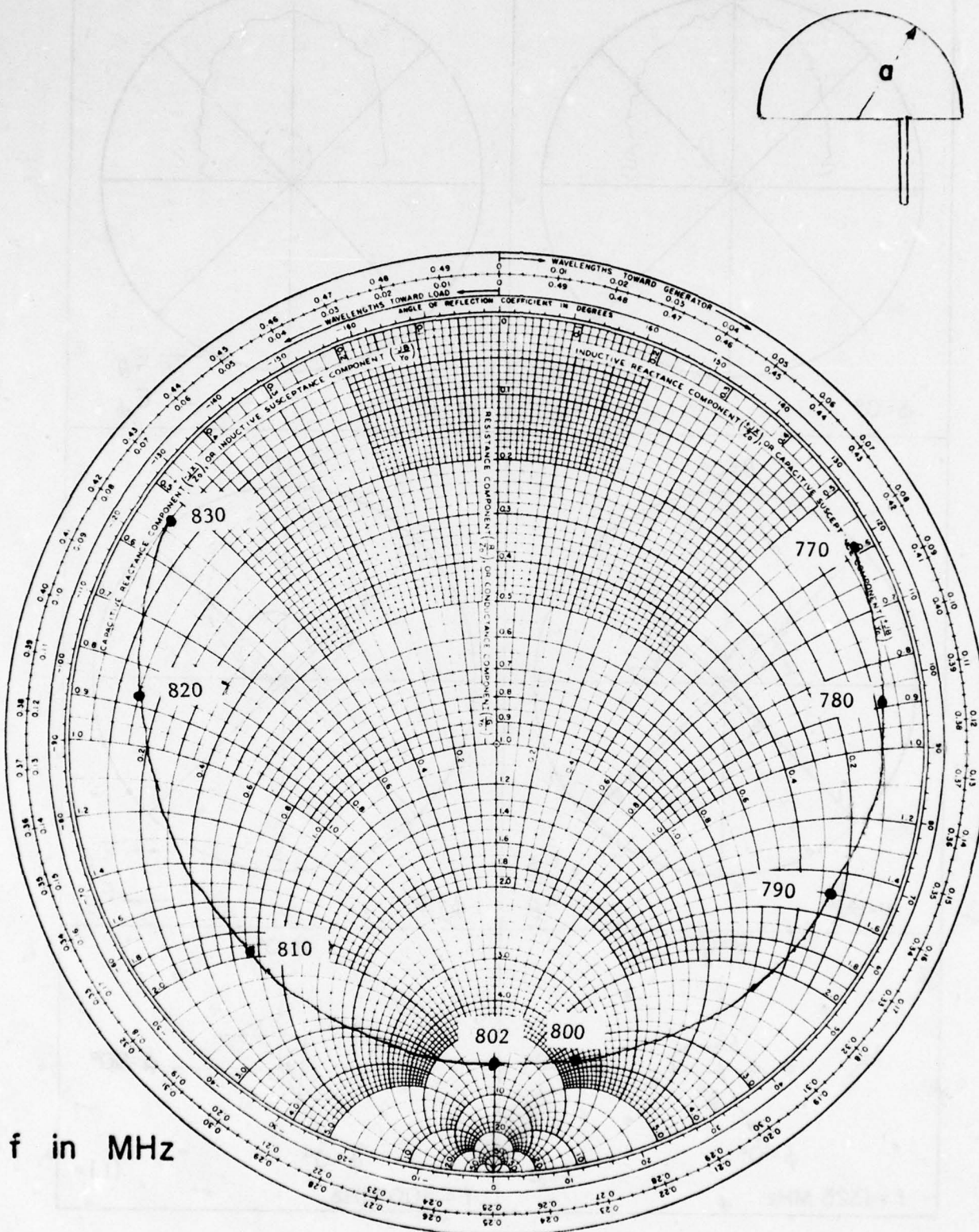


Figure B-22. Impedance of semicircular, center of straight side fed microstrip antenna near resonance of mode (0,1).



f in MHz

Figure B-23. Impedance of semicircular, off-center of straight side fed microstrip antenna near resonance of mode (1,1).

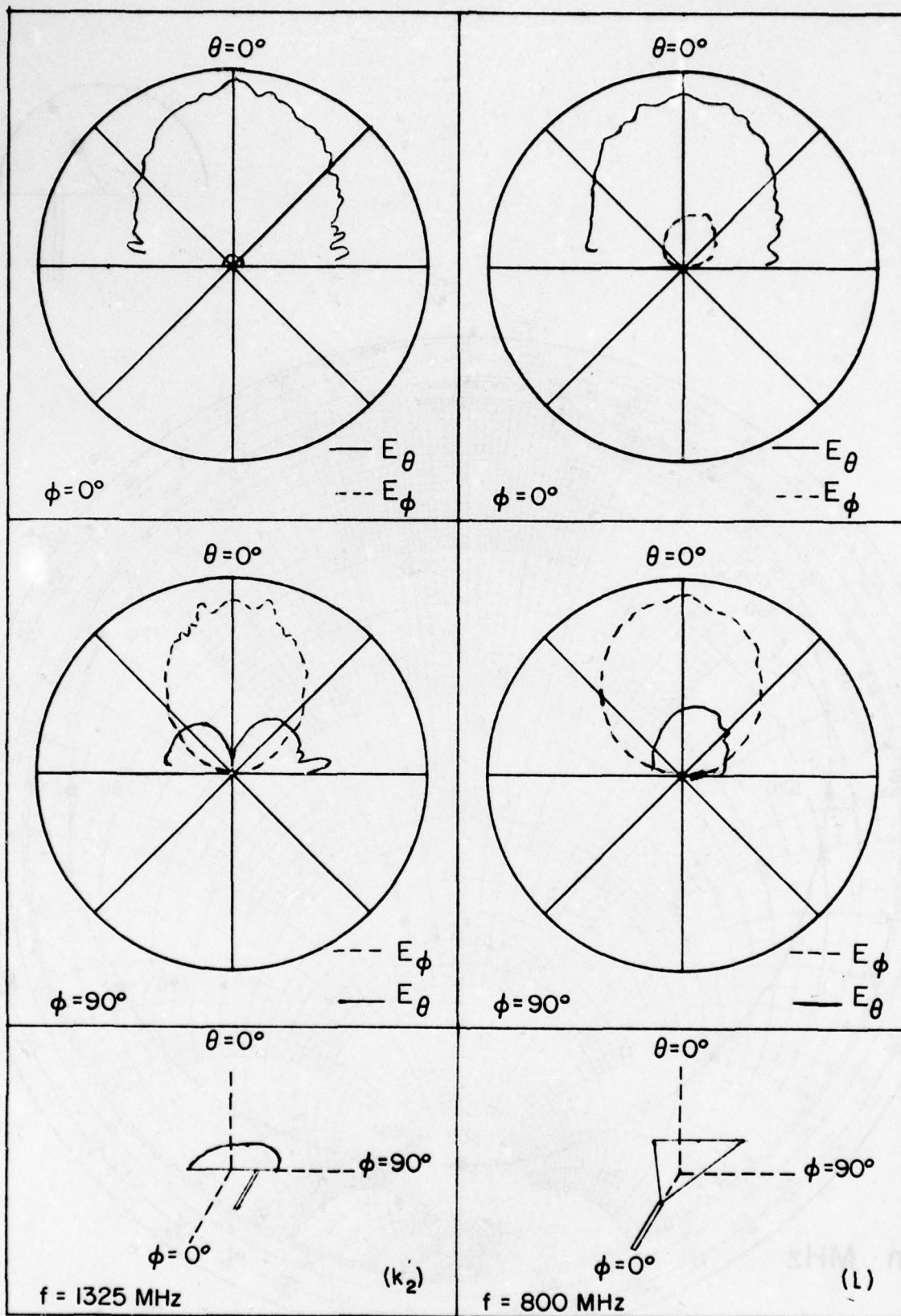


Figure B-24. Radiation patterns of (k₂) semicircular, off-center of straight side fed microstrip antenna of mode (2,1), (1) equiangular triangle, one tip fed microstrip antenna of modes (0,1), (1,0).

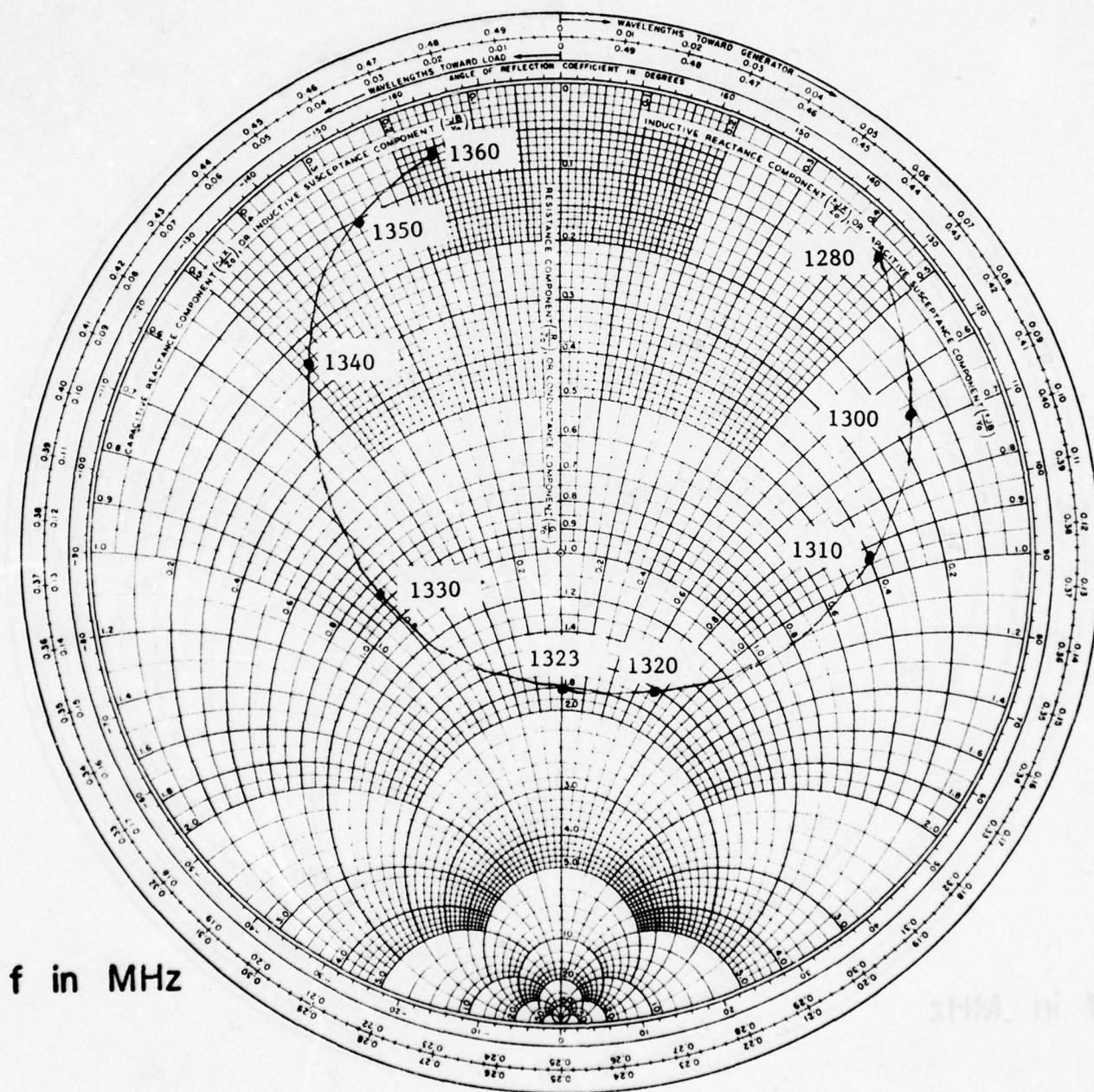
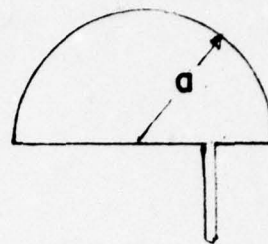
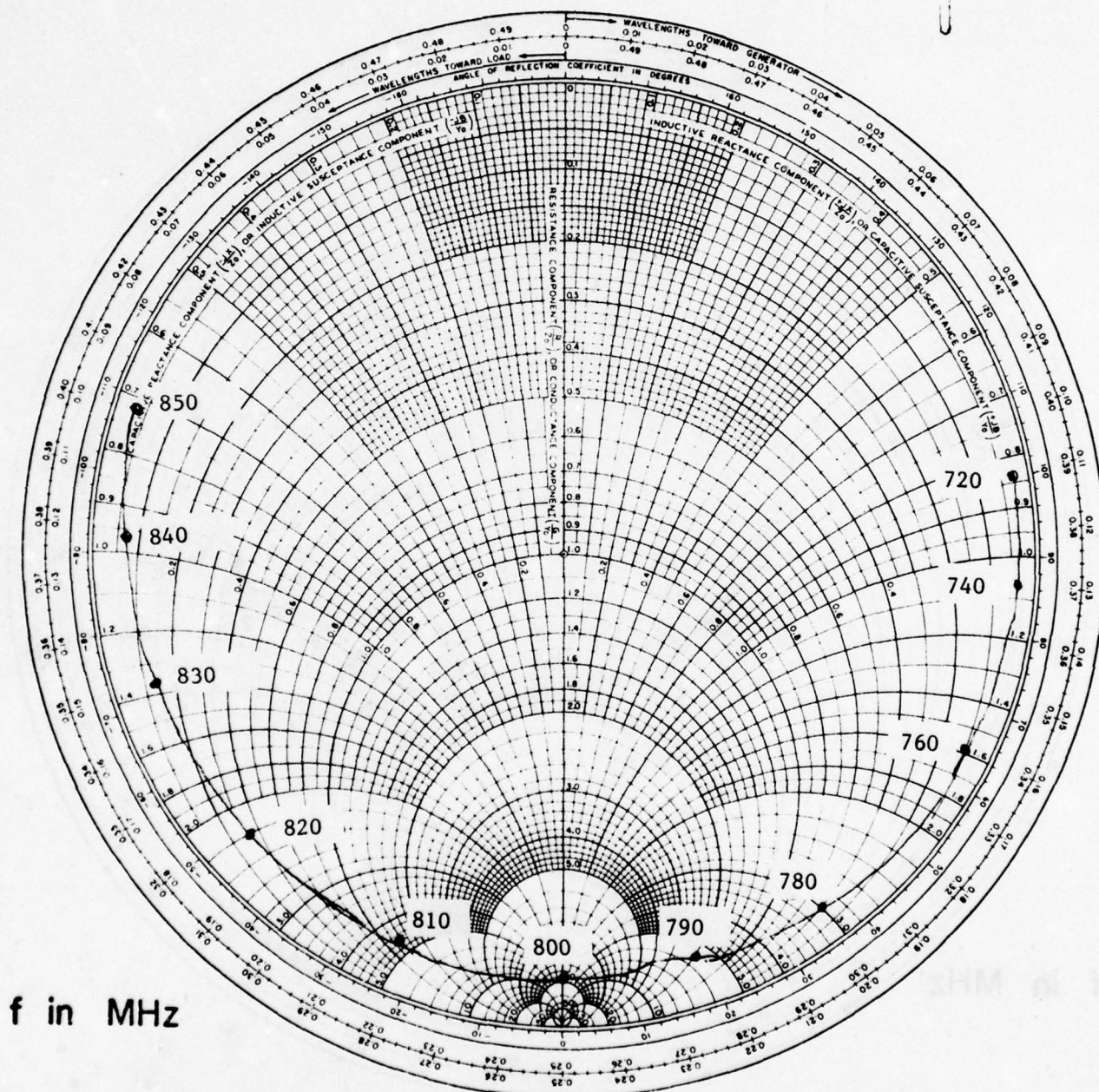


Figure B-25. Impedance of semicircular, off-center of straight side fed microstrip antenna near resonance of mode (2,1).



f in MHz

Figure B-26. Impedance of an equiangular triangle, one tip fed microstrip antenna near resonance of modes (0,1) and (1,0).

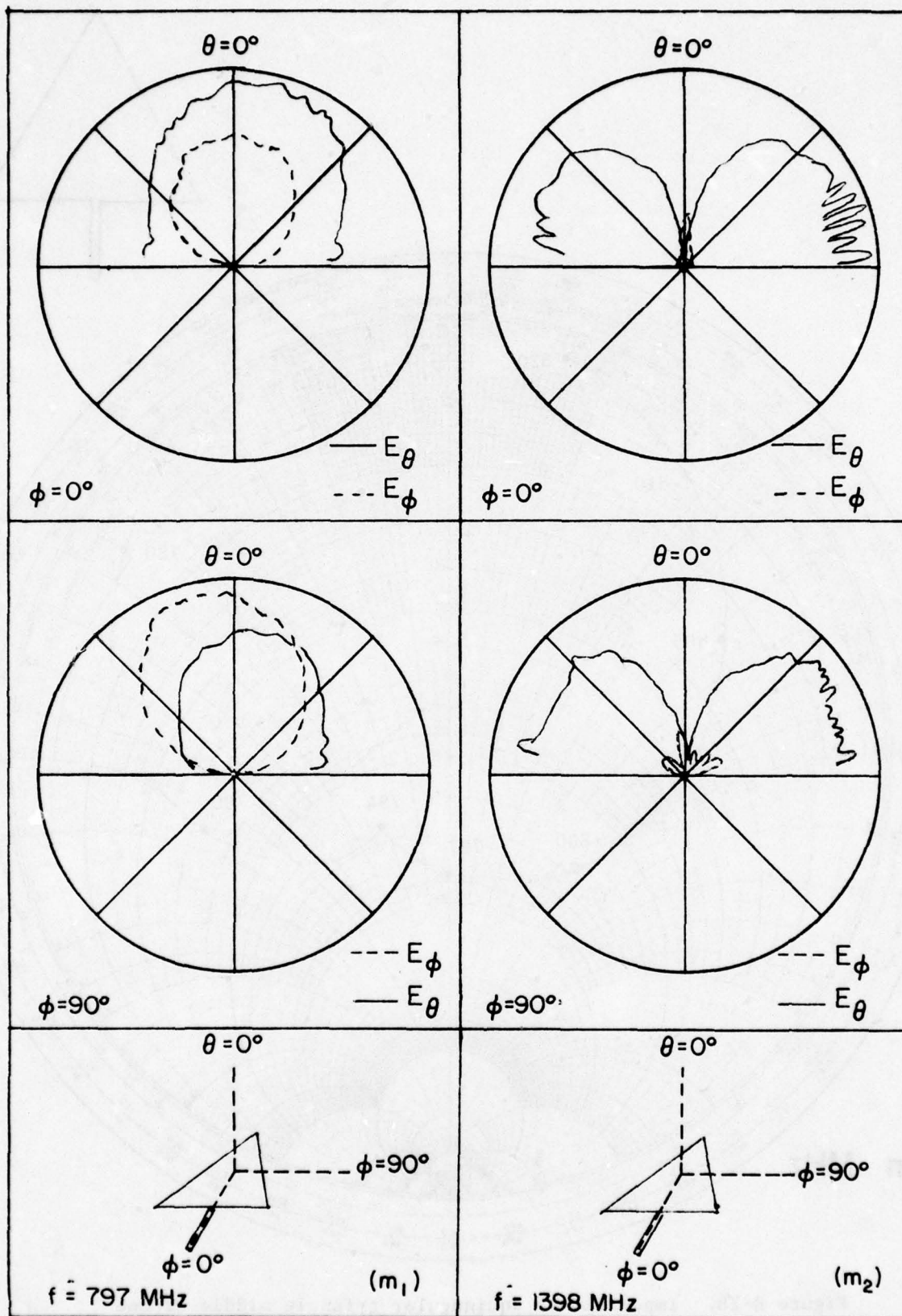
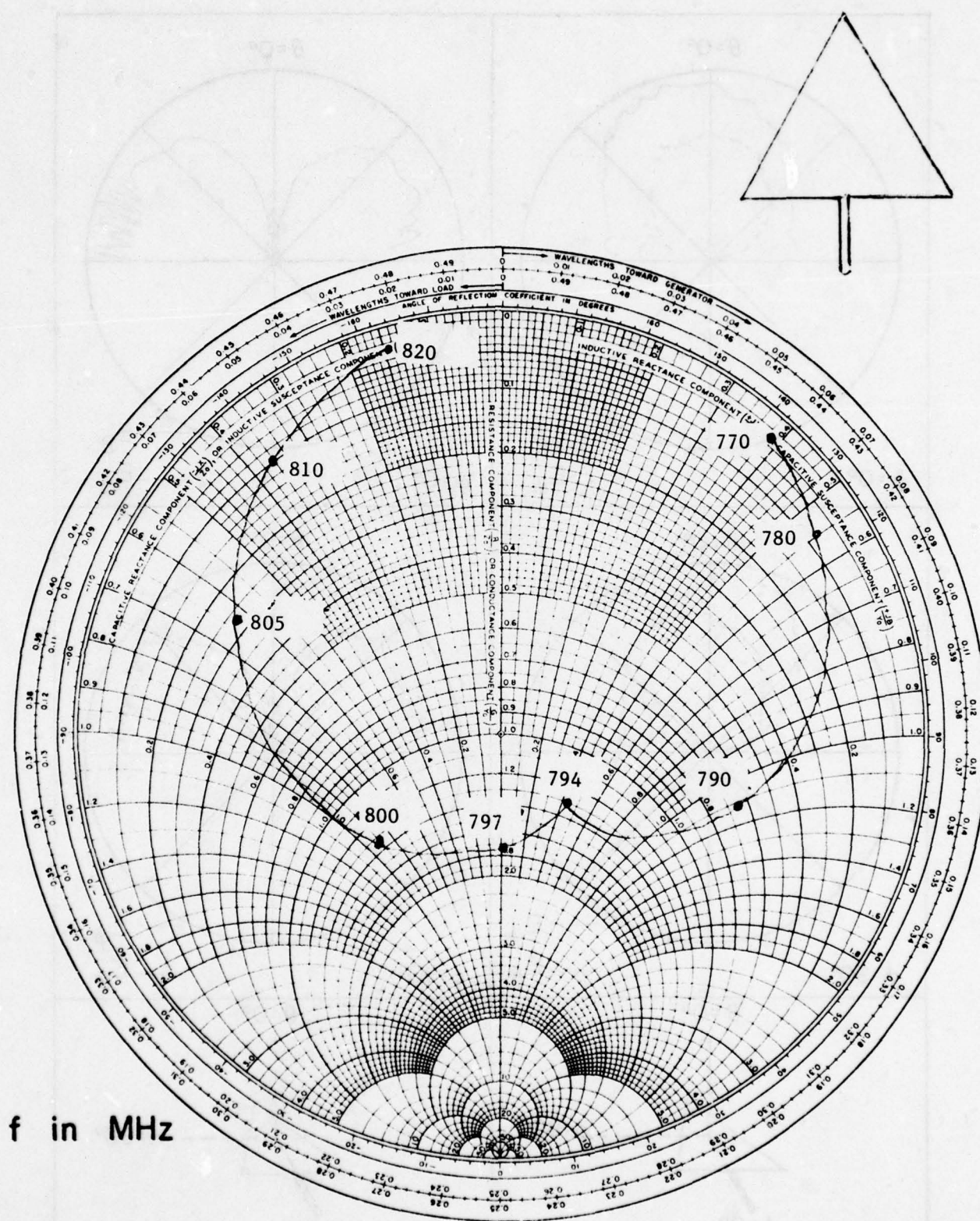
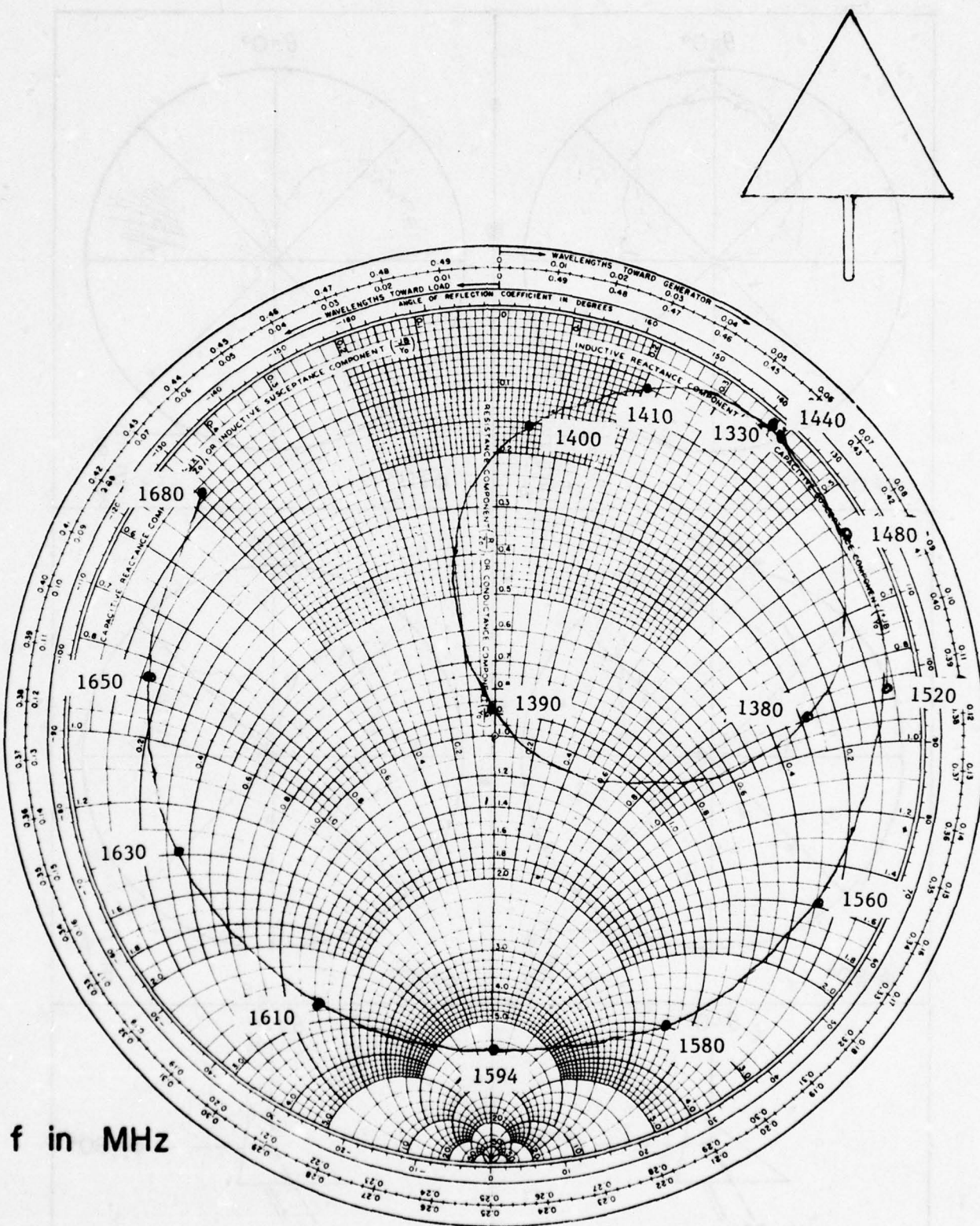


Figure B-27. Radiation patterns of equiangular triangle, middle of one side fed microstrip antennas, (m_1) of modes $(0,1)$ and $(1,0)$, (m_2) of mode $(1,1)$.



f in MHz

Figure B-28. Impedance of equiangular triangle middle of one side fed microstrip antenna near resonance of modes (0,1) and (1,0).



f in MHz

Figure B-29. Impedance of equiangular triangle middle of one side fed microstrip antenna near resonance of mode (1,1) (0,2) and (2,0).

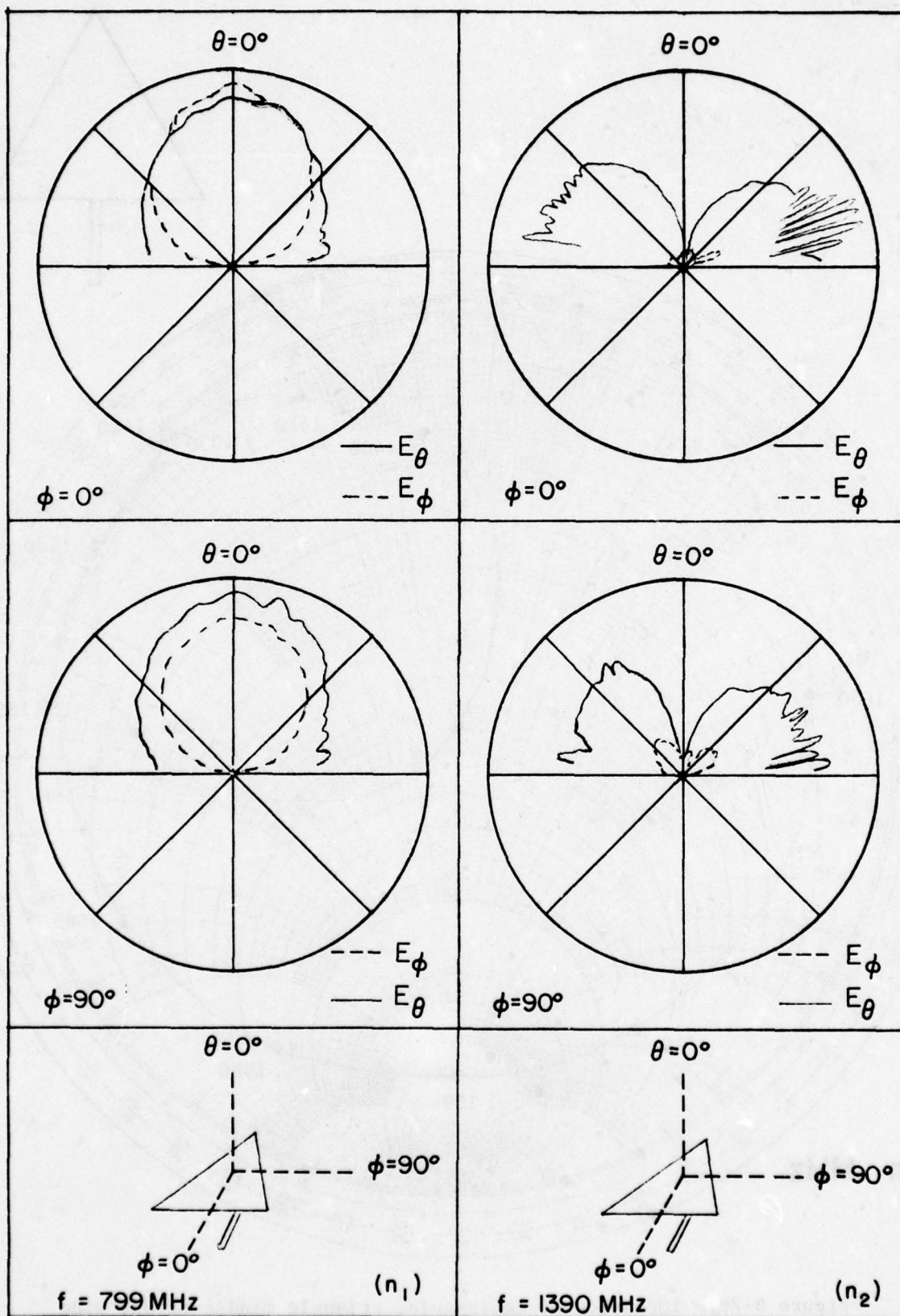
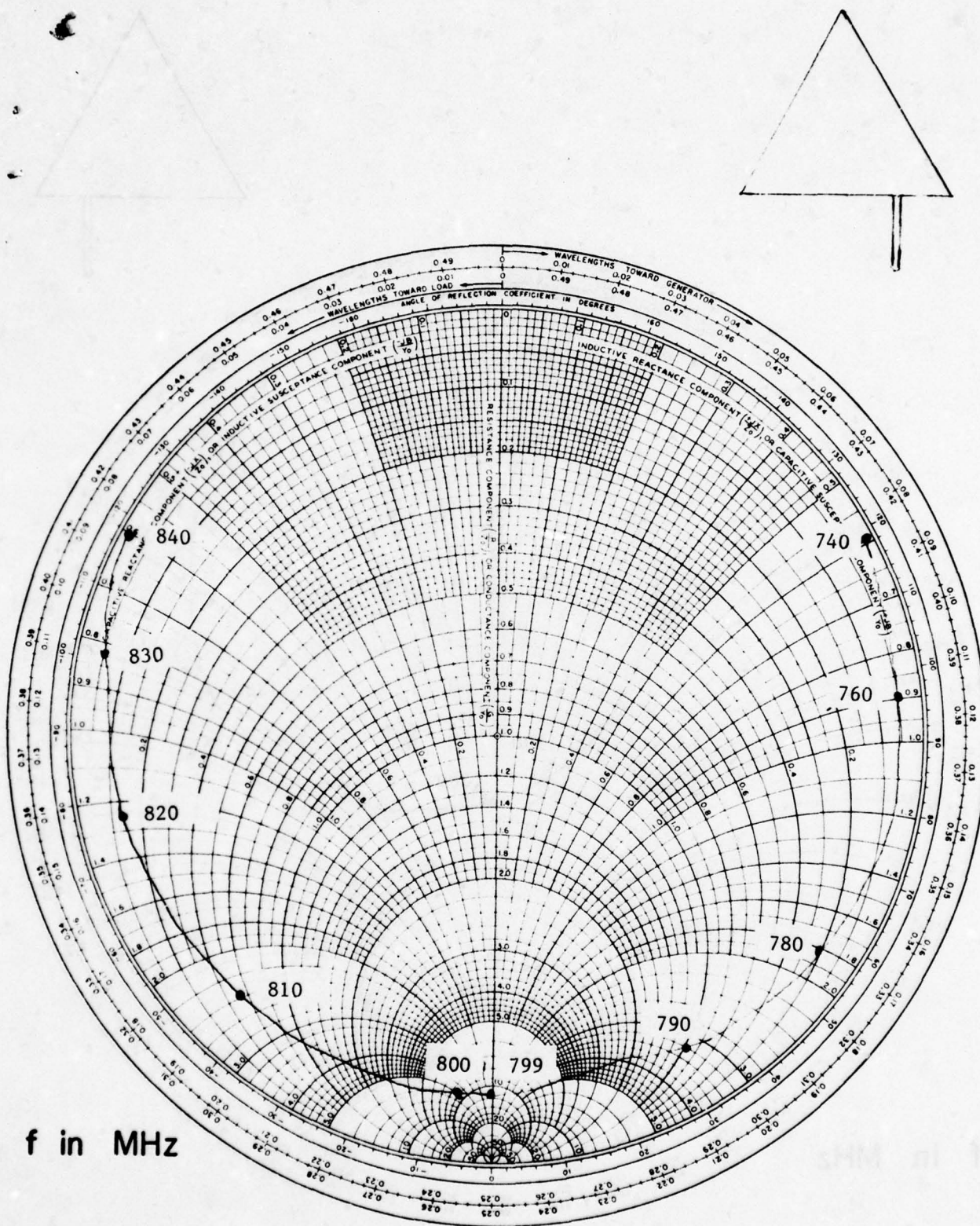


Figure B-30. Radiation patterns of equiangular triangles (n_1) off-center of one side fed microstrip antenna of modes $(0,1)$ and $(1,0)$, (n_2) off-center of one side fed microstrip antenna of mode $(1,1)$.



f in MHz

Figure B-31. Impedance of equiangular triangle off-center of one side fed microstrip antenna near resonance of modes (0,1) and (1,0).

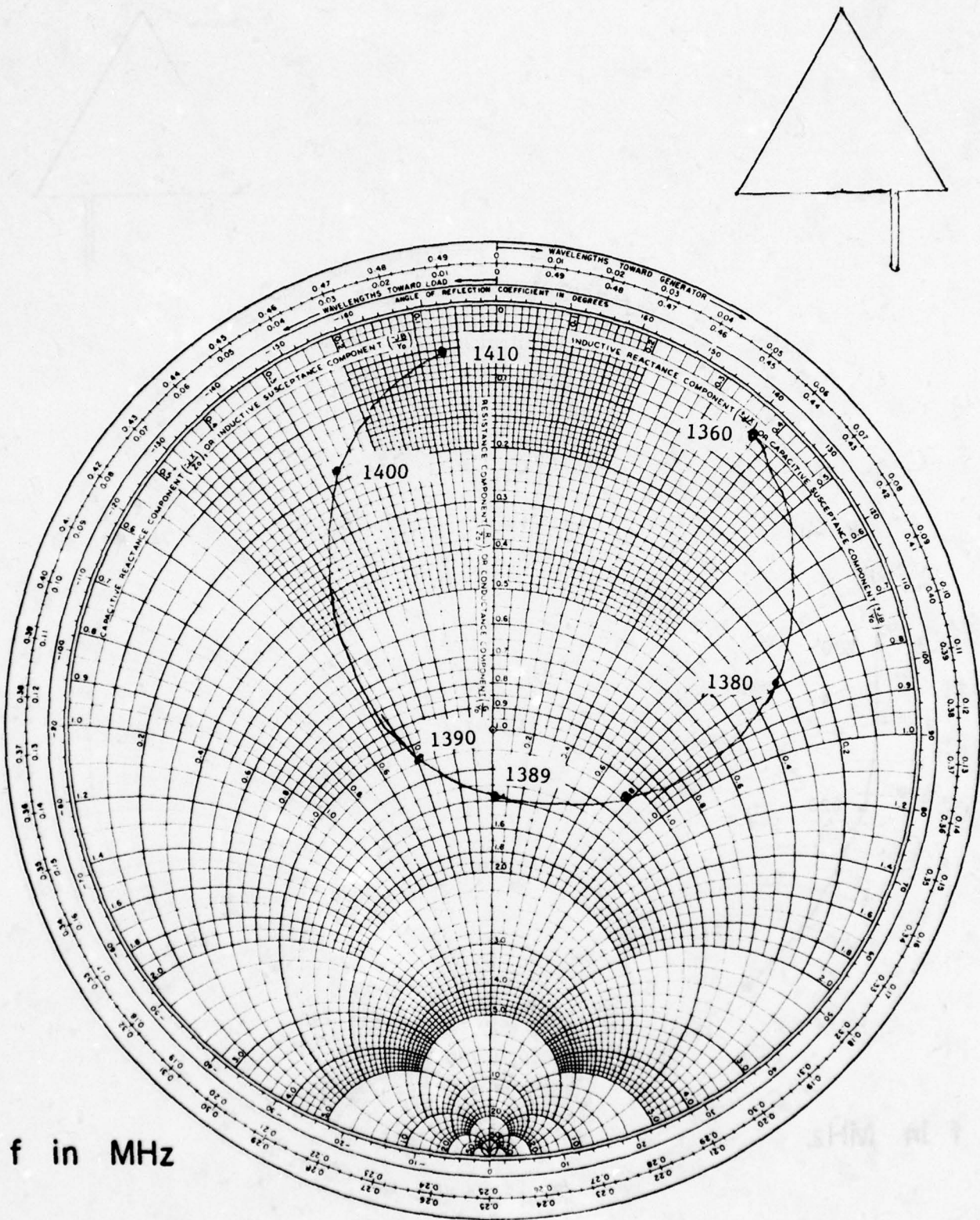


Figure B-32. Impedance of equiangular triangle off-center of one side fed microstrip antenna near resonance of mode (1,1).

that the useful bandwidth of each antenna was determined by its impedance characteristics and not by its radiation pattern characteristics. The radiation patterns near resonance are presented in this report (see the figures corresponding to the various antennas). When observing the radiation patterns, it will be noticed that some of the patterns exhibit narrow lobes near $\theta = 90^\circ$, especially on the right side of the patterns. These narrow lobes are due to diffractions by the edge of the ground plane pattern range and are not a characteristic of the antenna being measured. The true pattern shape can be approximated by taking the average magnitude of the lobes.

For the square in Fig. B-3(a) only the (01) mode is excited, while in Figs. B-3(b) and B-6(c) both (01) and (10) modes are excited. In fact, for the latter, the two modes are equally excited due to symmetry.

For the rectangle in Figs. B-6(d) and B-9(e₂), the mode (01) is excited, and in Fig. B-9(e₁) the mode (10) is excited, resulting in a pattern similar to those of the former except for a 90° rotation. The rectangle is next fed along its shorter side with an excitation of the mode (01) as shown in Figs. B-12(f) - (g₁) and the mode (10) in Fig. B-15(g₂). Again the pattern is similar to those of the former except for a 90° rotation.

Figure B-15(h₁) shows the pattern of a circular microstrip antenna excited in the lowest (11) mode. For this case the patterns are similar to those of the square in Fig. B-3(a) as expected. Both the circle and the semicircle in Fig. B-18 are excited in the (21) mode but have different patterns. This can easily be seen from the magnetic current distribution in each case. The semicircles in Figs. B-21 and B-24(k₂) are excited in the (01), (11) and (21) modes, respectively. As a result the patterns in

Fig. B-21(k_1) are similar to that in Fig. B-15(h_1), and the patterns in Fig. B-21(k_2) are similar to those in Fig. B-18 except for the orientation and cross-polarization components.

Figures B-24(e) through B-32 are patterns and impedance characteristics of an equilateral triangle. The modal structure for this antenna is very complex, and its theoretical evaluation is shown in Part A. In particular, the interesting feature of the presence of a cusp in the impedance plot as seen in Fig. B-28 is explained in Part A.

PART C.

IMPEDANCE VARIATION WITH THE FEED LOCATION

In the microstrip antenna, a given mode can be excited in many different ways. If the feed is moved along a certain coordinate where there is a field variation, such as the x-axis of a rectangle at the (1,0) mode or the circumference of a circular disk at the (1,1) mode, the input impedance varies over a wide range, thus providing a very simple means for impedance-matching. The variation of feed location may result in a small shift in resonant frequency due to the change in coupling between the feeder and the antenna, but the radiation pattern remains the same. The shift in frequency can always be compensated for by trimming the dimensions slightly.

To demonstrate the predicted variation of input impedance stated above, a rectangle of 11.43 cm \times 7.62 cm excited with the (1,0) mode, as shown in Fig. C-1, is considered.

When fed along the y axis it was found that the input impedance was independent of the feed location. For this reason the radiation pattern should also be independent of feed location, except for possibly small changes due to element to feedline coupling, which is discussed later.

When fed along the x axis, the feedpoint was found to have a large effect on the input impedance. The table in Fig. C-1 shows the dependence on d, the offset distance of the feed from the center, of the resonant input impedance and the resonant frequency, and the table also indicates the figure where the impedance plot for that feedpoint can be found.

As seen from Figs. C-2 through C-8, the resonant input impedance can be made to take on any value between nearly zero and a very high value by properly placing the feedpoint on the x axis.

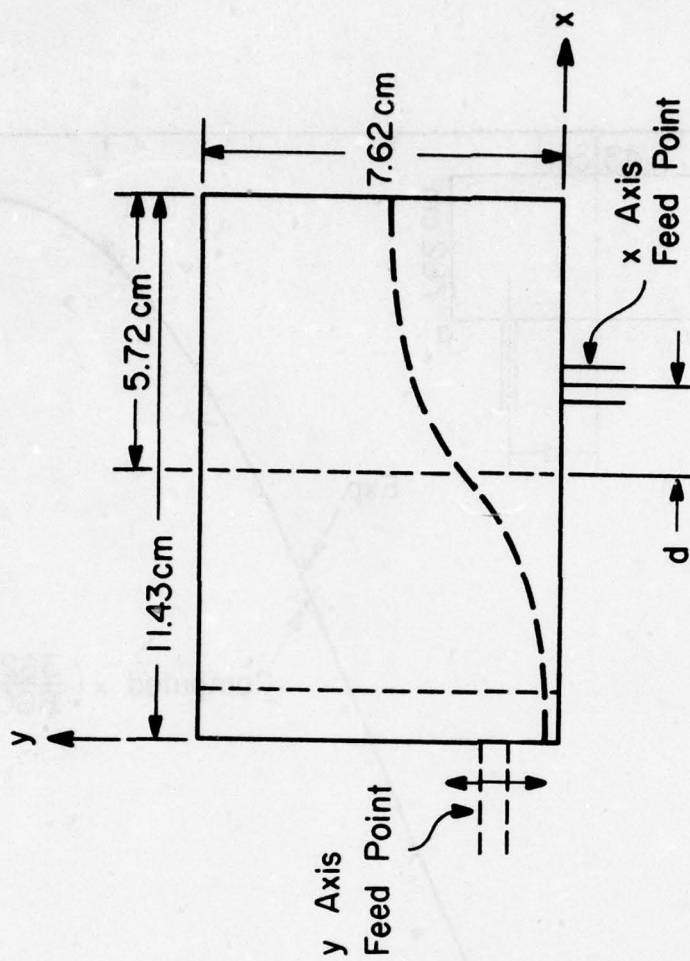


Figure C-1a. Input impedance test configuration for the rectangular element, near (1,0) mode resonance.

d(cm)	Zr(Ω)	Fig.#	f(MHz)
0.71	11	C-2	809.0
1.43	52.5	C-3	807.6
2.14	105	C-4	807.4
2.86	155	C-5	807.2
3.57	260	C-6	807.2
4.29	275	C-7	807.2
5.00	350	C-8	807.2

Figure C-1b. Table of results for the x-axis fed input impedance.

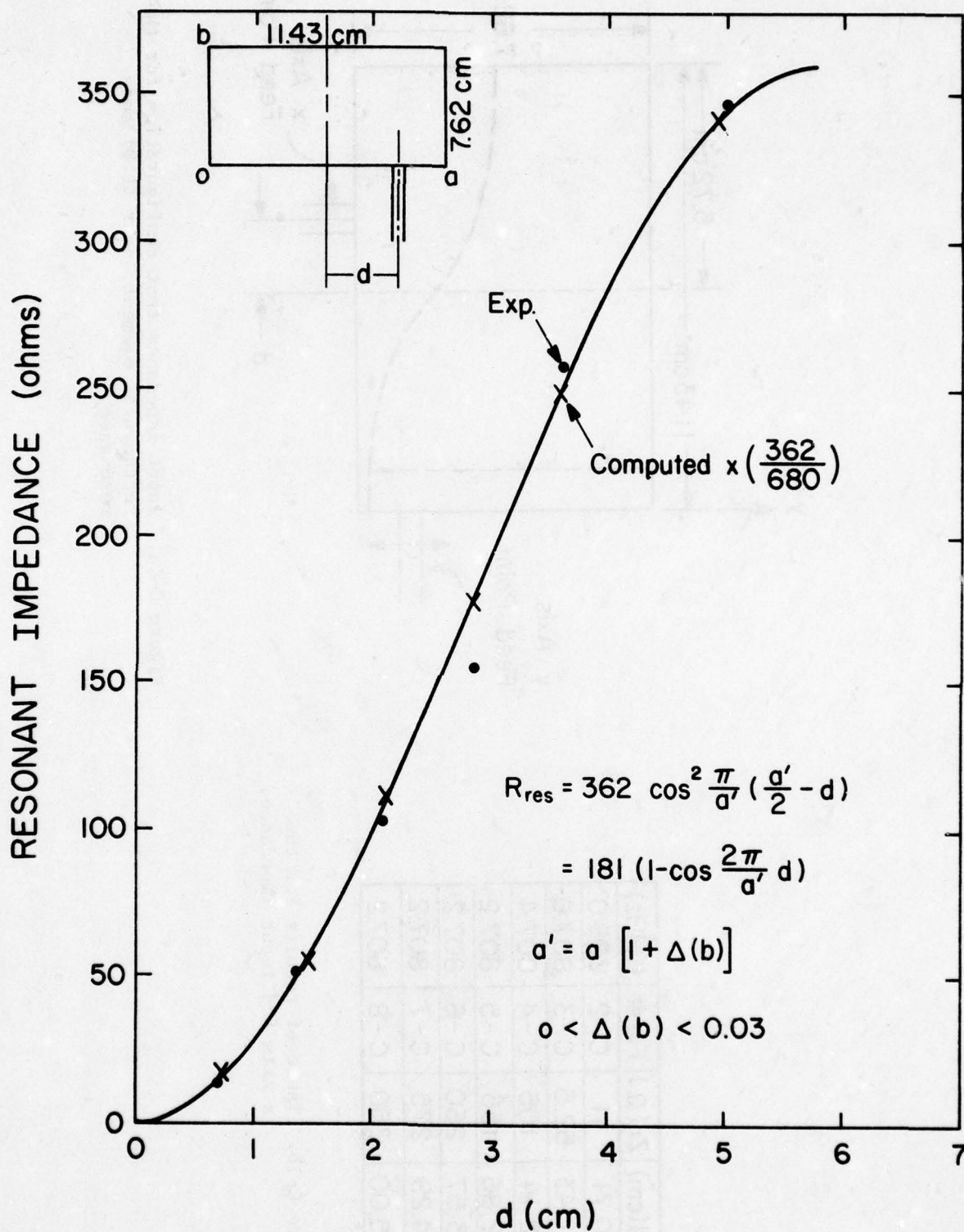


Figure C-1c. Variation of resonant impedance against the feed location.

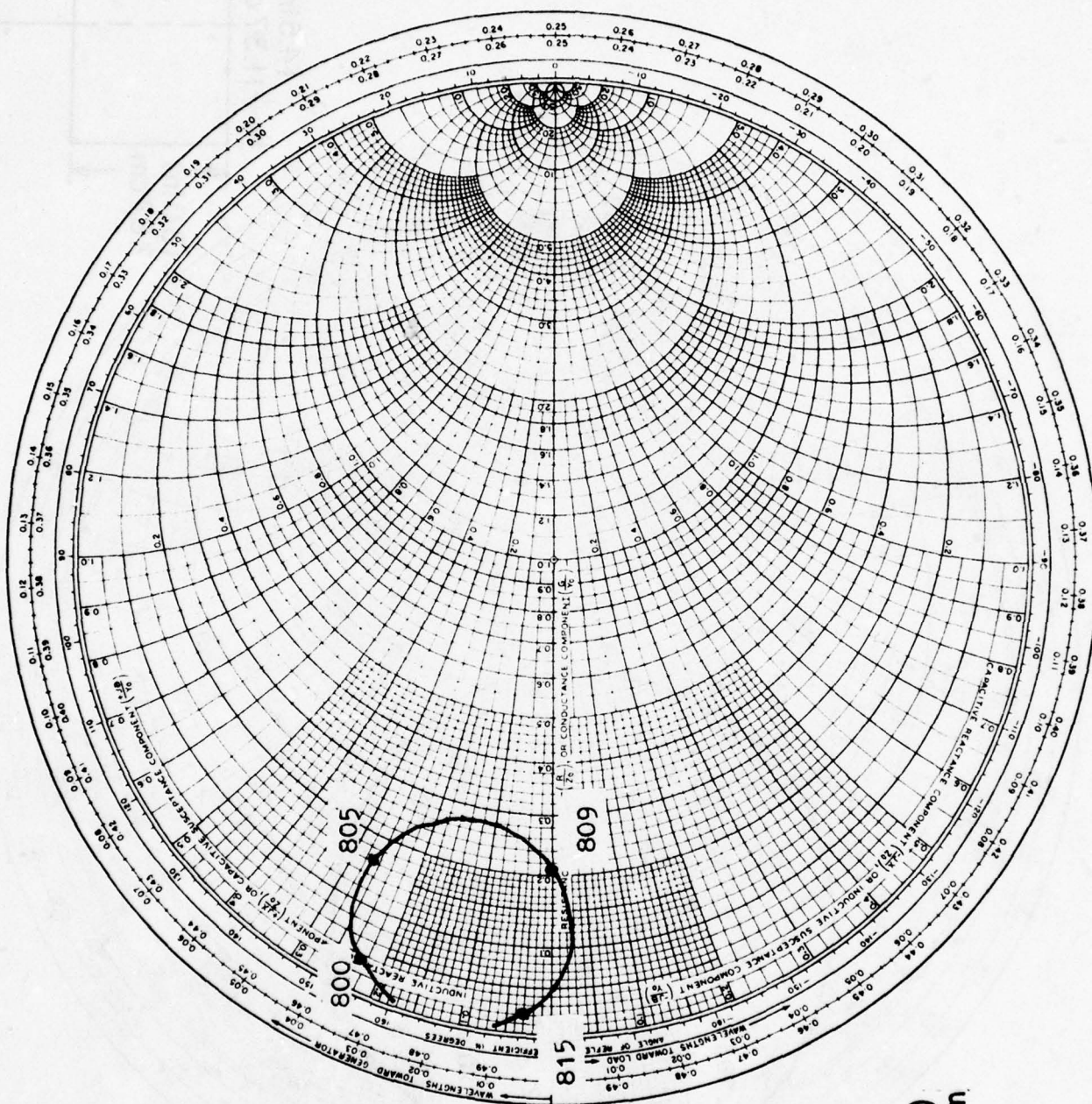
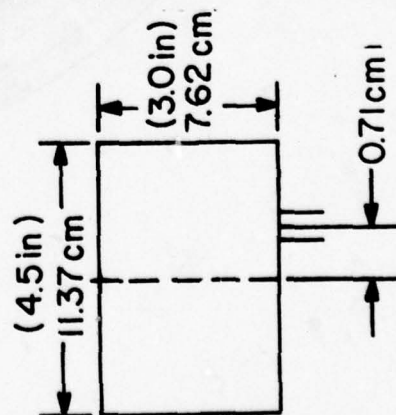


Figure C-2. Impedance plot for x-axis feed with $d = 0.71$ cm.



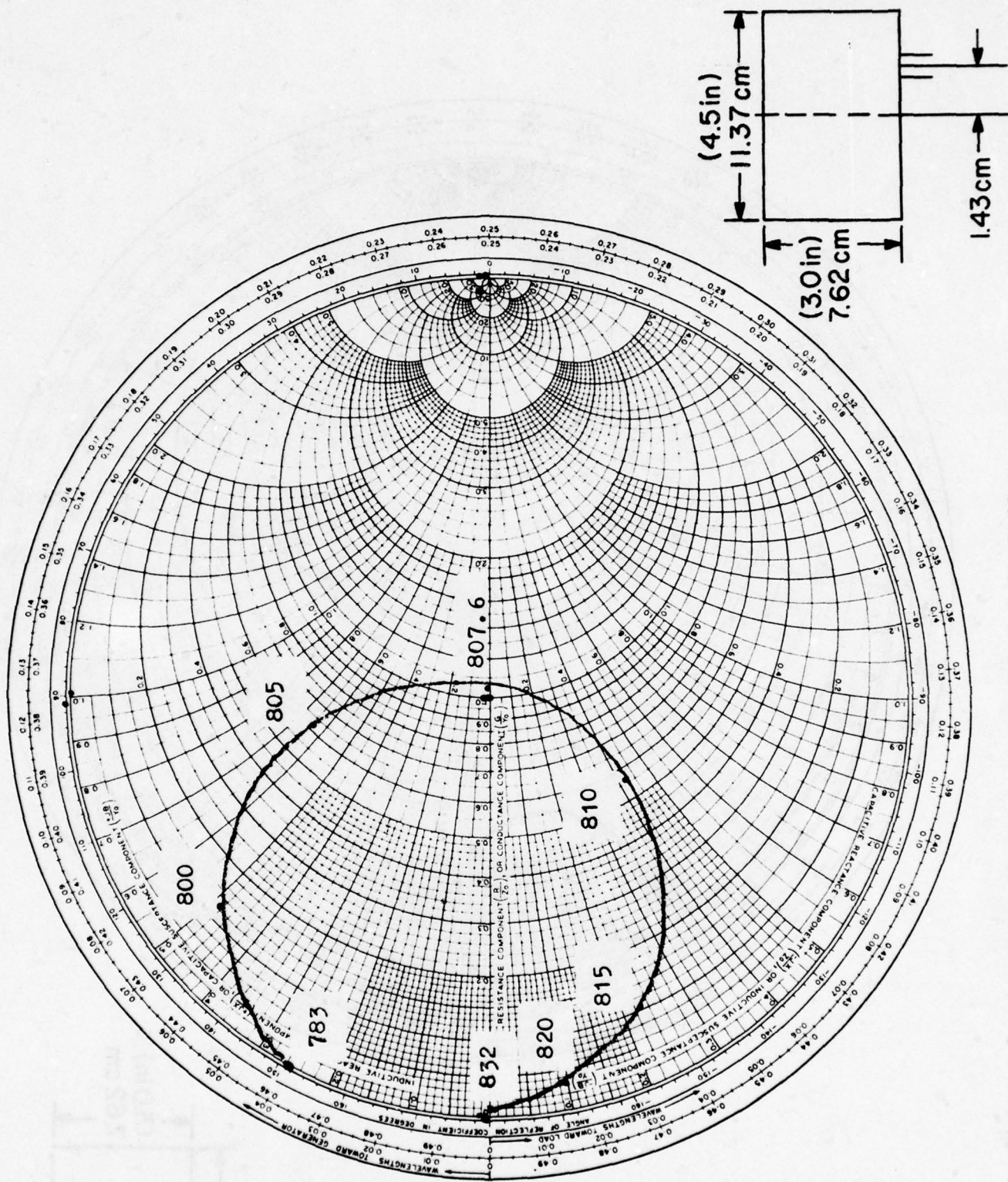


Figure C-3. Impedance plot for x-axis feed with $d = 1.43$ cm.

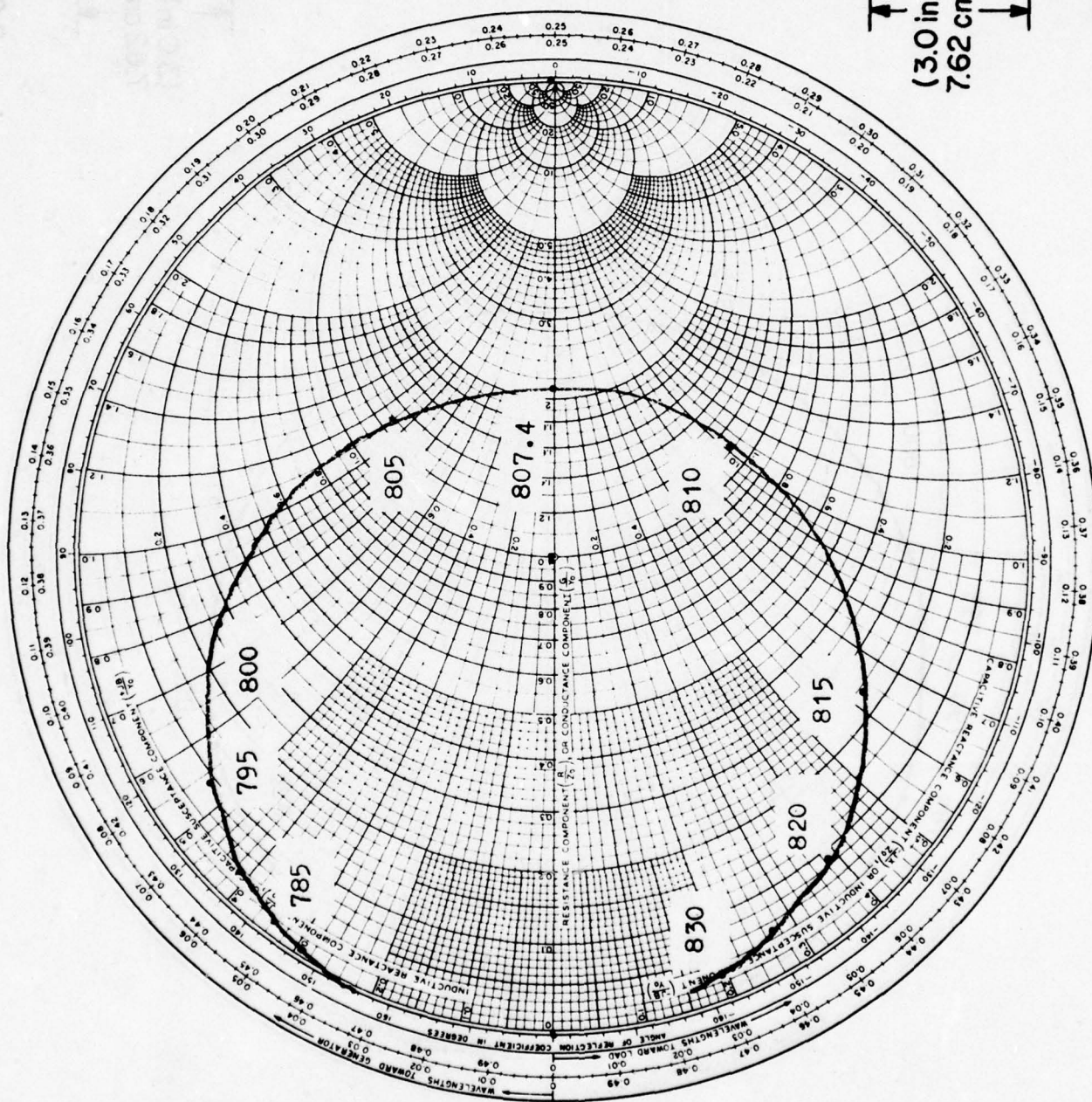


Figure C-4. Impedance plot for x-axis feed with $d = 2.14$ cm.

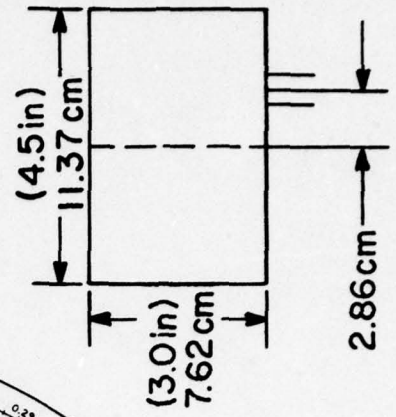
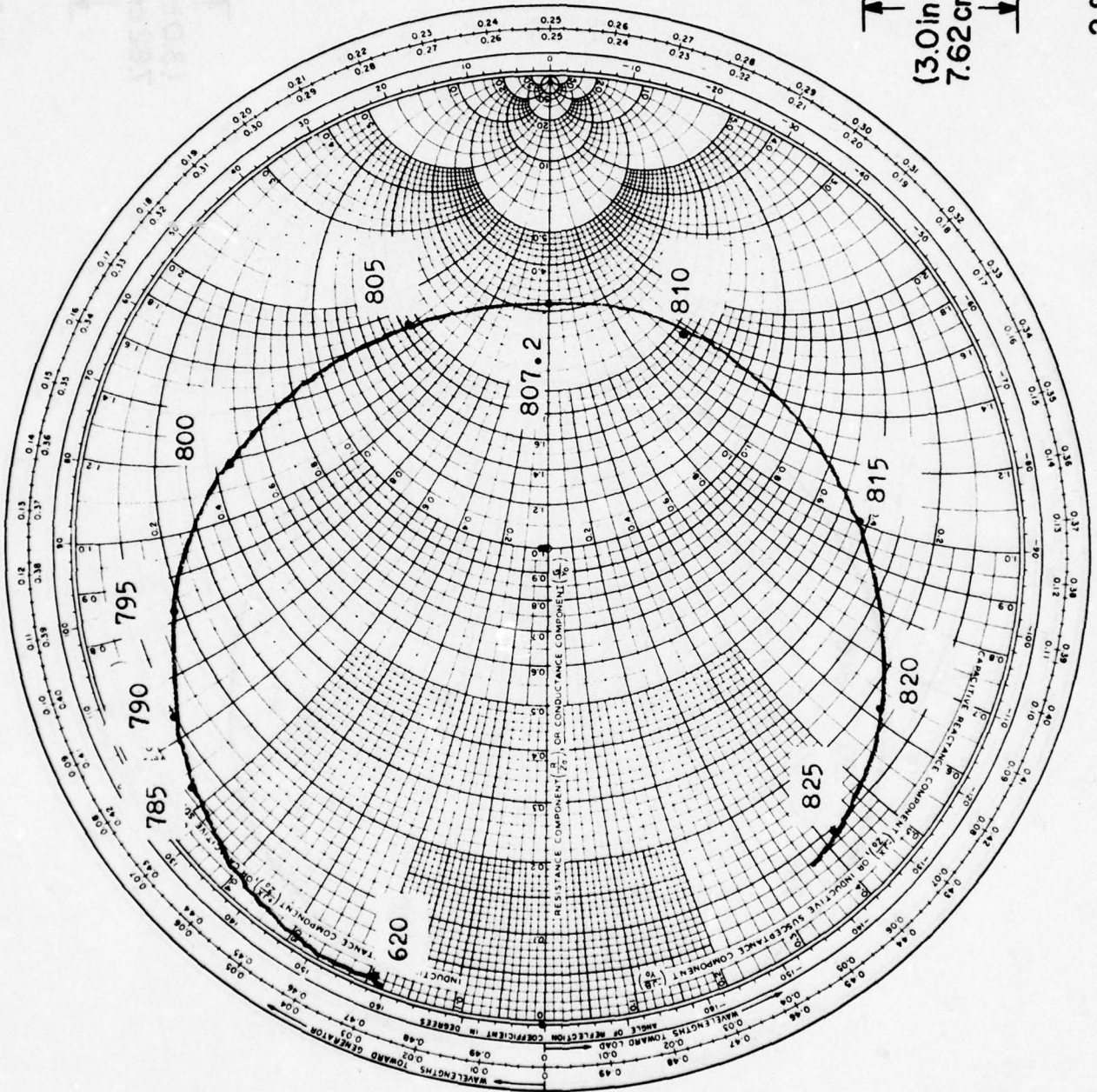


Figure C-5. Impedance plot for x-axis feed with $d = 2.86$ cm.

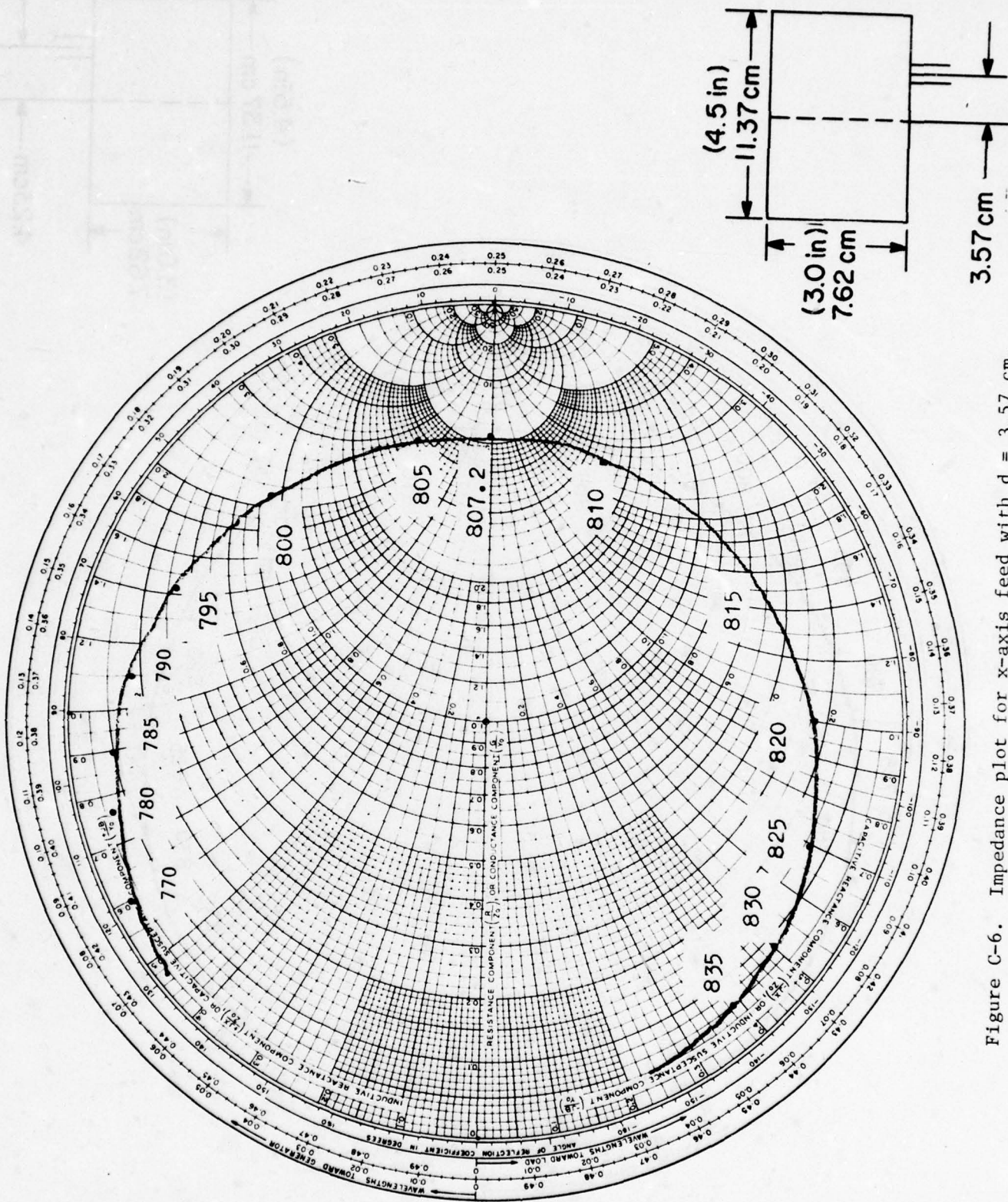


Figure C-6. Impedance plot for x-axis feed with $d = 3.57 \text{ cm}$.

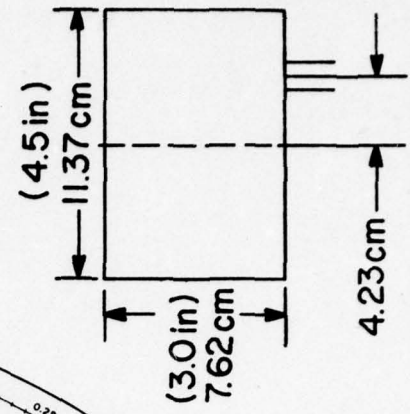
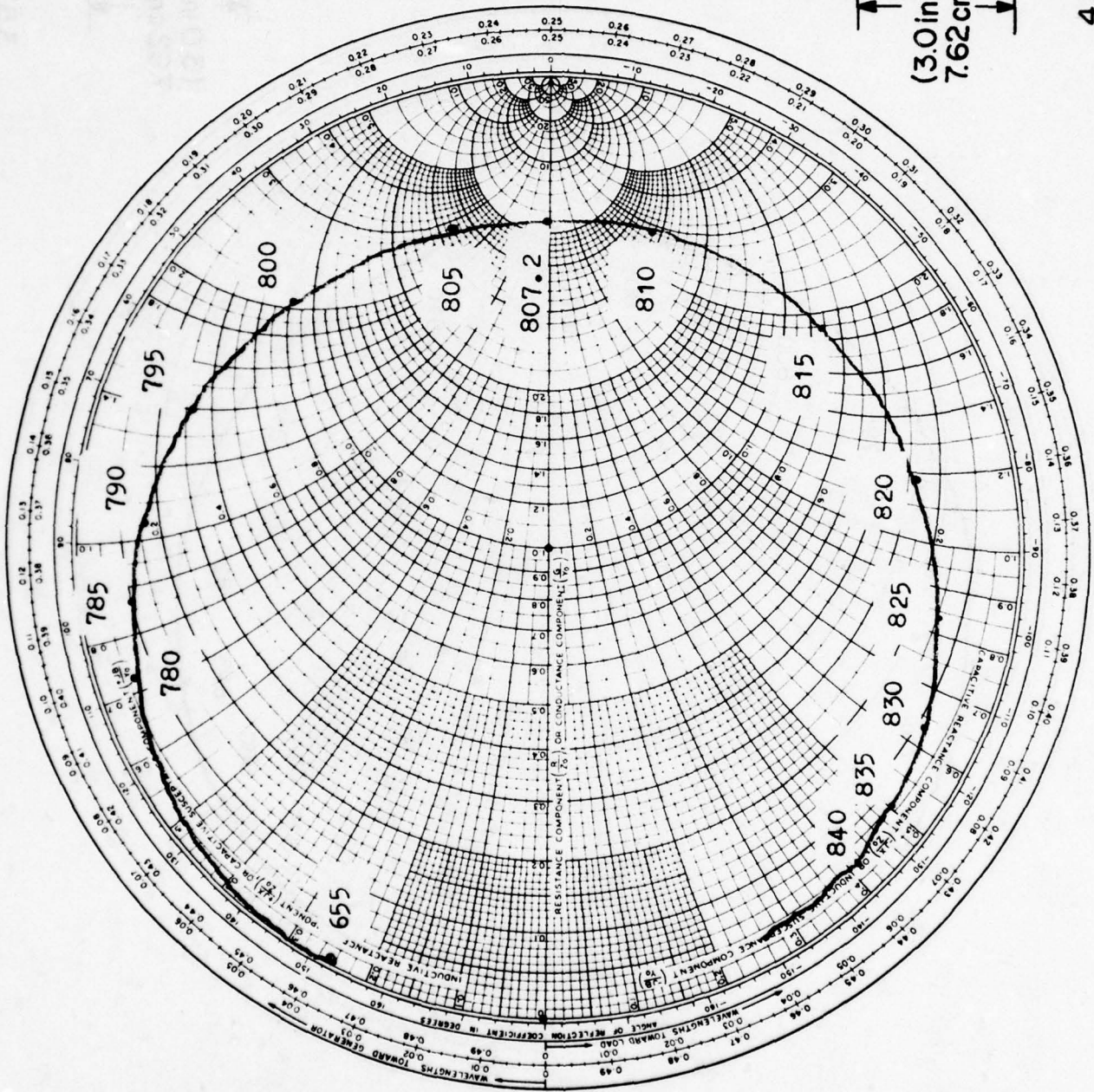


Figure C-7. Impedance plot for x-axis feed with $d = 4.29$ cm.

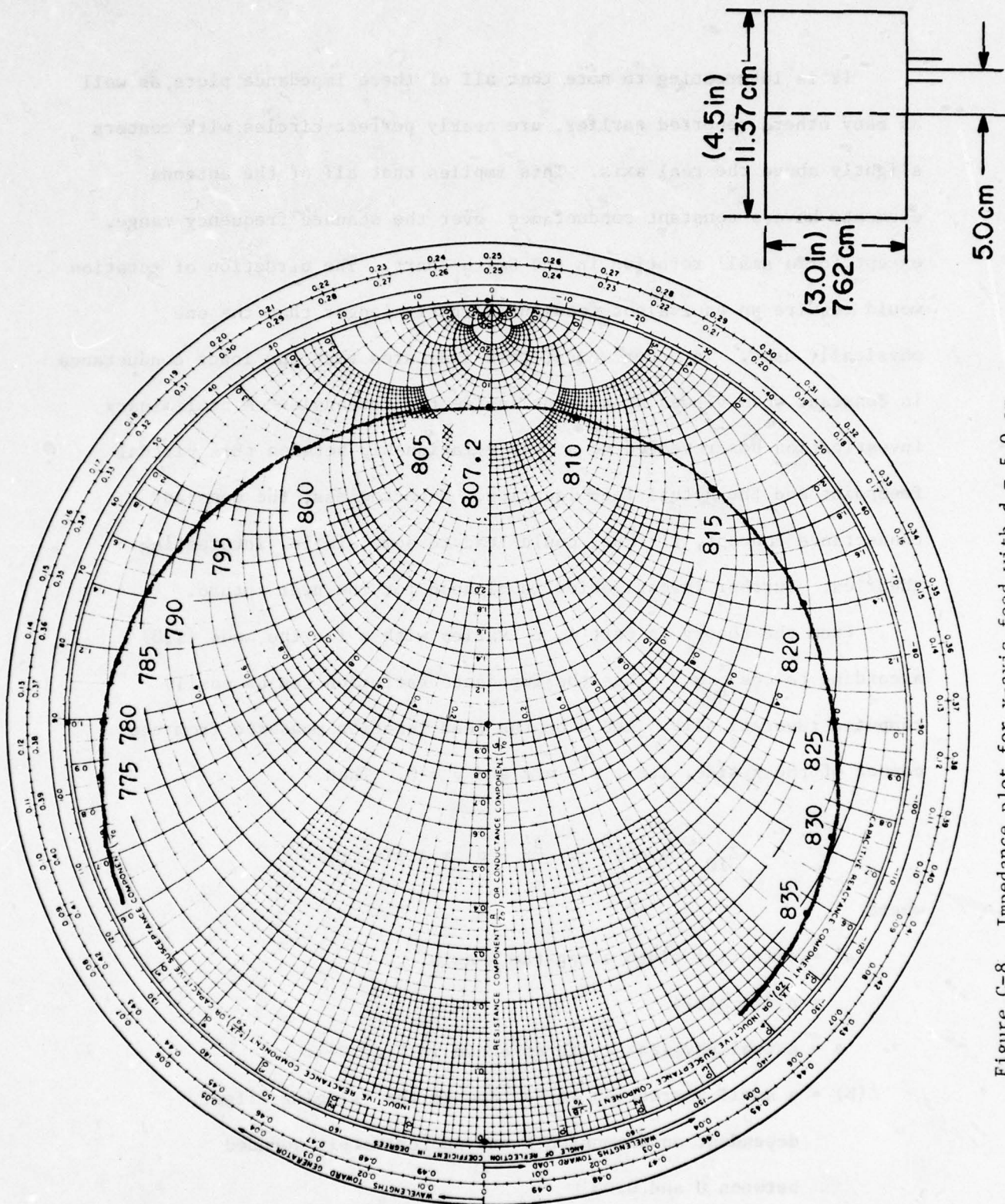


Figure C-8. Impedance plot for x-axis feed with $d = 5.0$ cm.

It is interesting to note that all of these impedance plots, as well as many others reported earlier, are nearly perfect circles with centers slightly above the real axis. This implies that all of the antenna elements have a constant conductance over the scanned frequency range, except for a small rotation in the Smith chart. The direction of rotation would require an equivalent feedline slightly longer than the one physically used. In other words, this indicates that the input conductance is constant when viewed at a point inside the rectangle. A preliminary investigation has revealed no simple relationship between this virtual feedpoint and the actual feed location. Nevertheless, the constant conductance concept, if true, could lead to some simple, interesting theories. Further investigation is planned for the near future.

From the theory in Part A, E_z varies with x for the mode (1,0) according to $\cos \frac{\pi}{a} x$. Thus the impedance variation can be easily computed theoretically. Let d be the feed location measured from the center of the x side, i.e., $x = a/2$ and $y = 0$. Then

$$Z_{10} = A \cos^2 \frac{\pi}{a'} \frac{a'}{2} - d = A \sin^2 \frac{\pi}{a'} d$$

where

a' = effective width along the x -axis

$$= a[1 + \Delta(b)]$$

a = actual physical width as shown in Fig. C-1c

$\Delta(b)$ = a small correction to " a " due to the fringing effect,

dependent on dimension b and approximately bounded

between 0 and 0.03

A = maximum input impedance which occurs when feed is at the corner ($x = a$, $y = 0$), depending on b .

For the dimensions under consideration, the measured value of A is $A \approx 362 \Omega$; however, according to theory, $A = 680 \Omega$. They differ by a factor of 1.875. If this factor is used to correct for the computed values, the agreement between the two sets of data becomes excellent, as seen in Fig. C-1c. This discrepancy could be caused by an error in computer programming, by experimental error in constructing the feed strip line, or by the inadequacy of the present theory to predict the input impedance with a feed along the edge where E_z is not constant. The latter has been noted in Part A. Further investigation is needed.

The radiation patterns for x-axis feedpoints were also measured to see if any major changes occurred when the feedpoint was moved. The plots in Figs. C-9 and C-10 indicate that the radiation patterns are relatively insensitive to changes in the feedpoint. At resonance, the patterns were indistinguishable. However, off resonance, the patterns showed a slight increase in the cross-polarized fields.

Similar results are expected for other geometries. This property can be used to match the antenna impedance over a wide range with little effect on the radiation pattern.

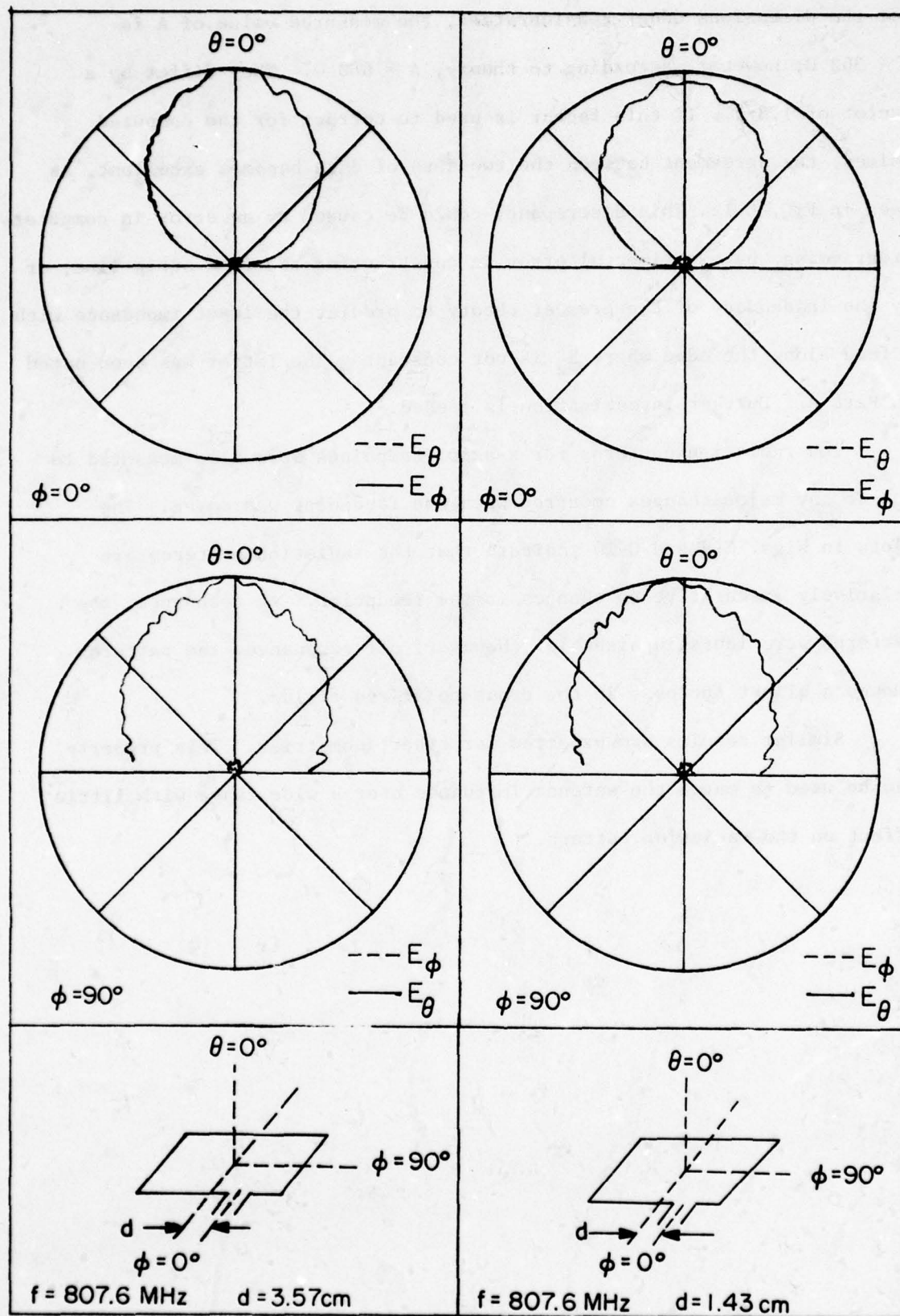


Figure C-9. Radiation patterns of the rectangular element at (1,0) mode resonance for different feedpoints.

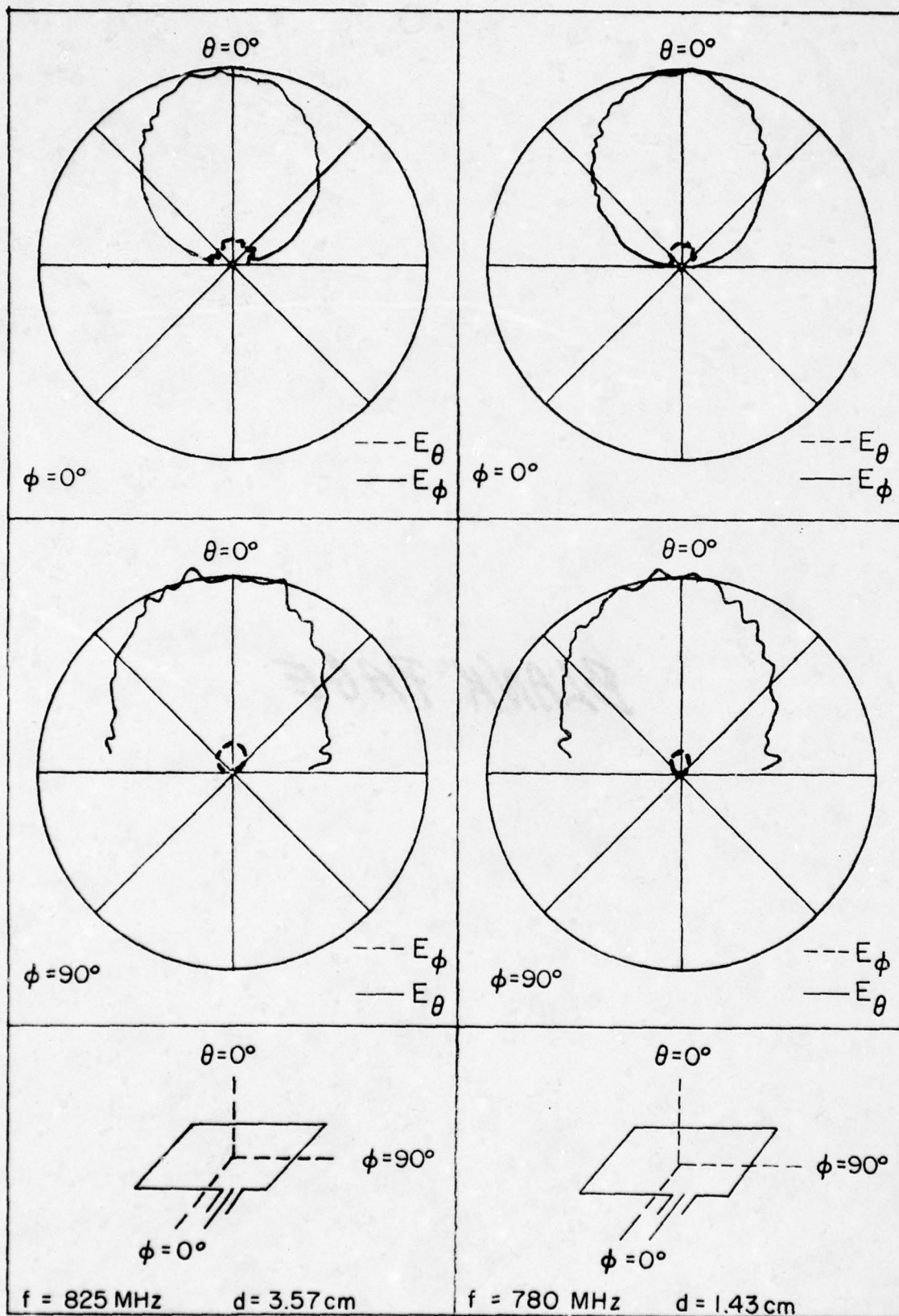


Figure C-10. Radiation patterns of the rectangular element near (1,0) mode resonance for different feedpoints.

PART D.

EVALUATION OF COUPLING EFFECTS ON IMPEDANCE

The understanding of coupling effects between microstrip antennas and between an antenna and its feeder is of great importance in the design of arrays. The complexity of this problem would undoubtedly require a major analytic effort for solution. In view of the success of our theory based on a cavity model in predicting many antenna performances, one could suppose that the field would generally be confined to the vicinity of the microstrip antenna structure, so that the interaction among elements might not be as strong as in other types of antennas, such as dipoles. Two simple experiments were designed to test the validity of the conjecture just stated. The first experiment is for the study of coupling between a rectangular microstrip antenna and its feeder, and the second for the study of interaction between two adjacent identical rectangular microstrip antennas at two typical orientations.

There is always a certain amount of fringing field which couples the antenna to its microstrip feeder as shown in Fig. D-1. This coupling causes two difficulties in our study. First, if the interaction is so strong that the field near the antenna input port "B" may no longer be TEM wave, then the antenna input impedance at port "B" can not be obtained from the measured impedance at port "A" (somewhat removed from "B") by a simple transmission line transformation. Second, the coupling, if strong, could contribute to the discrepancy between the measured and theoretical results since the present theory does not take this coupling into account.

To determine the first effect, two measurements were taken, one with a usual microstrip feeder and the other with a miniature 50 ohm coaxial cable, both shown in Fig. D-1. For the latter the cable was buried in a small channel cut through the substrate, with its outer conductor grounded.

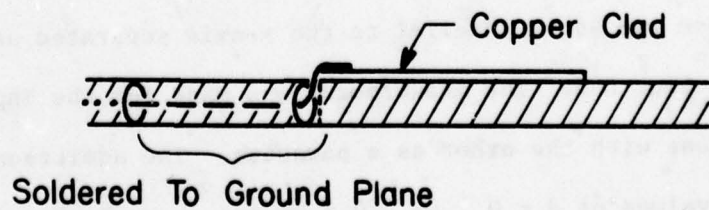
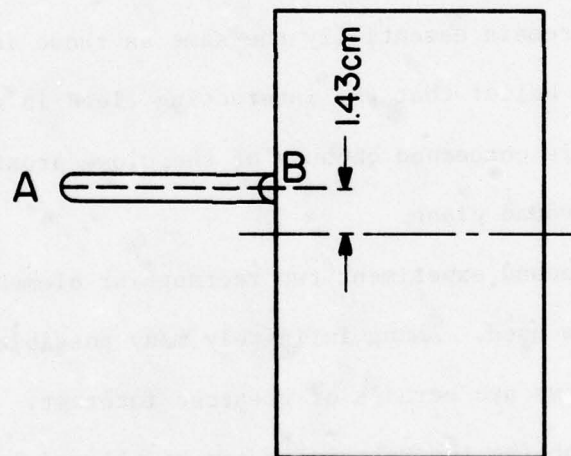
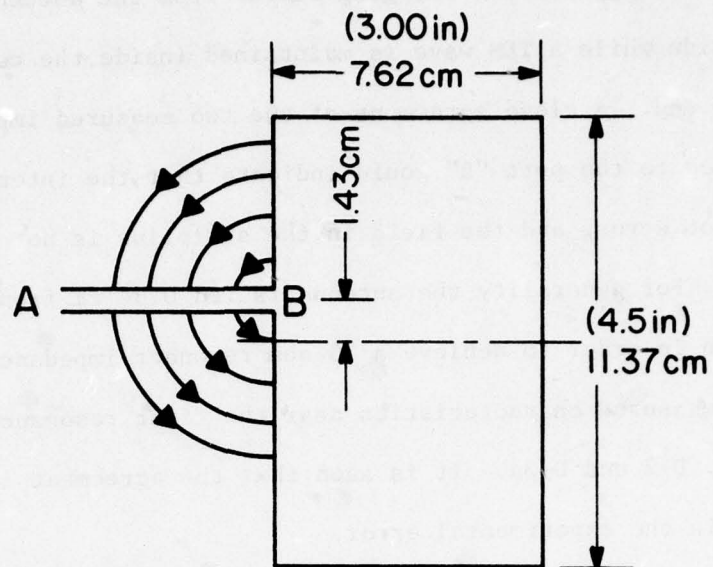


Figure D-1. General form of element to stripline coupling, and the configuration of the coaxial feed.

In so doing, similar fringing fields from the antenna are maintained outside while a TEM wave is maintained inside the cable, except near the open end. A close agreement of the two measured impedances after transformed to the port "B" would indicate that the interacting fringing field is not strong and the field in the stripline is not substantially disturbed.

For generality the antenna is fed 0.64 cm from the middle point as shown in order to achieve a 50 ohm resonant impedance for the (1,0) mode. The measured characteristics near the first resonance are shown in Figs. D-2 and D-3a. It is seen that the agreement is very close, perhaps within the experimental error.

Later, a third measurement was performed with the feeding cable beneath the ground plane. By doing so, the interacting fringing field was largely removed. The measured impedance characteristics, shown in Fig. D-3b, remain essentially the same as those in Fig. D-3a. This reinforces the belief that the interacting field is negligible so far as the impedance is concerned because of the close proximity of the antenna plate to the ground plane.

In the second experiment two rectangular elements of nearly the same dimensions were used. Among infinitely many possible relative orientations, the following two are perhaps of greatest interest. For the dominant mode (1,0) excitation the two rectangles can be aligned on the x-axis with those two edges parallel to the y-axis separated at a distance d as shown in Fig. D-4. Similarly the two rectangles can be aligned along the y-axis with those two edges parallel to the x-axis separated at a distance d as shown in Fig. D-5. The measurement was made for the input admittance of one element with the other as a parasite. The admittance loci for various values of $d = 0.1 \text{ cm} - 0.8 \text{ cm}$ are shown in Figs. D-6 through D-11

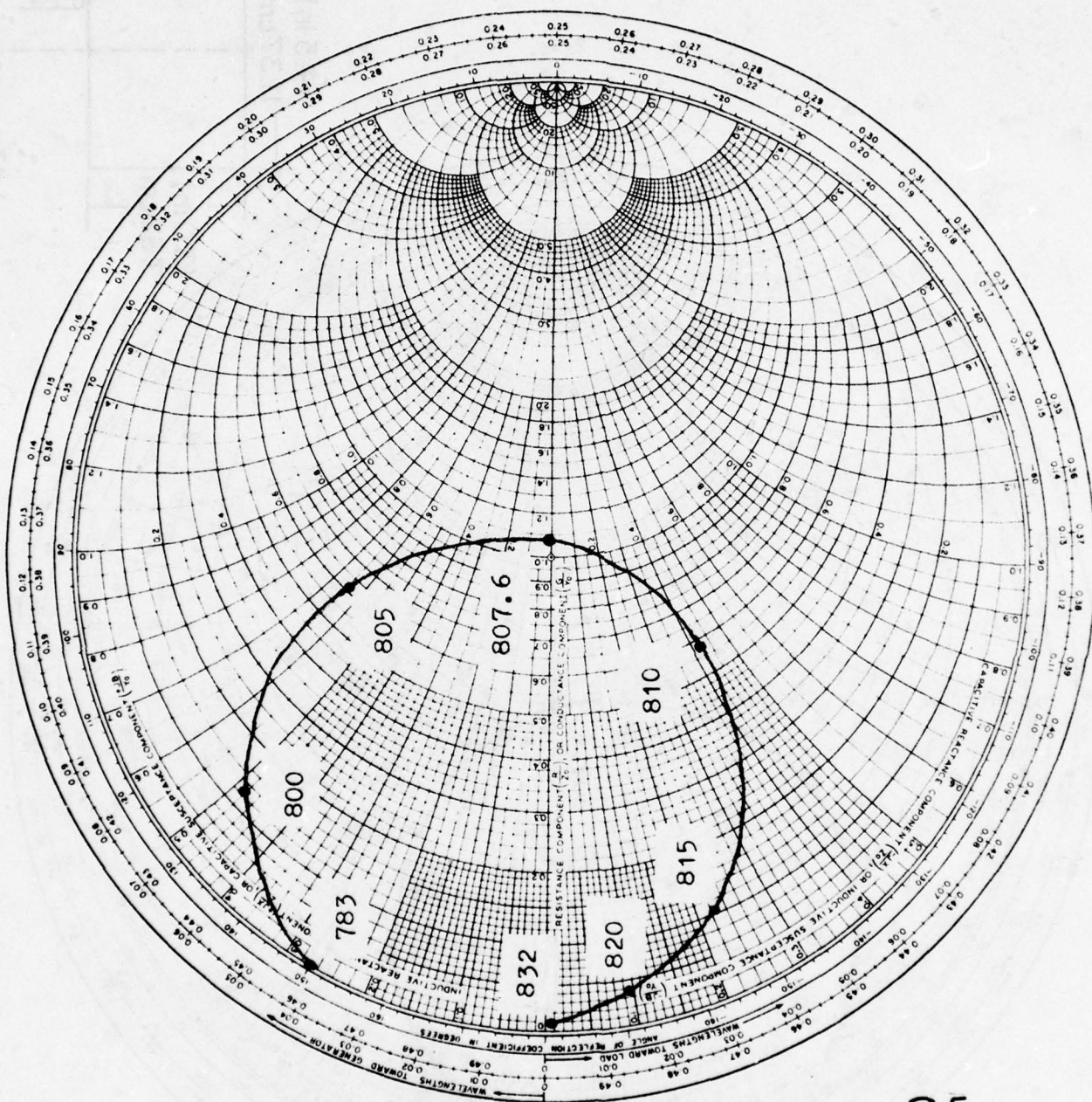
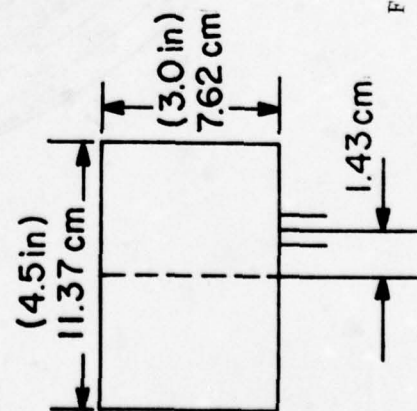


Figure D-2. Impedance plot of the rectangular element with stripline feed.



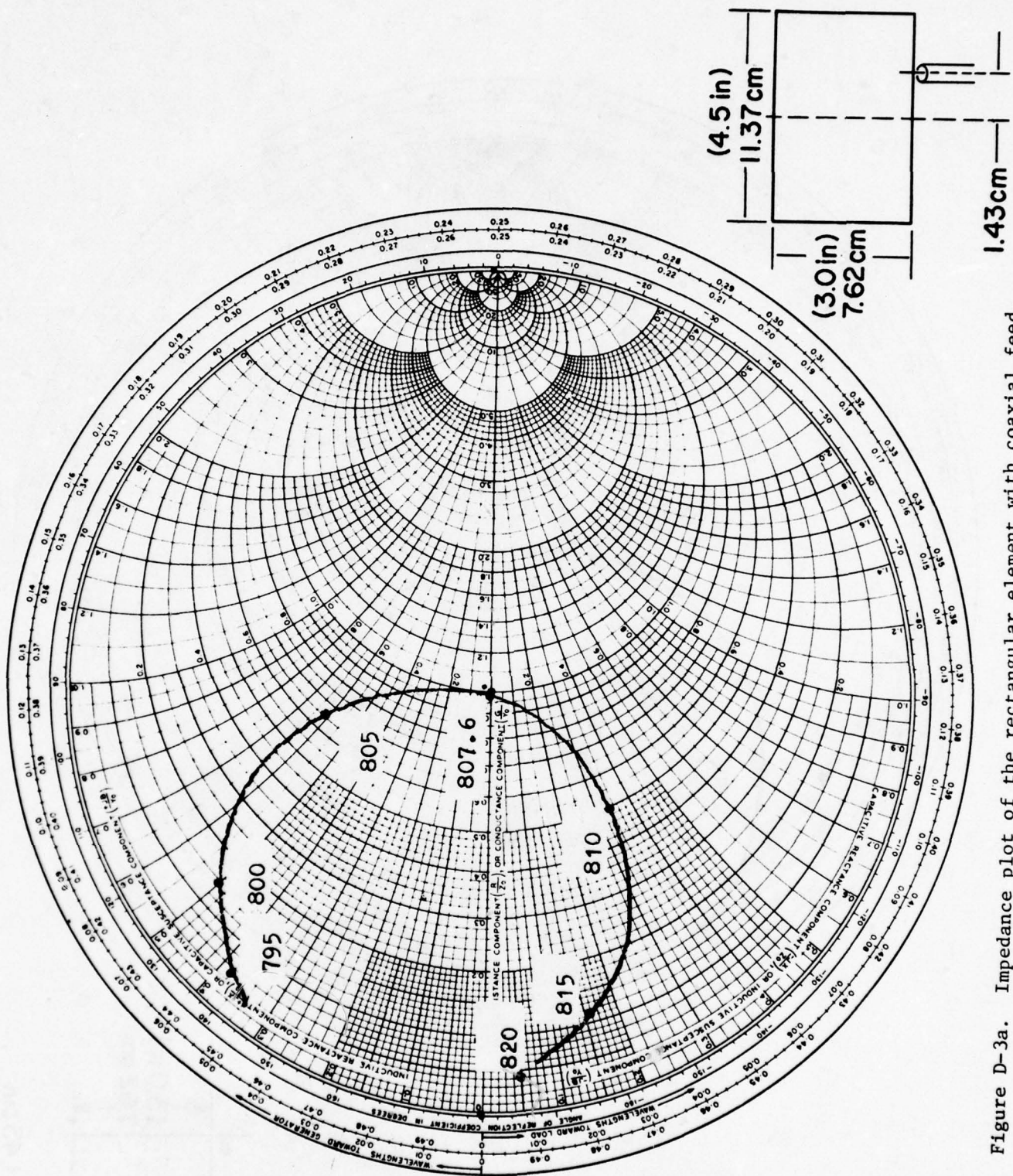


Figure D-3a. Impedance plot of the rectangular element with coaxial feed.

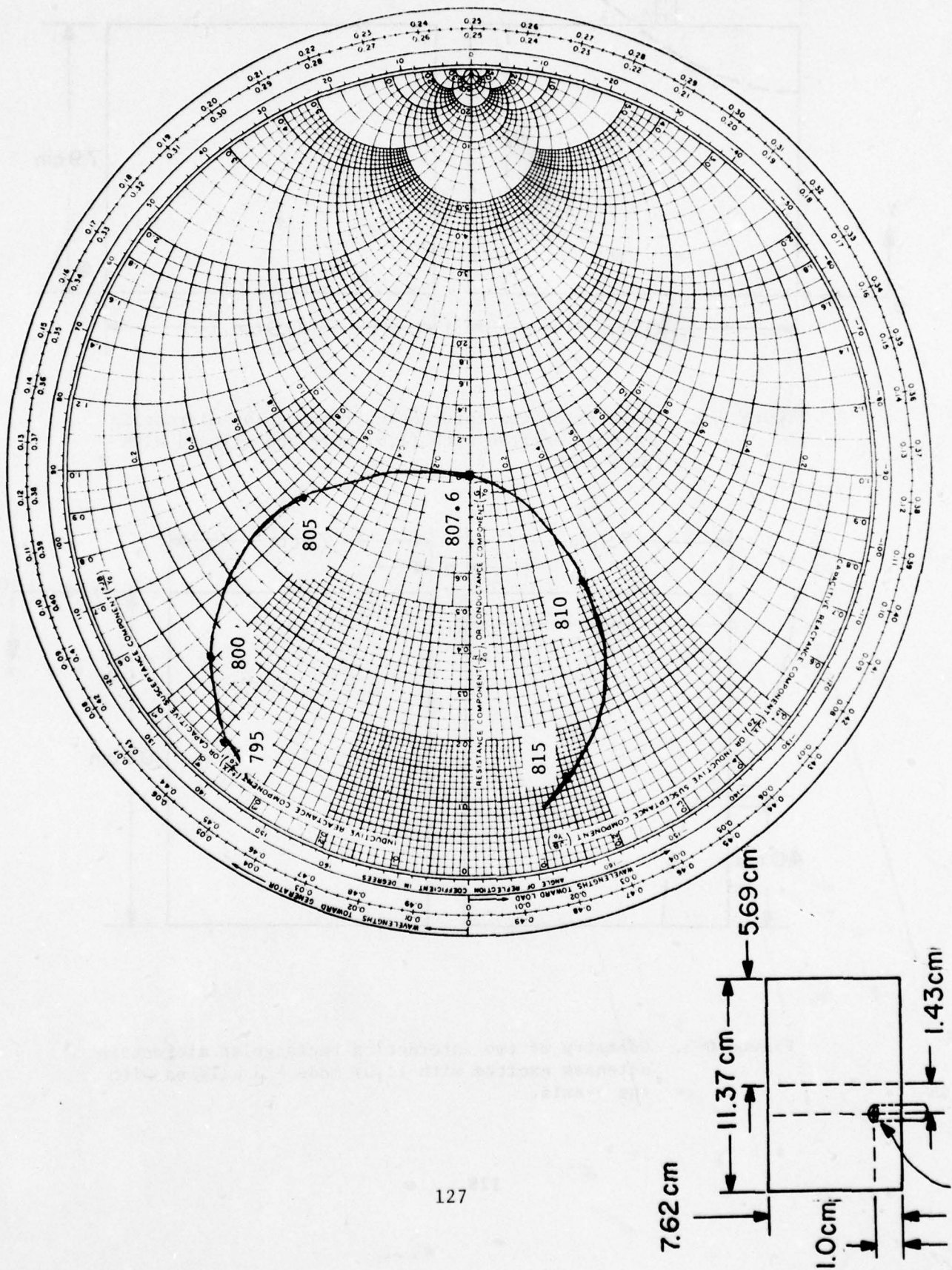


Figure D-3b. Impedance plot of the rectangular element with coaxial feed.

Back Feed

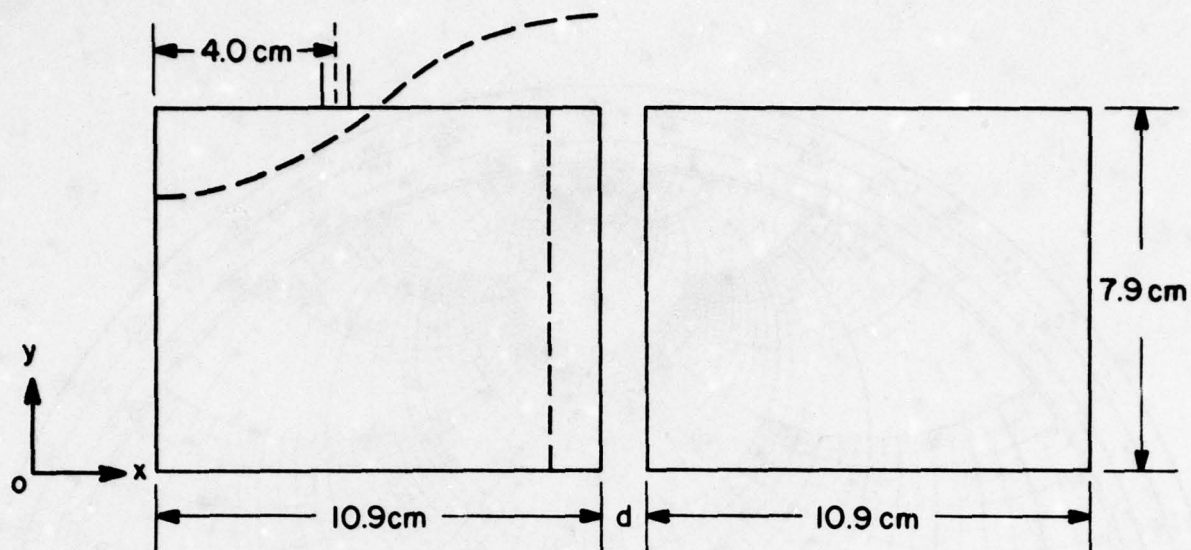


Figure D-4. Geometry of two interacting rectangular microstrip antennas excited with (1,0) mode and aligned with the x-axis.

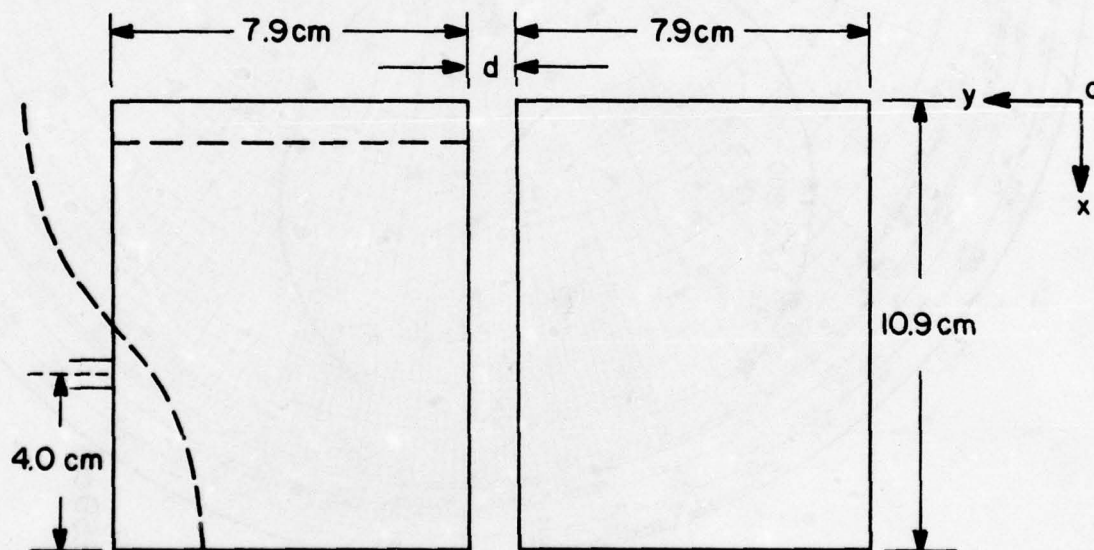
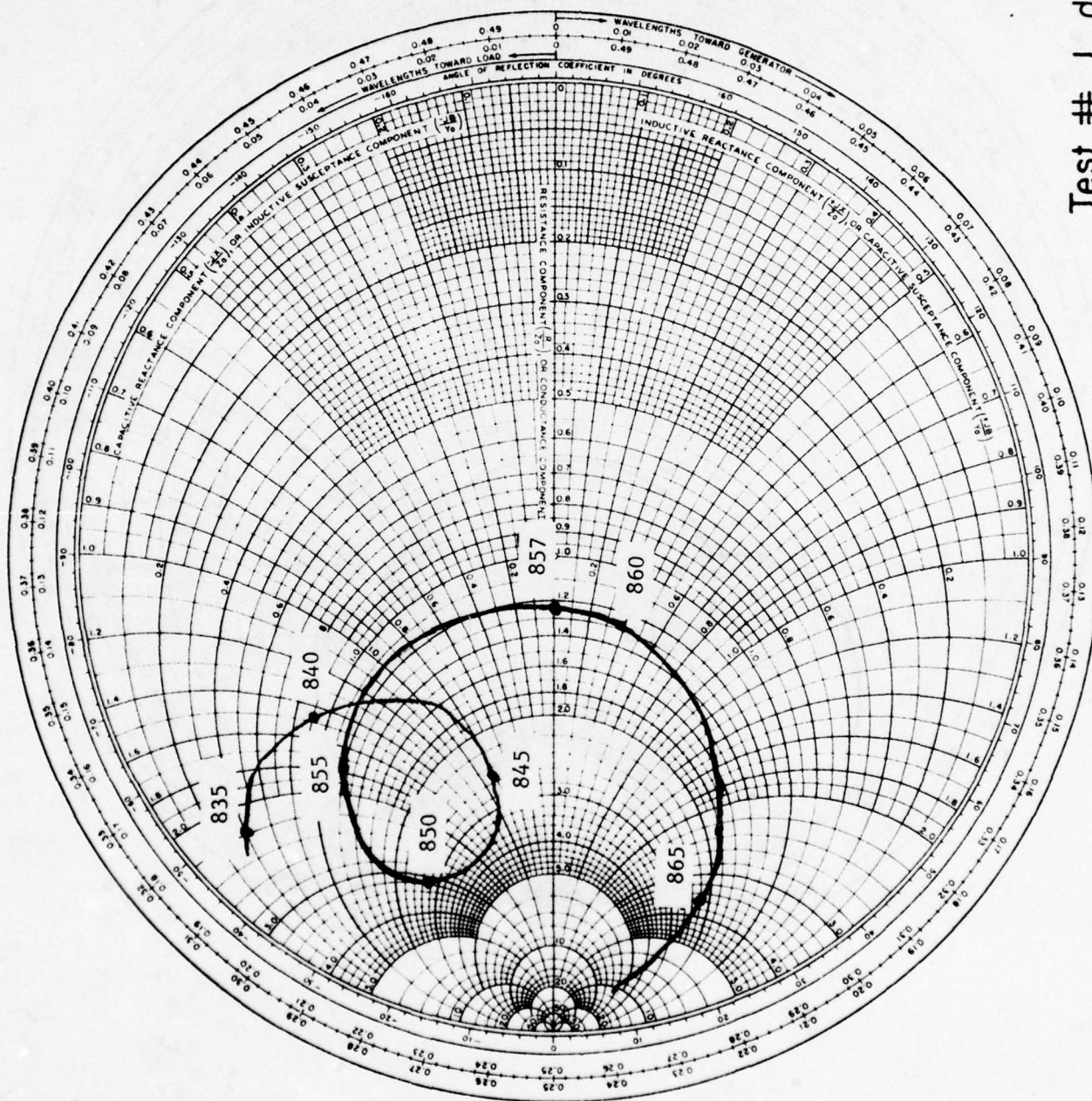


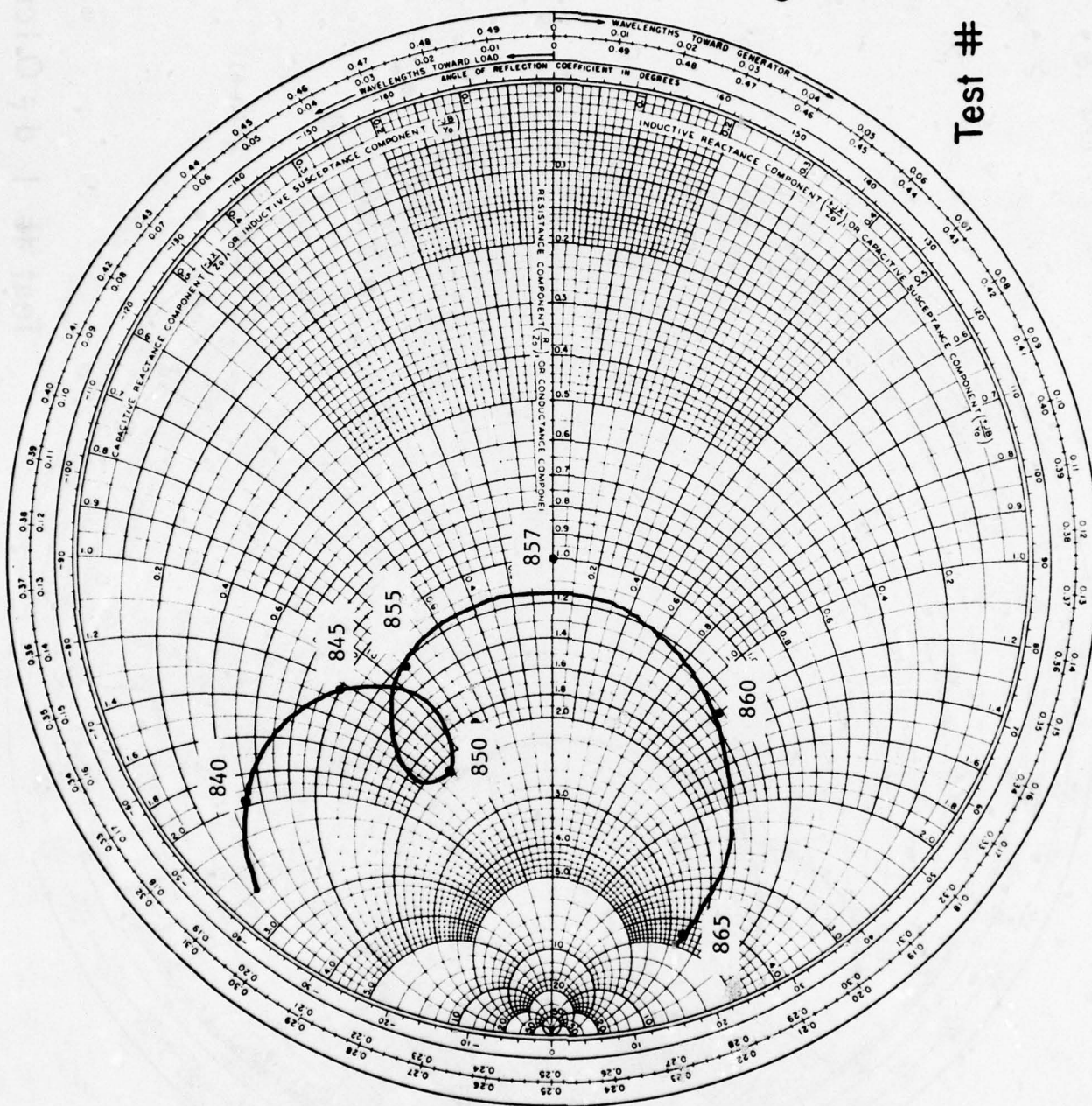
Figure D-5. Geometry of two interacting rectangular microstrip antennas excited with (1,0) mode and aligned with the y-axis.



(D-6)

Test # 1 $d = 0.1\text{cm}$

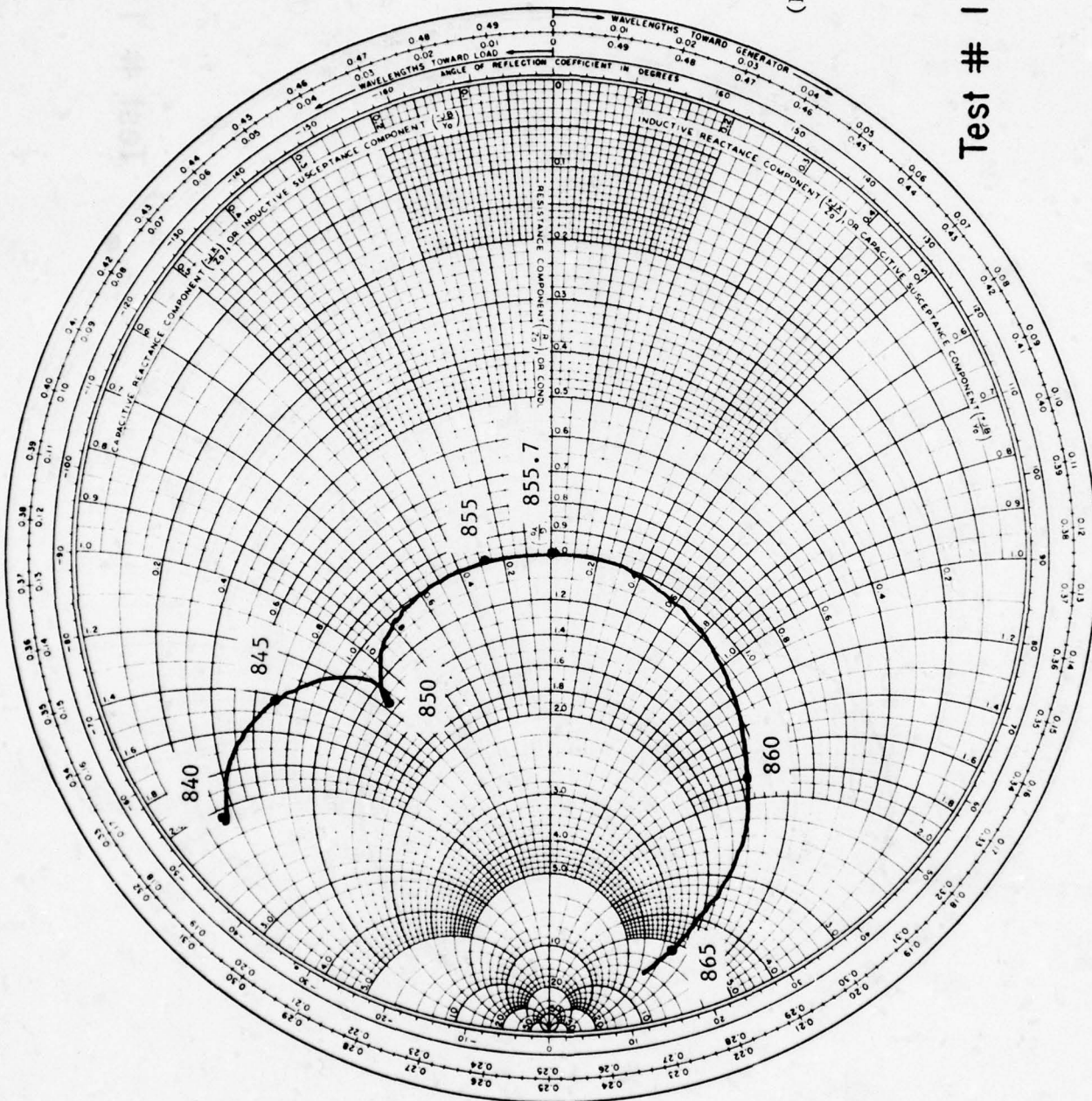
Figures D-6 to -11. Input admittance locus of a rectangular microstrip antenna in the presence of a parasitic element of the same geometry at various values of separation d along the x-axis as shown in Figure D-4.



(D-7)

Test # 1 d = 0.2cm

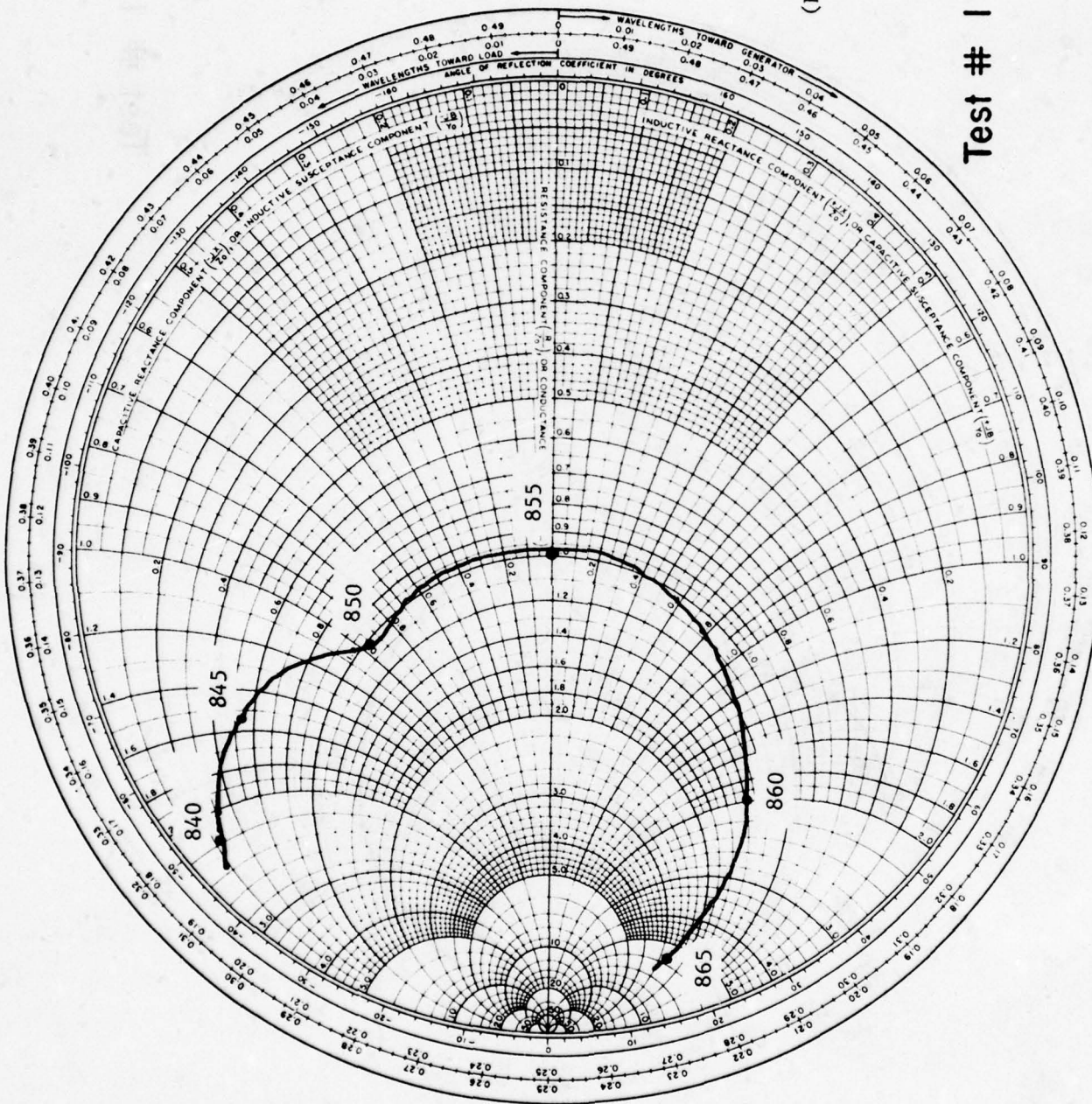
Figures D-6 to -11 (cont.).



(D-8)

Test # 1 d = 0.3cm

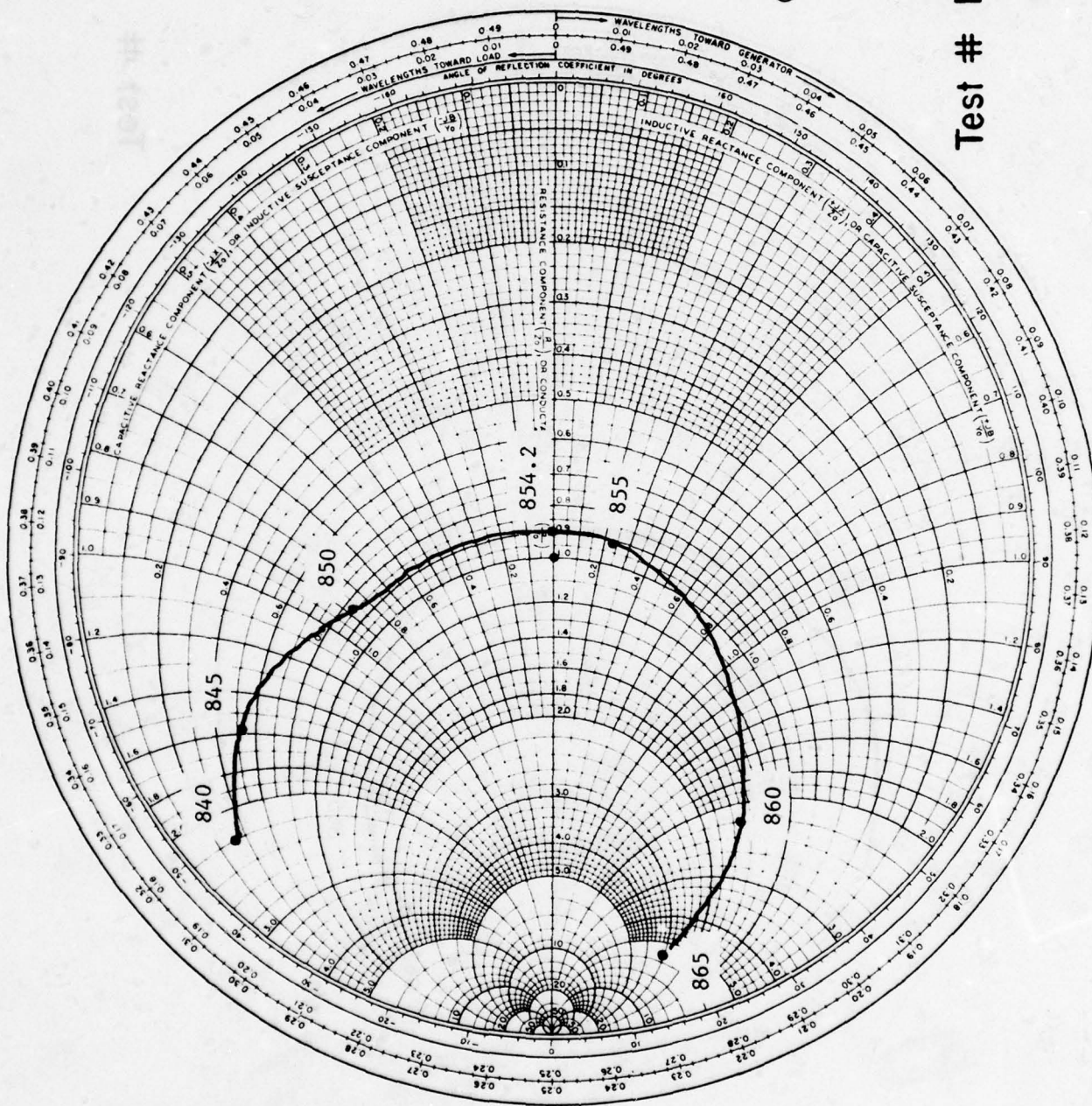
Figures D-6 to -11 (cont.).



(D-9)

Test # 1 d = 0.4cm

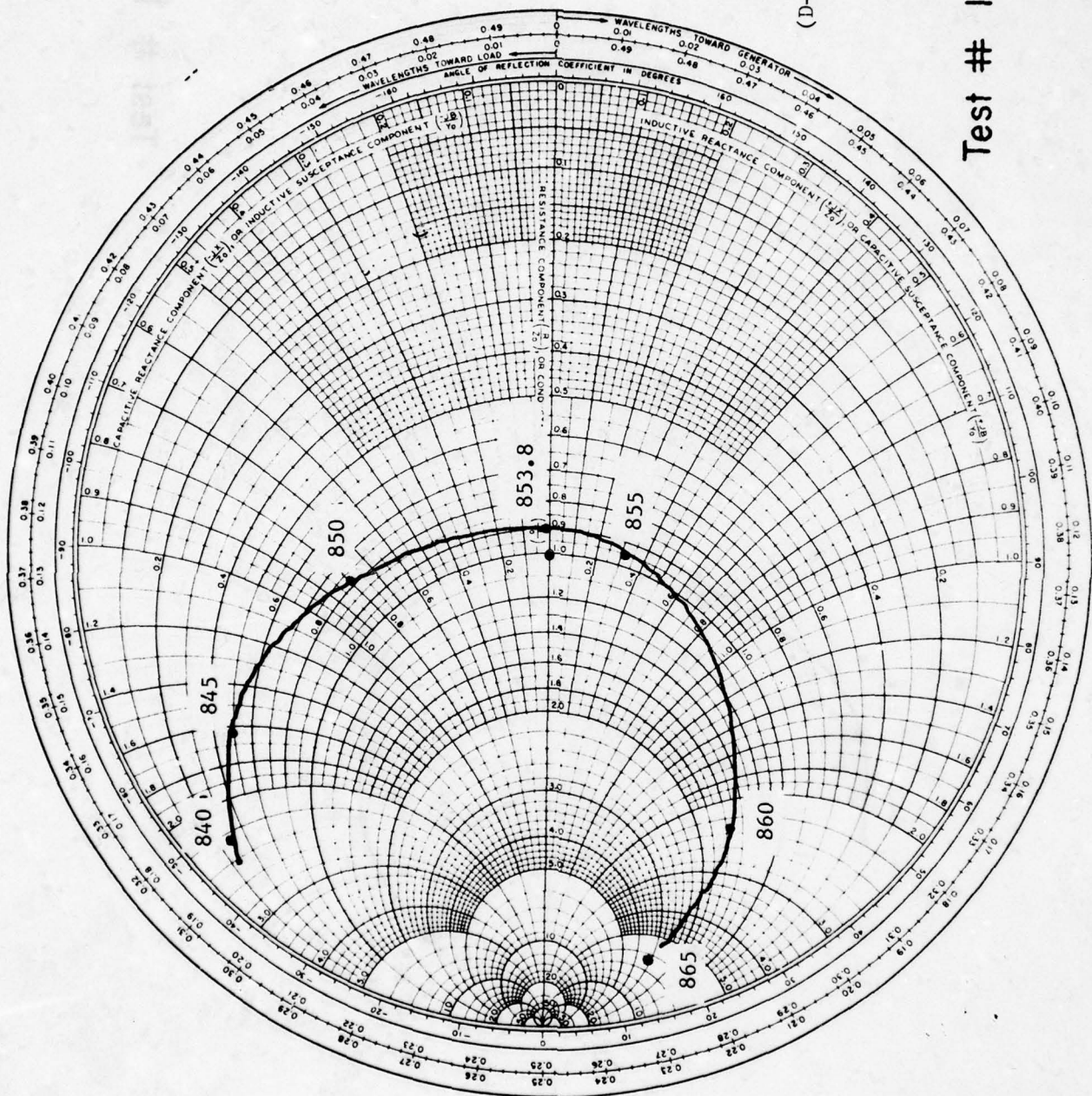
Figures D-6 to -11 (cont.).



(D-10)

Test # 1 $d = 0.6\text{cm}$

Figures D-6 to -11 (cont.).



(D-11)

Test # 1 d = 0.8cm

Figures D-6 to -11 (cont.).

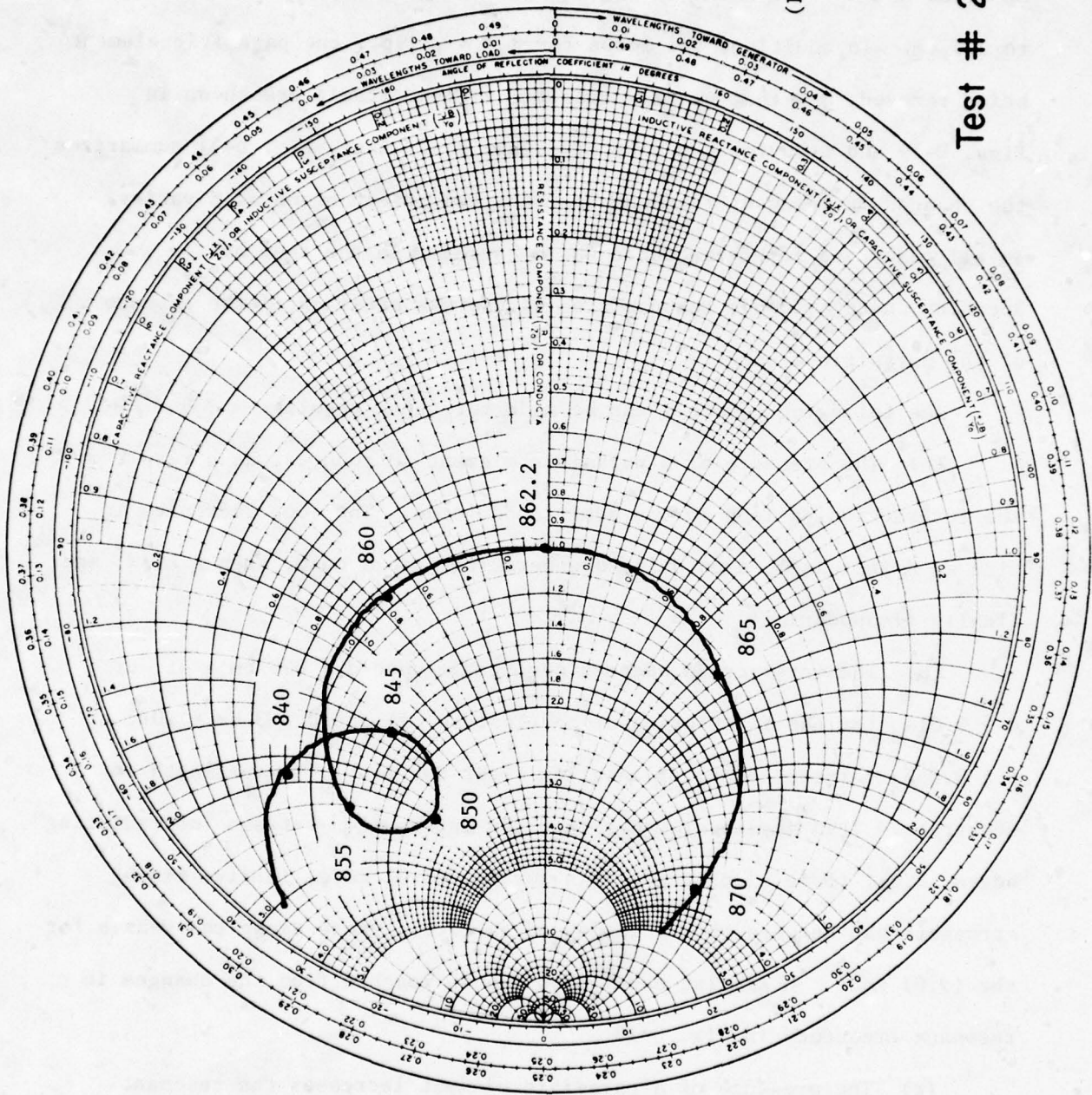
for the first orientation in Fig. D-4 (referred to as "Test No. 1"). A similar set of results for the second orientation in Fig. D-5 (referred to as "Test No. 2") are shown in Figs. D-12 through D-18, except that $d = 0.1$ cm to 3.5 cm. In addition, the locus for $d = \infty$, i.e., the parasitic element being removed, and that of the parasitic element itself are shown in Figs. D-19 and D-20 for the sake of comparison. Last, Fig. D-21 summarizes the changes in resonant frequency for the two orientations as d varies. In all cases the input impedance was measured with the feed at the location where a 50-ohm resonant resistance was obtained in the absence of the parasitic element.

The following comments can be made for these results:

(a) The presence of a parasitic element introduces, as a result of the interaction, a loop in the admittance locus. The loop decreases in size as d increases, eventually degenerating into a cusp, then a kink, and finally disappearing.

(b) The interaction becomes negligible when $d > 0.6$ cm $\approx 4t$, or $d > 0.01\lambda_d$ for the first orientation (Test No. 1) and $d > 3$ cm $\approx 20t$, or $d > 0.05\lambda_d$ for the second orientation (Test No. 2), λ_d = wavelength in substrate. This implies roughly that the interaction between "nonradiating" edges, i.e., those along the x-axis for the (1,0) mode, is five times stronger than between the radiating edges, i.e., those along the y-axis for the (1,0) mode. A similar conclusion can be reached from the changes in resonant frequency in Fig. D-18.

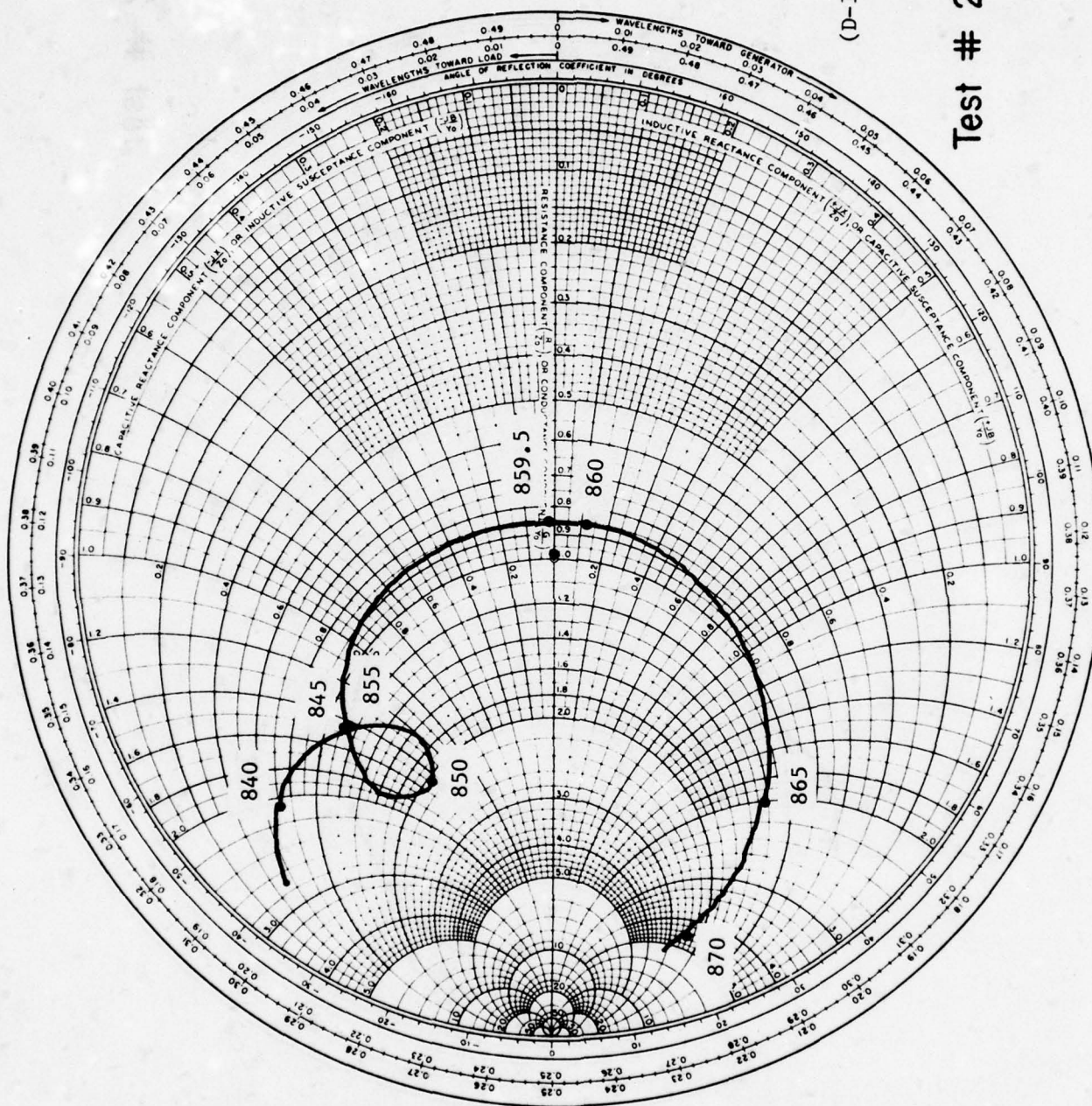
(c) The presence of a parasitic element increases the resonant frequency and slightly decreases the resonant conductance [of the (1,0) mode] for the first orientation and to a lesser degree for the second orientation.



(D-12)

Test # 2 $d = 0.1 \text{ cm}$

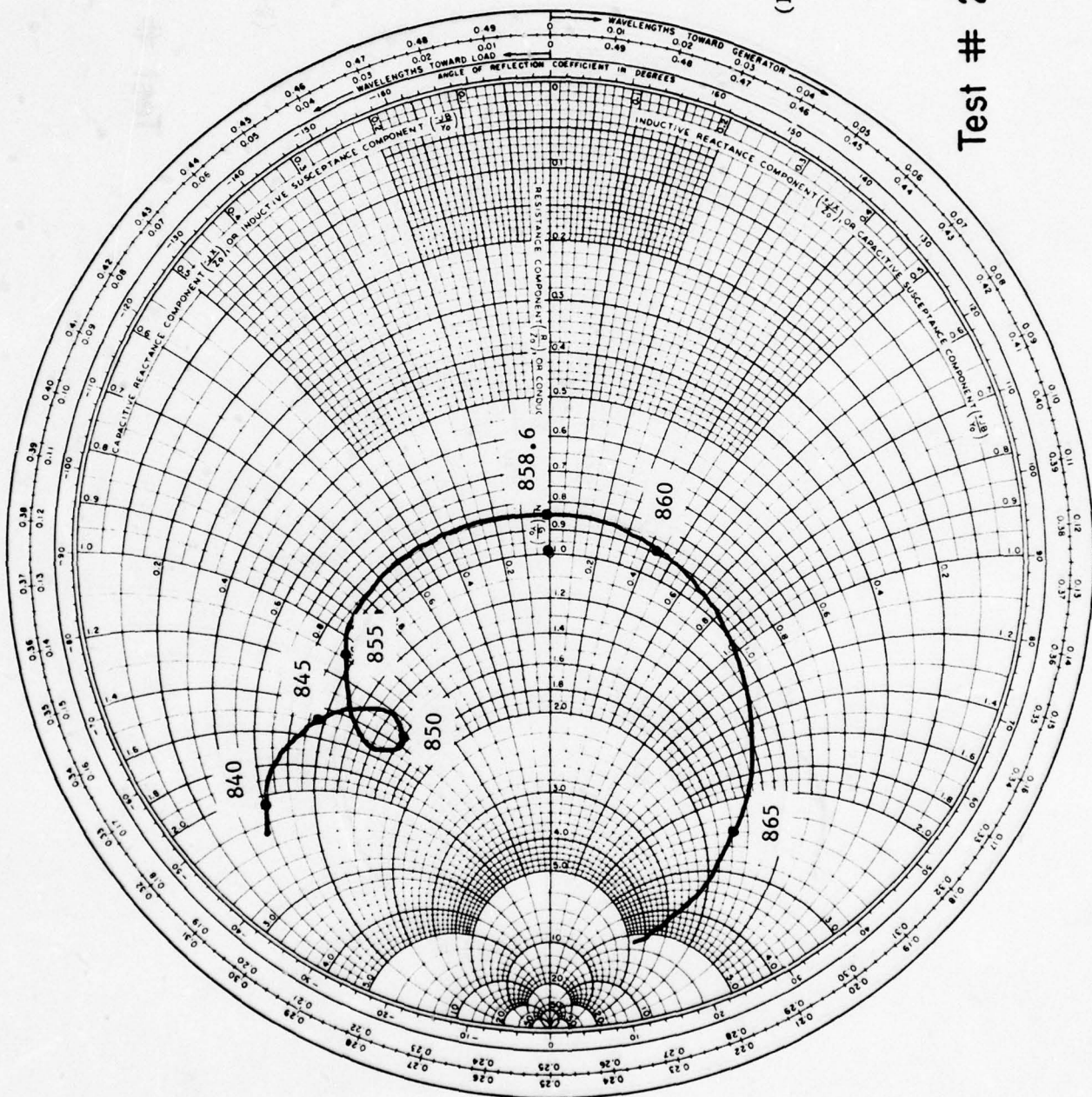
Figures D-12 to -18. Same as in Figures D-6 to D-11 except for the orientation being shown in Figure D-4 where d is the separation along the y-axis.



(D-13)

Test # 2 $d = 0.3\text{cm}$

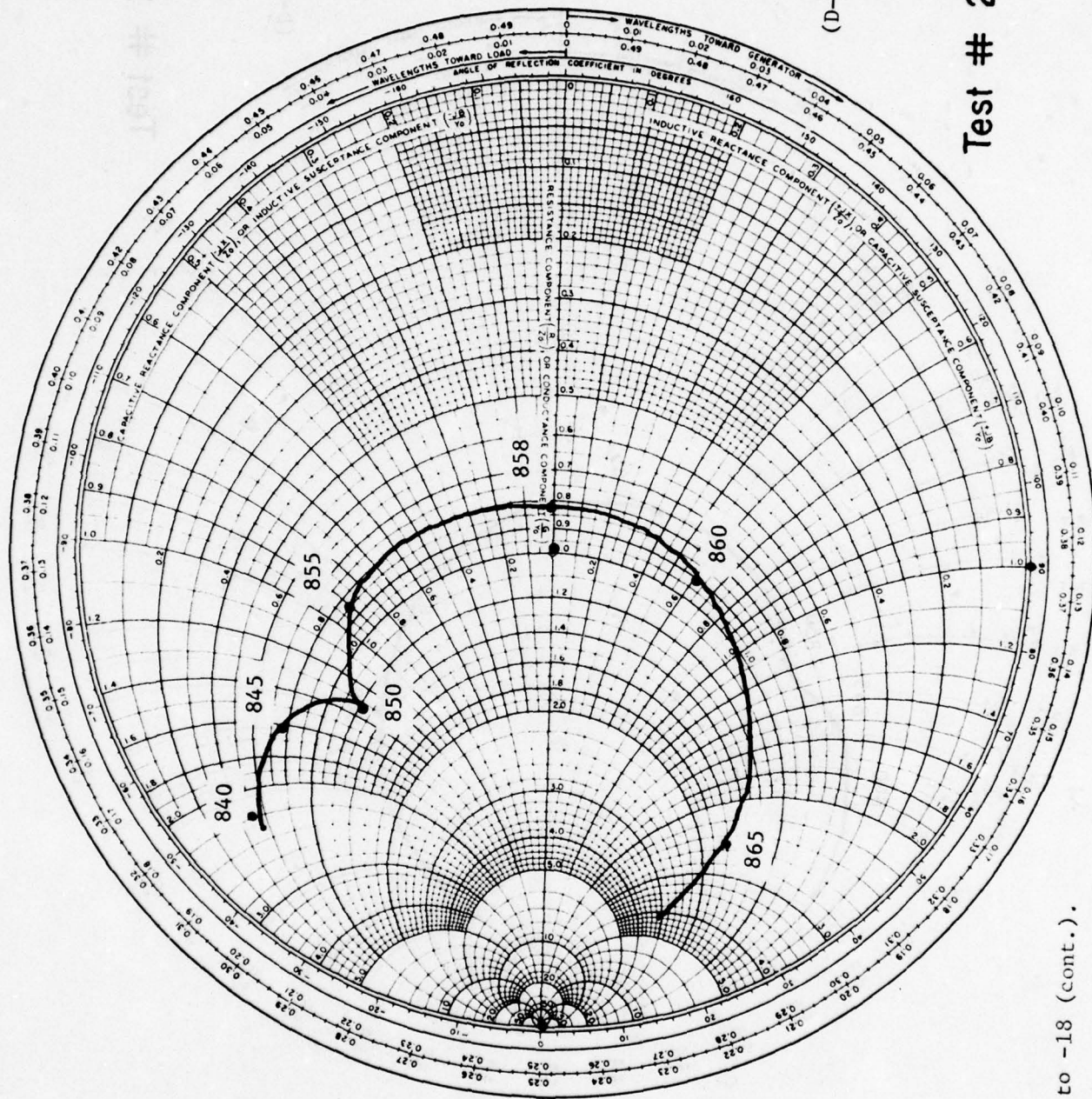
Figures D-12 to -18 (cont.).



(D-14)

Test # 2 $d = 0.5 \text{ cm}$

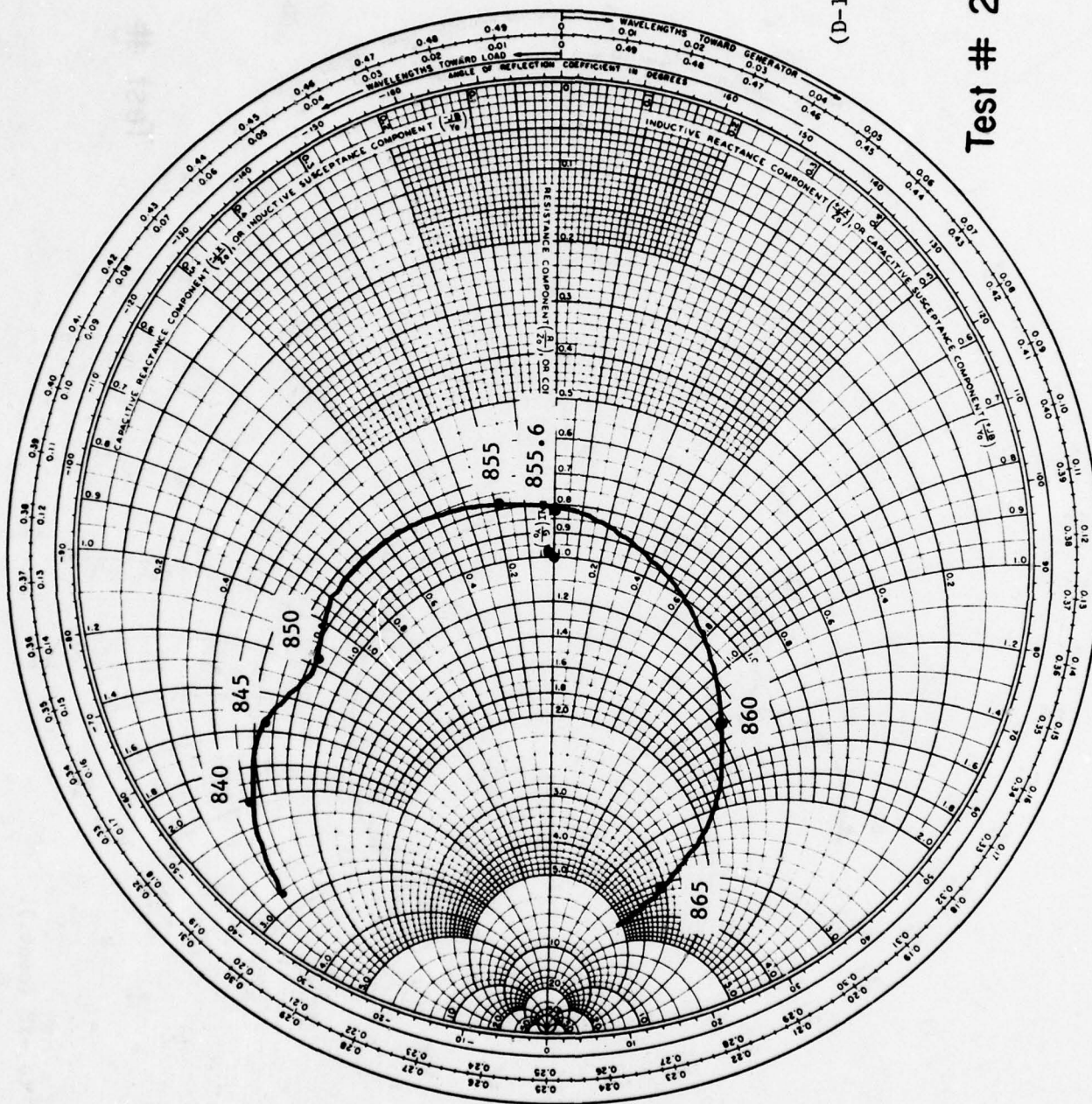
Figures D-12 to -18 (cont.).



(D-15)

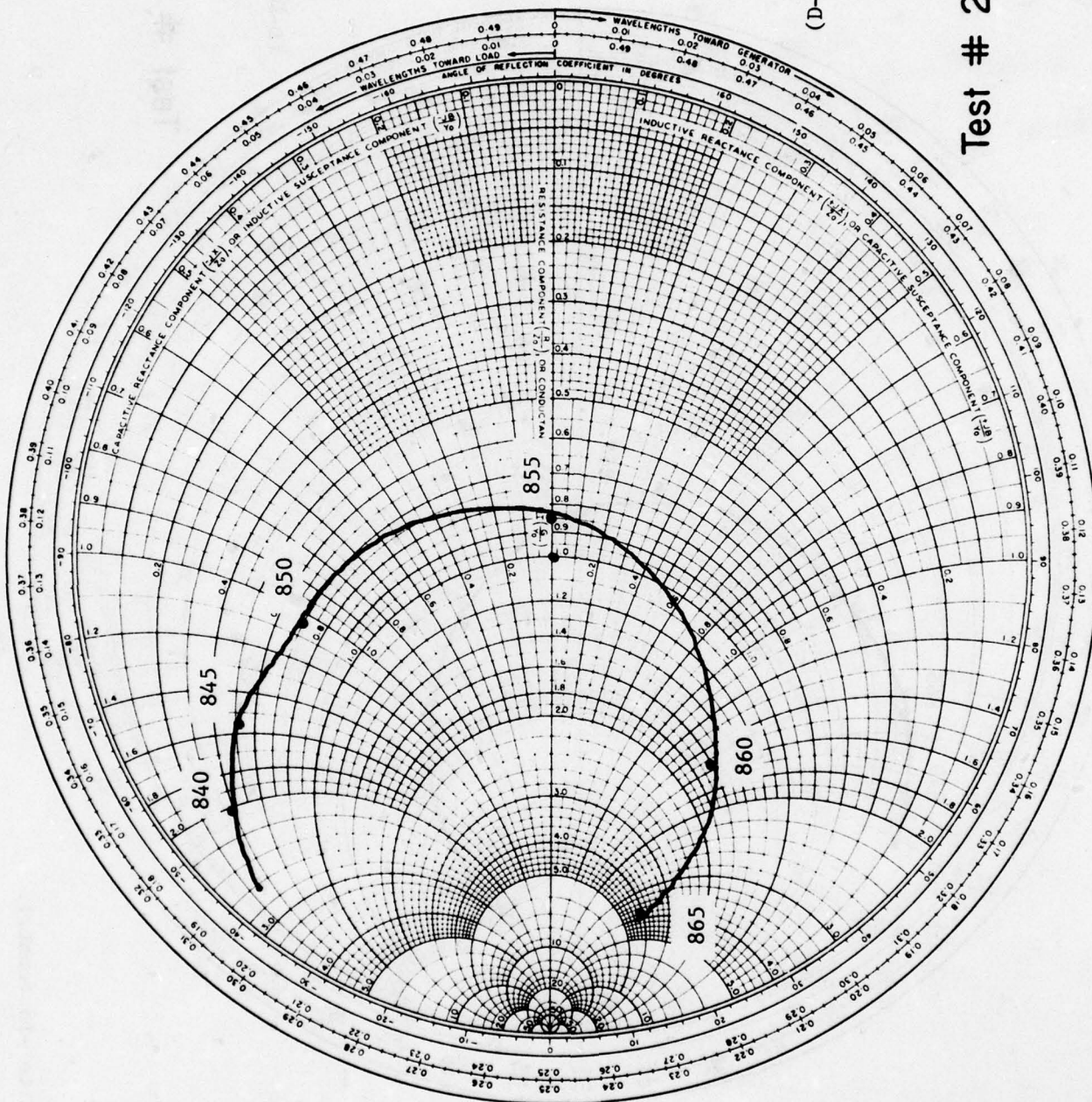
Test # 2 $d=0.8\text{cm}$

Figures D-12 to -18 (cont.).



Test # 2 d = 1.5 cm

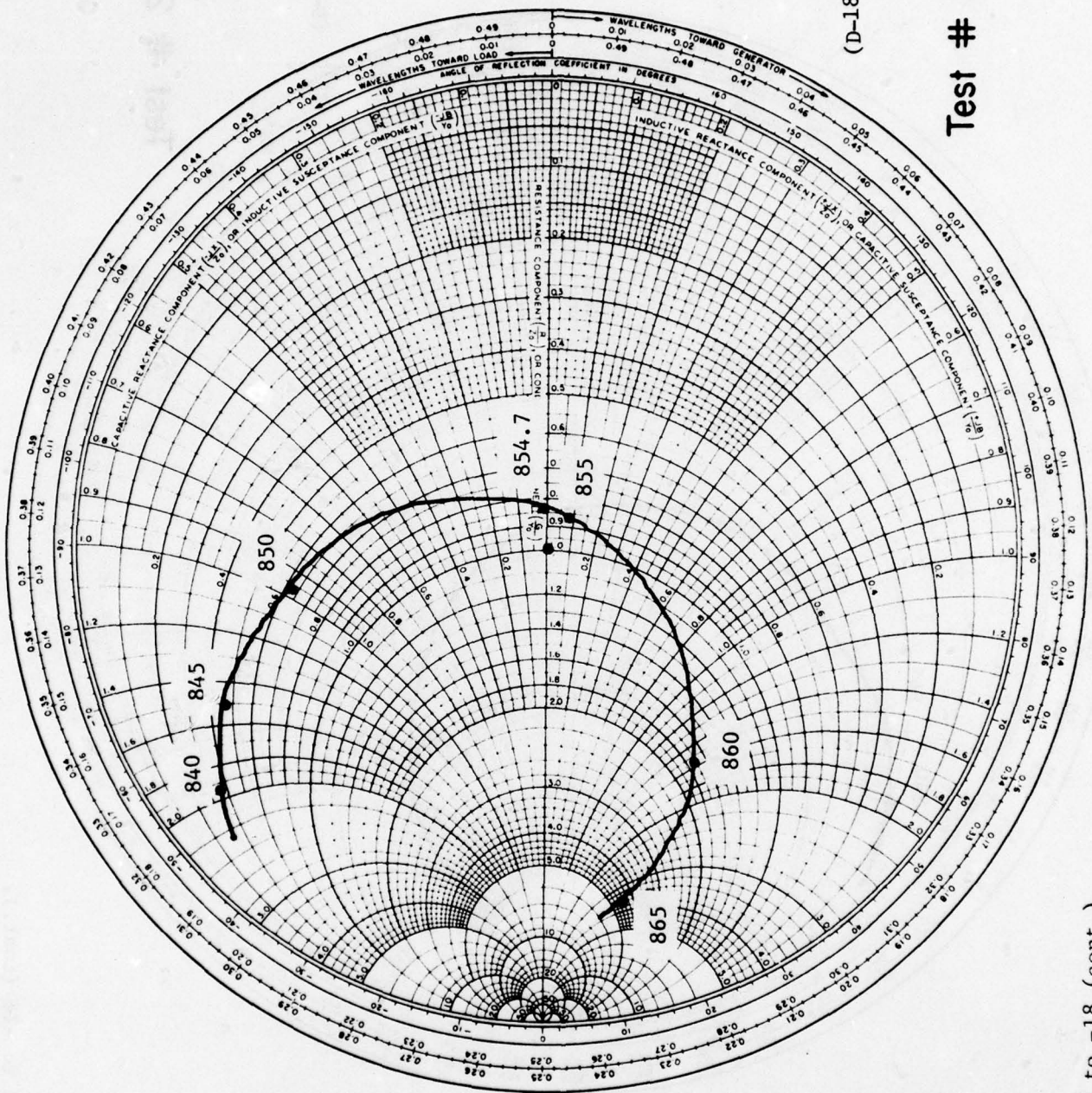
Figures D-12 to -18 (cont.).



(D-17)

Test # 2 d=2.5 cm

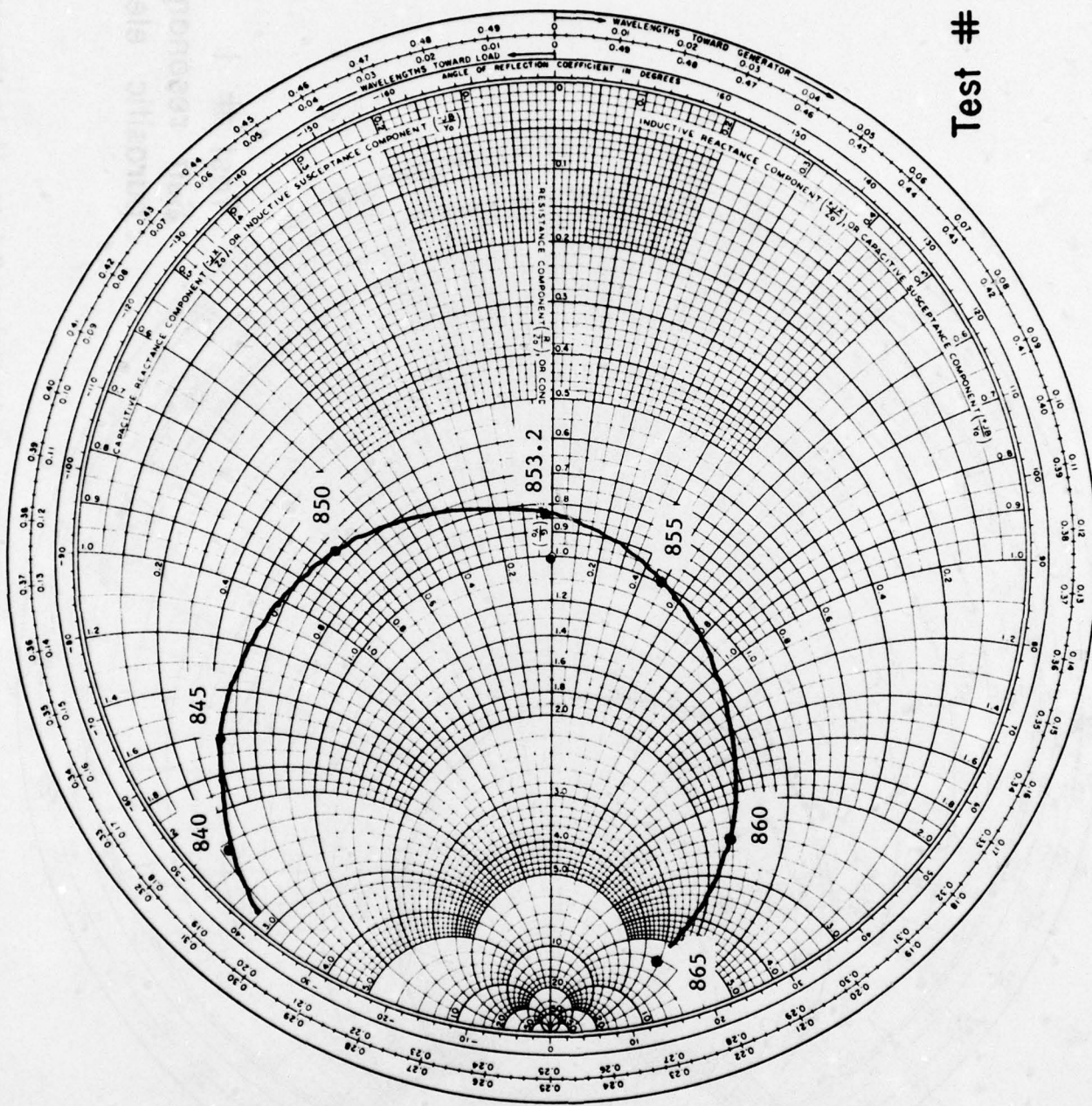
Figures D-12 to -18 (cont.).



(D-18)

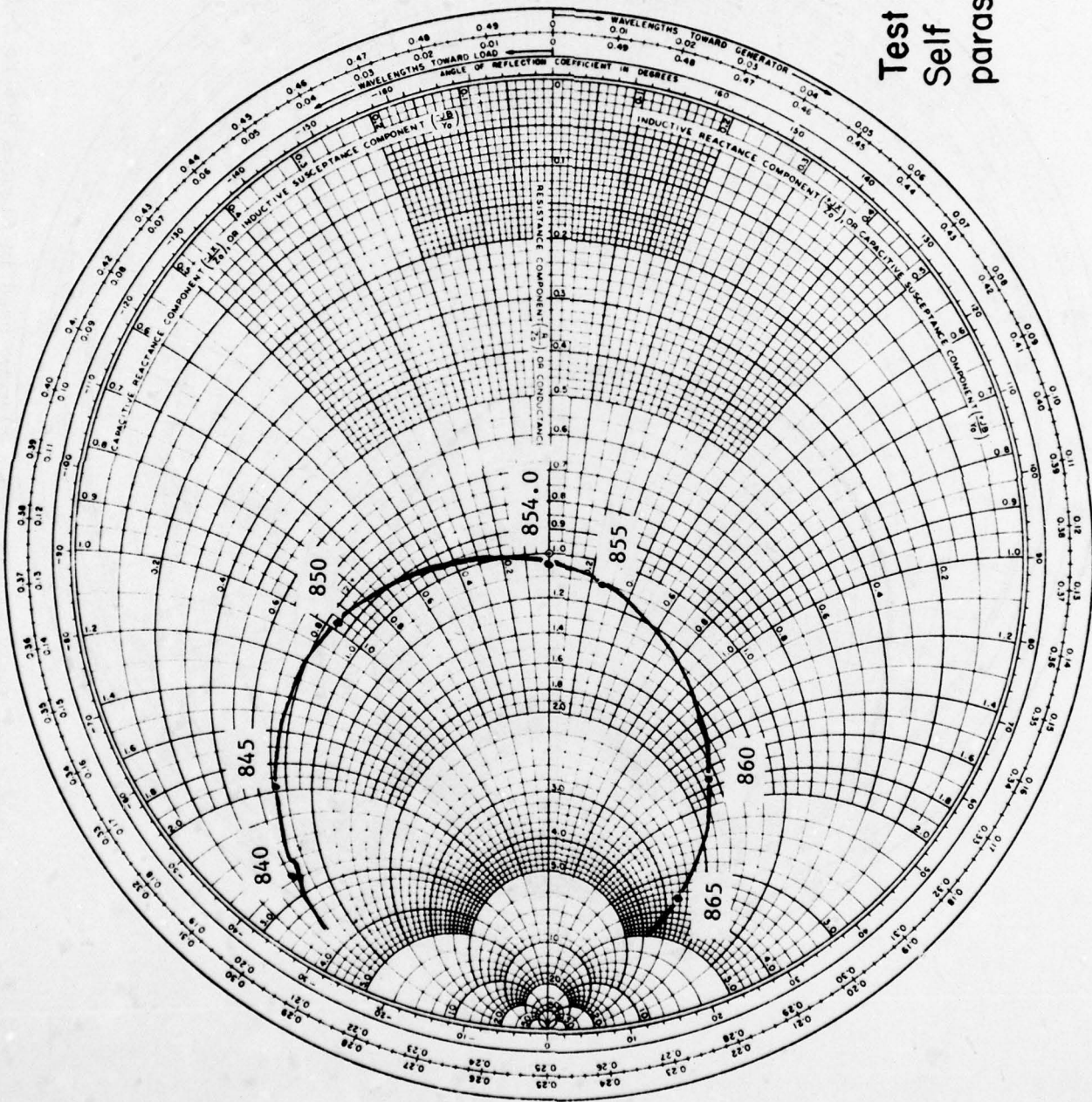
Test # 2 d = 3.5 cm

Figures D-12 to -18 (cont.).



Test # 1 $d = \infty$

Figure D-19. Input admittance locus of the driven element used in Figures D-6 to D-18 in the absence of the parasitic element.



Test # 1
Self resonance of
parasitic element

Figure D-20. Input admittance locus of the parasitic element used in Figures D-6 to -11 in the absence of the parasitic element.

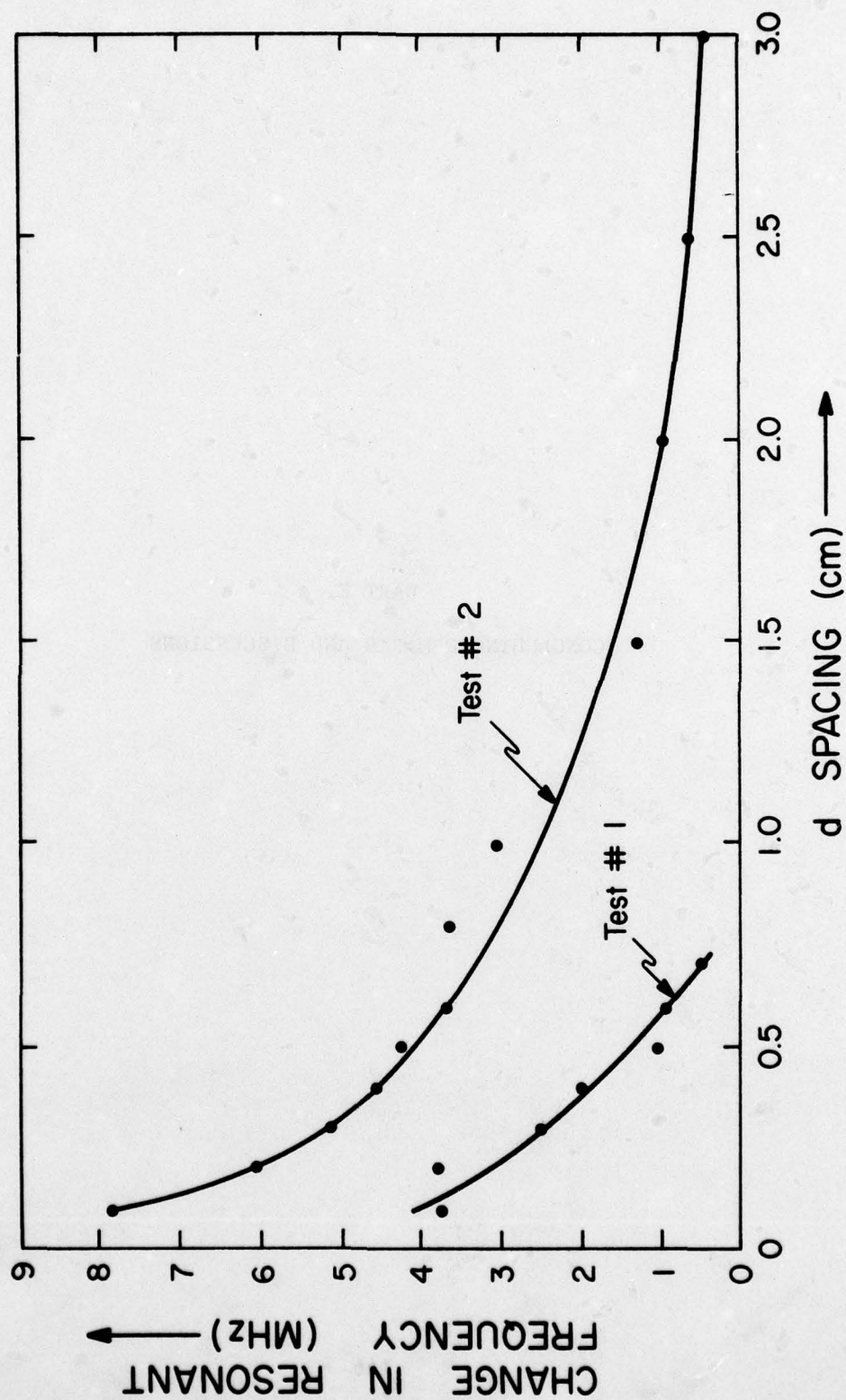
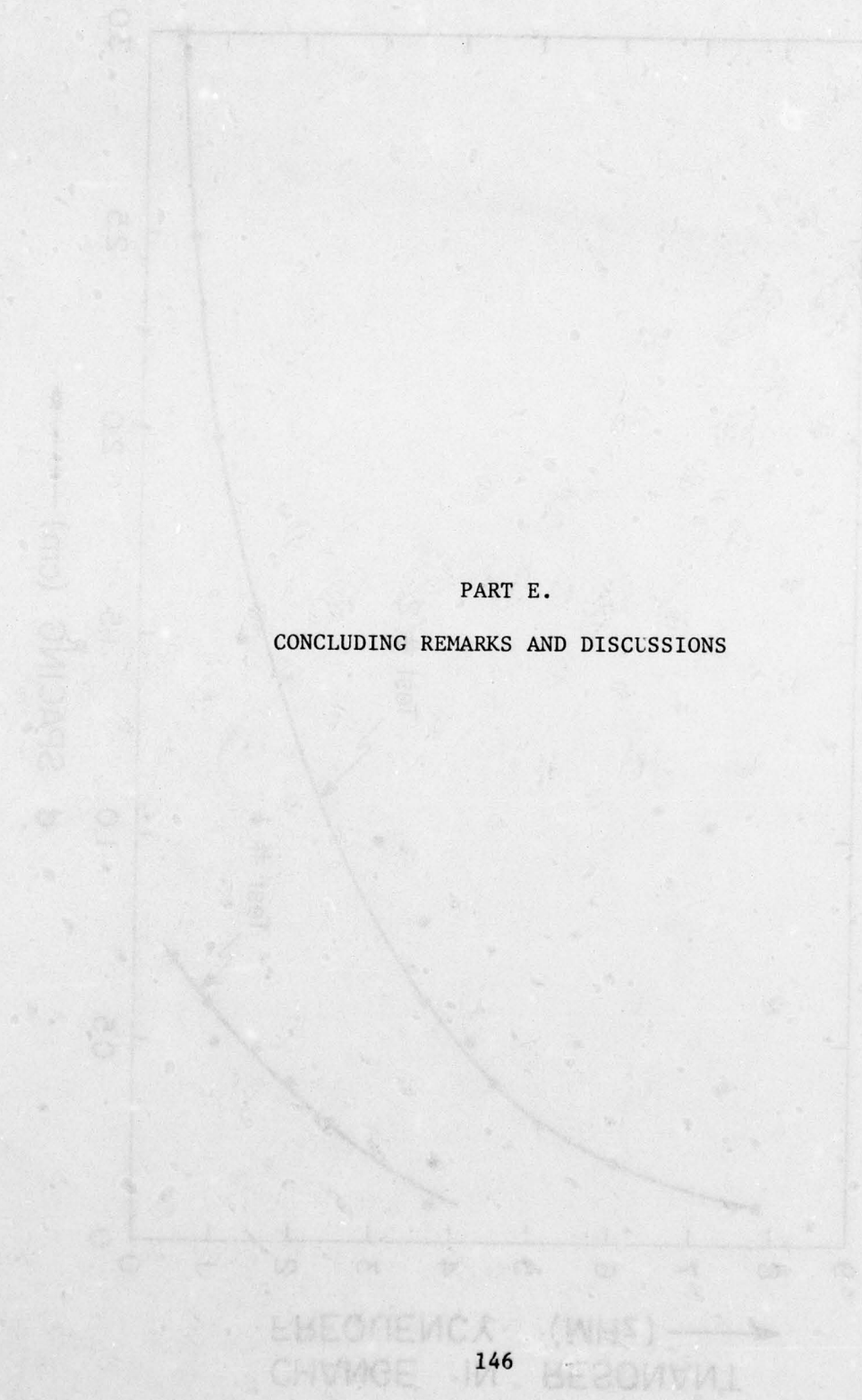


Figure D-21. Changes in resonant frequency vs. the separation d for the two orientations.

Figure 10. Plot of the change in the frequency of the resonant circuit as a function of the change in the inductance of the circuit.



PART E.

CONCLUDING REMARKS AND DISCUSSIONS

In this investigation a simple and useful theory has been established for analyzing and predicting two fundamental properties of microstrip antennas of many different shapes. To verify the theory numerous experiments were performed. In general there is a very good agreement between the theoretical and experimental results. The discrepancies appear to be within the accuracy of the present measuring system. It is possible to formulate the problem more rigorously, thus leading to a more accurate solution. Hopefully this work will be pursued further in the next contract period.

A few findings of interest are summarized in the following. It is hoped that this information will be useful in improving the design of microstrip antennas. An example is given at the end.

- (1) The behavior of the radiation pattern can be predicted by simply noting the relative modal field direction along the edges of the antenna. Even for a quantitative result, the needed computation is simple and straightforward.
- (2) In general, the impedance varies with frequency rapidly. Its locus in the Smith chart plot for frequencies around the resonance follows almost a perfect circle (at least for the dominant mode). The circle starts approximately at the zero impedance point at the low frequency end, crosses the real axis at real resonant impedance R_r at resonant frequency f_r , and goes back to nearly zero impedance at a frequency a few percent higher than f_r .

- (3) The resonant conductance can readily be computed from the formula $G_r = 1/R_r = P_t/|V|^2$ where P_t is the sum of real radiated power (computed from the pattern) and losses in the cavity (computed from the modal fields).
- (4) If the feed is located along the edge of the uniform modal field, the impedance is virtually independent of the feed location. If the feed is located along the edge of a non-uniform field, the impedance varies over a wide range, depending on the feed location. For example, for a rectangular microstrip antenna excited at (1,0) mode, G_r reaches a minimum when the feed is at the corner. The same conclusion applies for feed moving inside the cavity.
- (5) As the frequency sweeps through f_r , the susceptance changes the sign while the conductance G goes through a minimum, G_r . Thus G_r is a stationary point. Since B changes rapidly with frequency, the impedance locus would follow approximately a constant conductance circle G_r in the Smith chart plot.
- (6) For the dominant mode, most radiation takes place through the edge with uniform field (called the radiating edge). Thus G_r and efficiency both increase with the radiating edge length. For example, for a rectangular microstrip antenna of dimensions $a \times b$ (over a standard copper-cladded Rexolite 1/16" thick) and fed along the x-axis, G_r , normalized with respect to 1/50 mho, of the (1,0) mode has a value ranging from 0.1 (as $b \approx a/2$) to 1 (as $b \approx 4a$), corresponding to SWR of 1 to 10.
- (7) For higher-order modes, the radiating edge becomes longer in wavelength; thus in general from (6) G_r increases.

- (8) In general the coupling effect between a microstrip antenna and its feeder or between two microstrip antennas is small unless the spacing is very small (typically less than several times the thickness of the substrate). The interaction between two non-radiating edges is much stronger than between two radiating edges.
- (9) Parasitic elements behave like coupled multiple tuning circuits. With properly adjusted dimensions, the impedance locus tends to loop itself, in general, as many times as the number of parasites.
- (10) For some symmetrical geometries, such as squares and equilateral triangles, a degenerated eigenvalue may split into two close numbers if the symmetry is perturbed slightly. This may also result in the impedance-looping as stated in (9).
- (11) Because of the high frequency-sensitivity, the physical tolerance of the dimensions which are pertinent to a certain mode must be kept very small in order to obtain repeatable results.

The most challenging problem in microstrip antennas is how to broaden the bandwidth and increase the efficiency. Following the findings listed above, the bandwidth could be broadened by using a wide radiating edge and parasitic elements. To illustrate this possibility, four rectangular microstrip antennas were constructed, all having one side of the same dimension, 5.5", so as to maintain closely their resonant frequencies. The other sides are 3", 8.05" and 10", respectively. In addition, the fourth design consists of a rectangle 5.5" \times 8.05" with two parasitic elements of dimensions 5.7" \times 0.97", one on each side of the driven element. All of these are shown in Figs. E-1 to E-4 with their respective measured impedance loci. The feed point is roughly

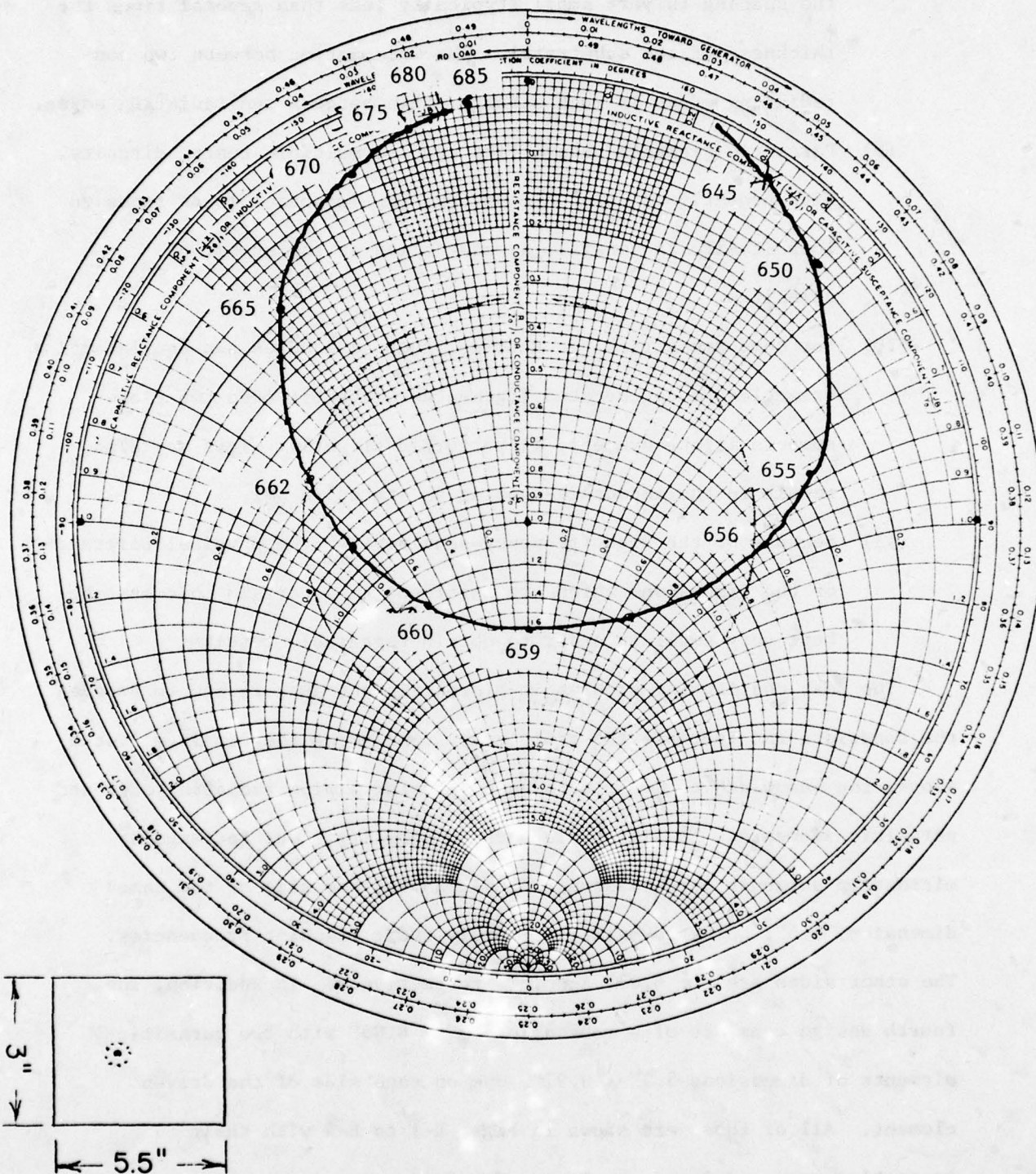


Figure E-1. Impedance locus of a rectangular microstrip antenna of 5.5" \times 3".

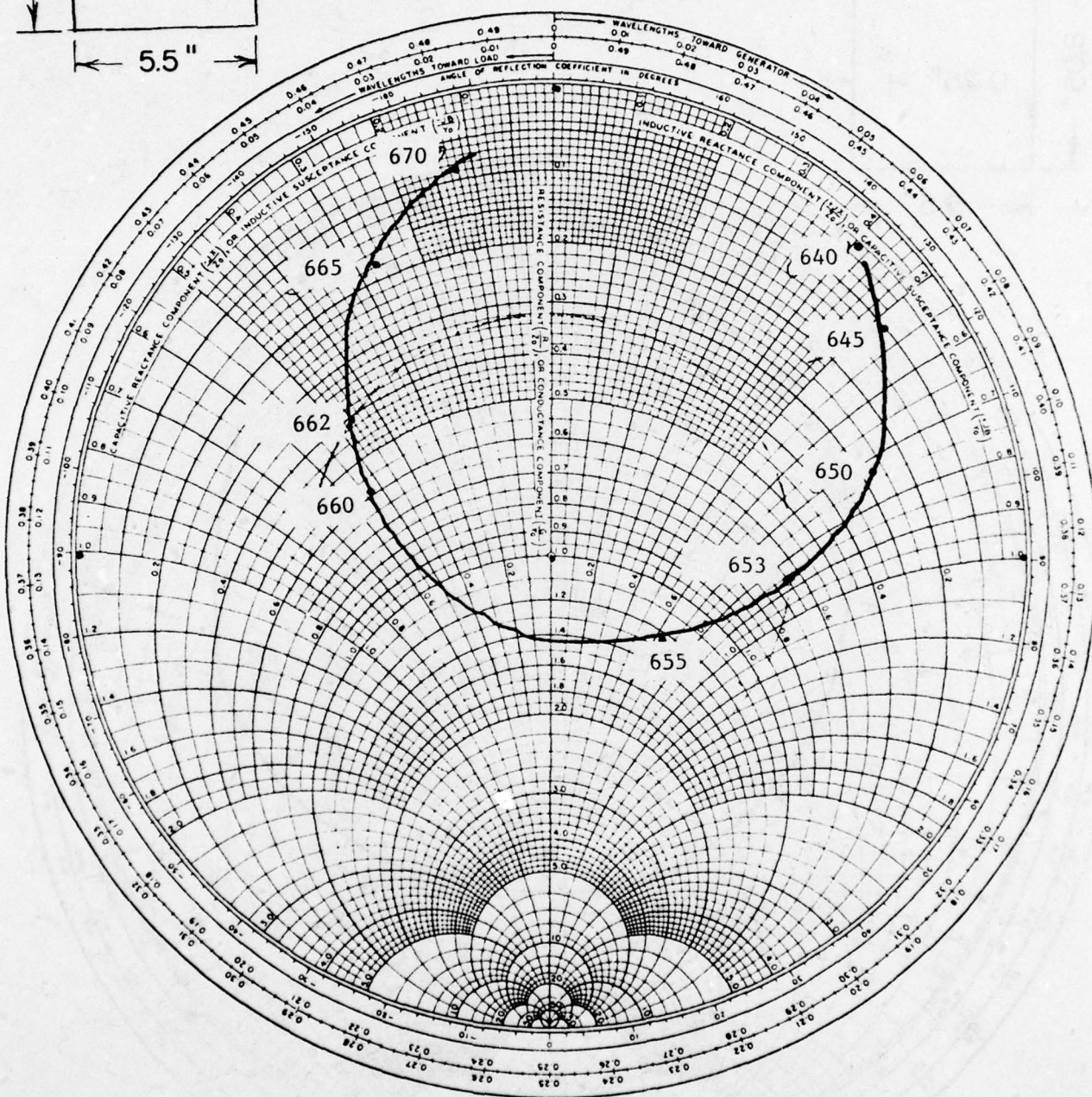
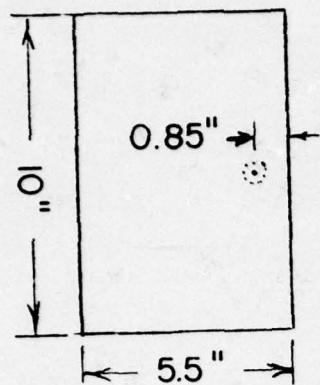


Figure E-3. Impedance locus of a rectangular microstrip antenna of 5.5" \times 10".

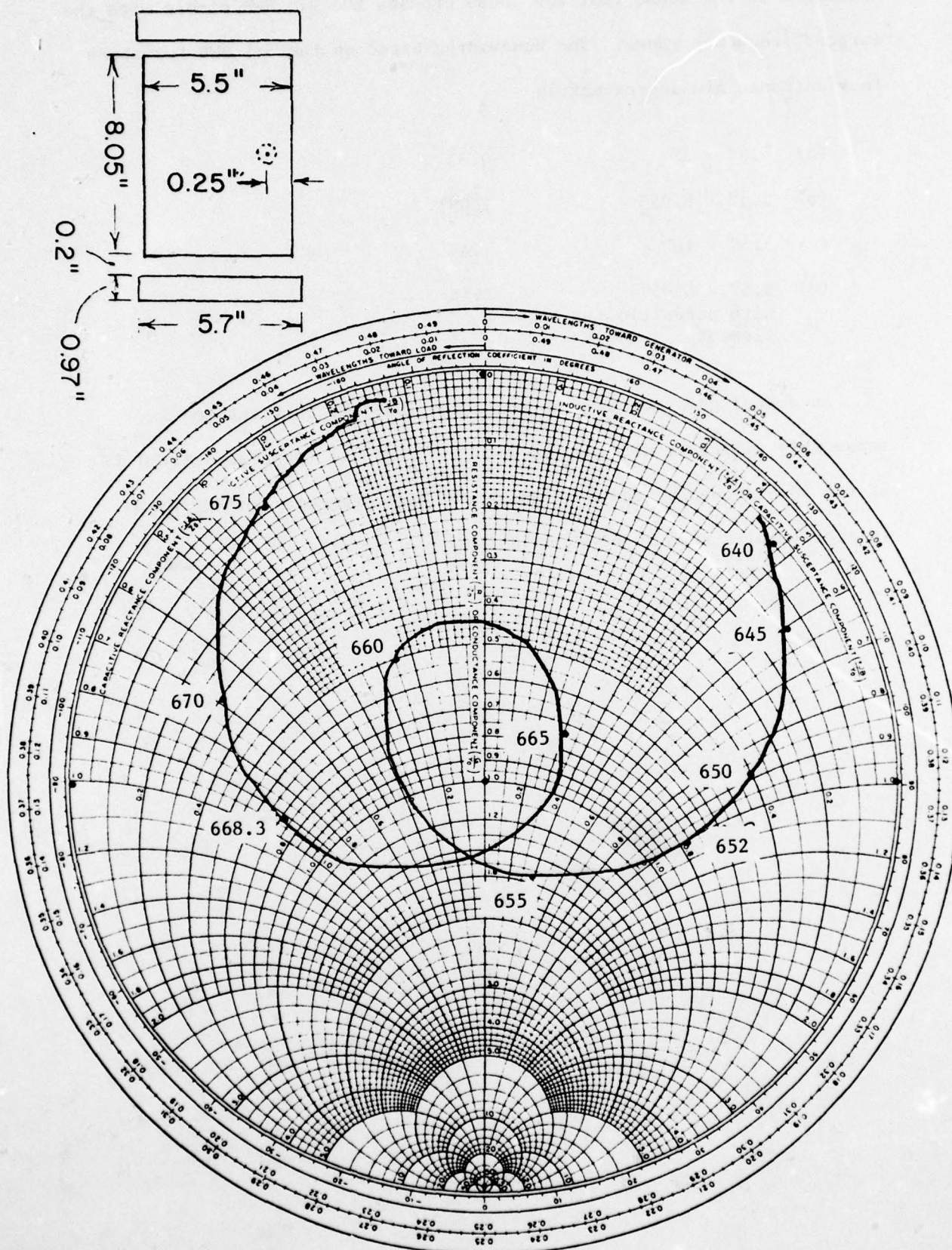


Figure E-4. Impedance locus of a rectangular microstrip antenna of 5.5" x 8.05" with two narrow parasitic elements, each of 5.7" x 0.97".

optimized in the sense that the locus crosses the 3:1 SWR circle with the largest frequency range. The bandwidths based on the 3:1 SWR for these four antennas are approximately

(a) 5.5" x 3"	0.9%
(b) 5.5" x 8.05"	1.09%
(c) 5.5" x 10"	1.4%
(d) 5.5" x 8.05" with parasitic elements	2.5%

An actual gain measurement indicated that the last antenna is reasonably efficient as compared with a $\lambda/2$ -dipole (approximately 0 dB at the low-frequency end to -5 dB at the high-frequency end). These initial results seem to be encouraging.

A decorative rectangular border with a repeating scroll-like pattern surrounds the central text.

MISSION *of* **Rome Air Development Center**

RADC plans and conducts research, exploratory and advanced development programs in command, control, and communications (C³) activities, and in the C³ areas of information sciences and intelligence. The principal technical mission areas are communications, electromagnetic guidance and control, surveillance of ground and aerospace objects, intelligence data collection and handling, information system technology, ionospheric propagation, solid state sciences, microwave physics and electronic reliability, maintainability and compatibility.